QUANTUM INFORMATION, ENTANGLEMENT AND MAGNETOMETRY WITH MACROSCOPIC GAS SAMPLES AND NON-CLASSICAL LIGHT

Kasper Jensen

QUANTOP
Niels Bohr Institute

The PhD School of Science
Faculty of Science
University of Copenhagen
Denmark

PhD thesis

February 2011

Academic supervisor

Prof. Eugene. S. Polzik

Assessment Committee

Local (Niels Bohr Institute) chairman

Prof. Christopher Pethick

External members

Prof. Gerhard Rempe
Prof. Irina Novikova

Summary

In the thesis several experiments using two room-temperature spin-polarized atomic ensembles are described.

Two-mode squeezed and entangled states of light are stored in a memory consisting of the two separate atomic ensembles. The fidelity of the storage surpasses a classical benchmark, demonstrating that our memory is a true quantum memory which is capable of preserving entanglement.

The atomic system is used as a sensor for radio-frequency magnetic fields. The magnetometer has a best sensitivity in the sub-femtoTesla/$\sqrt{\text{Hz}}$ range and is mainly limited by the quantum projection noise of the atoms. Using entanglement between the ensembles, the signal to noise ratio of the magnetometer is improved.

Long-lived entanglement between the two atomic ensembles is generated using dissipation as the entangling mechanism. By combining the dissipative dynamics with continuous measurements, the atomic ensembles can be maintained in an entangled steady state.

The atomic ensembles are used as a source for two-mode squeezed and entangled light. The squeezed light is generated in a single temporal mode and is naturally compatible with atomic systems based on the same (cesium) atom.

Resumé

I afhandlingen bliver adskillige eksperimenter diskuteret. Til forsøgene bliver der benyttet to ensembler af atomer, som er på gasform og bliver opbevaret i glasbeholdere ved stuetemperatur.

Par af sammenfiltrede lystilstande bliver overført til en kvantehukommelse bestående af de to ensembler. Overførslen af tilstandene sker med en større præcision end hvad er muligt med en klassisk hukommelse. Vores kvantehukommelse er dermed i stand til at gemme den ene halvdel af en sammenfiltret tilstand, og samtidig bevare sammenfiltringen med den anden halvdel.

Det atomare system bliver benyttet til at måle små radio-frekvens magnetfelter. Der opnås en sensitivitet til magnetiske felter i sub-femtoTesla/$\sqrt{\text{Hz}}$ området. Målingerne er hovedsageligt begrænset af kvante støj fra atomerne. Ved hjælp af sammenfiltrede atomer reduceres denne støj, således at signal til støj forholdet i målingen af magnetfeltet forbedres.

Ved hjælp af dissipative processer genereres sammenfiltrede atomare tilstande, som kan opretholdes i lang tid. Ved yderligere brug af kontinuerte målinger opretholdes atomerne i en stationær sammenfiltret tilstand.

Der genereres sammenfiltret lys ved hjælp at de to atomare ensembler. Lyset bliver udsendt i én enkelt tidslig mode og er kompatibelt med atomare systemer, som er opbygget af den samme slags atomer der er benyttet til at generere lyset.

Short abstract

In the thesis several experiments are described. Two-mode squeezed and entangled states of light are stored in a quantum memory consisting of two separate atomic ensembles. The atomic system is also used as a sensor for magnetic fields. The magnetometer has a high sensitivity mainly limited by quantum projection noise. Entanglement-assisted magnetometry is demonstrated. Long-lived atomic entanglement is generated by dissipation. By combining dissipation with continuous measurements, the atoms can be maintained in an entangled steady state. The atomic ensembles are used as a source for two-mode squeezed and entangled light. The squeezed light is generated in a single temporal mode and is naturally compatible with atomic systems based on the same (cesium) atom.

Preface

My PhD study has taken place at the Niels Bohr Institute in the QUANTOP [1] group led by professor Eugene Polzik. The thesis covers most of the work I have performed during my study. The experimental results presented in the thesis have been published or submitted [1, 2, 3, 4]. I have also worked on other experiments which are not discussed in this thesis. The results of those experiments have also been published [5, 6, 7]. All of the results have been obtained by a group effort, and the names of the people involved in the experiments can be found in the author listings of the relevant publications.

During my time in QUANTOP, I have worked with several people whom I would like to thank. In the beginning of my study Jacob Sherson and Thomas Fernholz taught me about the experiment and the setup. Hanna Krauter has been present during the whole time I have been part of the group. She has helped me countless times in the lab, and we have had a very good collaboration with many good results. I have enjoyed the long hours spent in the lab with Wojciech Wasilewski. During his stay I learned alot about both the theory and the experiment. Bo Melholt has been a good collaborator during the experiment with storage of squeezed light and a good office mate. I thank Misha Balabas for the good times when working together on the cells and the coatings. Jörg Helge Müller, Jürgen Appel and Anders Sørensen have always had the time to help when needed. It has been nice to spend time with Jonas Meyer Petersen, both when working together in the lab, but also during the breaks and outside on the bikes. In general, I thank the new and old members of the QUANTOP group for a friendly atmosphere during the years.

I also want to thank Dima Budker for his positive attitude and for a good stay in his group in Berkeley. There I enjoyed learning about atomic magnetometry. Thanks to Victor Acosta for good teamwork during my four month stay.

Finally I thank my supervisor Eugene Polzik for having me in the group. I started with a Bachelor project in the beginning of 2005, continued with a small project in 2006, a Master project from 2006 to 2007 and the PhD study from 2007 to 2011. It has been great learning so much physics from you and under your supervision.

[1] Danish National Research Foundation Center for Quantum Optics

List of publications

[I] K. Jensen, W. Wasilewski, H. Krauter, T. Fernholz, B. M. Nielsen, M. Owari, M. B. Plenio, A. Serafini, M. M. Wolf, and E. S. Polzik. Quantum memory for entangled continuous-variable states. *Nature Physics*, 7:13–16, 2011. http://dx.doi.org/doi:10.1038/nphys1819

[II] W. Wasilewski, K. Jensen, H. Krauter, J. J. Renema, M. V. Balabas, and E. S. Polzik. Quantum noise limited and entanglement-assisted magnetometry. *Phys. Rev. Lett.*, 104(13):133601, 2010. http://dx.doi.org/10.1103/PhysRevLett.104.133601

[III] H. Krauter, C. A. Muschik, K. Jensen, W Wasilewski, J. M. Petersen, J. I. Cirac, and E. S. Polzik. Entanglement generated by dissipation. arXiv:1006.4344v1, 2010. http://arxiv.org/abs/1006.4344

[IV] W. Wasilewski, T. Fernholz, K. Jensen, L. S. Madsen, H. Krauter, C. Muschik, and E. S. Polzik. Generation of two-mode squeezed and entangled light in a single temporal and spatial mode. *Opt. Express*, 17:14444–14457, 2009. http://dx.doi.org/doi:10.1364/OE.17.014444

[V] M. V. Balabas, K. Jensen, W. Wasilewski, H. Krauter, L. S. Madsen, J. H. Müller, T. Fernholz, and E. S. Polzik. High quality anti-relaxation coating material for alkali atom vapor cells. *Opt. Express*, 18(6):5825–5830, 2010. http://dx.doi.org/doi:10.1364/OE.18.005825

[VI] K. Jensen, V. M. Acosta, J. M. Higbie, M. P. Ledbetter, S. M. Rochester, and D. Budker. Cancellation of nonlinear Zeeman shifts with light shifts. *Phys. Rev. A*, 79(2):023406, 2009. http://dx.doi.org/10.1103/PhysRevA.79.023406

[VII] T. Fernholz, H. Krauter, K. Jensen, J. F. Sherson, A. S. Sørensen, and E. S. Polzik. Spin squeezing of atomic ensembles via nuclear-electronic spin entanglement. *Phys. Rev. Lett.*, 101(7):073601, 2008. http://dx.doi.org/10.1103/PhysRevLett.101.073601

[VIII] K. Jensen, W. Wasilewski, H. Krauter, T. Fernholz, B. M. Nielsen, J. M. Petersen, J. J. Renema, M. V. Balabas, M. Owari, M. B. Plenio, A. Serafini, M. M. Wolf, C. A. Muschik, J. I. Cirac, J. H. Müller, E. S. Polzik. Quantum memory, entanglement and sensing with room temperature atoms. ICAP 2010 conference proceedings. *J. Phys.: Conf. Ser.* 264:012022. http://dx.doi.org/10.1088/1742-6596/264/1/012022.

[IX] K. Jensen, W. Wasilewski, H. Krauter, Hanna; J. J. Renema, M. V. Balabas, E.S. Polzik. Quantum Noise Limited and Entanglement-Assisted Magnetometry. in Quantum Electronics and Laser Science Conference, OSA Technical Digest (CD) (Optical Society of America, 2010), paper QThN6.
http://www.opticsinfobase.org/abstract.cfm?URI=QELS-2010-QThN6

[X] K. Jensen, W. Wasilevski, H. Krauter, J. J. Renema, B. M. Nielsen, T. Fernholz and E. S. Polzik.
Room-temperature atomic ensembles for quantum memory and magnetometry. Proceedings of the 19th International Conference on Laser Spectroscopy (ICOLS 2009).

[XI] H. Krauter, J. F. Sherson, K. Jensen, T. Fernholz, J. S. Neergaard-Nielsen, B. M. Nielsen, D. Oblak, P. Windpassinger, N. Kjærgaard, A. J. Hilliard, C. Olausson, J. H. Müller, and E. S. Polzik. Quantum Interface between Light and Atomic Ensembles. Proceedings of the XVIII International Conference on Laser Spectroscopy (ICOLS 2007) p. 113 (World Scientific, Singapore, 2008).
http://www.worldscibooks.com/physics/6818.html

[XII] T. Fernholz, K. Jensen, B. Julsgaard, H. Krauter, J. F. Sherson, E.S. Polzik. Deterministic Quantum Interface between Light and Room Temperature Atomic Ensembles. Frontiers in Optics (FiO) 2007 paper.
http://www.opticsinfobase.org/abstract.cfm?URI=FiO-2007-FWN4

[XIII] Kasper Jensen, Daniel Oblak and Eugene S. Polzik. Kvanteinformation og kommunikation: den næste kvanterevolution (Quantum Information and Communications: the next quantum revolution). University of Copenhagen, Almanac 2010. ISBN: 978-87-17-04076-2

Contents

Chapter 1

Introduction

1.1 Entanglement

Entanglement is the common theme for the experiments presented in this thesis. EPR entanglement was first introduced by Einstein, Podolsky and Rosen in 1935 [8], and can be described as non-local non-classical correlations between two subsystems. In the original paper entanglement is described in terms of position and momentum operators of two particles which are correlated in the following way: $\hat{p}_1 + \hat{p}_2 = 0$ and $\hat{x}_1 - \hat{x}_2 = x_0$. Instead of the continuous position and momentum operators one can consider discrete variables such as the spin-up and spin-down of a spin-1/2 particle. An example of an entangled state is the singlet state $|\uparrow\rangle_1 |\downarrow\rangle_2 - |\downarrow\rangle_1 |\uparrow\rangle_2$, which describes the spins of two spin-1/2 particles. One imagines that the two particles interact in some way, such that the singlet state is produced. Then the two particles travel to two different locations. According to Quantum Mechanics, if one performs a measurement of the spin of particle one and obtain the result $|\uparrow\rangle_1$, the spin of the second particle is projected onto the state $|\downarrow\rangle_2$. The measurement of particle one therefore changes the state of particle two, even though the particles are at different locations. This was a paradox for Einstein, Podolsky and Rosen, since they assumed that the reality should be described by a local theory. They therefore concluded that Quantum Mechanics is an incomplete theory. One can think of alternative hidden variables theories which can be used to explain entanglement. The predictions of local hidden variable theories and Quantum Mechanics differs, and the theories can be tested using Bell inequalities [9]. Now we of course believe that Quantum Mechanics is the correct description of the reality, and we use entanglement to describe non-local and non-classical correlations.

1.2 Quantum Information

One can use small quantum systems to transmit, store and process information. A piece of information is typically described in terms of a bit, which can take the value 0 or 1. Quantum Mechanics allows a two-level system to be in a superposition of two states, which leads to the concept of quantum bits (qubits). A qubit can be in the states 0 and 1 simultaneously, and the general qubit can be written as $|\Psi\rangle = a\,|0\rangle + b\,|1\rangle$, where a and b are two complex numbers which satisfy $|a|^2 + |b|^2 = 1$. An important field in Quantum Information is Quantum Cryptography, where qubits are used to send secure information using for instance the BB84 protocol [10]. The qubits can also be used as building blocks for a quantum computer. The Hilbert space of N two-level systems has the dimension 2^N which grows exponentially with the number of qubits. Simulations of large quantum systems are therefore impossible on today's classical computers, since a classical computer needs (at least) 2^N bits to do the simulation. On the other hand, a future quantum computer would be able to simulate N two-level systems using only N qubits.

In Quantum Information, light is used as flying qubits for transmitting quantum information, while atomic systems are used as stationary qubits for storing quantum information. A memory for quantum information is therefore an important ingredient in a future quantum information network [11]. Due to optical losses entangled states can not be send directly over long distances. A solution to the problem is to use entanglement swapping between entangled intermediate repeater stations consisting of quantum memories [12].

Quantum teleportation [13] is one of the most intriguing possibilities in Quantum Communications. Using quantum teleportation, it is possible to transmit information from A to B in a way such that the information was never in between the two parties. This way of transmitting information is appealing. In order to teleport an unknown state, A and B need to share an entangled state. The creation and distribution of entanglement is therefore very important in Quantum Information.

1.3 Quantum Metrology

Quantum Mechanics imposes certain fundamental limits to measurements. These limits are related to the Heisenberg uncertainty relation. The limits can be surpassed only with the use of entanglement. Entanglement has therefore applications in metrology. One can for instance improve the phase sensitivity of a Mach-Zender interferometer by using entangled $NOON$-states [14]. Squeezed states which has reduced uncertainty in one variable (and increased uncertainty in the conjugate variable) can also be used to improve measurement sensitivity. If some parameter is measured using light, the shot noise of light will make the

measurement uncertain. Using squeezed light, it is possible to reduce the uncertainty below the shot noise level. Squeezed light is of importance in applications where very small signals are measured such as in a gravitation wave detector.

When performing a measurement on a quantum system, the system is disturbed by the measurement. This is called the backaction of the measurement. For instance, in an interferometer (such as a gravitational wave detector) the measurement of the phase shift can be limited by the radiation pressure from the light on the mirrors. However, backaction evading measurements can be done by using Quantum Non-Demolition (QND) techniques, where the backaction noise is directed into a variable which is conjugate to the measured variable.

Entangled states of atoms can also be used in metrology such as in atomic clocks where the projection noise of atoms limits the accuracy of time. Such an entanglement-assisted atomic clock was demonstrated recently in our group [15].

1.4 Cell experiment

The work presented in this thesis is based on earlier work done in the QUANTOP group led by Eugene Polzik. The subgroup of the QUANTOP group I have worked in is called the "cell experiment". The experiments in the cell experiment are done using one or two room-temperature atomic ensembles of cesium atoms kept in glass cells, and the experiments have been going on for more than 10 years now. Earlier achievements include entanglement between the ensembles [16], quantum memory for coherent light states [17] amd quantum teleportation [18]. Many details regarding our light-atom interface and discussions of the above mentioned experiments can be found in the recent review [19]. In the cell experiment, continuous variables are used for describing our system (see the book [20] for an overview of quantum information with continuous variables). Future work might involve experiments with single photons and single collective exitations in the atomic ensembles (see the outlook in Sec. 8.2).

1.5 Other atomic systems

All the experiments described in this thesis utilize room-temperature atomic ensembles of cesium atoms contained in paraffin-coated glass cells. There are of course many other systems which are used for quantum information purposes, and I would like to mention a few.

In our experiment, the paraffin coating prevents decoherence due to collisions with the cell walls. An alternative approach to avoid decoherence due to wall-collisions is to fill the glass cell with buffer gas, such that the room-temperature atoms can not move (instead they diffuse slowly) and thereby do not hit the cell walls. Buffer gas cells have been used as a memory for classical light pulses

[21] and squeezed vacuum [22] using the method of electro-magnetically induced transparancy (EIT). Single photons have been generated and stored using two separate buffer gas cells [23], and also squeezed light has been generated using a buffer gas cell [24].

Cold atomic ensembles have been used for many experiments in the fields of quantum information and quantum metrology. The ensembles have been entangled [25] using the DLCZ scheme [12], and similar to the experiments with buffer gas cells, single photons emitted from one ensemble have been stored in a second ensemble [26]. Recently storage times in the millisecond range have been demonstrated [27, 28]. Cold atomic ensembles can be used as magnetometers [29], and also magnetic field measurements with Bose-Einstein condensates have been demonstrated [30, 31]. Such cold atomic magnetometers have a high spatial resolution due to the small size of the ensemble. However, the cold atomic ensembles are less sensitive to the magnetic field as compared to the cm-sized atomic magnetometers based on room-temperature (or high temperature) atomic vapours due to the smaller number of atoms.

1.6 Outline

- Chapter 2: The interaction between atoms and light is discussed. Of particular importance is the Quantum Non-Demolition (QND) interaction by which one can measure an atomic spin componenent without changing it. The QND interaction can be used to measure the atomic state, to generate entanglement between the ensembles and as a component in a quantum memory protocol. Recently we discovered that the interaction between polarized light and spin-polarized atomic ensembles is better described by a "swap and squeezing" interaction. The discovery of the swap and squeezing interaction has been very important for the work presented in this thesis. Both in terms of understanding how atoms and light interact, but also in terms of motivating new experiments such as the generation of two-mode squeezed light presented in chapter 4 and the entanglement generated by dissipation as presented in chapter 7. The swap and squeezing interaction is described in detail in this chapter, and we calculate useful input-output equations for the light and atomic operators which are used throughout the thesis to describe the performed measurements and experiments.

- Chapter 3: The experimental details common to all the performed experiments are discussed in this chapter. Some of the experimental details are also presented in the earlier theses from our group [32, 33] and in the thesis of Hanna Krauter [34]. In the beginning of my PhD study, a new data-aquisition method was implemented where the two-time correlation function $C(t, t')$ of the detector signals was recorded instead of the inte-

grated signal variances (which are time-independent). Using the recorded two-time correlation function, more information can be extracted from the measurements than was possible before. The details of the data-analysis are described in this chapter and also in chapter 4.

After the discovery of the swap and squeezing interaction, a mean value method for measuring the light-atom coupling constant κ^2 was implemented. This coupling constant is an important parameter which is needed for reconstucting the atomic state from the measured light. The mean value method is also used to verify the swap and squeezing input-output equations. Finally, we present measurements of the atomic noise and of entanglement between the two atomic ensembles generated by near QND measurements.

- Chapter 4: Two-mode squeezed and entangled light is generated using the two atomic ensembles as a source. The squeezing is centered around the atomic Larmor frequency, which in our case is chosen to be 322 kHz, and has a bandwidth of a few hundred of Hertz set by the atomic transverse relaxation T_2-time. The obtained squeezing of 3.6 dB is in a single temporal and spatial mode and is naturally compatible with atomic memories based on the same atom (cesium) as was used to create the squeezing. The swap and squeezing interaction theory is here used to explain the generation of the two-mode squeezed light.

- Chapter 5: We demonstrate a radio-frequency atomic magnetometer consisting of two oppositely spin-polarized atomic ensembles. Using the swap and squeezing interaction, we achieve the backaction evading measurement of the magnetic field and the suppression of the meter noise (the shot noise of the probing light). The measurement is mainly limited by the projection noise of atoms orignating from the Heisenberg uncertainty relation. We obtain the best sensitivity in the sub-femtoTesla/$\sqrt{\text{Hz}}$ range comparable with the sensitivity of the state-of-the-art atomic magnetometer which operates with 10^4 times more atoms. Furthermore, using entanglement between the two atomic ensembles, we demonstrate that the magnetometer signal to noise ratio can be improved for high bandwidth RF magnetic pulses.

- Chapter 6: A new class of states, the displaced two-mode squeezed light states are stored in a quantum memory consisting of two separate atomic ensembles. The input light is squeezed by 6.0 dB, and 18 different light states with different squeezing phases and displacements in X-P phase space are stored in the memory. The storage is characterized in terms of the fidelity which is defined as the average overlap between the input and stored states for a given input distribution. A classical benchmark fidelity is calculated, and we obtain the experimental fidelity which is higher than the benchmark fidelity.

- Chapter 7: The two atomic ensembles are entangled using dissipation as the entangling mechanism. The method is robust and leads to states which are entangled for up to 40 ms. This duration is much longer than the millisecond lifetimes previously obtained with atomic ensembles entangled by QND measurements.

  We also combine the dissipative dynamics with continuous measurements of the atomic spins. With the combined method, entanglement is created in a steady state, and can in principle be maintained for ever. In the experiment we demonstrate the steady state entanglement which is maintained for the long duration of one hour.

- Chapter 8: We summarize the main results presented in the previous chapters. We also provide an outlook for the future of the cell experiment.

Chapter 2

Theory

2.1 Introduction

In this chapter it is described how a gas of spin-polarized atoms and a pulse of polarized light interact. First the two systems are introduced, and canonical operators are defined for both systems. Then we give both an overview and present detailed calculations describing the light-atom interaction. Several kinds of interactions are described: the Quantum Non-Demolition (QND) interaction, the single cell interaction, and the swap and squeezing interaction.

The QND interaction is implemented in the experiments using two oppositely oriented atomic ensembles. The QND interaction has been described earlier in the previous PhD theses [32, 33] and has been used in earlier experiments in our setup such as the creation of entanglement between the two ensembles [16] and for the quantum memory for coherent states [17].

Even though the input-output equations describing the QND interaction has been derived in the previous PhD theses, I will go through the details of some of the steps in the derivation. This is done since several of the steps in the derivation of the QND input-output equations are similar to the steps in the more complicated derivation of the input-output equations for the swap and squeezing interaction.

The interaction between a single ensemble and a pulse of light is also discussed. The presented input-output equations will be useful when comparing the single cell interaction and the two cell QND interaction.

The swap and squeezing interaction valid for two oppositely oriented ensembles was first described in our Optics Express paper [4]. The paper both presents the theory which is detailed in this chapter and also experimental results which are presented in chapter 4.

Atomic decoherence is not included in the swap and squeezing theory presented in [4]. However, in the derivation of the the swap and squeezing input-output equations in this chapter, decoherence is included in the model. The

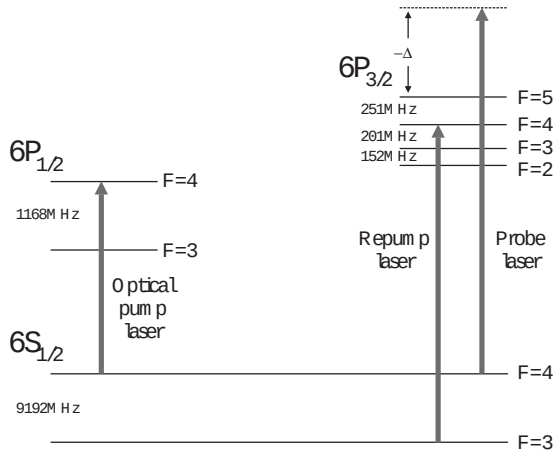

Figure 2.1: Cesium-133 level scheme and laser frequencies. Figure is from [32].

input-output equations with decoherence included are used throughout the thesis and in the experimental work when analyzing the data and extracting information of the atomic state from the measured light variables. The equations have been used in data-analysis of published data, but the equations themselves have not been published before. Details of the swap and squeezing interaction theory are also presented in the PhD thesis [34] of Hanna Krauter who has been working on the experiment during the same period as I.

Finally, the input-output equations and the coupling strength for the QND interaction and the swap and squeezing interaction are compared. Also, a simple expression for the coupling strength is derived.

2.2 Canonical variables

2.2.1 Atoms

In the experiment we work with a room-temperature gas of cesium atoms. The relevant quantum states of the cesium atoms are the two hyperfine ground states denoted $6S_{1/2}$ with quantum numbers $F = 3$ and $F = 4$, and the excited states $6P_{1/2}$ and $6P_{3/2}$ (see Fig. 2.1) The transitions from the groundstates $6S_{1/2}$ to the $6P_{1/2}$ states are called the $D1$-line, and the transitions from the $6S_{1/2}$ states to the $6P_{3/2}$ states are called the $D2$-line.

Using optical pumping methods, the atoms can be initialized in the state $F = 4, m_F = +4$ or the state $F = 4, m_F = -4$. An ensemble with N_A atoms pumped into $m_F = +4$ has total mean spin $\left\langle \vec{J} \right\rangle = J_x \cdot \hat{e}_x = 4N_A \cdot \hat{e}_x$ pointing in the $+x$-direction, and an ensemble pumped into $m_F = -4$ has total mean spin $\left\langle \vec{J} \right\rangle = J_x \cdot \hat{e}_x = -4N_A \cdot \hat{e}_x$ pointing in the $-x$-direction. Here we choose to denote

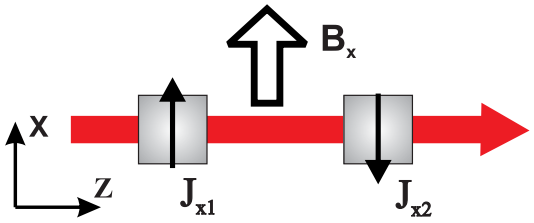

Figure 2.2: Illustration of light interacting with two oppositely polarized atomic ensembles one after the other.

the total angular momentum $\vec{J}$ instead of $\vec{F}$. Also, $\vec{J}$ is defined to be unitless, such that $\vec{J}$ is the total angular momentum divided by $\hbar$ (Planck's contant). This has been the convention in most of the publications from our group. $\hat{e}_x$ is a unit vector pointing in the x-direction.

Typically we use one ensemble polarized in the $+x$-direction and one ensemble polarized in the $-x$-direction. A pulse of light then interacts with the two ensembles one after the other as shown in Fig. 2.2. The atomic ensembles are futhermore kept in a bias magnetic field $B_x = 0.92$ Gauss pointing in the $+x$-direction. Located in this bias field the atomic spins precess at the Larmor frequency $\Omega_L = g_F \mu_B B_x/\hbar$, where g_F is the Landé g-factor and μ_B is the Bohr magneton. Cesium atoms in the $F = 4$ ground state located in the magnetic field $B_x = 0.92$ have the Larmor frequency $\Omega_L = 2\pi \cdot 322$ kHz.

The quantum state of an atomic ensemble is well defined by the collective spin $\vec{J} = \sum_{k=1}^{N_A} \vec{j}_k$, where $\vec{j}_k$ is the spin of the k'th atom. The spin components are non-commuting $[J_y, J_z] = iJ_x$ [1]. For an atomic ensemble polarized along the $\pm$x-direction, J_x has a large value and is considered a classical variable. On the other hand, the transverse spin components J_y and J_z are small quantum variables with zero (or small) mean values. For such an ensemble the Heisenberg uncertainty relation reads $\mathrm{Var}(J_y) \cdot \mathrm{Var}(J_z) \geq |J_x|^2/4$. For a fully polarized atomic ensemble we have the following uncertainties on the transverse spin components: $\Delta J_y = \Delta J_z = \sqrt{|J_x|/2}$. The fluctuations in the transverse spin components are smaller than the mean spin by a factor $\sqrt{2|J_x|}$, which for our case is approximately a factor 10^6. In this situation it is a good approximation to treat the mean spin J_x as a classical variable and the transverse spin components J_y and J_z as quantum variables.

[1] Often in the litterature, quantum operators like $\vec{J}$ are marked with a hat, but in this thesis I will leave out the hats. Hopefully it will clear when I am thinking about quantum operators and when I am thinking about classical values.

For a single atomic ensemble we can define canonical operators

$$x = \sigma^{j_x} \frac{J_y}{\sqrt{|J_x|}} \qquad p = \frac{J_z}{\sqrt{|J_x|}}. \tag{2.1}$$

I use the notation $\sigma^{j_x} = \pm 1$ depending on whether the atoms are polarized along the $\pm$x-direction. The canonical variables x and p are non-commuting with the commutation relation $[x, p] = i$. The Heisenberg uncertainty relation for canonical operators x and p is $\mathrm{Var}(x) \cdot \mathrm{Var}(p) \geq 1/4$. For a minimal uncertainty state with equal variances in the x and p-directions we have $\mathrm{Var}(x) = \mathrm{Var}(p) = 1/2$. Minimal uncertainty states with Gaussian statistics are denoted Coherent Spin States (CSS). The collective state of a fully spin-polarized atomic ensembles is such a CSS.

Atomic states close to the fully pumped CSS can also be described in terms of collective atomic exitations using the Holstein-Primakoff approximation [35]. The creation operator for a collective exitation is denoted $b^\dagger$ and is related to the spin components by $x = \sigma^{j_x} J_y / \sqrt{|J_x|} = \left(b + b^\dagger\right)/\sqrt{2}$ and $p = J_z/\sqrt{|J_x|} = \left(b - b^\dagger\right)/\left(\sqrt{2}i\right)$ such that $b = (x + ip)/\sqrt{2}$.

We can also write $b = \sum_{k=1}^{N_A} |4\rangle_k \langle 3|_k$. A single term $|4\rangle_k \langle 3|_k$ takes the k'th atom and moves it from the $F = 4, m = 3$ state to the $F = 4, m = 4$ state. The term does nothing the the rest of the $(k-1)$ atoms. The CSS is treated as the groundstate of a harmonic oscillator with creation operator $b^\dagger$. One collective excitation corresponds to the state proportional to the superposition state $b^\dagger |444...4\rangle \propto |344...4\rangle + |434...4\rangle + |443...4\rangle + ... |444...3\rangle$ where each ket labels the state of the N_A atoms, and the superposition has N_A terms of such kets.

In the experiments we utilize two oppositely oriented atomic ensembles with macroscopic classical spin components $\langle J_{x1}\rangle = -\langle J_{x2}\rangle = |J_x|$ along the x-direction. The subscript 1 refers to the first ensemble and the subscript 2 refers to the second ensemble (see Fig. 2.2). For such two ensembles, we define two sets c, s of non-local atomic operators [32]

$$\begin{aligned}
X_c &= \frac{J'_{y1} - J'_{y2}}{\sqrt{2\,|J_x|}} = \frac{x_1 + x_2}{\sqrt{2}} \\
P_c &= \frac{J'_{z1} + J'_{z2}}{\sqrt{2\,|J_x|}} = \frac{p_1 + p_2}{\sqrt{2}} \\
X_s &= -\frac{J'_{z1} - J'_{z2}}{\sqrt{2\,|J_x|}} = -\frac{p_1 - p_2}{\sqrt{2}} \\
P_s &= \frac{J'_{y1} + J'_{y2}}{\sqrt{2\,|J_x|}} = \frac{x_1 - x_2}{\sqrt{2}},
\end{aligned} \tag{2.2}$$

where the prime refers to that the spins are defined in a frame rotating with the Larmor frequency Ω_L. The indices c, s are abbreviations for cosine and sine

[2]. Note that in this chapter upper case atomic operators X, P are used to describe non-local two cell operators and lower case atomic operators x, p are used to describe for single cell operators. The canonical variables X_j and P_j are non-commuting with the commutation relation $[X_j, P_j] = i$ for $j = c, s$. The collective state of two oppositely oriented and fully polarized atomic ensembles has $\mathrm{Var}(X_j) = \mathrm{Var}(P_j) = 1/2$ and is a CSS.

2.2.2 Light

A pulse of polarized light can be described in terms of the Stokes vector $\vec{S} = (S_x, S_y, S_z)$ where the components are defined by

$$\begin{aligned} S_x &= \frac{1}{2} \cdot [N_{\mathrm{ph}}(x) - N_{\mathrm{ph}}(y)] \\ S_y &= \frac{1}{2} \cdot [N_{\mathrm{ph}}(+45^o) - N_{\mathrm{ph}}(-45^o)] \\ S_z &= \frac{1}{2} \cdot [N_{\mathrm{ph}}(\sigma_+) - N_{\mathrm{ph}}(\sigma_-)] \,. \end{aligned} \tag{2.3}$$

$N_{\mathrm{ph}}(x)$ is the number operator for photons polarized in the x-direction, $N_{\mathrm{ph}}(+45^o)$ is the number operator for photons polarized in the direction $+45$ degrees in between the x- and y-directions and $N_{\mathrm{ph}}(\sigma_+)$ is the number operator for σ_+ polarized photons. The Stokes operators satisfy the commutation relation $[S_x, S_y] = iS_x$. The operators (S_x, S_y, S_z) count photons within a certain pulse duration T, but we can also define time dependent Stokes operators $(S_x(t), S_y(t), S_z(t))$ which count photons per unit of time at the time t. These operators have the units of $1/\mathrm{time}$.

Let us assume that the light is strongly linearly polarized along either the x or y-direction, such that S_x has a large value and can be consider a classical variable. The Stokes components S_y and S_z are then small and can be considered as quantum variables. In this case, canonical operators for light can be defined:

$$y(t) = \sigma^{S_x} \frac{S_y(t)}{\sqrt{|S_x(t)|}} \qquad q(t) = \frac{S_z(t)}{\sqrt{|S_x(t)|}}. \tag{2.4}$$

$\sigma^{S_x} = \pm 1$ depending on the sign of S_x. If the light is strongly polarized in the y-direction, $y(t)$ and $q(t)$ will be the quadratures [3] of the x-polarized mode (and vica versa). In the above I chose to define time-varying canonical operators with the commutation relation $[y(t), q(t')] = i\delta(t - t')$. Since $\int_{-\infty}^{+\infty} \delta(t)dt = 1$, the $\delta(t - t')$ function has the units of $1/\mathrm{time}$. Therefore, the operators $y(t)$ and $q(t)$

[2] Later when discussing the QND interaction in Sec. 2.3.1 it is shown that the cosine atomic mode with canonical operators X_c and P_c only couples to a certain cosine light mode (and similar for the sine mode)

[3] The electrical field of a mode of light (with creation operater a and frequency ω) can be written using the quadratures: $E(t) \propto ae^{-i\omega t} + a^\dagger e^{-i\omega t} \propto y(t)\cos(\omega t) + q(t)\sin(\omega t)$.

have the units of $1/\sqrt{\text{time}}$. We can also define dimensionless integrated "cosine" and "sine" light variables y_c, q_c, y_s and q_s by

$$\begin{aligned} y_c &= \sigma^{S_x}\sqrt{\frac{2}{|S_x|\,T}}\int_0^T S_y(t)\cos(\Omega_L t)dt \\ q_c &= \quad\sqrt{\frac{2}{|S_x|\,T}}\int_0^T S_z(t)\cos(\Omega_L t)dt, \end{aligned} \tag{2.5}$$

where the operators y_s and q_s are similarly defined by replacing cos with sin. These integrated operators are the relevant light operators for the QND interaction and have the commutation relation $[y_j, q_j] = i$ for $j = c, s$. One can also consider integrated light operators with exponentially rising or falling temporal modes such as $y_{c,\pm} \propto \int_0^T S_y(t)\cos(\Omega_L t)e^{\pm\gamma t}dt$. These operators are the relevant ones for the swap and squeezing interaction.

2.3 Interactions between atoms and light: An overview.

2.3.1 Quantum Non-Demolition interaction

The off-resonant Faraday interaction between light propagating in the z-direction and atoms polarized in the $\pm x$-direction can for low interaction strengths be described with the Hamiltonian $\mathcal{H} \propto S_z J_z$ [4]. For two oppositely polarized atomic ensembles located in a magnetic field, we have the following set of input-output equations for the canonical operators [32]

$$\begin{aligned} X_j^{\text{out}} &= X_j^{\text{in}} + \tilde{\kappa} q_j^{\text{in}}, & P_j^{\text{out}} &= P_j^{\text{in}} \\ y_j^{\text{out}} &= y_j^{\text{in}} + \tilde{\kappa} P_j^{\text{in}}, & q_j^{\text{out}} &= q_j^{\text{in}}, \end{aligned} \tag{2.6}$$

where "in/out" means the state of atoms and light before/after the interaction and $j = c, s$ stands for "cosine" and "sine". Notice that the cosine atomic mode only couples to the cosine light mode, and that the sine atomic mode only couples to the sine light mode. The light-atom coupling strength is denoted $\tilde{\kappa}$ and is defined as

$$\tilde{\kappa}^2 = a^2\,|J_x(t)|\,|S_x(t)|\,T. \tag{2.7}$$

Typically $J_x(t)$ and $S_x(t)$ are time-independent macroscopic values (as discussed later). a is a coupling constant defined later in Eq. (2.28). In earlier publications this QND interaction strength was written without the tilde. However, in this thesis I reserve the symbol κ without the tilde for the coupling strength used in the swap and squeezing interaction described in Sec. 2.3.4.

[4] The Hamiltonian is described in detail later in Sec. 2.4.1.

With a measurement of the output light operator y_j^{out}, we gain information about the input atomic operator P_j^{in} which is conserved during the interaction. I.e., we have performed a Quantum Non-Demolition (QND) measurement of the atomic P-operator. After the QND interaction, the atoms are left in a collective spin-squeezed state, or equivalently, the two atomic ensembles are entangled [16]. The measurement also disturbs the atomic system, since the light operator q_j^{in} is transferred to the atomic X_j^{out} operator. After the interaction, the atomic X-quadrature is more noisy (anti-squeezed). This is called the backaction of light on atoms.

2.3.2 Entanglement criterion

Two continuous variables subsystems are entangled if the following Einstein-Podolsky-Rosen (EPR) variance criterion [36] is fulfilled

$$\Sigma_{\text{EPR}} \equiv \text{Var}\left(\frac{p_1 + p_2}{\sqrt{2}}\right) + \text{Var}\left(\frac{x_1 - x_2}{\sqrt{2}}\right) < 1. \tag{2.8}$$

Here x_1, p_1 are the canonical variables for subsystem 1 and x_2, p_2 are the canonical variables for subsystem 2. The criterion is easy to remember since for two uncorrelated coherent states (such as for instance vacuum) where the variances of x_1, p_1 and x_2, p_2 all equal $1/2$ we have $\Sigma_{\text{EPR}} = 1$. The two uncorrelated coherent states are therefore at the boundary for entanglement. Two subsystems which satisfy the EPR criterion are said to be entangled or two-mode squeezed.

Entanglement between the ensembles

In the above we did not specify the subsystems. If the subsystems are the two atomic ensembles with canonical operators defined by Eq. (2.1) and (2.2), the EPR criterion takes the following form

$$\Sigma_{\text{EPR}} = \text{Var}\left(\frac{J'_{z1} + J'_{z2}}{\sqrt{2\,|J_x|}}\right) + \text{Var}\left(\frac{J'_{y1} + J'_{y2}}{\sqrt{2\,|J_x|}}\right) = \text{Var}\,(P_c) + \text{Var}\,(P_s) < 1. \tag{2.9}$$

We see that entanglement between the ensembles is equivalent to having two-mode squeezing of the two non-local operators P_c and P_s. The EPR variance Σ_{EPR} is often also denoted the atomic noise in projection noise (PN) units.

QND interaction and entanglement between the ensembles

Suppose we are interested in measuring whether the two atomic ensembles are entangled. If the light-atom interaction is of the QND type, this can be done by considering the variances of the output light operators y_c^{out} and y_s^{out}. If we assume that the input light operators are in the vacuum state, we find that

$$\text{Var}\left(y_c^{\text{out}}\right) + \text{Var}\left(y_s^{\text{out}}\right) = 1 + \tilde{\kappa}^2 \cdot \Sigma_{\text{EPR}}. \tag{2.10}$$

I.e., from the measurement of the cosine and sine components of the output light together with the knowledge of the coupling constant $\tilde{\kappa}$, we can calculate Σ_{EPR} and find out whether the EPR criterion is fulfilled.

Entanglement between the upper and lower sideband modes

The two subsystems could also be two modes of the electro-magnetic light field. When discussing the interaction between atoms and light, we typically consider cosine and sine light modes as defined in Eq. (2.4.8). On the other hand, in figures showing atomic level schemes and light fields (such as in Fig. 4.3 which is shown later), we depict upper and lower sideband modes. We are interested in the upper and lower sideband modes with frequencies $\omega_\pm = \omega_0 \pm \Omega_L$ where ω_0 is the carrier frequency (of the local oscillator light field) and Ω_L is the Larmor frequency of the atoms. Only sidebands with frequencies $\omega_\pm$ couple coherently to the atoms (the level scheme picture is also discussed in Sec. 4.2 and 7.2.3).

A mode of light can be described by a creation operator. The creation operators for the upper and lower sideband modes a_+ and a_- and the creation operators for the cosine and sine modes a_c and a_s are related by the formulas

$$a_c = \frac{a_+ + a_-}{\sqrt{2}} \quad \text{and} \quad a_s = \frac{a_+ - a_-}{\sqrt{2}i}. \tag{2.11}$$

For any mode a, we can define canonical operators X and P such that $a = (X + iP)/\sqrt{2}$ [5]. With this definition we find the relations between the canonical operators

$$\begin{aligned} X_{Lc} &= \frac{X_+ + X_-}{\sqrt{2}} \quad \text{and} \quad P_{Lc} = \frac{P_+ + P_-}{\sqrt{2}} \\ X_{Ls} &= \frac{P_+ - P_-}{\sqrt{2}} \quad \text{and} \quad P_{Ls} = -\frac{X_+ - X_-}{\sqrt{2}}, \end{aligned} \tag{2.12}$$

where I here chose the subscripts Lc, Ls, $+$ and $-$ for the cosine, sine, upper sideband and lower sideband modes, respectively. The criterion for entanglement between the upper and lower sideband is

$$\Sigma_{\mathrm{EPR}} = \mathrm{Var}\left(\frac{X_+ + X_-}{\sqrt{2}}\right) + \mathrm{Var}\left(\frac{P_+ - P_-}{\sqrt{2}}\right) = \mathrm{Var}\left(X_{Lc}\right) + \mathrm{Var}\left(X_{Ls}\right) < 1. \tag{2.13}$$

We see that the EPR type entanglement between the upper and lower sideband is equivalent to squeezing of the *cosine* and *sine* modes in the X_L-direction.

[5] Two notations are used for the canonical operators for light. For instance, a cosine light mode has canonical operators y_c, q_c (notation 1) or X_{Lc}, P_{Lc} (notation 2).

2.3.3 Single cell interaction with light

The input-output equations for a single atomic ensemble interacting with light are a bit more complicated. Again, assuming that the atoms are located in a static magnetic field pointing in the x-direction and that the interaction Hamiltonian $\mathcal{H} \propto S_z J_z$, then the input-output equations for a single ensemble are [33]

$$\begin{aligned}
y_c^{\text{out}} &= y_c^{\text{in}} + \frac{\tilde{\kappa}}{\sqrt{2}} p^{\text{in}} \mp \left(\frac{\tilde{\kappa}}{2}\right)^2 q_s^{\text{in}} \mp \frac{1}{\sqrt{3}} \left(\frac{\tilde{\kappa}}{2}\right)^2 q_{s,1}^{\text{in}} \\
y_s^{\text{out}} &= y_s^{\text{in}} \pm \frac{\tilde{\kappa}}{\sqrt{2}} x^{\text{in}} \pm \left(\frac{\tilde{\kappa}}{2}\right)^2 q_c^{\text{in}} \pm \frac{1}{\sqrt{3}} \left(\frac{\tilde{\kappa}}{2}\right)^2 q_{c,1}^{\text{in}} \\
q_c^{\text{out}} &= q_c^{\text{in}} \quad \text{and} \quad \mathrm{q_s^{out}} = \mathrm{q_s^{in}} \\
x^{\text{out}} &= x^{\text{in}} + \frac{\tilde{\kappa}}{\sqrt{2}} q_c^{\text{in}} \quad \text{and} \quad \mathrm{p^{out}} = \mathrm{p^{in}} \mp \frac{\tilde{\kappa}}{\sqrt{2}} \mathrm{q_s^{in}}.
\end{aligned} \tag{2.14}$$

The top/bottom signs in $\pm$ and $\mp$ are valid for the first/second ensemble. The operator $q_{c,1}^{\text{in}}$ is orthogonal to the q_c^{in} mode and defined by

$$q_{c,1}^{\text{in}} = \sqrt{3} \left(\frac{2}{T}\right)^{3/2} \int_0^T \left(\frac{T}{2} - t\right) \cos(\Omega_L t) q_L^{\text{in}}(t) dt. \tag{2.15}$$

The $q_{s,1}^{\text{in}}$ mode is similarly defined by replacing cos by sin.

We see from Eq. (2.14) that the interaction is not of the QND type since neither the x nor the p atomic operator are conserved during the interaction. I.e., the backaction of light onto the atoms is directed into both atomic operators. Many quantum information protocols are based on the QND interaction, but still the single cell interaction is interesting. The teleportation experiment [18] was for instance carried out using only one ensemble.

It is possible to derive the two cell QND input-output equations given by Eq. (2.6) from the single cell equations given by Eq. (2.14). For light interacting with two oppositely oriented ensembles one after the other we find by using Eq. (2.14) twice that

$$\begin{aligned}
y_c^{\text{out}} &= y_c^{\text{in}} + \frac{\tilde{\kappa}}{\sqrt{2}} \left(p_1^{\text{in}} + p_2^{\text{in}}\right) \\
y_s^{\text{out}} &= y_s^{\text{in}} + \frac{\tilde{\kappa}}{\sqrt{2}} \left(x_1^{\text{in}} - x_2^{\text{in}}\right).
\end{aligned} \tag{2.16}$$

The above equations equals the two-cell equations given in Eq. (2.6). We can also find the output two-cell atomic operators by using Eq. (2.14) twice, one time

for each ensemble, and we find

$$\begin{aligned}
\left(x_1^{\rm out}+x_2^{\rm out}\right) &= \left(x_1^{\rm in}+x_2^{\rm in}\right)+\tilde{\kappa}q_c^{\rm in}\\
\left(p_1^{\rm out}-p_2^{\rm out}\right) &= \left(p_1^{\rm in}-p_2^{\rm in}\right)-\tilde{\kappa}q_s^{\rm in}\\
\left(p_1^{\rm out}+p_2^{\rm out}\right) &= \left(p_1^{\rm in}+p_2^{\rm in}\right)\\
\left(x_1^{\rm out}-x_2^{\rm out}\right) &= \left(x_1^{\rm in}-x_2^{\rm in}\right).
\end{aligned} \tag{2.17}$$

Again, these equations match the two cell Eq. (2.6).

2.3.4 Swap and squeezing interaction

Cesium atoms are multi-level atoms with a hyperfine structure given by the quantum numbers F, m. Atoms are polarizable, and the Hamiltonian describing the light-atom interaction (which is described later in Sec. 2.4.1) includes the rank 0 (scalar), the rank 1 (vector) and the rank 2 (tensor) polarizability [37].

A spin-1/2 atom has no tensor polarizability. When deriving the QND interaction, we are neglegting the tensor polarizability of the atoms, and we are therefore basically treating the $F = 4$ multi-level cesium atom as a spin-1/2 atom. This is problematic, in particular for large interaction strengths.

If one includes the tensor polarizability in the model of light interacting with two highly polarized oppositely oriented atomic ensembles one ends up with a swap and squeezing interaction [4] instead of the more simple QND interaction. The input-output equations for the swap and squeezing interaction are [4] (omitting the c, s subscripts)

$$\begin{aligned}
X^{\rm out} &= \sqrt{1-\frac{\kappa^2}{Z^2}}X^{\rm in}+\kappa q^{\rm in}, \qquad & P^{\rm out} &= \sqrt{1-\frac{\kappa^2}{Z^2}}P^{\rm in}-\frac{\kappa}{Z^2}y^{\rm in},\\
y^{\rm out} &= \sqrt{1-\frac{\kappa^2}{Z^2}}y^{\rm in}+\kappa P^{\rm in}, \qquad & q^{\rm out} &= \sqrt{1-\frac{\kappa^2}{Z^2}}q^{\rm in}-\frac{\kappa}{Z^2}X^{\rm in},
\end{aligned} \tag{2.18}$$

where $\kappa = Z\sqrt{1-\exp\left(-2\gamma_{\rm sw}T\right)}$, and the swap rate $\gamma_{\rm sw}$ is proportional to light intensity and density of atoms. Z is a function of the light detuning only, and $1/Z^2$ measures the deviation from the QND interaction. I will also use the notation $\zeta^2 = 1/Z^2$ later on. For our experimental probe detuning $\Delta = -850$ MHz (blue detuning) from the $F = 4 \rightarrow F' = 5$ D2 transition, we have $Z^2 \approx 6.4$ (see Sec. 3.6.1 for measurements of Z^2).

For large interaction times $\gamma_{\rm sw}T \gg 1$, the coupling strength $\kappa \rightarrow Z$ and we obtain the output operators

$$\begin{aligned}
X^{\rm out} &= Zq^{\rm in}, \qquad & P^{\rm out} &= -y^{\rm in}/Z,\\
y^{\rm out} &= ZP^{\rm in}, \qquad & q^{\rm out} &= -X^{\rm in}/Z.
\end{aligned} \tag{2.19}$$

Wee see that the light and atomic operators have been swapped and squeezed by the factor Z^2 in the variances. The input-output Eqs. (2.18) and (2.19) and their

application to the creation of squeezed light, atomic magnetometry, quantum memory and the generation of entangled atoms will be further discussed in the following chapters.

It should be noted that the complete swap described by Eq. (2.19) is hard to achieve in the experiment due to atomic decoherence. The decoherence will also limit the degree of squeezing which can be produced in the experiment. Later in this chapter we derive more complicated equations where atomic decoherence is included in the model. Finally, I stress that Eqs. (2.18) and (2.19) are only valid for highly polarized ensembles. If the atomic polarization is reduced significantly during the interaction one has to take this into account. This can be done by assuming that the swap rate $\gamma_{\rm sw}$ is time-dependent, and that there are some atoms in the ensemble which do not contribute to the collective interaction but still give rise to additional noise.

2.4 Interactions between atoms and light: Detailed input-output equations.

After having presented the interactions between light and one or two atomic ensembles, we now turn to the actual derivations of the input-output equations. We start by going through the QND interaction. Then we move on to the more complicated situation where the tensor polarizability and atomic decoherence are included in the model. The equations of motions for light interacting with a single polarized ensemble are first derived. Then the results are used to derive how two oppositely polarized ensembles interact with light.

2.4.1 Hamiltonian

The full Hamiltonian describing the off-resonant [6] interaction between polarized atoms and polarized light is [32]

$$\begin{aligned}\mathcal{H}_{\rm int} &= -\frac{\hbar c\gamma}{8A\Delta}\frac{\lambda^2}{2\pi}\int_0^L \big(a_0\phi(z,t) + a_1 S_z(z,t)j_z(z,t) \\ &\quad + a_2\left[\phi(z,t)j_z^2(z,t) - S_-(z,t)j_+^2(z,t) - S_+(z,t)j_-^2(z,t)\right]\big)\rho A dz.\end{aligned} \tag{2.20}$$

A and L are the cross-section and length of the atomic cloud, respectively. The wavelength of the probe light is $\lambda = 852$ nm for all of the experiments presented in this thesis. The FWHM linewidth of the excited $P_{3/2}$ state is $\gamma = 2\pi\cdot 5.21$ MHz. z is the coordinate along the light propagation direction and goes from 0 to L. The continuous operators $\phi(z,t)$, $S_z(z,t)$ and $S_\pm(z,t) = S_x(z,t) \pm iS_y(z,t)$ have the units of 1/length, such that $c\cdot\phi(z,t)$ is the number of photons passing through

[6] For the case of room-temperature atoms, the laser detuning should be greater than the Doppler width of the atomic resonance.

the area A at the position z per second. $j_z(z,t)$ and $j_\pm(z,t) = j_x(z,t) \pm i j_y(z,t)$ are dimensionless continuous atomic spin operators at the position z such that $\vec{j}(z,t)\rho A dz$ is the angular momentum divided by $\hbar$ of the atoms which are located in the slice dz. ρ is the density of atoms. The total angular momentum divided by $\hbar$ is $\vec{J}(t) = \int_0^L \vec{j}(z,t)\rho A dz$.

a_0, a_1, and a_2 are the dimensionless scalar, vector and tensor polarizabilities [7] which are a function of the detuning Δ. For the $F = 4$ hyperfine ground states coupled to the $D2$ line, we have the following expressions for the polarizabilities [32]:

$$\begin{aligned} a_0 &= \frac{1}{4}\left(\frac{1}{1-\Delta_{3'5'}/\Delta} + \frac{7}{1-\Delta_{4'5'}/\Delta} + 8\right) \\ a_1 &= \frac{1}{120}\left(-\frac{35}{1-\Delta_{3'5'}/\Delta} - \frac{21}{1-\Delta_{4'5'}/\Delta} + 176\right) \\ a_2 &= \frac{1}{240}\left(\frac{5}{1-\Delta_{3'5'}/\Delta} - \frac{21}{1-\Delta_{4'5'}/\Delta} + 16\right). \end{aligned} \tag{2.21}$$

$\Delta_{3'5'}$ and $\Delta_{4'5'}$ are the excited state hyperfine splittings (see level scheme in Fig. 2.1). As in [32], the detuning $\Delta<0$ when the laser frequency is greater than the atomic transition.

2.4.2 Propagation equations

In the experiments, pulses of light are sent through a cloud of cesium atoms. We would therefore like some input-output relations that describe the spin and the Stokes operators before and after the interaction. To derive these relations we need the interaction Hamiltonian, the Heisenberg equation of motion for the spin vector and the Maxwell-Bloch equation [8] for the Stokes vector

$$\frac{\partial \vec{j}(z,t)}{\partial t} = \frac{1}{i\hbar}\left[\vec{j}(z,t), \mathcal{H}_{\text{int}}\right] \tag{2.22}$$

$$\left(\frac{\partial}{\partial t} + c\frac{\partial}{\partial z}\right)\vec{S}(z,t) = \left[\vec{S}(z,t), \mathcal{H}_{\text{int}}\right]. \tag{2.23}$$

The speed of light is set to infinity such that we can neglect the term $\frac{\partial}{\partial t}$ in Eq. (2.23). Using Eq. (2.22) and Eq. (2.23) together with the Hamiltonian Eq. (2.20),

[7] The scalar, vector and tensor polarizabilities are also denoted population, orientation and alignment, respectively. See [38] for a nice way to visualize atomic polarization.

[8] The Maxwell-Bloch equation can be derived from the Heisenberg equation of motion for the creation and annihilation operators for the light field (one would also need the Hamiltonian for the light field).

one finds the following equations of motion [32] for the spin operators

$$\begin{aligned}
\frac{\partial}{\partial t}j_x(z,t) &= \frac{c\gamma}{8A\Delta}\frac{\lambda^2}{2\pi}\left\{a_1 S_z j_y + a_2\left(2S_y\left[j_x j_z + j_z j_x\right] - \left(2S_x - \phi\right)\left[j_z j_y + j_y j_z\right]\right)\right\} \\
\frac{\partial}{\partial t}j_y(z,t) &= \frac{c\gamma}{8A\Delta}\frac{\lambda^2}{2\pi}\left\{-a_1 S_z j_x + a_2\left(-\left(2S_x + \phi\right)\left[j_x j_z + j_z j_x\right] - 2S_y\left[j_z j_y + j_y j_z\right]\right)\right\} \\
\frac{\partial}{\partial t}j_z(z,t) &= \frac{c\gamma}{8A\Delta}\frac{\lambda^2}{2\pi}a_2\left\{4S_x\left[j_x j_y + j_y j_x\right] - 4S_y\left[j_x^2 - j_y^2\right]\right\},
\end{aligned} \tag{2.24}$$

and the Stokes operators

$$\begin{aligned}
\frac{\partial}{\partial z}S_x(z,t) &= \frac{\gamma\rho}{8\Delta}\frac{\lambda^2}{2\pi}\left\{a_1 S_y j_z + a_2 \cdot 2S_z\left[j_x j_y + j_y j_x\right]\right\} \\
\frac{\partial}{\partial z}S_y(z,t) &= \frac{\gamma\rho}{8\Delta}\frac{\lambda^2}{2\pi}\left\{-a_1 S_x j_z - a_2 \cdot 2S_z\left[j_x^2 - j_y^2\right]\right\} \\
\frac{\partial}{\partial z}S_z(z,t) &= \frac{\gamma\rho}{8\Delta}\frac{\lambda^2}{2\pi}a_2\left\{2S_y\left[j_x^2 - j_y^2\right] - 2S_x\left[j_x j_y + j_y j_x\right]\right\}.
\end{aligned} \tag{2.25}$$

For simplicity we omitted the (z,t) dependence on the right hand side of the equations. Notice that terms consisting of two spin operators such as $\left[j_x j_y + j_y j_x\right](z,t) \neq j_x(z,t)j_y(z,t) + j_y(z,t)j_x(z,t)$.

2.4.3 QND interaction

For large detunings, the vector polarizability $a_1(\Delta) \to 1$, and the tensor polarizability $a_2(\Delta) \to 0$ (see Eq. 2.21). Then it is a good approximation [9] to neglect the tensor polarizability and only keep terms in the equations of motion (2.24) and (2.25) which are proportional to a_1. In this case we find the following equations for the spin operators

$$\begin{aligned}
\frac{\partial}{\partial t}j_x(z,t) &= -acS_z(z,t)j_y(z,t) \\
\frac{\partial}{\partial t}j_y(z,t) &= acS_z(z,t)j_x(z,t) \\
\frac{\partial}{\partial t}j_z(z,t) &= 0
\end{aligned} \tag{2.26}$$

and the Stokes operators

$$\begin{aligned}
\frac{\partial}{\partial z}S_x(z,t) &= -\rho A \cdot a \cdot S_y(z,t)j_z(z,t) \\
\frac{\partial}{\partial z}S_y(z,t) &= \rho A \cdot a \cdot S_x(z,t)j_z(z,t) \\
\frac{\partial}{\partial z}S_z(z,t) &= 0.
\end{aligned} \tag{2.27}$$

[9] As detailed in Sec. 2.5, the approximation is only good for small coupling strengths.

The parameter a is defined by

$$a \equiv -\frac{\gamma}{8A\Delta}\frac{\lambda^2}{2\pi} \cdot a_1, \tag{2.28}$$

and describes the coupling strength between the spin and Stokes operators. Notice that $j_z(z,t)$ is conserved during the interaction in the sense that it does not depend on t, and that $S_z(z,t)$ is conserved in the sense that it does not depend on z.

For the case of a room-temperature atomic ensemble, the atoms are moving fast on the timescale of the interaction. Therefore, in Eq. (2.27) for the Stokes vector, the spin operators can be replaced by their average values over the cell length. The equations for Stokes operators now read

$$\begin{aligned}
\frac{\partial}{\partial z}S_x(z,t) &= -\rho A \cdot a \cdot S_y(z,t)\left\langle j_z(z,t)\right\rangle_z \\
\frac{\partial}{\partial z}S_y(z,t) &= \rho A \cdot a \cdot S_x(z,t)\left\langle j_z(z,t)\right\rangle_z \\
\frac{\partial}{\partial z}S_z(z,t) &= 0.
\end{aligned} \tag{2.29}$$

The average value of the spin is defined by $\left\langle j_z(z,t)\right\rangle_z = \frac{1}{L}\int_0^L j_z(z,t)dz$. Similarly, in the equations for the spin operators, the Stokes operators should be averaged over the cell length. We find

$$\begin{aligned}
\frac{\partial}{\partial t}j_x(z,t) &= -c \cdot a \cdot \left\langle S_z(z,t)\right\rangle_z j_y(z,t) \\
\frac{\partial}{\partial t}j_y(z,t) &= c \cdot a \cdot \left\langle S_z(z,t)\right\rangle_z j_x(z,t) \\
\frac{\partial}{\partial t}j_z(z,t) &= 0.
\end{aligned} \tag{2.30}$$

The average Stokes operator is defined by $\left\langle S_z(z,t)\right\rangle_z = \frac{1}{L}\int_0^L S_z(z,t)dz$.

I now introduce the integrated collective atomic operators: $\vec{J}(t) = \int_0^L \vec{j}(z,t)\rho A dz$. We also have the relation $\left\langle \vec{j}(z,t)\right\rangle_z = \frac{1}{L\rho A}\vec{J}(t)$. By inserting these expressions into the above equations, we find the equations of motions in terms of collective spin operators $\vec{J}(t)$

$$\begin{aligned}
\frac{\partial}{\partial z}S_x(z,t) &= -\frac{a}{L} \cdot S_y(z,t)J_z(t) \\
\frac{\partial}{\partial z}S_y(z,t) &= \frac{a}{L} \cdot S_x(z,t)J_z(t) \\
\frac{\partial}{\partial z}S_z(z,t) &= 0
\end{aligned} \tag{2.31}$$

$$\frac{\partial}{\partial t}J_x(t) = -c \cdot a \cdot \langle S_z(z,t)\rangle_z J_y(t)$$
$$\frac{\partial}{\partial t}J_y(t) = c \cdot a \cdot \langle S_z(z,t)\rangle_z J_x(t)$$
$$\frac{\partial}{\partial t}J_z(t) = 0. \tag{2.32}$$

QND input-output equations

We can find the z-dependence of the Stokes vector $\vec{S}(z,t)$ by solving the differental equation (2.31). We now choose to use the input-output notation $\vec{S}^{\rm in}(t) = c\vec{S}(z = 0,t)$ and $\vec{S}^{\rm out}(t) = c\vec{S}(z = L,t)$ for the Stokes vector. The in/out operators $\vec{S}^{\rm in/out}(t)$ have the units of 1/time. For the input/output operators we have

$$\begin{pmatrix} S_x^{\rm out}(t) \\ S_y^{\rm out}(t) \\ S_z^{\rm out}(t) \end{pmatrix} = \begin{pmatrix} \cos(\theta) & \sin(\theta) & 0 \\ -\sin(\theta) & \cos(\theta) & 0 \\ 0 & 0 & 1 \end{pmatrix} \begin{pmatrix} S_x^{\rm in}(t) \\ S_y^{\rm in}(t) \\ S_z^{\rm in}(t) \end{pmatrix}. \tag{2.33}$$

We see that the effect of the atoms on the light is a rotation of the Stokes vector in the x-y plane by the angle $\theta = -aJ_z(t)$ (where $J_z(t)$ is independent of t).

Since $\langle S_z(z,t)\rangle_z$ is independent of both z and t, we can solve Eq. (2.32). The effect of the light on the atoms is a rotation of the spin vector in the x-y plane by the angle $\widetilde{\omega}T = -aS_z(t)T$ (where $S_z(t)$ is independent of t)

$$\begin{pmatrix} J_x(T) \\ J_y(T) \\ J_z(T) \end{pmatrix} = \begin{pmatrix} \cos(\widetilde{\omega}T) & \sin(\widetilde{\omega}T) & 0 \\ -\sin(\widetilde{\omega}T) & \cos(\widetilde{\omega}T) & 0 \\ 0 & 0 & 1 \end{pmatrix} \begin{pmatrix} J_x(0) \\ J_y(0) \\ J_z(0) \end{pmatrix}. \tag{2.34}$$

In the experiments, we are often in the situation with small rotation angles $\theta \ll 1$ and $\widetilde{\omega}T \ll 1$ and large classical values of $S_x(t)$ and $J_x(t)$. In this case, the equations of motion (2.31) and (2.32) are particulary simple. We find the following input-ouput equations for the Stokes operators

$$S_x^{\rm out}(t) = S_x^{\rm in}(t)$$
$$S_y^{\rm out}(t) = S_y^{\rm in}(t) + aJ_z(t)S_x(t)$$
$$S_z^{\rm out}(t) = S_z^{\rm in}(t), \tag{2.35}$$

and the following differential equations for the spin operators

$$\frac{\partial}{\partial t}J_x(t) = 0$$
$$\frac{\partial}{\partial t}J_y(t) = aS_z(t)J_x(t)$$
$$\frac{\partial}{\partial t}J_z(t) = 0. \tag{2.36}$$

The above equations for the spin operators can be integrated and we find

$$\begin{aligned} J_x(T) &= J_x(0) \\ J_y(T) &= J_y(0) + aTJ_x(t)S_z(t) \\ J_z(T) &= J_z(0). \end{aligned} \tag{2.37}$$

Notice that we have kept the time-dependence on the operators $J_x(t)$ and $S_x(t)$ in the above equations even though those operators are time-independent. The reason for this is to keep track of the units of those operators. For instance, throughout the thesis, $S_x(t)$ has the units of 1/time while $S_x(z,t)$ has the units of 1/length and S_x is dimensionless.

In the above calculations, we considered one atomic ensemble located in zero magnetic field. The tensor polarizability was neglected. In this situation, the interaction *is* of the QND type. One can measure the atomic $J_z(t)$-operator (see Eq. 2.35) while the same operator is conserved during the interaction (see Eq. 2.36). On the other hand, for a single ensemble located in a non-zero magnetic field, one can show that the interaction *is not* of the QND type. Instead, the input-output equations are given by Eq. (2.14). Also, for two oppositely oriented ensembles located in a non-zero magnetic field, one can show that the interaction *is* of the QND type. In this case, the input-output equations are given by Eq. (2.6).

2.4.4 Tensor polarizability

We now move on to the more complicated case of interaction of light with multi-level atoms which both have vector and tensor polarizability. The starting point is the equations of motion (2.24) and (2.25). We now have to consider atomic tensor operators such as for instance $[j_y j_z + j_z j_y](z,t)$. These operators can be approximated by the vector operators if the atoms are highly polarized. To be specific, highly polarized means that that atoms are only located in the two quantum states $F = 4, m = 4$ and $F = 4, m = 3$ with the largest angular momentum projection.

In terms of the density matrix σ_{mm}, this means that we are only including density matrix elements σ_{44}, σ_{43}, σ_{34} and σ_{33}. By only keeping such density matrix elements, we can simplify the tensor operators. Assuming $F = 4$, we find [32]

$$\begin{aligned} [j_y j_z + j_z j_y](z,t) &\approx 0 \\ [j_x j_y + j_y j_x](z,t) &= \sigma^{j_x} \cdot 7 j_y(z,t) \\ [j_x j_z + j_z j_x](z,t) &= \sigma^{j_x} \cdot 7 j_z(z,t) \\ \left[j_x^2 - j_y^2\right](z,t) &\approx \sigma^{j_x} \frac{7}{2} j_x(z,t) \end{aligned} \tag{2.38}$$

In the last equation for $j_x^2 - j_y^2$, we also assumed $4\sigma_{44} \gg \sigma_{33}$. By inserting the approximations given by Eq. (2.38) into Eqs. (2.24) and (2.25), we find

$$\begin{aligned}
\frac{\partial}{\partial t} j_x(z,t) =& - c \cdot a \left\{ S_z j_y + \sigma^{j_x} \xi^2 S_y j_z \right\} \\
\frac{\partial}{\partial t} j_y(z,t) =& c \cdot a \left\{ S_z j_x + \frac{1}{2} \sigma^{j_x} \xi^2 \left(2S_x + \phi \right) j_z \right\} \\
\frac{\partial}{\partial t} j_z(z,t) =& - c \cdot a \cdot \xi^2 \sigma^{j_x} \left\{ 2S_x j_y - S_y j_x \right\}
\end{aligned} \tag{2.39}$$

$$\begin{aligned}
\frac{\partial}{\partial z} S_x(z,t) =& - \rho A \cdot a \left\{ S_y j_z + \sigma^{j_x} \xi^2 S_z j_y \right\} \\
\frac{\partial}{\partial z} S_y(z,t) =& \rho A \cdot a \left\{ S_x j_z + \frac{1}{2} \sigma^{j_x} \xi^2 S_z j_x \right\} \\
\frac{\partial}{\partial z} S_z(z,t) =& - \rho A \cdot a \cdot \xi^2 \sigma^{j_x} \left\{ \frac{1}{2} S_y j_x - S_x j_y \right\},
\end{aligned} \tag{2.40}$$

The coupling constant a was defined in Eq. (2.28). We also defined the parameter $\xi^2 \equiv 14 a_2/a_1$. Note that ξ^2 can be both positive and negative. I.e., we define $\xi \equiv \sqrt{14 a_2/a_1}$ if $a_2/a_1 > 0$, and $\xi \equiv i \cdot \sqrt{14 a_2/a_1}$ if $a_2/a_1 < 0$. The parameter ξ^2 depends on the detuning. For our experimental detuning, we have the value $\xi^2 \approx 1/6.4$. This means that ξ^2 is a small parameter. Still, as we will see later, a non-zero ξ^2 has a large effect for long interaction times.

2.4.5 Approximations

In the following we assume that the atomic ensemble is polarized along either the $+x$ or $-x$-direction, and that the probe light is propagating in the z-direction and is linearly polarized along either the x or y-direction. With these assumptions, the x-components of the Stokes and spin vectors $S_x(z,t)$ and $j_x(z,t)$ are large and macroscopic and are not changed by the interaction. We also assume that $S_x(z,t)$ is independent of time.

In the differential equations (2.40) for $S_y(z,t)$ and $S_z(z,t)$, we neglect the terms proportional to j_x, since these terms only lead to a small rotation of the Stokes vector in the S_y-S_z-plane. As discussed earlier in Sec. 2.4.3, atoms are moving fast on the timescale of the interaction. Therefore, in Eq. (2.40) for the Stokes vector, the spin operators are replaced by their average values over the cell length. The equations for the Stokes operators now read

$$\begin{aligned}
\frac{\partial}{\partial z} S_x(z,t) =& 0 \\
\frac{\partial}{\partial z} S_y(z,t) =& \rho A \cdot a \cdot S_x(z,t) \left\langle j_z(z,t) \right\rangle_z \\
\frac{\partial}{\partial z} S_z(z,t) =& \rho A \cdot a \cdot \xi^2 \cdot \sigma^{j_x} \cdot S_x(z,t) \left\langle j_y(z,t) \right\rangle_z .
\end{aligned} \tag{2.41}$$

Similarly, in Eq. (2.39) for the spins, the Stokes vector should be averaged over the cell length. We also neglect the terms proportional to ϕ and S_x which lead to a small rotation of the spin vector in the j_y-j_z plane. This is known as the AC Stark shift. Using these approximations, the equations for the spin operators now read

$$\begin{aligned}
\frac{\partial}{\partial t} j_x(z,t) &= 0 \\
\frac{\partial}{\partial t} j_y(z,t) &= c \cdot a \cdot \langle S_z(z,t) \rangle_z \, j_x(z,t) \\
\frac{\partial}{\partial t} j_z(z,t) &= c \cdot a \cdot \xi^2 \cdot \sigma^{j_x} \cdot \langle S_y(z,t) \rangle_z \, j_x(z,t).
\end{aligned} \tag{2.42}$$

As was done in Sec. 2.4.3, we now introduce the integrated atomic spin vector $\vec{J}(t)$. In terms of $\vec{J}(t)$, Eq. (2.41) reads

$$\begin{aligned}
\frac{\partial}{\partial z} S_y(z,t) &= \frac{a}{L} \cdot S_x(z,t) J_z(t) \\
\frac{\partial}{\partial z} S_z(z,t) &= \frac{a}{L} \cdot \xi^2 \cdot \sigma^{j_x} \cdot S_x(z,t) J_y(t),
\end{aligned} \tag{2.43}$$

while Eq. (2.42) for the spin components reads

$$\begin{aligned}
\frac{\partial}{\partial t} J_y(t) &= c \cdot a \cdot \langle S_z(z,t) \rangle_z \, J_x(t) \\
\frac{\partial}{\partial t} J_z(t) &= c \cdot a \cdot \xi^2 \cdot \sigma^{j_x} \cdot \langle S_y(z,t) \rangle_z \, J_x(t).
\end{aligned} \tag{2.44}$$

We can solve the equations for the Stokes operatos by integrating over z, since $S_x(z,t)$ is constant in z and t as discussed earlier. We obtain

$$\begin{aligned}
S_y(L,t) &= S_y(0,t) + a S_x(z,t) J_z(t) \\
S_z(L,t) &= S_z(0,t) + a \xi^2 \sigma^{j_x} S_x(z,t) J_y(t).
\end{aligned} \tag{2.45}$$

The average values of $S_y(z,t)$ and $S_z(z,t)$ over the cell length are simply

$$\begin{aligned}
\langle S_y(z,t) \rangle_z &= S_y(0,t) + \frac{1}{2} a S_x(z,t) J_z(t) \\
\langle S_z(z,t) \rangle_z &= S_z(0,t) + \frac{1}{2} a \xi^2 \sigma^{j_x} S_x(z,t) J_y(t).
\end{aligned} \tag{2.46}$$

Inserting this in Eq. (2.44) for the spin gives

$$\begin{aligned}
\frac{\partial}{\partial t} J_y(t) &= a S_z^{\text{in}}(t) J_x(t) + \frac{1}{2} a^2 \xi^2 \sigma^{j_x} S_x(t) J_x(t) J_y(t) \\
\frac{\partial}{\partial t} J_z(t) &= a \xi^2 \sigma^{j_x} S_y^{\text{in}}(t) J_x(t) + \frac{1}{2} a^2 \xi^2 \sigma^{j_x} S_x(t) J_x(t) J_z(t),
\end{aligned} \tag{2.47}$$

where we used the input/output notation for the Stokes operators. Also, using this notation, we find

$$\begin{aligned} S_y^{\text{out}}(t) &= S_y^{\text{in}}(t) + aS_x(t)J_z(t) \\ S_z^{\text{out}}(t) &= S_z^{\text{in}}(t) + a\xi^2\sigma^{j_x}S_x(t)J_y(t). \end{aligned} \tag{2.48}$$

Equations (2.47) and (2.48) reduce to the single cell QND input-output equations (2.35) and (2.36) in the limit $\xi^2 \to 0$.

2.4.6 Single cell canonical operators

The equations of motion will soon start to be longer. In order to keep the notation simple, we now switch to the canonical operator language. We define

$$\begin{aligned} x(t) &= \sigma^{j_x}\frac{J_y(t)}{\sqrt{|J_x(t)|}} \qquad & p(t) &= \frac{J_z(t)}{\sqrt{|J_x(t)|}} \\ y^{\text{in}}(t) &= \sigma^{S_x}\frac{S_y^{\text{in}}(t)}{\sqrt{|S_x(t)|}} \qquad & q^{\text{in}}(t) &= \frac{S_z^{\text{in}}(t)}{\sqrt{|S_x(t)|}}. \end{aligned} \tag{2.49}$$

$y^{\text{out}}(t)$ and $q^{\text{out}}(t)$ are similarly defined by replacing "in" with "out". Equation (2.47) for the spin operators can be rewritten using the canonical operator language:

$$\begin{pmatrix} \dot{x}(t) \\ \dot{p}(t) \end{pmatrix} = \widetilde{a}\begin{pmatrix} q^{\text{in}}(t) \\ -\zeta^2 y^{\text{in}}(t) \end{pmatrix} - \frac{\widetilde{a}^2\zeta^2}{2}\begin{pmatrix} x(t) \\ p(t) \end{pmatrix}. \tag{2.50}$$

When deriving the above equation, it is assumed that $J_x(t)$ and $S_x(t)$ are constant in time. This means that the atomic T_1 time (representing the decay of the mean spin $J_x(t)$) should be long compared to the interaction time T. If this is not the case, one should also add terms in Eq. (2.50) proportional to the time derivative of $1/\sqrt{|J_x(t)|}$. For an exponential decay $J_x(t) = J_x(0)e^{-t/T1}$, this leads to a term $\dot{x} = ... + \frac{1}{2T_1}x$ in the x-quadrature and similar in the p-quadrature. However, in most of the experiments, the T_1-decay is small and can be neglected. In Eq. (2.50), we used the coupling constant $\widetilde{a}$ between the time-dependent canonical operators which is defined by

$$\widetilde{a} \equiv a\sqrt{|J_x(t)|\,|S_x(t)|}. \tag{2.51}$$

We also used the definition $\zeta^2 \equiv -\xi^2\sigma^{S_x}$. In the experiments presented in this thesis, the probe is polarized along the y-direction. $\sigma^{S_x} < 0$ for this probe polarization. We therefore choose to define ζ^2 such that it is positive for a y-polarized probe.

2.4.7 Magnetic field and rotating frame

In the experiment, the atoms are located in a magnetic field pointing in the x-direction. This situation can in the theory be described by the total Hamiltonian $\mathcal{H}_{\rm tot} = \mathcal{H}_{\rm int} + \mathcal{H}_B$ where $\mathcal{H}_{\rm int}$ is given by Eq. (2.20) and $\mathcal{H}_B = g_F \mu_B \vec{J} \cdot \vec{B}$. We already calculated the contribution from $\mathcal{H}_{\rm int}$ to the time evolution of the spin operators using the Heisenberg equation of motion given by Eq. (2.22). Now, we calculate the contribution to the time evolution due to $\mathcal{H}_B$. We find

$$\frac{dJ_y}{dt} = -\Omega_L J_z \qquad \text{and} \qquad \frac{dJ_z}{dt} = \Omega_L J_y. \tag{2.52}$$

In the canonical operator language this reads

$$\begin{pmatrix} \dot{x} \\ \dot{p} \end{pmatrix} = \Omega \begin{pmatrix} -p \\ x \end{pmatrix}, \tag{2.53}$$

where we defined $\Omega \equiv \sigma^{j_x} \Omega_L$. This term should be added to the right hand side of Eq. (2.50) in order to include the time evolution from both $\mathcal{H}_{\rm int}$ and $\mathcal{H}_B$.

In order to solve the equations of motion for an atomic ensemble located in a magnetic field, it is convinent to consider rotating frame operators x', p' defined by

$$\begin{pmatrix} x' \\ p' \end{pmatrix} = \begin{pmatrix} \cos\Omega t & \sin\Omega t \\ -\sin\Omega t & \cos\Omega t \end{pmatrix} \begin{pmatrix} x \\ p \end{pmatrix}. \tag{2.54}$$

In terms of the rotating frame operators, the equations of motion (2.50) and (2.53) now read

$$\begin{pmatrix} \dot{x}' \\ \dot{p}' \end{pmatrix} = \widetilde{a} \begin{pmatrix} \cos\Omega t & \sin\Omega t \\ -\sin\Omega t & \cos\Omega t \end{pmatrix} \begin{pmatrix} q^{\rm in}(t) \\ -\zeta^2 y^{\rm in}(t) \end{pmatrix} - \gamma \begin{pmatrix} x'(t) \\ p'(t) \end{pmatrix} + \sqrt{2\gamma_{\rm bad}} \begin{pmatrix} F_x(t) \\ F_p(t) \end{pmatrix}. \tag{2.55}$$

In the above equation we added the term: $\dot{x}' = ... - \gamma_{\rm bad} x' + \sqrt{2\gamma_{\rm bad}} F_x(t)$ in order to include atomic decoherence processes in the theory. The rate $\gamma_{\rm bad}$ is the rate of the "bad" decoherence processes which leads to a decay of x' and p'. The operators $F_x(t)$ and $F_p(t)$ are rotating frame noise operators with zero mean. We will assume that the noise is "white" and that the decay is towards the vacuum state. This means that the noise operators have the correlation $\langle F_x(t) F_x(t') \rangle = {\rm Var}\,(F_x)\,\delta(t-t')$ with ${\rm Var}\,(F_x) = 1/2$ [10]. In Eq. (2.55) we also used the parameter γ which is defined by

$$\gamma \equiv \frac{\widetilde{a}^2 \zeta^2}{2} + \gamma_{\rm bad}. \tag{2.56}$$

[10] In the experiment, there can be several different sources of bad decoherence. Some, such as the loss of atoms from the $F = 4$ manifold, will lead to a decay towards the vacuum state. Other processes can induce decay to states which have noise higher than vacuum. An example of such a process is in-elastic collisions within the $F = 4$ manifold where population is transferred to m-levels different from $m = 4$. However, to keep things simple, we will assume that the decay is towards the vacuum state.

γ is the total decay rate and has two contributions. The first term $\widetilde{a}^2\zeta^2/2$ is due to the coherent interaction between light and atoms, and the second term $\gamma_{\rm bad}$ is due to incoherent processes. In the experiment γ is easily measurable. The inverse of γ is called the transverse relaxation time $T_2 \equiv 1/\gamma$. The first term in Eq. (2.56) is an important parameter and is denoted the swap rate. It can be rewritten as

$$\gamma_{\rm sw} \equiv \frac{\widetilde{a}^2\zeta^2}{2} = 14 a_1 a_2 \left(\frac{\gamma}{8\Delta}\frac{\lambda^2}{2\pi}\right)^2 \frac{N_A \Phi}{A^2}, \tag{2.57}$$

where Φ is the photon flux which has the units $1/\mathrm{s}$ and is defined as $\Phi = 2\,|S_x(t)|$. We can formally solve Eq. (2.55), and we find

$$\begin{aligned}\begin{pmatrix} x'(t) \\ p'(t) \end{pmatrix} = &\int_{t'=0}^{t} e^{-\gamma(t-t')}\widetilde{a} \begin{pmatrix} \cos\Omega t' & \sin\Omega t' \\ -\sin\Omega t' & \cos\Omega t' \end{pmatrix} \begin{pmatrix} q^{\rm in}(t') \\ -\zeta^2 y^{\rm in}(t') \end{pmatrix} dt' \\ &+ \int_{t'=0}^{t} e^{-\gamma(t-t')}\sqrt{2\gamma_{\rm bad}} \begin{pmatrix} F_x(t') \\ F_p(t') \end{pmatrix} dt' + e^{-\gamma t}\begin{pmatrix} x'(0) \\ p'(0) \end{pmatrix}. \end{aligned} \tag{2.58}$$

These are the input-output equations for the single cell rotating frame canonical operators.

2.4.8 Integrated light modes

Instead of the time-dependent light operators, we can define integrated exponentially rising and falling temporal light modes such as

$$\begin{aligned} y^{\rm in}_{c,\pm} &= \frac{1}{N_{c,\pm}} \int_0^T y^{\rm in}(t)\cos(\Omega_L t) e^{\pm\gamma t} dt \\ y^{\rm out}_{c,\pm} &= \frac{1}{N_{c,\pm}} \int_0^T y^{\rm out}(t)\cos(\Omega_L t) e^{\pm\gamma t} dt. \end{aligned} \tag{2.59}$$

Notice, that these modes are defined to oscillate at the Larmor frequency Ω_L and not at the frequency $\Omega = \sigma^{j_x}\Omega_L$. In general, for any temporal mode function $h(t)$, we can define a (temporal) mode y_h as

$$y_h = \frac{1}{N_h}\int_0^T y(t)h(t)dt, \tag{2.60}$$

The normalization constant N_h is chosen to satisfy $|N_h|^2 = \int_0^T |h(t)|^2\,dt$. With this choice, one can show that $\mathrm{Var}\,(y_h) = \mathrm{Var}\,(y)$ if $\langle y(t)y(t')\rangle = \mathrm{Var}\,(y)\,\delta(t-t')$

and $\langle y(t)\rangle = 0$. For specific cases we have

$$\begin{aligned} h(t) &= \cos(\Omega t)e^{+\gamma t} \quad \Rightarrow \quad |N_{c,+}|^2 = \frac{e^{2\gamma T}-1}{4\gamma} \\ h(t) &= \cos(\Omega t)e^{-\gamma t} \quad \Rightarrow \quad |N_{c,-}|^2 = \frac{1-e^{-2\gamma T}}{4\gamma} \\ h(t) &= e^{+\gamma t} \quad \Rightarrow \quad |N_{+}|^2 = \frac{e^{2\gamma T}-1}{2\gamma} \\ h(t) &= \cos(\Omega t) \quad \Rightarrow \quad |N_{c}|^2 = \frac{T}{2}. \end{aligned} \tag{2.61}$$

In the above, we considered light modes which are integrated from $t = 0$ to the duration of the probe pulse T. These integrated light modes do not depend on the intermediate time t. On the other hand, sometimes it is convinient to introduce time-dependent cosine and sine modes. For instance, we can define a time-dependent mode $y_c^{\rm out}(t)$:

$$y_c^{\rm out}(t) = \sqrt{\frac{2}{\delta t}} \int_{t'=t}^{t+\delta t} y^{\rm out}(t') \cos\left(\Omega_L t'\right) dt'. \tag{2.62}$$

The integration interval δt should be much larger than $1/\Omega_L$ but still much shorter than the relevant light-atom interaction time $1/\gamma$. The time-dependent modes $y_c^{\rm out}(t)$ and $y_s^{\rm out}(t)$ are measured in the experiment and corresponds to the raw data. From the measurements of these time-dependent modes, one can calculate all other integrated modes as discussed later in Sec. 3.7.

Using the definitions of the integrated light modes, we can rewrite Eq. (2.58) for the atomic operators as

$$\begin{aligned} \begin{pmatrix} x'(T) \\ p'(T) \end{pmatrix} = \widetilde{a}\sqrt{\frac{1-e^{-2\gamma T}}{4\gamma}} \begin{pmatrix} q_{c,+}^{\rm in} \\ -\sigma^{j_x} q_{s,+}^{\rm in} \end{pmatrix} - \widetilde{a}\zeta^2 \sqrt{\frac{1-e^{-2\gamma T}}{4\gamma}} \begin{pmatrix} \sigma^{j_x} y_{s,+}^{\rm in} \\ y_{c,+}^{\rm in} \end{pmatrix} \\ + \sqrt{2\gamma_{\rm bad}} \sqrt{\frac{1-e^{-2\gamma T}}{2\gamma}} \begin{pmatrix} F_{x,+} \\ F_{p,+} \end{pmatrix} + e^{-\gamma T} \begin{pmatrix} x'(0) \\ p'(0) \end{pmatrix}. \end{aligned} \tag{2.63}$$

We now define the important parameters

$$\kappa^2 = \frac{1-e^{-2\gamma T}}{\zeta^2} \qquad \text{and} \qquad \epsilon^2 = \frac{\gamma_{\rm bad}}{\gamma}. \tag{2.64}$$

Strictly speaking, using these definitions, both κ^2 and ϵ^2 can be negative. However, in the following it is assumed that ζ^2 is positive (which implies that also $\gamma > 0$, $\kappa^2 > 0$ and $\epsilon^2 > 0$) and $\widetilde{a}$ is positive. We now rewrite the solution for the

atomic operators as

$$\begin{pmatrix} x'(T) \\ p'(T) \end{pmatrix} = \frac{\kappa\sqrt{1-\epsilon^2}}{\sqrt{2}} \begin{pmatrix} q^{\rm in}_{c,+} \\ -\sigma^{j_x} q^{\rm in}_{s,+} \end{pmatrix} - \frac{\kappa\sqrt{1-\epsilon^2}\zeta^2}{\sqrt{2}} \begin{pmatrix} \sigma^{j_x} y^{\rm in}_{s,+} \\ y^{\rm in}_{c,+} \end{pmatrix} + \epsilon\kappa\zeta \begin{pmatrix} F_{x,+} \\ F_{p,+} \end{pmatrix} + \sqrt{1-\kappa^2\zeta^2} \begin{pmatrix} x'(0) \\ p'(0) \end{pmatrix}. \tag{2.65}$$

Notice that the atomic operators only couple to exponentially rising input light modes. Equation (2.65) is the final result for the input-output equations for the atomic canonical variables for the case of a single cell located in a magnetic field and where both the tensor polarizability and the decay is included.

2.4.9 Light operators

The next step is to calculate the input-output equations for the appropriate light modes. We first rewrite Eq. (2.48) for the Stokes operators in terms of the canonical light operators $y^{\rm out}(t)$ and $q^{\rm out}(t)$ and the rotating frame atomic operators:

$$\begin{aligned} y^{\rm out}(t) &= y^{\rm in}(t) + \widetilde{a}p(t) \quad = y^{\rm in}(t) + \widetilde{a}\left[\cos(\Omega_L t)p' + \sigma^{j_x}\sin(\Omega_L t)x'\right] \\ q^{\rm out}(t) &= q^{\rm in}(t) - \widetilde{a}\zeta^2 x(t) = q^{\rm in}(t) - \widetilde{a}\zeta^2\left[\cos(\Omega_L t)x' - \sigma^{j_x}\sin(\Omega_L t)p'\right]. \end{aligned} \tag{2.66}$$

Now, Eq. (2.58) for $x'(t)$ and $p'(t)$ are inserted. Actually, we are interested in finding equations for the integrated operators $y^{\rm out}_{c,-}$, $y^{\rm out}_{s,-}$, $q^{\rm out}_{c,-}$ and $q^{\rm out}_{s,-}$. This can be done by using the approximation $\Omega_L \gg \gamma$. With this approximation we have $\cos^2(\Omega_L t)e^{-\gamma t} \approx \frac{1}{2}e^{-\gamma t}$ and $\cos(\Omega_L t)\sin(\Omega_L t)e^{-\gamma t} \approx 0$. Using the assumption $\zeta^2 > 0$, we find (using matrix notation)

$$\begin{pmatrix} y^{\rm out}_{c,-} \\ y^{\rm out}_{s,-} \\ q^{\rm out}_{c,-} \\ q^{\rm out}_{s,-} \end{pmatrix} = \begin{pmatrix} y^{\rm in}_{c,-} \\ y^{\rm in}_{s,-} \\ q^{\rm in}_{c,-} \\ q^{\rm in}_{s,-} \end{pmatrix} - \frac{1-\epsilon^2}{2} \begin{pmatrix} 1 & 0 & 0 & \frac{\sigma^{j_x}}{\zeta^2} \\ 0 & 1 & -\frac{\sigma^{j_x}}{\zeta^2} & 0 \\ 0 & -\sigma^{j_x}\zeta^2 & 1 & 0 \\ \sigma^{j_x}\zeta^2 & 0 & 0 & 1 \end{pmatrix} \begin{pmatrix} y^{\rm in}_{c,-} - \sqrt{1-\kappa^2\zeta^2}y^{\rm in}_{c,+} \\ y^{\rm in}_{s,-} - \sqrt{1-\kappa^2\zeta^2}y^{\rm in}_{s,+} \\ q^{\rm in}_{c,-} - \sqrt{1-\kappa^2\zeta^2}q^{\rm in}_{c,+} \\ q^{\rm in}_{s,-} - \sqrt{1-\kappa^2\zeta^2}q^{\rm in}_{s,+} \end{pmatrix}$$

$$+\frac{\kappa\sqrt{1-\epsilon^2}}{\sqrt{2}} \begin{pmatrix} 0 & 1 \\ \sigma^{j_x} & 0 \\ -\zeta^2 & 0 \\ 0 & \sigma^{j_x}\zeta^2 \end{pmatrix} \begin{pmatrix} x'(0) \\ p'(0) \end{pmatrix} + \frac{\epsilon\sqrt{1-\epsilon^2}}{\sqrt{2}\zeta} \begin{pmatrix} 0 & 1 \\ \sigma^{j_x} & 0 \\ -\zeta^2 & 0 \\ 0 & \sigma^{j_x}\zeta^2 \end{pmatrix} \begin{pmatrix} F_{x,-} - \sqrt{1-\kappa^2\zeta^2}F_{x,+} \\ F_{p,-} - \sqrt{1-\kappa^2\zeta^2}F_{p,+} \end{pmatrix}. \tag{2.67}$$

The above equation for the output light operators is a bit complicated. First of all, notice that the right hand side contains terms with both rising and falling light modes. This is not desirable, in fact, we would like to decompose the modes such that the equation only contains orthogonal light modes. This will be discussed in detail in Sec. 2.4.12.

The main focus in this thesis is on the interaction between light and two oppositely oriented atomic ensembles. Equation (2.67), which is valid for light interacting with a single ensemble, will later in Sec. 2.4.11 be used to derive the two cell input-output equations. Otherwise, we will not go into more details with the above equation.

2.4.10 Two cell atomic operators

We now focus on the interaction between light and two oppositely oriented atomic ensembles (see the illustration in Fig. 2.2). In this case, a significant simplification of the input-output equations occurs.

The equations of motion for the first cell operators x_1' and p_1' have already been derived and are given by Eq. (2.58) or (2.65), if one replaces x' with x_1', p' with p_1' and uses $\sigma^{j_x} = +1$ and $\Omega = +\Omega_L$. When considering the equations of motion for the second cell operators x_2' and p_2' one has to be careful. The light interacts with the two atomic ensembles one after the other. This means that the light, which enters the second cell, has already interacted with the first cell. Below we show that even though the light has interacted with the first cell this has no influence on evolution of the second cell operators. This means that we can also use Eq. (2.58) or (2.65) for the second cell, if we replace x' with x_2', p' with p_2' and use $\sigma^{j_x} = -1$ and $\Omega = -\Omega_L$.

In order to describe the situation with light interacting with both ensembles, we use the following notation for the different input-output light operators

$$y^{\text{in}} \xrightarrow{\text{cell 1}} y^{\text{out},1} = y^{\text{in},2} \xrightarrow{\text{cell 2}} y^{\text{out},2}, \tag{2.68}$$

where the light which outputs cell 1 is used as input to cell 2. We can write $y^{\text{out},1}$ and $q^{\text{out},1}$ given by Eq. (2.66) again using explicitly the cell 1 operators:

$$\begin{aligned} y^{\text{out},1}(t') &= y^{\text{in}}(t') + \widetilde{a}\left[\cos(\Omega_L t')p_1'(t') + \sin(\Omega_L t')x_1'(t')\right] \\ q^{\text{out},1}(t') &= y^{\text{in}}(t') - \widetilde{a}\zeta^2\left[\cos(\Omega_L t')x_1'(t') - \sin(\Omega_L t')p_1'(t')\right]. \end{aligned} \tag{2.69}$$

We now calculate what happens to the cell 2 operators by using the light operators which are output from the cell 1:

$$\begin{aligned} \begin{pmatrix} x_2'(t) \\ p_2'(t) \end{pmatrix} &= \int_{t'=0}^{t} e^{-\gamma(t-t')}\widetilde{a} \begin{pmatrix} \cos\Omega t' & \sin\Omega t' \\ -\sin\Omega t' & \cos\Omega t' \end{pmatrix} \begin{pmatrix} q^{\text{out},1}(t') \\ -\zeta^2 y^{\text{out},1}(t') \end{pmatrix} dt' \\ &\quad + \int_{t'=0}^{t} e^{-\gamma(t-t')}\sqrt{2\gamma_{\text{bad}}} \begin{pmatrix} F_x(t') \\ F_p(t') \end{pmatrix} dt' + e^{-\gamma t} \begin{pmatrix} x'(0) \\ p'(0) \end{pmatrix}. \end{aligned} \tag{2.70}$$

The light operators in Eq. (2.69) can be inserted in Eq. (2.70) for the cell 2 operators. The cell 2 operators have terms similar to the ones given by Eq. (2.58), and have extra terms which are proportional to the cell 1 operators such

as

$$x_2'(t) = ... - \widetilde{a}\zeta^2 \int_{t'=0}^{t} e^{-\gamma(t-t')} \left\{ x_1'(t') \cos(2\Omega_L t') - p_1'(t') \sin(2\Omega_L t') \right\} dt',$$

and similarly for $p_2'(t)$. Such extra terms average out for times greater than $1/\Omega_L$ and we neglect these. Doing this, we find that the cell 2 operators are also given by Eq. (2.58) and (2.65) with $y^{\text{in}}(t')$ and $q^{\text{in}}(t')$ being the light mode that inputs cell 1. It is as if the atoms in the cell 2 do not know that the light has interacted with the atoms in the cell 1.

We can now calculate the time evolution of the two cell non-local operators defined in Eq. (2.2) using the single cell Eq. (2.65). For two oppositely oriented ensembles, several terms cancel since $\sigma^{j_x} = +1$ for the first ensemble and $\sigma^{j_x} = -1$ for the second ensemble. We arrive at a quite simple expression for the two cell operators

$$\begin{pmatrix} X_c^{\text{out}} \\ P_c^{\text{out}} \end{pmatrix} = \sqrt{1-\kappa^2\zeta^2} \begin{pmatrix} X_c^{\text{in}} \\ P_c^{\text{in}} \end{pmatrix} + \kappa\sqrt{1-\epsilon^2} \begin{pmatrix} q_{c,+}^{\text{in}} \\ -\zeta^2 y_{c,+}^{\text{in}} \end{pmatrix} + \epsilon\kappa\zeta \begin{pmatrix} F_{xc,+} \\ F_{pc,+} \end{pmatrix}, \quad (2.71)$$

and a similar equation for the sine atomic operators. In the above, we used the notation in/out for atomic operators at time $t = 0$ and $t = T$, respectively. $F_{xc,+}$ and $F_{pc,+}$ are noise operators [11]. In the limit $\epsilon^2 \to 0$, which is the case when decoherence is negligible, Eq. (2.71) reduces to Eq. (2.18) which was presented in the beginning of the chapter when discussing the swap and squeezing interaction.

2.4.11 Two cell light operators

We can also find the light operators which output cell 2. Using the single cell equation (2.66) twice, we find

$$\begin{aligned} y^{\text{out},2}(t) &= y^{\text{out},1}(t) + \widetilde{a}p_2(t) \quad &= y^{\text{in}}(t) + \widetilde{a}\left\{p_1(t) + p_2(t)\right\} \\ q^{\text{out},2}(t) &= q^{\text{out},1}(t) - \widetilde{a}\zeta^2 x_2(t) &= q^{\text{in}}(t) - \widetilde{a}\zeta^2\left\{x_1(t) + x_2(t)\right\}. \end{aligned} \quad (2.72)$$

In the previous Sec. 2.4.10, we showed that the time-evolution of the cell 2 operators is independent of the cell 1 operators. The output light operators can therefore be found in the same way as when we derived Eq. (2.67). Due to the fact that $\sigma^{j_x} = +1$ for atoms in the first ensemble and $\sigma^{j_x} = -1$ for atoms in the

[11] The noise operator $F_{xc,+}$ is defined by $F_{xc,+} \equiv (F_{x1,+} + F_{x2,+})/\sqrt{2}$. 1 and 2 refers to the noise operators for atoms in cell 1 and 2. This means that $F_{xc,+}$ is a non-local noise operator. The other noise operators are similarly defined as either the sum or difference of the single cell noise operators.

second ensemble some terms cancel, and we find

$$\begin{pmatrix} y_{c,-}^{\text{out},2} \\ q_{c,-}^{\text{out},2} \end{pmatrix} = \epsilon^2 \begin{pmatrix} y_{c,-}^{\text{in}} \\ q_{c,-}^{\text{in}} \end{pmatrix} + \kappa\sqrt{1-\epsilon^2} \begin{pmatrix} P_c^{\text{in}} \\ -\zeta^2 X_c^{\text{in}} \end{pmatrix} + \left(1-\epsilon^2\right)\sqrt{1-\kappa^2\zeta^2} \begin{pmatrix} y_{c,+}^{\text{in}} \\ q_{c,+}^{\text{in}} \end{pmatrix} + \frac{\epsilon\sqrt{1-\epsilon^2}}{\zeta} \begin{pmatrix} F_{pc,-} - \sqrt{1-\kappa^2\zeta^2}F_{pc,+} \\ -\zeta^2\left\{F_{xc,-} - \sqrt{1-\kappa^2\zeta^2}F_{xc,+}\right\} \end{pmatrix}, \tag{2.73}$$

and similarly for the sine modes. In most cases it is clear from the context whether the light interacts with one or two atomic ensembles. Therefore, from now on we will not write the superscript $out, 2$ on the cell 2 output light operators but instead just use the superscript out. The above equation for the output light operators together with Eq. (2.71) for the atomic operators are the final input-output equations for the full swap and squeezing interaction theory with decoherence included in the model.

We would also like to have an expression for the variances of the output light operators such as $\text{Var}\left(y_{c,-}^{\text{out}}\right)$ (where the superscript out is used instead of $out, 2$). As mentioned earlier, this requires some work since the right hand side of Eq. (2.73) contains both rising and falling light modes. The problem is that the rising and falling light modes are not orthogonal. This implies that the variance of a linear combination of the two light modes cannot be "easily" calculated since

$$\text{Var}\left(Ay_{c,+}^{\text{in}} + By_{c,-}^{\text{in}}\right) \neq A^2\text{Var}\left(y_{c,+}^{\text{in}}\right) + B^2\text{Var}\left(y_{c,-}^{\text{in}}\right), \tag{2.74}$$

where A and B are some arbitrary constants. Notice, that the right hand side and left hand side of Eq. (2.74) are *not* equal. To solve the problem we have to decompose the rising and falling modes into two orthogonal modes.

2.4.12 Orthogonal modes

Suppose we have two normalized temporal modes $h_1(t)$ and $h_2(t)$. We would like to find the variance of a linear combination of the light operator $Ay_{h_1} + By_{h_2}$. Assuming $\langle y(t)y(t')\rangle = \text{Var}\left(y\right)\delta(t-t')$ and $\langle y(t)\rangle = 0$, a small calculation shows that

$$\text{Var}\left(Ay_{h_1} + By_{h_2}\right) = \left[A^2 + B^2 + 2AB\left\langle h_1 \middle| h_2\right\rangle\right] \cdot \text{Var}\left(y\right). \tag{2.75}$$

The inner product between two modes is defined by $\langle h_1 | h_2\rangle = \int_0^T h_1(t)h_2(t)dt$. We see that only if the two modes are orthogonal $\langle h_1 | h_2\rangle = 0$, then the variance can be found from the simple relation:

$$\text{Var}\left(Ay_{h_1} + By_{h_2}\right) = \left[A^2 + B^2\right] \cdot \text{Var}\left(y\right) \Leftrightarrow \left\langle h_1 \middle| h_2\right\rangle = 0. \tag{2.76}$$

The right hand side of the input-output equation (2.73) for the light operators contains terms with both exponentially rising and falling modes. It is

convinient to introduce a mode orthogonal to $h_{c,+} = \cos(\Omega_L t)e^{-\gamma t}/N_{c,+}$. This mode is denoted $h_{c,+,\perp}$ or $h_{c,\perp}$ for short. Using the method of Gram-Schmidt orthonormalization we find the relation for the modes

$$h_{c,-} = \sqrt{1-C^2}h_{c,+,\perp} + Ch_{c,+}, \tag{2.77}$$

where the parameter C is defined as

$$C = \frac{\gamma T}{\sinh(\gamma T)}. \tag{2.78}$$

A similar equation holds for the sine modes and also for the modes h_- and h_+ which are used for the noise operators (such as $F_{x,-}$). To be specific, we also have the relation

$$h_- = \sqrt{1-C^2}h_{+,\perp} + Ch_+. \tag{2.79}$$

Notice, that even though the normalizations of the modes $h_{c,+}$ and h_+ differs by a factor of 2 ($|N_{c,+}| = |N_+|/2$), the decomposition into orthogonal modes is similar for the two cases.

Equation (2.77) for the mode-function $h(t)$ also holds for the light operators y_h. In particular, for the input modes we have the relation

$$y^{\text{in}}_{c,-} = \sqrt{1-C^2}y^{\text{in}}_{c,\perp} + Cy^{\text{in}}_{c,+}. \tag{2.80}$$

The input falling light mode has now been decomposed into two orthogonal modes: the rising mode and the "perpendicular" mode. The expression (2.80) can now be inserted into the one cell Eq. (2.67) and the two cell Eq. (2.73). This way, the equations for the output light operators can be rewritten in terms of orthogonal modes only. The noise operators should also be decomposed into orthogonal modes. I will not write out the expressions explicitly since the equations will be slightly longer and because the rewriting is straight forward.

2.4.13 Atomic Noise

We now have an expression (not written down) for the output light operators in terms of orthogonal modes only. With this expression, we can calculate the variances of the output operators since for two orthogonal operators such as $y^{\text{in}}_{c,+}$ and $y^{\text{in}}_{c,\perp}$ the variances can be calculated from the following equation

$$\text{Var}\left(Ay^{\text{in}}_{c,+} + By^{\text{in}}_{c,\perp}\right) = A^2\text{Var}\left(y^{\text{in}}_{c,+}\right) + B^2\text{Var}\left(y^{\text{in}}_{c,\perp}\right), \tag{2.81}$$

where A and B are some factors. If we assume that the input light operators and the noise operators are vacuum with variance 1/2, we find

$$\text{Var}\left(y^{\text{out}}_{c,-}\right) = t_m^2 \cdot \frac{1}{2} + \kappa_m^2\text{Var}\left(P^{\text{in}}_c\right), \tag{2.82}$$

where we defined the two parameters

$$t_m^2 = \frac{\sinh(2\gamma T) + \left(1-2\epsilon^2\right)\left(1-\cosh(2\gamma T)\right) - 2\epsilon^2\left(1-\epsilon^2\right)\left(Z^2-1\right)\left(2\gamma T - \sinh(2\gamma T)\right)}{e^{2\gamma T}-1} \tag{2.83}$$

and

$$\kappa_m^2 = \left(1-\epsilon^2\right) Z^2 \left(1-e^{-2\gamma T}\right). \tag{2.84}$$

Using Eq. (2.82), it is possible to find the variance of the atomic P_c^{in} operator from the measured variance of the output light operator $y_{c,-}^{\text{out}}$. One would also need the values of the parameters κ_m^2 and t_m^2. Usually, κ_m^2 is measured with the mean value transfer method described in Sec. 3.6.1, and t_m^2 is calculated using Eq. (2.83) together with measured values of γ and κ_m^2 and estimated values of Z^2 and T.

If we measure both the cosine and sine components of the output light, we have the following relation

$$\begin{aligned} \text{Var}\left(y_{c,-}^{\text{out}}\right) + \text{Var}\left(y_{s,-}^{\text{out}}\right) &= t_m^2 + \kappa_m^2\left(\text{Var}\left(P_c^{\text{in}}\right) + \text{Var}\left(P_s^{\text{in}}\right)\right) \\ &= t_m^2 + \kappa_m^2 \cdot \Sigma_{\text{EPR}}. \end{aligned} \tag{2.85}$$

From the measurement of the variances of the cosine and sine output light operaters, we can calculate the atomic noise in PN-units Σ_{EPR}. In particular, we can determine whether the two atomic ensembles are entangled ($\Sigma_{\text{EPR}} < 1$). I want to emphasize that the above equation is only true if the temporal mode function of the output light is chosen to be exponentially falling with time constant $T_2 = 1/\gamma$. Equation (2.85) is very important and is used throughout the thesis when analyzing experimental data and reconstructing atomic variances from the measured output light variances.

2.5 Final remarks on the light-atom interaction theories

The input-output equations (2.18) for the swap and squeezing interaction theory differ from the input-output equations (2.6) for the QND interaction theory. Firstly, the coupling strengths κ^2 and $\tilde{\kappa}^2$ are defined differently, and secondly, the input operators are reduced in the swap and squeezing interaction theory while not changed in the QND interaction theory.

In this section, we discuss how the two sets of input-output equations are related. We compare the two coupling constants $\tilde{\kappa}^2$ and κ^2, and we also rewrite $\tilde{\kappa}^2$ into a simple expression involving the optical depth and the probability for spontaneous emission.

Comparison between the swap and squeezing interaction theory and the QND interaction theory

For short interaction times one can Taylor expand the coupling constant $\kappa^2 = \left(1 - e^{-2\gamma_{\rm sw}T}\right)/\zeta^2 \approx 2\gamma_{\rm sw}T/\zeta^2$. Inserting the definition for the swap rate $\gamma_{\rm sw} \equiv \widetilde{a}^2\zeta^2/2$ given by Eq. (2.57), we find the relation $\kappa^2 \approx \widetilde{a}^2 T$. This is exactly the definition of $\tilde{\kappa}^2$ given in Eq. (2.7). So $\kappa^2 \approx \tilde{\kappa}^2$ for short interaction times $2\gamma_{\rm sw}T \ll 1$. For the intermediate coupling strength $\kappa^2 = 1$ and at our experimental detuning where $\zeta^2 \approx 1/6.4$, we have $2\gamma_{\rm sw}T \approx 0.17$. This leads to the value $\tilde{\kappa}^2 = 2\gamma_{\rm sw}T/\zeta^2 \approx 1.12$ which is not too far from the value of $\kappa^2 = 1$.

In the swap and squeezing interaction theory, the input variances are reduced by the factor $1 - \kappa^2\zeta^2$ while in the QND interaction theory the input variances are not changed. For $\zeta^2 \approx 1/6.4$ and for small coupling strengths, the factor $1 - \kappa^2\zeta^2$ is close to 1. At the intermediate coupling strength $\kappa^2 = 1$, the input variances are reduced by the factor $1 - 1/6.4 \approx 0.84$.

The above small calculations demonstrate that the QND input-output equations are a good approximation to the swap and squeezing input-output equations as long as the coupling is weak ($2\gamma_{\rm sw}T \ll 1$).

However, in most of our experiments the coupling is of intermediate strength ($\kappa^2 \approx 1$). Then, the light-atom interaction is described better with the swap and squeezing interaction theory than with the QND interaction theory.

In some of the experiments (the generation of two-mode squeezed light described in chapter 4 and entanglement generated by dissipation & and steady state entanglement described in chapter 7) where long interaction times are utilized ($2\gamma_{\rm sw}T \gg 1$), the QND interaction theory is not valid, and the interaction has to be described by the swap and squeezing interaction theory.

Finally, note that it is possible to realize the QND interaction in multi-level atoms with a tensor polarizability using special methods such as dynamical decoupling. In [39], the QND interaction is realized by switching the probe polarization from vertical to horisontal on a fast timescale. Using our description of the light-atom interaction, this can be understood from the fact that ζ^2 changes sign by changing the probe polarization (see below Eq. (2.51)).

Simple expression for the coupling strength

We can try to rewrite the QND coupling constant $\tilde{\kappa}^2$ in terms of some physically relevant parameters. Using the definition of $\tilde{\kappa}$ and the constant $a(\Delta)$ given by Eq. (2.28), we find

$$\begin{aligned}\tilde{\kappa}^2 &= a^2\,|J_x(t)|\,|S_x(t)|\,T \\ &= \left[\frac{N_A\sigma_{\rm CS}}{A}\right]\cdot\left[\frac{N_{\rm ph}\sigma_{\rm CS}}{A}\frac{(\gamma/2)^2}{\Delta^2}\right],\end{aligned} \tag{2.86}$$

where we used $|J_x(t)| = 4N_A$ for the fully pumped ensemble and $|S_x(t)|\,T = N_{\mathrm{ph}}/2$ and defined the atomic cross section

$$\sigma_{\mathrm{CS}} = \left(\frac{\lambda^2}{2\pi}\right) a_1(\Delta)\frac{1}{\sqrt{8}}, \tag{2.87}$$

which has the units of an area. The two terms in Eq. (2.86) can be interpreted as the optical depth on resonance α and the depumping parameter η_T defined here as

$$\alpha = \frac{N_A\sigma_{\mathrm{CS}}}{A} \quad \text{and} \quad \eta_T = \frac{N_{\mathrm{ph}}\sigma_{\mathrm{CS}}}{A}\frac{(\gamma/2)^2}{\Delta^2}. \tag{2.88}$$

The depumping parameter is interpreted as the probability of spontaneous emission and equals the spontaneous emission rate η_{sp} times the probe duration T such that $\eta_T = \eta_{\mathrm{sp}} \cdot T$. In total we find the relation

$$\tilde{\kappa}^2 = \alpha \cdot \eta_T. \tag{2.89}$$

In general, spontaneous emission is a source of decoherence. But we also see that without spontaneous emission, the coupling is not possible. The optimal situation is a high optical depth and a tolerable depumping parameter.

Chapter 3

Experimental details

3.1 Introduction

In this chapter we present the experimental details which are in common to all of the performed experiments. The lasers and the experimental setup are described and the measurement procedures are discussed. We present results for calibration measurements of the Faraday angle, decay rates and the coupling parameters. It is described how the atomic state can be characterized using a measurement of the light which has interacted with the atoms. We demonstrate that it is possible to initialize the atoms in a CSS and then entangle the two atomic ensembles. Since many of the experimental details have been described earlier in the PhD theses by B. Julsgaard [32] and J. Sherson [33], some parts are discussed only briefly.

3.2 Setup

3.2.1 Lasers

Several different lasers are used in the experiments. The atoms are probed using either a Toptica DFB diode laser or a Titanium-Saphire laser. Two homebuild external cavity pump lasers denoted the "pump" and the "repump" laser are used for optical pumping. The laser frequencies are shown in Fig. 2.1 together with the relevant cesium level structure. Cesium has the ground state $6S_{1/2}$ with the hyperfine levels $F = 3, 4$, the excited state $6P_{1/2}$ with hyperfine levels $F' = 3, 4$ and the excited state $6P_{3/2}$ with hyperfine levels $F' = 2, 3, 4, 5$. The pump light is resonant with the $D1$ transition, and the repump light is resonant with the $D2$ transition. The probe light is blue detuned from the $F = 4 \rightarrow F' = 5$ $D2$ transition with detuning Δ. The typical value of the probe detuning is around $\Delta = -850$ MHz.

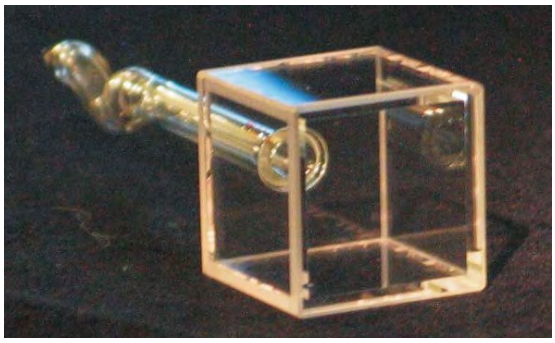

Figure 3.1: Cubic cesium vapor cell. In the end of the stem there is a drop of metallic cesium.

3.2.2 Cells

The heart of the experiment is the two cesium vapor cells which are custom made by the company Hellma [1]. Such a vapor cell is shown in Fig. 3.1. The cells are qubic with inside length $L = 22$ mm. There is a stem attached to the cell, and at the bottom of the stem there is a drop of metallic cesium. The cesium evaporate from the metallic drop and passes from the stem to inside the cell through a small hole. The density of atoms inside the cell depends on the temperature. In many cases, the experiments are performed at room-temperature, however, the cells can be heated by a flow of hot air if one wants to increase the density of atoms.

The cells have been anti-relaxation coated with paraffin by M. Balabas. With such a coating the moving cesium atoms can bounce of the inside glass surface many times without depolarizing. The quality of the coating can be estimated from measured relaxation times T_1 and T_2. Different coating materials have been investigated in our group [7]. Recently, relaxation times in the excess of 1 minute was demonstrated [40] by another group. Such a coating could be useful for our cells also. In particular, the quantum memory experiment should benefit from such long relaxation times since the storage time in the dark is directly related to the relaxation rates.

The cells have two anti-reflection coated windows attached in order to reduce probe transmission losses (these windows are not shown in the Fig. 3.1). The two cells are located in separate magnetic shieldings. Several coils are used to create the bias magnetic field, compensation fields and RF fields. The bias magnetic field is pointing in the x-direction and has the magnitude of 0.92 Gauss. This bias field makes the atoms Larmor precess with the frequency $\Omega_L = 322$ kHz. The frequency of the RF field is typically chosen to match the Larmor frequency.

[1] www.hellma.com

3.2.3 Optical pumping

The basic setup common to all of the experiments is shown in Fig. 3.2. The atomic ensembles are polarized by the pump and repump laser light travelling in the x-direction. The pump and repump light used for the first ensemble is σ_+-polarized such that the atoms in the first ensemble are polarized in the $+x$-direction. Similarly, the pump and repump light used for the second ensemble is σ_--polarized such that the atoms in the second ensemble are polarized in the $-x$-direction. The pump and repump light is expanded by lenses to a size comparable with the cell size. The pump and repump light can be turned on and off using acousto-optical modulators (AOM's).

3.2.4 Probing and homodyning

The probe light is propagating along the z-direction and is typically polarized in the y-direction. The probe light is expanded to a top hat spatial intensity profile with the diameter of 21 mm using a π-shaper [2]. The probe light traverse the two cells one after the other and is detected by a balanced homodyne setup consisting of waveplates, a polarizing beamsplitter and two detectors. In Fig. 3.2 both a half-wave plate and a quarter-wave plate is shown. Depending on the setting of the waveplates, the S_y or S_z component of the Stokes vector can be measured.

The homodyne signal (which equals the difference between the two detector signals) is sent to a lock-in amplifier where the Stokes operator is demodulated at the detection frequency $\Omega_{\text{det}} = 322$ kHz which also equals the atomic Larmor frequency Ω_L. The output of the lock-in amplifier is then send to the computer where it is measured by a data aquisition card and stored for later data analysing. More details of the data analysis can be found in Sec. 3.7.

3.2.5 Pulse sequence

Most of our experiments are pulsed, and the pulse sequence used most often is seen in Fig. 3.3. The atoms are first initialized in the CSS using the resonant pump and repump light. The atomic ensembles can the be probed by a 1st and a 2nd probe pulse. We can also apply optional magnetic RF pulses. The first RF pulse is used to create a mean perpendicular component of the spin (see Sec. 3.4). The second RF pulsed is used when generating unconditional entanglement (see Sec. 3.8). The pump and repump pulses are shaped by AOM's, the probe pulse is shaped by an electro-optical modulator (EOM), and the RF pulses are generated by a computer card.

[2] www.pishaper.com

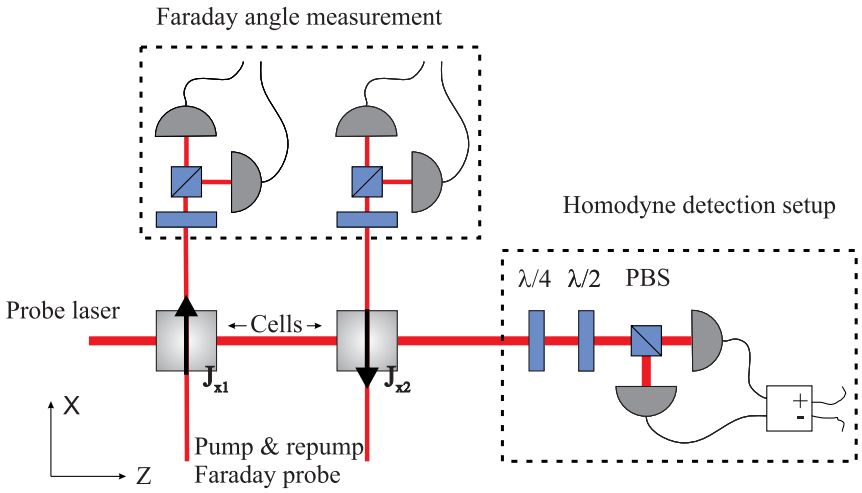

Figure 3.2: Setup. The figure shows the two oppositely oriented atomic ensembles and several laser beams denoted probe, Faraday probe, pump and repump. The probe light and the Faraday probe light can be measured with separate homodyne setups.

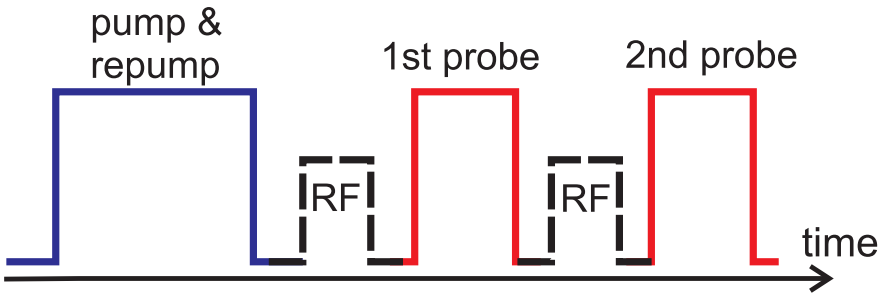

Figure 3.3: Typical experimental pulse sequence. The atoms are first initialized in the CSS using the pump and repump light. The atomic state can be probe by a 1st and a 2nd probe pulse. The two magnetic RF pulses are optional. The first RF pulse can be used to create a transverse spin component, as detailed in Sec. 3.4. The second RF pulse can be used to feed the measured 1st probe results back to the atomic spins as done when creating unconditional entanglement, as explained in Sec. 3.8.

3.3 Faraday angle

In the experiments we utilize a weak Faraday probe to measure the mean spin $\langle J_x(t)\rangle$ of each atomic ensemble. The mean spin is an important parameter in the experiment, since the atomic noise $\mathrm{Var}\,(J_y)$ and $\mathrm{Var}\,(J_z)$ and the coupling parameters such as κ^2 and γ_{sw} depends on the mean spin.

The Faraday probe is linearly polarized and is propagating in the x-direction, as seen in Fig. 3.2. When traversing the atomic ensemble, the polarization of the Faraday probe is rotated by an angle θ_F proportional the mean spin $\langle J_x\rangle$. Using Eq. (2.33), we find

$$\theta_F = -\frac{a_1\,(\Delta)\,\gamma\lambda^2\,\langle J_x\rangle}{32\pi A_{\mathrm{cell}}\Delta}. \tag{3.1}$$

The Faraday angle and the rotation angle θ of the Stokes vector are related by the formula $2\theta_F = \theta$ where $\theta = -a\,\langle J_x\rangle$. The Faraday probe is on DC (i.e. it is not pulsed) and is measured continuously in time $\theta_F = \theta_F(t)$. This way, the time evolution of the mean spin $\langle J_x(t)\rangle$ can be monitored continuously.

For a fully pumped ensemble $|\langle J_x\rangle| = 4N_A$, the number of atoms can be determined from the measured Faraday angle. The number of atoms is related to the Faraday angle by the equation

$$N_A = \left|\frac{32\pi A_{\mathrm{cell}}\theta_F\Delta}{a_1\,(\Delta)\,\gamma\lambda^2 4}\right|, \tag{3.2}$$

as seen from Eq. (3.1).

3.4 T_1 and T_2 times

The atomic spins decay in time due to for instance spontaneous emission, atomic collisions, loss of atoms and magnetic field inhomogeneities. Often, the decay is modelled as an exponential decay in time. The decay time of the mean spin is denoted T_1 and the decay time of a transversal/perpendicular (to the magnetic field direction x) spin component is denoted T_2. We have

$$J_x(t) = J_x(0)\exp\left(-t/T_1\right) \quad \text{and} \quad \mathrm{J_\perp(t) = J_\perp(0)\exp\left(-t/T_2\right).} \tag{3.3}$$

The model with an exponential decay is often a good approximation to the experimental situation in particular for short times [3].

[3] In some situations the decay is not neccesarily exponential. The exact time dependence of the spins depends on the specific decay mechanisms and the quantum state of the atoms (which often vary with time). When investigating anti-reflection coatings [7], the decay was for instance modelled as a sum of two exponentials. In the "entanglement generated by dissipation" experiment discussed in chapter 7, we measured the decay of the mean spin for long times. In that case, different decay mechanisms (mainly spontaneuos emission from different light fields) were included in a model used to fit the non-exponential time dependence of the mean spin $\langle J_x(t)\rangle$.

The decay time of the mean spin can be measured by the Faraday probe since $\theta_F(t) \propto \langle J_x(t) \rangle$. From such a measurement, the T_1-time can be determined by an exponential fit to $\langle J_x(t) \rangle$. The decay time of the transversal spin can be measured by applying an RF magnetic field in the y-z-plane after the optical pumping stage (see Fig. 3.3). When the RF field is resonant with the Larmor frequency, a perpendicular component $\langle J_\perp \rangle$ is created as described later in Sec. 5.3. The decay of the perpendicular component can be measured by the probe light. From the measurement of $\langle J_\perp(t) \rangle$, one can extract the T_2-time from an exponential fit. Note, that the measurement of the T_2-time is very similar to the measurement of the amplitude of the RF magnetic field. The latter measurement is presented in detail in chapter 5. A different (but very related) method to measure the T_2-time is the Magneto-Optical Resonance Signal (MORS) method [41] also described in the previous theses [32, 33]. With this method, frequency resolved spectra of the atomic resonances are measured. The spectra can be fitted and the widths of the resonances are related to the T_2-time.

In the experiments, the probe power and the number of atoms are often varied. It is therefore important to know how the T_2-time depends on these parameters. As will be clear later, it is convinient to consider the decay rate $\gamma = 1/T_2$ instead of the decay time. The probe power is measured as the sum of the light power hitting the two detectors which are part of the homodyne setup, see Fig. 3.2. In our experiment, the probe power is measured in Volts where 1 Volt corresponds to the power of 1.65 mW. For a fully pumped atomic ensemble, the Faraday angle can be used as a measure for the number of atoms as discussed in Sec. 3.3. To compare the two cases where either the probe power or the number of atoms are changed, it is convinient to plot γ as a function of the product of the Faraday angle and the probe power $\theta_F \cdot P$ (which has the unit deg$\cdot$ V).

Figure 3.4 shows the measured rate γ as a function of $\theta_F \cdot P$. For these measurements, the probe power was fixed to $P = 3.5$ V and the number of atoms was changed by heating the cells. Circles represent the decay rate for atoms in cell 1 and squares for atoms in cell 2. The solid lines are linear fits to the measured decay rates. For the measured Faraday angles (in the range 8-14 deg), γ is linear with the Faraday angle θ_F. This will often be the case when changing the number of atoms by heating the cells. Later, we show results demonstrating that the decay rate increases quadratically with the probe power. In Fig. 3.4, we see that the decay rate is larger for cell 1 than for cell 2. This can partially be explained by the fact that the probe light power is higher on cell 1 than on cell 2 due to optical losses in between the two cells.

The total decay rate γ includes both the coherent decay rate γ_{sw} and the incoherent decay rate γ_{bad}. Using measurements of κ^2, it is possible to separate the two contributions $\gamma = \gamma_{\mathrm{sw}} + \gamma_{\mathrm{bad}}$. This way, one gains better understanding of both the coherent and incoherent processes. These measurements are described later in Sec. 3.10.

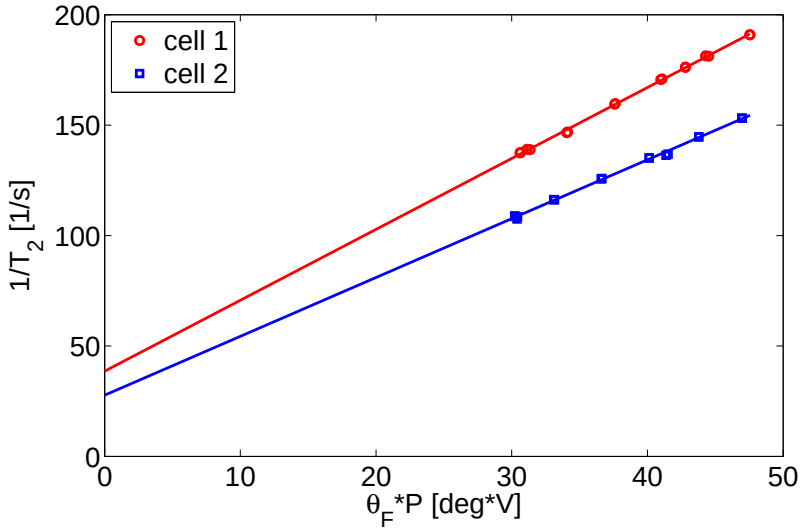

Figure 3.4: Vary the temperature, $P = 3.5$ V probe power. The figure shows the measured decay rate $\gamma = 1/T_2$ for the two atomic ensembles (cell 1 with red circles and cell 2 with blue squares) together with linear fits.

3.5 Detection efficiency

The probe light experiences optical losses due to reflections on the glass cells and due to optics after the cells. Each cell has four air-glass or glass-air interfaces which normally introduce around 4% of reflection losses. Since the cells have anti-reflection coated windows attached on the outside, the total reflection losses from both cells are reduced by a factor of two down to around 16% (or slightly more). There are also optical losses in the detection system from lenses, mirrors, waveplates, beamsplitters and the photodiodes. The total detection efficiency is denoted η_{det} and is typically estimated to be around 0.8. When estimating the detection efficiency, we include only half of the reflection losses through the cells. Measurements of losses are presented later in Sec. 6.3.4 when discussing the memory experiment.

Optical losses can be modelled as a beamsplitter which transmits only part of the light (see Fig. 3.5). In quantum mechanics one needs to take the vacuum into account which enters through the unused port of the beamsplitter. When modelling detection losses, we assume that all detection losses occur after the light has interacted with the atoms. The light states before/after the detection losses are denoted output/measured. Using the beamsplitter model, we find the relation between the measured and output light operators

$$y^{\text{meas}}(t) = \sqrt{\eta_{\text{det}}}\, y^{\text{out}}(t) + \sqrt{1-\eta_{\text{det}}}\, y^{\text{vac}}(t), \tag{3.4}$$

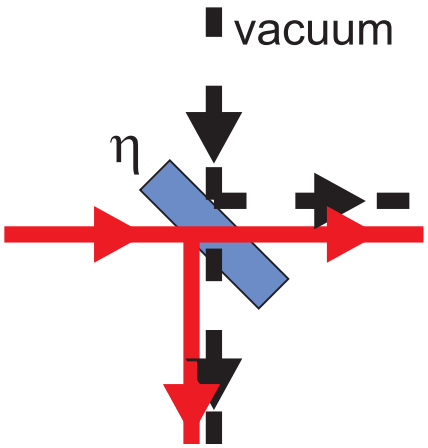

Figure 3.5: Optical losses can be modelled as a beamsplitter with transmission coefficient η. In the quantum mechanical treatment of the beamsplitter vacuum (dashed line) will enter through an unused port.

where $\eta_{\rm det}$ is the intensity detection loss parameter and $y^{\rm vac}(t)$ is a vacuum operator with zero mean and variance 1/2. We can define $q^{\rm meas}(t)$ similarly.

Detection losses have a different effect on mean values than on variances. We have

$$\begin{aligned} \langle y^{\rm meas} \rangle &= \sqrt{\eta_{\rm det}} \langle y^{\rm out} \rangle \\ {\rm Var}\left(y^{\rm meas}\right) &= \eta_{\rm det} {\rm Var}\left(y^{\rm out}\right) + (1-\eta_{\rm det}) \cdot \frac{1}{2}, \end{aligned} \tag{3.5}$$

as found from Eq. (3.4). The effect of the detection efficiency is always included in the data analysis in particular when measuring atomic noise (see Sec. 3.11). However, to keep things simple when discussing the equations and the results, the detection efficiency is often not mentioned in the text.

3.6 Kappa calibration

The light-atom coupling parameter κ^2 is by far the most important parameter in our experiment. In the QND interaction theory, the coupling parameter is denoted $\tilde{\kappa}^2$, in the swap and squeezing interaction theory, the coupling paremeter is denoted κ^2, and when also including bad decay in the swap and squeezing interaction theory, the coupling constant is denoted κ_m^2. When referring to the coupling parameter in general, I will just call it the κ^2 parameter. I.e. the term "the κ^2 parameter" can refer both to $\tilde{\kappa}^2$, κ^2 or κ_m^2. A large κ^2 parameter is important in almost all applications. Also, the κ^2 parameter is used when estimating the noise of the atomic state in projection noise units.

The κ^2 parameter can be measured in several ways. For a single atomic ensemble, one can estimate $\tilde{\kappa}^2$ by measuring the noise of a thermal unpolarized atomic ensemble. This method has the advantage that unpolarized states should be easy to produce. The method has the disadvantage that it can not be used

to verify the input-output equations for the QND interaction or the swap and squeezing interaction. When deriving those input-output equations, we assumed that the atoms are highly polarized and have a large macroscopic spin component J_x. Both of these assumptions are not valid for a thermal ensemble. The input-output equations for the thermal ensemble are therefore different than the input-output equations for a highly polarized ensemble. For instance, there is no backaction of light on atoms when measuring on thermal ensembles.

Using the thermal noise method, the projection noise was estimated in the first paper demonstrating spin-squeezing of an atomic ensemble using QND measurements [42]. The method has also been used more recently in our group's paper on single ensemble spin squeezing [5] and in papers on single ensemble QND measurements for magnetometry purposes [29, 43].

For the situation with two oppositely spin-polarized ensembles, one can find $\tilde{\kappa}^2$ by producing the highly oriented CSS and measure the noise of this state for different number of atoms. To be sure that one really has produced a highly oriented state, the orientation should be measured using for instance the Magneto-Optical Resonance Signal (MORS) method [41]. In our experiments, we typically obtain orientations in the range 98-99.9%. When probing the CSS, the measured output light noise variance should be linear with the number of atoms for a QND interaction since $\tilde{\kappa}^2 \propto N_A$. This linearity of the output light noise together with the high orientation is enough to find the $\tilde{\kappa}^2$. Note, that this linearity is actually only true if the interaction is of the QND type. For the case of the swap and squeezing interaction, the output light noise is only linear with N_A for short interaction times $2\gamma_{\mathrm{sw}}T \ll 1$. The above described method was used in our previous experiments [16, 17, 18] for estimating the projection noise.

In this thesis, the measurements of the κ^2 parameter is done by a "mean value transfer" method. The mean value transfer method is based on mean value measurements instead of noise measurements. This is an advantage, since measurements of mean values are less uncertain than measurements of noise. The method is also valid for long interaction times where the interaction is not of the QND type but instead of the swap and squeezing type.

Finally, it is possible to estimate the κ^2 parameter based on the number of photons, probe detuning and number of atoms using Eq. (2.86). This is a bit similar to estimating the projection noise level from the number of atoms as is done in the magnetometry experiment (see Sec. 5.6.1). This method of estimating the κ^2 parameter is however quite uncertain due to the relatively large uncertainties in the number of atoms and number of photons.

3.6.1 Mean value transfer method

The mean value transfer method is now described. The method can be used to verify the input-output equations for the swap and squeezing interaction. In particular, it can can be used to measure the coupling constant κ_m^2. The language of canonical operators is used to describe the procedures. The results obtained with the mean value method do not depend on the detection efficiency η_{det}, and the detection efficiency is therefore neglected. We now go through the different steps in the procedure.

Input displacements

In many of our experiments, the input light quadrature operators $y^{\text{in}}(t)$ and $q^{\text{in}}(t)$ are vacuum operators. However, it is possible to create non-zero mean values $\langle y^{\text{in}} \rangle$, $\langle q^{\text{in}} \rangle$ in these operators using electro-optical modulators (EOM's). A typical modulation of the light will be on the form $\langle y^{\text{in}}(t) \rangle = A \cos(\Omega_L t)$ where A here is some amplitude. Notice, that we here choose the modulation frequency which equals the Larmor frequency of the atoms. With such an input modulation, a small calculation using the mode functions defined in Sec. 2.4.8 gives $\langle y_{c,+}^{\text{in}} \rangle = \langle y_{c,-}^{\text{in}} \rangle$. Depending on the voltages to the EOM's, we can choose whether a mean value is created in y, in q or in both.

Two cell mean value input-output equations

We can write up how the mean values are changed during the light-atom interaction using the full swap and squeezing interaction theory which includes decoherence parametrized by ϵ^2. The input-output equations for the mean values are a bit simpler than the input-ouput equations (2.71) and (2.73) for the operators since noise operators such as $F_{xc,+}$ have zero mean. We find the mean of the output atomic operators

$$\begin{pmatrix} \langle X_c^{\text{out}} \rangle \\ \langle P_c^{\text{out}} \rangle \end{pmatrix} = \sqrt{1-\kappa^2\zeta^2} \begin{pmatrix} \langle X_c^{\text{in}} \rangle \\ \langle P_c^{\text{in}} \rangle \end{pmatrix} + \kappa\sqrt{1-\epsilon^2} \begin{pmatrix} \langle q_{c,+}^{\text{in}} \rangle \\ -\zeta^2 \langle y_{c,+}^{\text{in}} \rangle \end{pmatrix}, \tag{3.6}$$

and the mean of the output light operators

$$\begin{pmatrix} \langle y_{c,-}^{\text{out}} \rangle \\ \langle q_{c,-}^{\text{out}} \rangle \end{pmatrix} = \left\{ \epsilon^2 + (1-\epsilon^2)\sqrt{1-\kappa^2\zeta^2} \right\} \begin{pmatrix} \langle y_{c,-}^{\text{in}} \rangle \\ \langle q_{c,-}^{\text{in}} \rangle \end{pmatrix} + \kappa\sqrt{1-\epsilon^2} \begin{pmatrix} \langle P_c^{\text{in}} \rangle \\ -\zeta^2 \langle X_c^{\text{in}} \rangle \end{pmatrix}. \tag{3.7}$$

In the above equations we assumed that $\langle y_{c,+}^{\text{in}} \rangle = \langle y_{c,-}^{\text{in}} \rangle$ which is true when the input light mean values are created with EOM's as discussed above.

ζ^2 measurement

The parameter $\zeta^2 = -14a_2/a_1$ is an important parameter for the swap and squeezing interaction theory. ζ^2 depends on the atomic transition (cesium $D2$

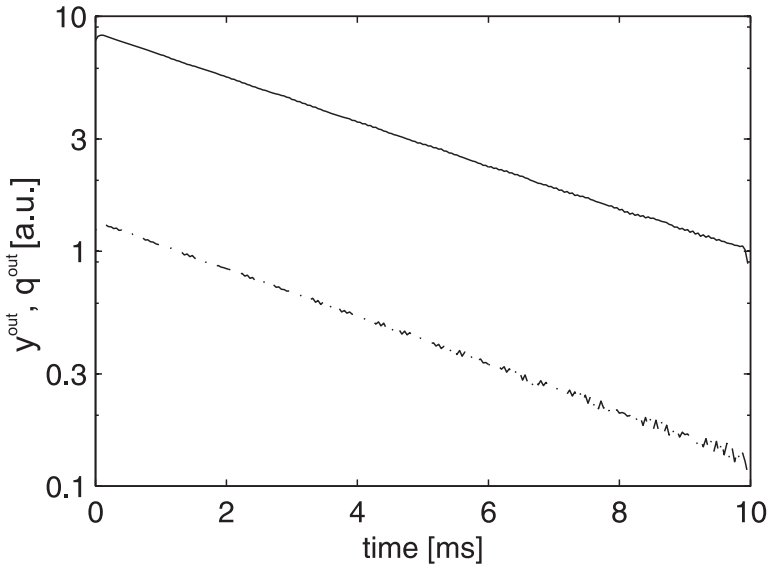

Figure 3.6: The figure shows $y_c^{\text{out}}(t)$ (solid line) and $q_c^{\text{out}}(t)$ (dashed line) as a function of time. Prior to the probing, an RF magnetic field created equal mean values $\langle P_c(t=0)\rangle = \langle X_c(t=0)\rangle$ in the atomic collective operators.

transition in our case) and on the probe detuning Δ. Using the expressions for the vector and tensor polarizabities given in Eq. (2.21), we calculate $\zeta^{-2}_{\text{theory}} = 6.4$ for our usual detuning $\Delta = -850$ MHz.

It is possible to measure ζ^2 using the mean value transfer method. Starting from a CSS, equal mean values $\langle P_c(t=0)\rangle = \langle X_c(t=0)\rangle$ in the collective atomic spin operators are created using the RF coils. Then, two separate measurements are performed where $\langle y_c^{\text{out}}(t)\rangle$ and $\langle q_c^{\text{out}}(t)\rangle$ are measured, respectively. These light operators describe the cosine component of the output light operators at time t and are defined in Eq. (2.62). The mean values of the cosine output light operators equal

$$\begin{pmatrix} \langle y_c^{\text{out}}(t)\rangle \\ \langle q_c^{\text{out}}(t)\rangle \end{pmatrix} = \widetilde{a}\exp\left(-\gamma t\right)\begin{pmatrix} \langle P_c(t=0)\rangle \\ -\zeta^2\langle X_c(t=0)\rangle \end{pmatrix}. \tag{3.8}$$

The above equation can be calculated using techniques similar to the ones used when deriving the swap and squeezing input-output equations. In the above it is assumed that the input light operators have zero mean. The measurements are shown in Fig. 3.6. From the measured ratio $\langle y_c^{\text{out}}(0)\rangle \,/\, \langle q_c^{\text{out}}(0)\rangle$, we find the value $\zeta^{-2}_{\text{meas}} = 6.3$. The measured value is very close to the theoretical value $\zeta^{-2}_{\text{theory}} = 6.4$. This measurement is therefore supporting that we indeed realize the swap and squeezing interaction in the experiment.

Reduction of the light noise

In the swap and squeezing interaction theory, the input light operators are reduced by a certain factor. If decoherence is not included in the model, the reduction equals $e^{-\gamma_{\rm sw}T} = \sqrt{1-\kappa^2\zeta^2}$. When including decoherence, the situation is a bit more complicated. However, if only mean mean values of the operators are considered, the reduction equals $\epsilon^2+(1-\epsilon^2)\sqrt{1-\kappa^2\zeta^2}$ as seen from Eq. (3.7). It is a highly non-trivial fact that the input mean values are reduced. For instance, in the QND interaction theory, the input operators are *not* reduced.

The procedure used for measuring the reduction of the input mean values is now briefly discussed. First, an input mean value $\langle y_{c,+}^{\rm in}\rangle$ is created in the y-quadrature. This input modulation can be measured when the atoms are "off". The atoms are denoted off when the atomic Larmor precession frequency is outside the detection bandwidth which is centered around 322 kHz [4]. Then, the atoms are turned "on" by matching the Larmor frequency with the detection frequency of 322 kHz, and the output light mean value can be measured. The signal when the atoms are on is

$$\langle y_{c,-}^{\rm out}\rangle = \left(\epsilon^2+\left(1-\epsilon^2\right)\sqrt{1-\kappa^2\zeta^2}\right)\langle y_{c,+}^{\rm in}\rangle \tag{3.9}$$

The reduction of the input mean value $\epsilon^2+(1-\epsilon^2)\sqrt{1-\kappa^2\zeta^2}$ can be calculated from the ratio of the two measurements results $\langle y_{c,-}^{\rm out}\rangle$ / $\langle y_{c,+}^{\rm out}\rangle$.

The fact that the input light operators are reduced is beneficial in almost all applications including magnetometry (chapter 5), quantum memory (chapter 6) and generation of entanglement by near QND measurements. This is because in these applications the output light is used to estimate an atomic quadrature. When the input light operator is reduced, the output light operator will be less noisy and one can estimate the atomic quadrature better.

κ^2 measurement

The coupling strength κ^2 can be measured with a mean value transfer method using two probe pulses (see pulse sequence in Fig. 3.3). The procedure is now described.

We first create an input displacement $\left\langle q_{c,+}^{\rm in,1st}\right\rangle$ in the 1st probe pulse. The size of the displacement can be measured when atoms are off. During the interaction between atoms and the 1st probe pulse, the input light mean value of the 1st probe pulse is transferred to the atomic $\langle X_c^{\rm out}\rangle$ operator with a certain gain. Using a 2nd probe pulse, the mean value of the atomic operator can be measured. This is done by first using a magnetic π-pulse positioned in between the two probe pulses) to rotate X_c into P_c and then measure the atomic quadrature with a 2nd

[4] The Larmor precession frequency can be tuned by changing the current through the coils which generate the static bias magnetic field B_x pointing in the x-direction.

probe pulse y-quadrature measurement. The following equations describe the procedure:

$$\begin{aligned}\left\langle y_{c,-}^{\text{out,2nd}}\right\rangle &= \kappa\sqrt{1-\epsilon^2}\left\langle P_c^{\text{out},\pi}\right\rangle \qquad \text{(atomic state after } \pi\text{-pulse)} \\ &= \kappa\sqrt{1-\epsilon^2}\left\langle X_c^{\text{out}}\right\rangle \qquad \text{(atomic state before } \pi\text{-pulse)} \\ &= \kappa^2\left(1-\epsilon^2\right)\left\langle q_{c,+}^{\text{in,1st}}\right\rangle \end{aligned} \tag{3.10}$$

From the ratio of the two measurement results $\left\langle y_{c,-}^{\text{out,2nd}}\right\rangle / \left\langle q_{c,+}^{\text{in,1st}}\right\rangle$, we can find the factor $\kappa_m^2 = \kappa^2\left(1-\epsilon^2\right)$. The actual measurements of κ_m^2 are presented later in Sec. 3.10.

3.7 Measured data

In the experiment, either $S_y^{\text{out}}(t)$ or $S_z^{\text{out}}(t)$ are measured using the homodyne detection setup. But let us assume in this section that $S_y^{\text{out}}(t)$ is measured. The homodyne detector signal is sent to a lock-in amplifier and demodulated at the detection frequency $\Omega_{\text{det}} = 322$ kHz. The lock-in amplifier has two outputs: a cosine and a sine component. The outputs of the lock-in amplifier are sent to a computer data aquisition card. The measured data are on the form

$$X(t) \propto \int_{t'=t}^{t+\delta t}\left[S_y^{\text{out}}(t')\cos(\Omega_{\text{det}}t') + iS_y^{\text{out}}(t')\sin(\Omega_{\text{det}}t')\right]dt', \tag{3.11}$$

where the multiplication with $\cos(\Omega_{\text{det}}t')$ and $\sin(\Omega_{\text{det}}t')$ are done by the lock-in amplifier. The integration over the small time δt is done by the lock-in bandwidth and the data card sampling rate. The data $X(t)$ is here written using complex notation where the real part corresponds to the cosine component of $S_y^{\text{out}}(t)$ and the imaginary part corresponds to the sine component. The data is denoted $X(t)$, but it should not be confused with the two cell atomic canonical operators X_c and X_s. We can also write up a simpler expression for the measured data $X(t) \propto y_c^{\text{out}}(t) + i \cdot y_s^{\text{out}}(t)$ by using the definitions of the time-depending canonical operators given in Eq. (2.62).

Time is treated as a continuous variable in Eq. (3.11). However, data points are acquired at a certain rate $1/\delta t$ using a computer data aquisition card. The sampling rate δt is typically 80 or 160 μs. One can say that time is discretized. The data is therefore represented by a column vector denoted $\vec{X}$ or the row vector denoted

$$\vec{X}^{\dagger} = \begin{pmatrix} X^*(t_1) & X^*(t_2) & \ldots & X^*(t_N)\end{pmatrix}. \tag{3.12}$$

The star $*$ denotes complex conjugation. The $\dagger$ symbol means complex conjugate and transpose. To keep notation simple, I will not write the arrow over the data

vector. Instead I use the notation $X \equiv \vec{X}$. If we utilize a probe pulse of T =1 ms duration, a sampling rate $\delta t = 80$ μs and the total number of samples $N = 13$ in each cycle, the total sampling time will be $\delta t \cdot N = 1.04$ ms. In this case, the data X is a vector of length $N = 13$.

From the measured $X(t)$ we can calculate the integrated canonical operators. We have for instance

$$y_{c,-}^{\text{out}} \propto \int_{t'=0}^{T} Real\left[X(t')\right] e^{-\gamma t'} dt'$$
$$y_{s,-}^{\text{out}} \propto \int_{t'=0}^{T} Imag\left[X(t')\right] e^{-\gamma t'} dt'. \tag{3.13}$$

In the above equation the normalization constant is not specified. In the experiment, this constant is found by measuring the shot noise of light, see Sec. 3.9. For now we just assume that it is possible to normalize the canonical operators correctly such that vacuum has the variance of 1/2.

In the experiment, the measurements are repeated many times (typically 1000's of times) and the mean value $\langle X(t)\rangle$ is recorded. From the measured $\langle X(t)\rangle$, one can calculate the mean value of any output temporal light mode such as for instance $\left\langle y_{c,-}^{\text{out}}\right\rangle$. We also record the integrated variances of *one* particular mode such as for instance Var $\left(y_{c,+}^{\text{out}}\right)$. This means that we choose a certain mode (exponentially falling or rising with time constant $1/\gamma = T_2$) and for this mode, we record the variance. The covariance matrix is also recorded. From this matrix, it is possible to calculate the variance of *any* output mode.

3.7.1 Covariance matrix and variances

In this section the covariance matrix is defined and it is explained how the variance of any output light mode can be calculated from the covariance matrix. The complex covariance function is defined as

$$\begin{aligned} C(t,t') &\equiv \left\langle \left\{X(t) - \overline{X}(t)\right\} \left\{X^*(t') - \overline{X}^*(t')\right\}]\right\rangle \\ &= \langle X(t)X^*(t')\rangle - \langle X(t)\rangle \langle X^*(t')\rangle . \end{aligned} \tag{3.14}$$

$\overline{X}(t) = \langle X(t)\rangle$ is the average value of $X(t)$ (it is an average of independent and identical measurements and not over time). Time is treated as a continuous variable in Eq. (3.14). For discretized time, we instead define the covariance matrix as $C \equiv \left\langle XX^\dagger\right\rangle - \langle X\rangle \left\langle X^\dagger\right\rangle$ which satisfy $C^\dagger = C$. Since $X^\dagger$ is a row vector of length N and X is a column vector of length N, the outer product C of X and $X^\dagger$ is an $N \times N$ matrix.

When analyzing data, we are typically interested in integrating the signal with some temporal modefunction here denoted $u(t)$. For discrete data u is a column

vector. We have the integrated signal $X_u = \int_0^T u^*(t)X(t)dt$ which in the discrete version is a inner product $X_u = u^\dagger X$. The normalization of the modefunction should be $\int_0^T |u(t)|^2 dt = 1$ or $u^\dagger u = 1$. Using matrix notation we can easily find the variance of any mode u as

$$\mathrm{Var}\left(X_u\right) = \left\langle u^\dagger X X^\dagger u \right\rangle = u^\dagger C u. \tag{3.15}$$

In the experiment, the covariance matrix is recorded and Eq. (3.15) is used when analyzing the data. Typically, we use the covariance matrix to find the variances of the exponentially rising and falling modes $\mathrm{Var}\left(y_{c,+}^{\mathrm{out}}\right)$ and $\mathrm{Var}\left(y_{c,-}^{\mathrm{out}}\right)$ where the time constant of the exponential mode function is set to T_2. However, the variance $\mathrm{Var}\left(y_u^{\mathrm{out}}\right)$ of *any* temporal mode $u(t)$ can be calculated from the measured covariance matrix.

3.8 Conditional variances and entanglement

We now discuss how entanglement between two atomic ensembles can be generated by a QND measurement. The procedures and experimental results are discussed extensively in the thesis [33]. Using this method, entanglement was first generated in our setup in 2001 [16]. Since this first demonstration, we have realized that the interaction between atoms and light is better described with the swap and squeezing model. However, for small or intermediate coupling strengths, the swap and squeezing interaction and the QND interaction are quite similar, and both interactions can be used to generate entanglement via a measurement. For small or intermediate coupling strengths, I will therefore say that the swap and squeezing interaction is of a "near QND" type. In the quantum memory experiment (chapter 6) and in the magnetometry experiment (chapter 5) the near QND interaction is used to generate entanglement. In chapter 7, the near QND method for generating entanglement is refined and is used to generate steady state entanglement.

First assume that light and atoms interact via the QND interaction described in Sec. 2.3.1. One can utilize a 1st probe pulse to make QND measurements of the collective atomic operators $P_c \propto (J'_{z1} + J'_{z2})$ and $P_s \propto \left(J'_{y1} + J'_{y2}\right)$. This is done by measuring the integrated ouput light operators $y_c^{\mathrm{out,1st}}$ and $y_s^{\mathrm{out,1st}}$ defined in Sec. 2.4.8. After the interaction, these atomic operators are squeezed. This is equivalent to having entanglement between the ensembles. In order to verify the squeezing, one can utilize a 2nd probe pulse to measure P_c and P_s again. The 2nd pulse measurements results are denoted $y_c^{\mathrm{out,2nd}}$ and $y_s^{\mathrm{out,2nd}}$. If the results obtained from the 1st and 2nd probe pulses are close to each other (or identical for the case of perfect QND measurements), the atomic operators are squeezed.

For a coherent spin state, the operators P_c and P_s are random variables with zero mean and variance 1/2. This means that the outcome of the 1st measure-

ment result is also random. As discussed in [33], this implies that the generated squeezed state will be displaced away from zero by a random amount. If we repeat the sequence with a 1st and 2nd probe pulse several times, the displacement will take random values in each shot. This means that the squeezing will not be apparent in the measured variances $\mathrm{Var}\left(y_c^{\mathrm{out,1st}}\right)$ and $\mathrm{Var}\left(y_c^{\mathrm{out,2nd}}\right)$ of the 1st and 2nd probe pulse measurements (sine operators are also measured). To verify the entanglement, we instead have to consider the conditional variance here defined as the variance of the operator

$$y_c^{\mathrm{cond}} = y_c^{\mathrm{out,2nd}} - \alpha y_c^{\mathrm{out,1st}}. \tag{3.16}$$

The optimal α-parameter is the one which minizes the conditional variance $\mathrm{Var}\left(y_c^{\mathrm{cond}}\right)$. In the experiment, the optimal α_{opt} is be calculated from the measured data. This optimal α_{opt} will have a value between 0 and 1 depending on how good the QND measurement is. If the QND measurements are perfect, such that the 1st and 2nd pulse measurement results are identical, we have $\alpha_{\mathrm{opt}} = 1$. From the measured conditional light variance, we can find the "conditional EPR variance". For the QND interaction we have (see Sec. 2.3.2)

$$\mathrm{Var}\left(y_c^{\mathrm{cond}}\right) + \mathrm{Var}\left(y_s^{\mathrm{cond}}\right) = 1 + \tilde{\kappa}^2 \cdot \Sigma_{\mathrm{EPR}}^{\mathrm{cond}}, \tag{3.17}$$

where we assumed that input light operators are vacuum. The two ensembles are conditionally entangled if $\Sigma_{\mathrm{EPR}}^{\mathrm{cond}} < 1$. The term conditional is used since the entanglement depends on the 1st probe pulse measurement.

We can also find the conditional entanglement for the case of the near QND measurement. In this case, the conditional light operator is defined as

$$y_c^{\mathrm{cond}} = y_{c,-}^{\mathrm{out,2nd}} - \alpha y_{c,+}^{\mathrm{out,1st}}. \tag{3.18}$$

The only differences between this equation and the previous definition (3.16) are the subscripts which indicate that the temporal mode functions are rising for the 1st pulse and falling for the 2nd pulse. The conditional EPR variance can be calculated from the output light noise variances using the following equation

$$\mathrm{Var}\left(y_c^{\mathrm{cond}}\right) + \mathrm{Var}\left(y_s^{\mathrm{cond}}\right) = t_m^2 + \kappa_m^2 \cdot \Sigma_{\mathrm{EPR}}^{\mathrm{cond}}, \tag{3.19}$$

where we used the full swap and squeezing interaction theory which has bad decay included, see Eq. (2.82).

We can also consider "unconditional" entanglement. The term unconditional refers to entanglement which does not depend on the 1st probe measurement results. Such entanglement can be achieved by doing a feedback in between the two pulses (see pulse sequence in Fig. 3.3) to the atomic operators P_c and P_s proportional to the 1st probe measurement results $y_c^{\mathrm{out,1st}}$ and $y_s^{\mathrm{out,1st}}$. The feedback is in

the experiment done by RF coils located around the ensembles. With the optimal feedback gain, the atomic operators will be squeezed with a zero displacement in each shot. This implies that the entanglement between the two ensembles Σ_{EPR} can be measured directly using the 2nd probe measurement results $\mathrm{Var}\left(y_c^{\mathrm{out,2nd}}\right)$ and $\mathrm{Var}\left(y_s^{\mathrm{out,2nd}}\right)$ using the formula given by Eq. (2.10) (which is valid for the QND interaction) or the formula given by Eq. (2.85) (which is valid for the swap and squeezing interaction).

Conditional and unconditional entanglement are basically the same things for the case of QND or near QND measurements. When creating unconditional entanglement, the feedback is done by the RF coils. On the other hand, when generating conditional entanglement, a kind of feedback is done in the data-analysis stage using the α-parameter when comparing 1st and 2nd pulse results. For the same experimental settings (number of atoms, number of photons, laser detunings, and so on), the amount of conditional entanglement which can be generated is equal to the amount of unconditional entanglement which can be generated. Depending on the application of the entanglement it may be preferable to use either conditional or unconditional entanglement. For instance, in the memory experiment we utilize unconditional entanglement while in the magnetometry we utilize conditional entanglement.

3.8.1 Covariance matrix and conditional variances

The conditional variance can be calculated from the measured covariance matrix. Typically, the covariance matrix contains information about two probe pulses: the 1st and the 2nd probe pulse. Let u_1 be the modefunction for the 1st probe pulse and u_2 the modefunction for the 2nd probe pulse. u_1 and u_2 are orthogonal since the two pulses are not overlapping in time. This means that the inner product $u_1^\dagger u_2 = 0$. Let the data vector X contain both the 1st and 2nd pulse data. We can calculate the variance $\mathrm{Var}\left(X_{u_1}\right) = u_1^\dagger C u_1$ of the 1st pulse and the variance $\mathrm{Var}\left(X_{u_2}\right) = u_2^\dagger C u_2$ of the 2nd pulse for the specific mode functions u_1 and u_2.

We choose the mode function u_2 to be an exponential falling mode with time constant T_2. This is because we want to use Eq. (2.85) to calculate the atomic noise in projection noise units from the measured 2nd pulse variances. On the other hand, the mode function 1 can be optimized to achieve the best conditional variance. Typically we choose the mode 1 to be exponentially rising with time constant $1/\gamma_m \approx \frac{1}{2} \cdot T_2$.

The data representing the measurements of the conditional operators y_c^{cond} and y_s^{cond} is denoted Q. We have $Q \propto y_c^{\mathrm{cond}} + i \cdot y_s^{\mathrm{cond}}$. Q can be calculated from the measured data X using the formula $Q = u_2^\dagger X - \alpha u_1^\dagger X$. We can calculate the

variance of Q as

$$\mathrm{Var}\,(Q) = |Q|^2 = u_2^\dagger C u_2 + \alpha^2 u_1^\dagger C u_1 - \alpha\left(u_1^\dagger C u_2 + u_2^\dagger C u_1\right), \tag{3.20}$$

where we assumed that α is a real number [5]. By solving the equation $d\,|Q|^2\,/d\alpha = 0$, we find the minimum

$$\mathrm{Var}\,(Q)_{|\min} = u_2^\dagger C u_2 - \frac{\left(u_1^\dagger C u_2 + u_2^\dagger C u_1\right)^2}{4u_1^\dagger C u_1}, \tag{3.21}$$

using the value

$$\alpha_{\mathrm{opt}} = \frac{u_1^\dagger C u_2 + u_2^\dagger C u_1}{2u_1^\dagger C u_1}. \tag{3.22}$$

We see that $\mathrm{Var}\,(Q)$ can be reduced below the 2nd pulse variance $\mathrm{Var}\,(X_{u_2})$ if there are correlations between the 1st and the 2nd pulse manifested in non-zero values of $u_1^\dagger C u_2$ and $u_2^\dagger C u_1$. The conditional variance can then be found using the equation

$$\mathrm{Var}\left(y_c^{\mathrm{cond}}\right) + \mathrm{Var}\left(y_s^{\mathrm{cond}}\right) \propto \mathrm{Var}\,(Q)_{|\min}\,. \tag{3.23}$$

The proportionality constant is found by calculating the shot noise for the u_2 mode. Once we have found the conditional light variance, we can calculate the conditional atomic noise $\Sigma_{\mathrm{EPR}}^{\mathrm{cond}}$ using Eq. (3.19).

3.9 Light noise

An important calibration measurement is the measurement of the shot noise of light. This calibration enables us to find the proportionality constant between the raw data and the canonical operators $X(t) \propto y_c^{\mathrm{out}}(t) + i \cdot y_s^{\mathrm{out}}(t)$.

In polarization homodyning, the large and classical y-polarized mode of the probe light is used as a local oscillator when measuring the quantum fluctuations in the x-polarized mode. The homodyne detection is well balanced when classical intensity noise of the local oscillator is cancelled when subtracting the two detector signals. When the x-polarized mode is vacuum, the well balanced homodyne signal is proportional to the amplitude of the local oscillator. In this case we say that the detection is shot noise limited.

In terms of variances, shot noise limited detection means that the variance of the data Y_u (integrated with some modefunction) is proportional to the light power. We here chose to denote the data representing the shot noise measurements as $Y(t)$ while leaving the data $X(t)$ to represent some general measurement. We have

$$\mathrm{Var}\,(Y_u) = snslope \cdot P. \tag{3.24}$$

[5] We also assume that the cosine and sine components are uncorrelated.

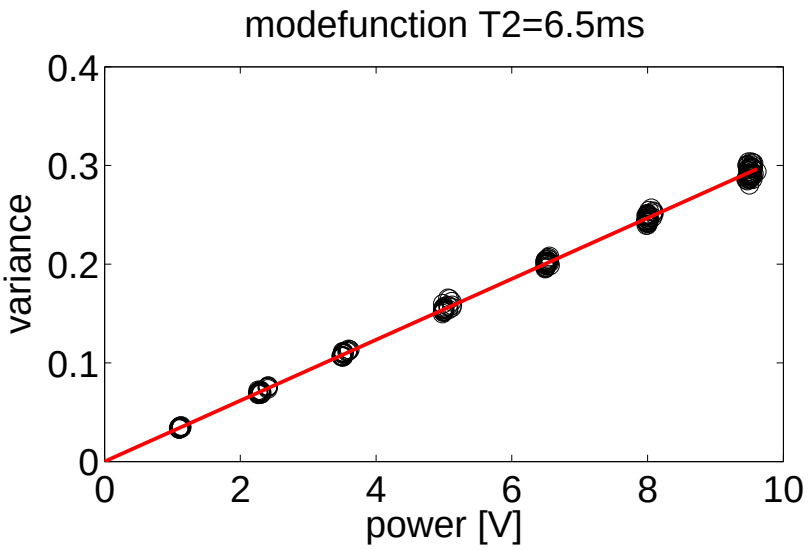

Figure 3.7: Light noise measurements. Measured variance as a function of probe power together with a linear fit.

The proportionality constant is denoted *snslope* which is an abbreviation for "shot noise slope". The linearity is checked experimentally for probe powers P=0-10 V. In order to observe the linearity, it is important that the homodyne detectors are balanced. If the detectors are not well balanced, one will observe that $\mathrm{Var}\,(Y_u)$ also has a quadratic component proportional to P^2. Fig. 3.7 shows measurements of the light noise variance for the specific mode function which is exponentially falling with time constant of $T_2 = 6.5$ ms. Also shown is a linear fit. The variance scales linearly with the probe power which implies that the detection system is shot noise limited.

Once we have determined *snslope*, we can find the proportionality constant between the raw data and the canonical operator. For the general data X_u we have

$$\mathrm{Var}\,(y_u) = \frac{\mathrm{Var}\,(X_u)}{snslope \cdot P} \cdot \frac{1}{2}. \tag{3.25}$$

If we insert $X_u = Y_y$ in Eq. (3.25), we find the relation $\mathrm{Var}\,(y_u) = 1/2$ as it should be since vacuum has the variance of $1/2$.

If the shot noise is delta-correlated such that $\langle y(t)y(t')\rangle = \mathrm{Var}\,(y)\,\delta(t-t')$ then the variance $\mathrm{Var}\,(y_u)$ is independent of the modefunction $u(t)$. Delta-correlation in time corresponds to a flat frequency spectum. However, in the experiment the spectrum of the shot noise is *not* flat due to a peaked detection system (measured spectra are presented later in Fig. 4.5). This implies that *snslope* depends on the modefunction. For exponentially falling modes with temporal mode constant T_2,

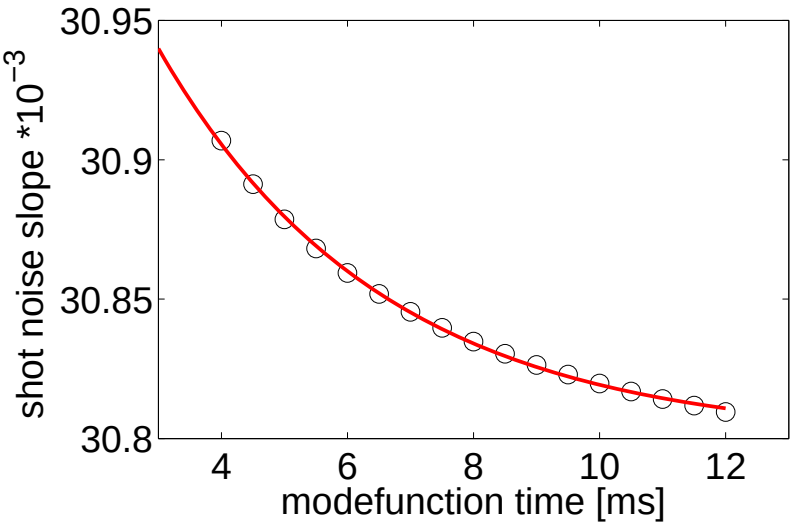

Figure 3.8: The shot noise slope as a function of the mode function time T_2 for exponentially falling mode. The data are fitted to a function of the form given by Eq. (3.26).

snslope has the following empirical dependence on the mode constant

$$snslope(T_2) = a + b \cdot \exp\left(-c \cdot T_2 + d\right), \tag{3.26}$$

where a, b, c, d are fit parameters. Data of *snslope* as a function of T_2 is presented in Fig. 3.8 together with a fit of the form given by Eq. (3.26). For each mode function time, *snslope* is found from a linear fit similar to what is shown in Fig. 3.7. We see that *snslope* vary with only a fraction of a percent within the range of $T_2 = 4$-12 ms.

3.10 Measurements of κ^2

Using the mean value transfer method described in Sec. 3.6.1, the coupling strength $\kappa_m^2 = \kappa^2\left(1-\epsilon^2\right)$ can be measured for a given set of experimental settings including the number of atoms N_A, probe power P, probe duration T and detuning Δ. For the same experimental settings, the transverse relaxation time T_2 is also measured. Measurements of the T_2-time was presented earlier in Sec. 3.4. I.e., for a set of experimental settings, we have the two measurements κ_m^2 and T_2.

There are different ways of expressing the measured data. From the two measurements, ϵ^2 can be calculated using the swap and squeezing interaction theory. The two parameters κ_m^2 and ϵ^2 carry the same information as the two

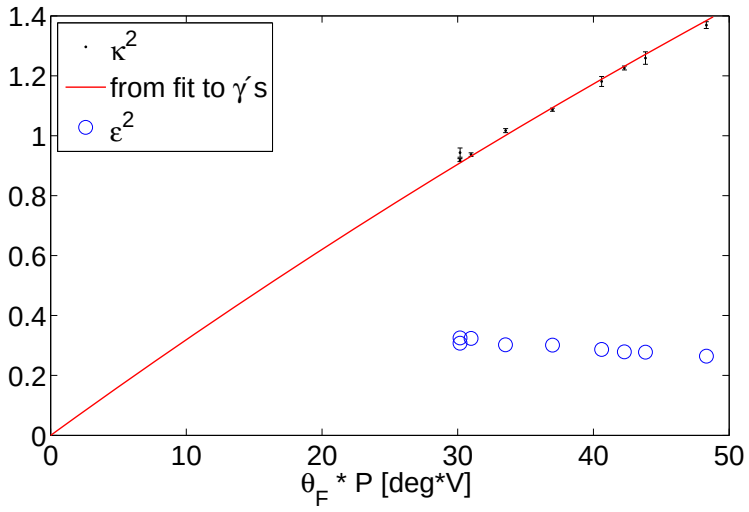

Figure 3.9: Vary the temperature, $P = 3.5$ V probe power. The figure shows the measured κ_m^2 with black dots, the calculated ϵ^2 with blue circles and a function as a red line calculated from the fits to the $\gamma, \gamma_{\rm sw}, \gamma_{\rm bad}$ presented in Fig. 3.10. The uncertainties on the κ_m^2 data points are due to statistical uncertainties.

measured parameters κ_m^2 and T_2. One can also calculate the two parameters $\gamma_{\rm sw}$ and $\gamma_{\rm bad}$ and the sum of them $\gamma = \gamma_{\rm sw} + \gamma_{\rm bad} = 1/T_2$. Again, the three parameters $\gamma_{\rm sw}, \gamma_{\rm bad}, \gamma$ carry the same information as the two measured parameters κ_m^2 and T_2.

Vary the number of atoms

We start by presenting measurements of κ_m^2 and ϵ^2 for probe pulses of duration $T = 1$ ms and power $P = 3.5$ V. For these measurements, the number of atoms was changed by increasing the temperature of the glass cells. The results are plotted in Fig. 3.9 as a function of the parameter $\theta_F \cdot P$ which has the units deg·V. Black dots represent measurements of κ_m^2 and blue circles represent measurements of ϵ^2. We see that κ_m^2 increases with the number of atoms. On the other hand, ϵ^2 decreases with number of atoms. Since $\epsilon^2 = \gamma_{\rm bad}/\gamma$ equals the ratio of the bad decay rate to the total decay rate it is a good thing to have a small ϵ^2. It would be best to have $\epsilon^2 = 0$, but in the measurements presented here ϵ^2 is around 0.3.

In Fig. 3.10 we instead plot$\gamma, \gamma_{\rm sw}, \gamma_{\rm bad}$ with red circles, blue squares and green diamonds, respectively. We also plotted linear fits to the three rates. The linear dependence of the $\gamma's$ (when varying the temperature) is an empirical fact. The fact that the swap rate $\gamma_{\rm sw}$ is proportional to the number of atoms is very nice and is expected from the swap and squeezing theory as seen in Eq. (2.57). The bad decay rate $\gamma_{\rm bad}$ is also proportional to the number of atoms. This is expected if the

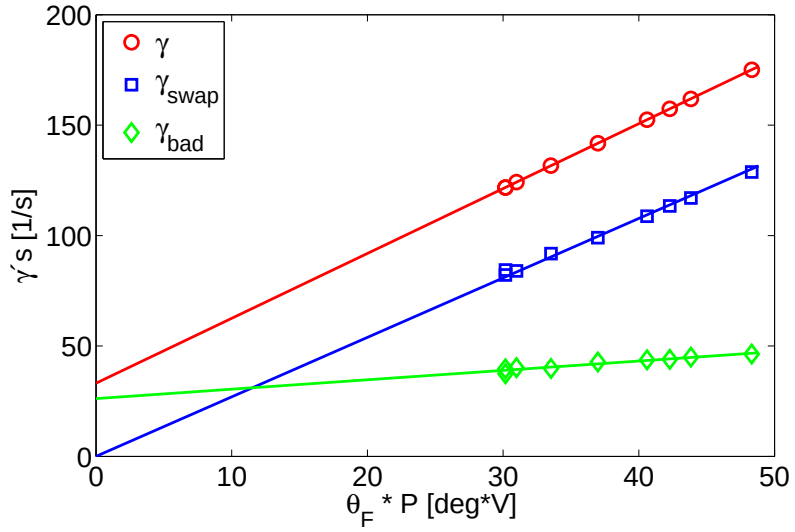

Figure 3.10: Vary the temperature, $P = 3.5$ V probe power. The figure shows the rates $\gamma, \gamma_{\rm sw}, \gamma_{\rm bad}$ together with linear fits.

decay is due to two-body collisions [6]. Based on the linear fits, we can obtain an expression for κ_m^2 as a funtion of the fit parameters since $\kappa_m^2 = \frac{\gamma_{\rm sw}}{\gamma} Z^2 \left(1 - e^{-2\gamma T}\right)$. This is plotted in Fig. 3.9 as a red line. The measured data points for κ_m^2 lies close to this line demonstrating that the two ways of representing the data (by either the set κ_m^2 and ϵ^2 or the set $\gamma, \gamma_{\rm sw}, \gamma_{\rm bad}$) are consistent.

In Fig. 3.10 we present data for temperatures corresponding to values of $\theta_F \cdot P$ in the range 30-50 deg·V. In this range, γ, $\gamma_{\rm sw}$ and $\gamma_{\rm bad}$ are all linear. This is very encouraging. If this linearity is also true for higher values of $\theta_F \cdot P$, the ϵ^2-parameter will decrease towards 0 for large number of atoms. In this case, the bad decay is negligable and we have a true swap and squeezing interaction as given by Eq. (2.18). A non-zero ϵ^2-parameter will limit applications of the swap and squeezing interaction. A very important limitation is for instance that the maximum value for κ_m^2 is $Z^2 (1 - \epsilon^2)$. I.e., it is not possible to reach high values of κ_m^2 if ϵ^2 is large. In conclusion, it would be nice if we could increase the number of atoms even more such that $\epsilon^2 \to 0$.

Vary the probe power

We also measured κ_m^2 and T_2 for the case when the probe power was varied. For the experimental settings of $\theta_F \approx 8.5$ deg and probe powers in the range $P =$ 1-

[6] The probability that two atoms collide is proportional to the density of atoms.

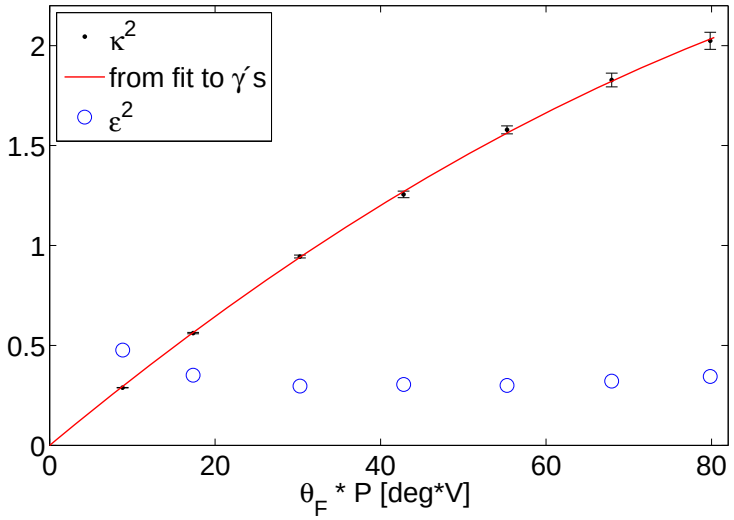

Figure 3.11: Vary the probe power P. Room-temperature data. The figure shows the measured κ_m^2 with black dots, the calculated ϵ^2 with blue circles and a function as a red line calculated from the fits to the $\gamma, \gamma_{\rm sw}, \gamma_{\rm bad}$ presented in Fig. 3.12. The uncertainties on the κ_m^2 data points are due to statistical uncertainties.

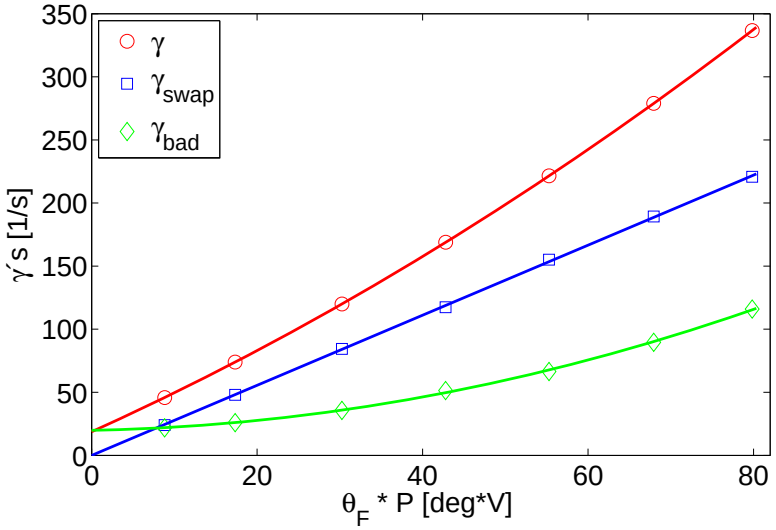

Figure 3.12: Vary the probe power P. Room-temperature data. The figure shows the rates $\gamma, \gamma_{\rm sw}, \gamma_{\rm bad}$ together with linear or quadratic fits.

9.5 V [7], we obtain the results plotted in Figs. 3.11 and 3.12. The data are plotted as a function of the product $\theta_F \cdot P$, but it should be kept in mind that only the probe power was varied. Figure 3.12 shows that $\gamma_{\rm sw}$ is proportional to the probe power. This is expected from the theory as seen in Eq. (2.57). On the other hand, the total decay rate γ and the bad decay rate $\gamma_{\rm bad}$ are both quadratic (with also a constant and linear term) with the probe power. A quadratic dependence is not as good as a linear dependence since it means extra bad decay for large values of $\theta_F \cdot P$. Notice, that a decay due to single atom spontaneous emission is supposed to scale linearly with the number of photons and is therefore not the reason for the quadratic dependence. The quadratic dependence is not fully understood. We expect that the quadratic decay could originate from a small misalignment of the probe beam, imperfect polarization or an inhomogenous intensity profile of the light.

In the limit of zero probe power, $\gamma_{\rm sw}$ goes to zero and $\gamma_{\rm bad}$ goes to some non-zero value as seen in Fig. 3.12. The decay rate at zero probe power is called the decay rate "in the dark" $\gamma_{\rm dark}$. The decay time in the dark is denoted $T_2^{\rm dark} = 1/\gamma_{\rm dark}$. In Fig. 3.11, we see that ϵ^2 has a minimum. For low probe powers, the dark decay dominates over the swap rate and ϵ^2 is large. Increasing the probe power then lowers ϵ^2 until the quadratic component of $\gamma_{\rm bad}$ takes over and ϵ^2 increases. Compared to the case where the temperature is varied, ϵ^2 is higher when the probe power is varied.

We have now seen that it is better to increase the temperature than to increase the probe power, if we want a low ϵ^2. However, increasing the probe power does have some advantages. In the experiment, increasing the probe power is an easy way to increase κ_m^2 since the probe power can be changed simply by turning a waveplate. On the other hand, increasing the temperature takes a bit more effort. With our current setup, the temperature is changed by blowing hot air on the cells. The heating (and in particular the cooling) takes time (time-scale is around 10's of minutes to hours). Also, there is the risk of over-heating the cells, which might result in a damaged cell. The most convinient setting is therefore room-temperature. However, usually results get better with higher temperatures, as also visible in ϵ^2 measurements.

3.11 Atomic noise

In almost all applications it is important that the atoms can be initialized in a coherent spin state. This is done by optical pumping. If the atoms are perfectly pumped into the $F = 4, m = \pm 4$ states, the variance of the atomic operators should equal $\mathrm{Var}\,(X_c) = \mathrm{Var}\,(X_s) = \mathrm{Var}\,(P_c) = \mathrm{Var}\,(P_s) = 1/2$. In many ex-

[7] The DC output of the homodyne detectors is limited by 10 V, so typically we use less than 10 V probe power.

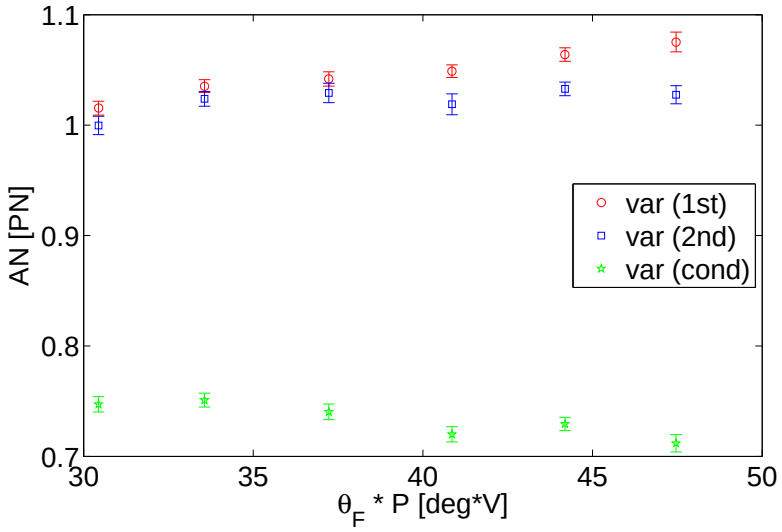

Figure 3.13: Vary the temperature, $P = 3.5$ V probe power. The figure shows the initial atomic noise Σ_{EPR} measured by the 1st probe pulse with red circles, the atomic noise $\Sigma_{\mathrm{EPR}}^{\mathrm{2nd}}$ measured by a 2nd probe pulse with blue squares and the conditional atomic noise $\Sigma_{\mathrm{EPR}}^{\mathrm{cond}}$ as green stars. Errorbars are calculated from the statistical uncertainties of the measured raw variances $\mathrm{Var}\,(X_u)$, where u is a suitable exponentially decaying modefunction.

perimental situations it is not possible to realize the CSS perfectly. Then the variances of the atomic canonical operators are (slightly) greater than $1/2$.

The initial atomic state can be measured using a probe pulse. From the measured covariance matrix, the variance of the $y_{c,-}^{\mathrm{out}}$ operator can be calculated (see Sec. 3.7). From this output variance, we can calculate the atomic noise $\mathrm{Var}\,(P_c)$ by using Eq. (2.82) which is repeated here

$$\mathrm{Var}\left(y_{c,-}^{\mathrm{out}}\right) = t_m^2 \cdot \frac{1}{2} + \kappa_m^2 \mathrm{Var}\left(P_c^{\mathrm{in}}\right). \tag{3.27}$$

If κ_m^2 and ϵ^2 have been measured beforehand (as discussed in Sec. 3.10), t_m^2 can be calculated using Eq. (2.83). Using the values for κ_m^2 and t_m^2, $\mathrm{Var}\,(P_c)$ can be determined using Eq. (3.27) [8]. $\mathrm{Var}\,(P_s)$ can similarly be determined from the measured $\mathrm{Var}\left(y_{s,-}^{\mathrm{out}}\right)$. The two variances are in most cases equal and we therefore consider the EPR variance $\Sigma_{\mathrm{EPR}} = \mathrm{Var}\,(P_c) + \mathrm{Var}\,(P_s)$ instead. This EPR variance is also called the atomic noise in projection noise (PN) units. Whenever $\Sigma_{\mathrm{EPR}} < 1$, the two atomic ensembles are entangled. When $\Sigma_{\mathrm{EPR}} = 1$ we say that the atomic noise is PN-limited.

[8] One should also include the detection efficiency in the analysis of the noise, see Sec. 3.5. However, for simplicity the detection efficiency is not included in Eq. (3.27). When stating numbers for the atomic noise, the detection efficiency has been taken into account.

In order to fully characterize the atomic state we should also measure the sum $\mathrm{Var}(X_c) + \mathrm{Var}(X_s)$. Often this is not done since for atoms in the CSS there is no reason why this sum should not equal $\mathrm{Var}(P_c) + \mathrm{Var}(P_s)$. On the other hand, when producing spin-squeezed atomic states by (near) QND measurements, the operators X_c and X_s are anti-squeezed, leading to higher noise in the sum $\mathrm{Var}(X_c) + \mathrm{Var}(X_s)$. In order to measure these variances one needs to utilize a magnetic π-pulse prior to the probe pulse. This π-pulse rotates the atomic operators X_c and X_s into P_c and P_s such that they can be measured later with $y^{\mathrm{out}}_{c,-}$ and $y^{\mathrm{out}}_{s,-}$ measurements. Such measurements are presented in the Sec. 6.3.3. But for now we will focus on the measurements of the atomic P-operators.

Figure 3.13 shows the atomic noise Σ_{EPR} plotted with red circles as a function of $\theta_F \cdot P$ for the case where the temperature and thereby the number of atoms is varied. At room-temperature (corresponding to the first point which has $\theta_F \approx 8.5$ deg), the noise is $\Sigma_{\mathrm{EPR}} = 1.02(6)$ [9]. The atomic noise is indeed very close to being PN-limited. For higher number of atoms, the atomic noise increase up to $\Sigma_{\mathrm{EPR}} = 1.08(6)$ (for the last point which has $\theta_F \approx 13.5$ deg). Sometimes we have also measured the atomic noise in PN units for even higher Faraday angles than presented in Fig. 3.13. The typical situation is that the atomic noise variance grows linearly with θ_F for small Faraday angles. For higher Faraday angles the noise grows even faster. We are therefore not able to produce the CSS for high Faraday angles [10]. Since most of our experiments require that atoms can be initialized in the CSS, this is a severe limitation.

In Fig. 3.13 we also plot the atomic noise measured with a 2nd probe pulse $\Sigma^{\mathrm{2nd}}_{\mathrm{EPR}}$ and the conditional variance $\Sigma^{\mathrm{cond}}_{\mathrm{EPR}}$. The 2nd pulse atomic noise is slightly lower than the 1st pulse atomic noise. This is expected from the swap and squeezing interaction theory. The reduction of the atomic noise by the 1st probe pulse is the subject of chapter 7. The conditional noise for the number of atoms shown in Fig. 3.13 is in the range $\Sigma^{\mathrm{cond}}_{\mathrm{EPR}}$=0.70-0.75(4). Since $\Sigma^{\mathrm{cond}}_{\mathrm{EPR}} < 1$, the two atomic ensembles are entangled. The degree of entanglement is similar to what was obtained in the magnetometry experiment (see Sec. 5.7.1) and slightly better than what was obtained in the memory experiment (see Sec. 6.3.3).

[9] The uncertainties on Σ_{EPR} and $\Sigma^{\mathrm{cond}}_{\mathrm{EPR}}$ are estimated to be 6%. Uncertainties on the detection efficiency, the shot noise, the measured output variances, the coupling constant κ^2_m and the reduction of the light noise t^2_m are included.

[10] The initial atomic state is created by optical pumping. If the pumping is not perfect, this leads to higher atomic noise. The problem is most severe for large atom numbers.

3.12 Conclusions

In this chapter we presented calibration measurements supporting the swap and squeezing theory. The parameter ζ^2 was measured experimentally. We also verified that the swap rate γ_{sw} is proportional to the product $\theta_F \cdot P$ when varying either the number of atoms or the probe power. This proportionality is predicted by the swap and squeezing theory. Measurements of the important coupling constant κ_m^2 was presented, and it was explained how to calculate the atomic noise from the measured output light noise. The initial atomic state was characterized, and it was shown that it is possible to reach nearly PN-limited atomic noise. We also presented results demonstrating entanglement between the two atomic ensembles. The ensembles were in this case entangled by a near QND measurement.

We have shown that the interaction gets closer to the pure swap and squeezing interaction (with $\epsilon^2 = 0$) when the number of atoms is increased. Unfortunately, the initial atomic noise Σ_{EPR} also increases with the number of atoms. A future goal would be to realize PN-limited atomic noise with high number of atoms. In order to do so, this requires perfect optical pumping which can be hard to achieve for large number of atoms. The combination of a pure swap and squeezing interaction and PN-limited atomic noise will improve all the main results discussed in this thesis.

Chapter 4

Generation of two-mode squeezed and entangled light in a single temporal and spatial mode

4.1 Introduction

In this chapter we will discuss the experimental demonstration of the "generation of two-mode squeezed and entangled light in a single temporal and spatial mode" [4]. The squeezed light is generated using two cesium vapor cells kept at room-temperature. In the experiment, we obtain 3.6 dB of non-degenerate quadrature squeezing in a single temporal mode. The two entangled sidebands are separated by twice the Larmor frequency of the atoms which can be widely tuned. The squeezed state is generated in the same spatial mode as the local oscillator.

The paper [4] includes the theory describing the generation of the entangled light. The theory was discussed in detail in chapter 2 where it was denoted the swap and squeezing interaction theory. Also, the paper includes some mean value measurements where the important parameter $Z^2 = \zeta^{-2}$ was determined. These measurements were presented earlier in Sec. 3.6.1. Since both the theory and the measurement of Z^2 have been presented, we focus in this chapter on the noise measurements demonstrating the squeezed light generation and on the characterization of the spectrum and the temporal modes of the squeezed light.

Quadrature entangled or squeezed light has application in many areas of physics including quantum cryptography [44], teleportation [45], computation [46] and quantum non-demolition (QND) measurements [42].

In many situations where light is used to measure some parameter, the shot noise of the probing light makes the measurement uncertain. In this case, utilizing quadrature squeezed light can improve the signal to noise ratio leading to a better estimate of the parameter of interest. One important application of squeezed light

is for gravitational wave detection [47]. Regarding the experiments performed in our group, squeezed light may help in many of them including generation of entanglement between the two ensembles [16] and quantum teleportation [18]. In atomic magnetometry, squeezed light can improve the magnetometer sensitivity beyond the shot noise limit as demonstrated recently in [48].

The typical way to produce entangled or squeezed light is to use a sub threshold optical parametric amplifier (OPA) first demonstrated in [49]. The method is still of importance and the attainable degree of squeezing is getter higher and higher [50]. Atomic vapour has been used for generating entangled light using the method of four wave mixing with an atomic beam [51] and later also with cold atoms [52, 53]. Using polarization self-rotation squeezed light has been produced [54, 24]. The above mentioned methods generate multimode squeezed light in the sense that the output light contains many pairs of freqencies which are independently entangled. This can be a disadvantage in for instance quantum cryptography. If the many modes carry the same information this might compromise the security since many copies of the same state is sent to the reciever. An eavesdropper might detect one of the many multiple modes unnoticed if not all of them are measured by the reciever.

The entangled light generated in our experiment is in a single spatial mode and in a near single temporal mode. As discussed, this might be an advantage in cryptography protocols. Also, the entangled light is generated by atoms, and the light is therefore naturally compatible with the same kind of atoms in terms of wavelength and bandwidth. This is of importance if the entangled light should be interfaced with atoms in an application.

4.2 Theory

The two-mode squeezed light is generated using two spin-polarized atomic ensembles. The setup is shown in Fig. 4.1 and the pulse sequence is shown in Fig. 4.2. The atomic ensembles are located in a bias magnetic field B_x pointing in the x-direction leading to the precession of the atomic spins with the Larmor frequency Ω_L.

During the initial optical pumping stage, the atoms in the first (second) ensemble are prepared in the ground state $F = 4, m = 4$ ($F = 4, m = -4$), where we chose the x-direction as the quantization axis. The level schemes of the atoms in the two atomic ensembles are depicted in Fig. 4.3. In the theory describing the light-atom interaction, only two ground state levels ($m = \pm 4$ and $m = \pm 3$) for each atomic ensemble are included in the model. In the level-scheme picture, the bias field splits the relevant ground state levels $m = \pm 4$ and $m = \pm 3$ by the Larmor frequency.

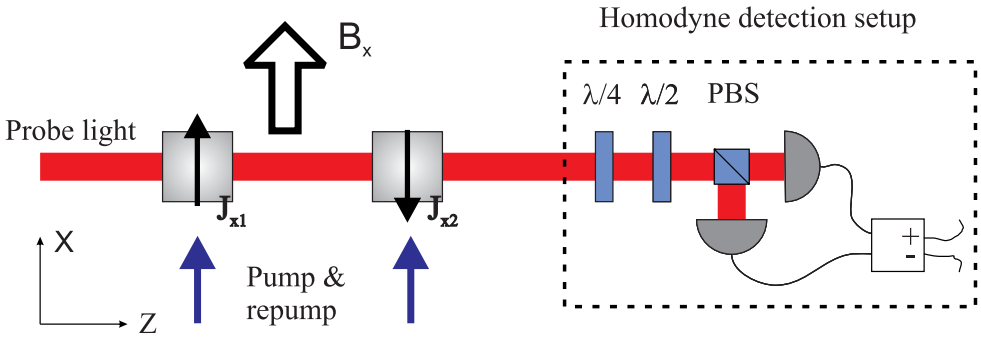

Figure 4.1: The two atomic ensembles are located in a bias magnetic field B_x and oppositely polarized using pump and repump light. The probe light is propagating in the z-direction, interacting with the two atomic ensembles, and the output light is measured with the homodyne detection setup.

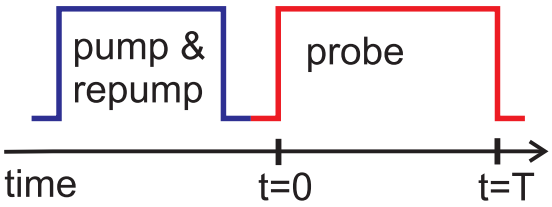

Figure 4.2: Pulse sequence. First, optical pumping with pump and repump light intializes the two atomic ensembles in oppositely oriented states. Then, the probe light with duration T interacts with the two atomic ensembles.

After the optical pumping stage, a pulse of probe light interacts with the two ensembles. The input light is linearly polarized in the y-direction. The y-polarized mode serves as a strong and classical local oscillator depicted in the level scheme in Fig. 4.3 as a sum of right hand and left hand circular polarized light. The probe light is detuned from the atomic $D2$ transition by the amount $\Delta = -850$ MHz.

The x-polarized mode is initially in the vacuum state, but during the light-atom interaction, atoms in the two ensembles emit x-polarized photons propagating in the forward direction [1]. Since the ground state energy levels are split by the Larmor frequency, the x-polarized photons are emitted in the upper and lower sidebands with frequencies $\omega_\pm = \omega_0 \pm \Omega_L$, where ω_0 is the optical frequency of the local oscillator light. In the level scheme depicted in Fig. 4.3, the x-polarized upper and lower sideband modes are denoted a_+ and a_-. The emission of x-polarized photons is accompanied by the creation or annihilation of atomic collective excitations in either the first or second ensemble. The level scheme picture of the interaction is also discussed in Sec. 7.2.3. As will be shown

[1] Spontaneous emission of photons propagating in the forward direction is enhanced by the optical depth as compared to spontaneous emission of photons which are propagating in other directions.

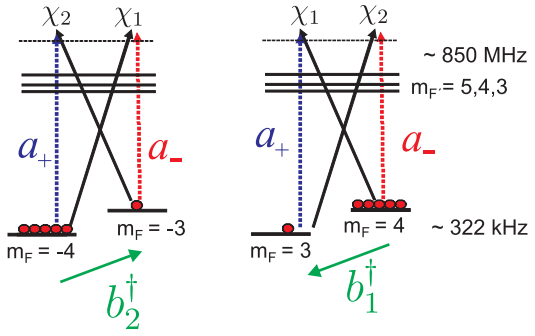

Figure 4.3: Level structure and light fields for the two atomic ensembles. $\hat{a}_+$ and $\hat{a}_-$ are annihilation operators for the upper and lower sidebands. $\hat{b}_1^\dagger$ and $\hat{b}_2^\dagger$ are creation operators for the collective atomic excitation for the first and second ensemble. χ_1 and χ_2 are coupling strengths.

in the next section and also demonstrated in the experiment, the photons emitted in the upper and lower sidebands are correlated (entangled). Also note that the entangled photons are emitted in the same spatial (flat-top) mode as the local oscillator.

4.2.1 Input-output equations

The swap and squeezing interaction theory presented in chapter 2 was first introduced in our paper [4] where it was used to explain how entangled light was generated from the atomic ensembles. In the absence of atomic decoherence, the swap and squeezing interaction theory leads to the input-output equations given by Eq. (2.18) which for the light variables read

$$\begin{aligned} y_{c,-}^{\text{out}} &= \sqrt{1-\frac{\kappa^2}{Z^2}}\, y_{c,+}^{\text{in}} + \kappa P_c^{\text{in}}, & y_{s,-}^{\text{out}} &= \sqrt{1-\frac{\kappa^2}{Z^2}}\, y_{s,+}^{\text{in}} + \kappa P_s^{\text{in}}, \\ q_{c,-}^{\text{out}} &= \sqrt{1-\frac{\kappa^2}{Z^2}}\, q_{c,+}^{\text{in}} - \frac{\kappa}{Z^2} X_c^{\text{in}}, & q_{s,-}^{\text{out}} &= \sqrt{1-\frac{\kappa^2}{Z^2}}\, q_{s,+}^{\text{in}} - \frac{\kappa}{Z^2} X_s^{\text{in}}. \end{aligned} \tag{4.1}$$

If the initial atomic state is vacuum [2] then for long interaction times $2\gamma_{\text{sw}}T \gg 1$ where $\kappa^2 \to Z^2$ we obtain

$$\begin{aligned} \text{Var}\left(y_{c,-}^{\text{out}}\right) &= Z^2/2, & \text{Var}\left(y_{s,-}^{\text{out}}\right) &= Z^2/2, \\ \text{Var}\left(q_{c,-}^{\text{out}}\right) &= 1/\left(2Z^2\right), & \text{Var}\left(q_{s,-}^{\text{out}}\right) &= 1/\left(2Z^2\right). \end{aligned} \tag{4.2}$$

We see that the output cosine and sine light modes are squeezed by the amount Z^2 in the variance in the q-direction. For our experimental detuning $\Delta \approx -850$ MHz

[2] The variances of the canonical operators equal $\text{Var}(X_c) = \text{Var}(X_s) = \text{Var}(P_c) = \text{Var}(P_s) = 1/2$ for the vacuum state.

we should expect the squeezing of a factor $Z^2 \approx 6.4$ in the variance. Two-mode squeezing of the cosine and sine mode is equivalent to entanglement between the upper and lower sidebands (see Sec. 2.3.2) which were discussed in the previous section.

The input-output equations (4.1) describe coherent evolution and predict squeezing by a factor Z^2 in the variances in a single temporal mode (an exponentially falling mode with time constant $1/\gamma_{\rm sw}$). However, in the model leading to Eq. (4.1), atomic decoherence due to for instance collisions and spontaneous emission was neglected.

When including atomic decoherence, several things change. First, the squeezing is instead emitted in a temporal mode with time constant T_2 (which is faster than $1/\gamma_{\rm sw}$). Second, the expected degree of squeezing decreases [3]. Third, not only a single temporal mode will be squeezed. This can be understood by the following argument. While the squeezed light leaves the cells, the atomic state decays back to the initial CSS due to bad decoherence processes. The squeezing process then starts anew in an incoherent fasion leading to several squeezed temporal modes.

4.3 Experimental results

In the experiment, a 10 ms long probe pulse is sent through the two atomic ensembles (see Figs. 4.1 and 4.2) and the output light is measured with a homodyne setup consisting of waveplates and two detectors. In polarization homodyning the quadratures of the x-polarized light can be measured with the help of the strong y-polarized local oscillator. Depending on whether we choose a half wave plate or a quarter waveplate, we can measure either the y or the q-quadrature of the output light. Since the squeezing is in the q-quadrature, we utilize the quarter waveplate for the noise measurements.

4.3.1 Covariance matrices

When measuring the output light, the signals from the two detectors are subtracted and sent to a lock-in amplifier. The lock-in detection frequency is set to 322 kHz which also equals the atomic Larmor precession frequency Ω_L. The output of the lock-in amplifier is sent to the computer and the data $X(t) \propto q_c^{\rm out}(t) + i \cdot q_s^{\rm out}(t)$ (here written using complex notation) is sampled as described in Sec. 3.7. The time-dependent quadrature operators $q_c^{\rm out}(t)$ and $q_s^{\rm out}(t)$ are

[3] For a non-zero ϵ parameter (which describe the decoherence processes) the degree of squeezing can be calculated from Eq. (2.72) by using the orthogonal mode decompostion method explained in Sec. 2.4.12.

defined in Eq. (2.62). In the experiment both the mean value $\langle X(t)\rangle$ and the covariance matrix $C_X(t,t')$ (which is defined in Eq. (3.14)) are recorded. In the noise measurements presented in this chapter, the measured mean values are close to zero.

In the experiment, we perform two separate noise measurements. In one of the measurements the shot noise of light is recorded. The data representing the "shot noise measurement" is denoted $Y(t) \propto q_c^{\text{in}}(t) + i \cdot q_s^{\text{in}}(t)$. In these measurements the atoms are not present. This is achived experimentally by changing the Larmor frequency Ω_L such that it is outside the detection bandwidth which is a few kHz wide and centered around 322 kHz. This covariance matrix for the shot noise measurement is denoted $C_Y(t,t')$. In the other measurement, the output light noise is measured when the atoms are present (with Larmor frequency $\Omega_L = 322$ kHz) such that squeezed light is generated. The data representing the "light noise measurement" is denoted $X(t)$. The covariance matrix for the light noise measurement is denoted C_X.

As described in Sec. 3.7, data points are acquired at a certain rate $1/\delta t$, where $\delta t = 160$ μs for the experiments presented in this chapter. For a total measurement time $T = 10.24$ ms (corresponding to a 10.24 ms probe pulse), this gives $N = 64$ data points. This way the measured covariance function is actually a $N \times N$ matrix. Similarly the data $X(t)$ is a vector of length N.

In Fig. 4.4 we plot the difference between the light noise and the shot noise covariance matrices $|C_X| - |C_Y|$. We see that along the diagonal the light noise covariance matrix has smaller values than the shot noise covariance matrix. This is a clear evidence of squeezed light. The noise reduction is largest at $t = 0$ and then gets smaller with increasing times (along the diagonal). This is related to the fact that the squeezing is in a falling exponential temporal mode. The temporal modes will be discussed later in more detail.

4.3.2 Calculation of the spectrum

From the covariance matrix, several things can be calculated such as the spectrum of the noise and the degree of squeezing for any temporal mode. We will first describe how to calculate the spectrum from the covariance matrix. The spectrum is here defined as the norm squared of the Fourier transform of the signal. Neglegting constants (such as 2π), the Fourier transform of $X(t)$ is given by

$$X(\omega) \propto \int_0^T X(t) e^{-i\omega t} dt, \tag{4.3}$$

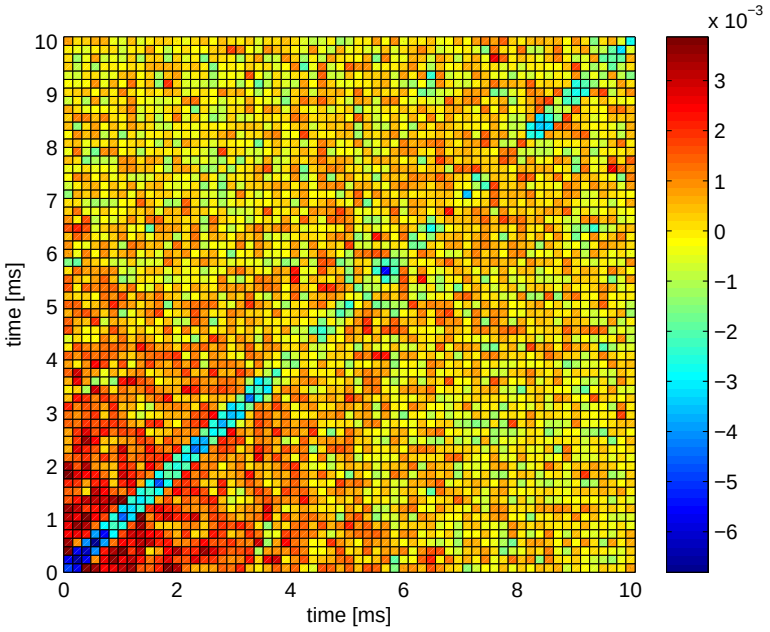

Figure 4.4: The difference between the light noise covariance matrix $|C_X|$ and the shot noise covariance matrix $|C_Y|$.

where T is the total duration of the pulse of light. The spectrum is then

$$S(\omega) \propto X(\omega)X^*(\omega) \propto \int\int X(t)X^*(t')e^{-i\omega(t-t')}dtdt'. \tag{4.4}$$

By averaging over measurements and using the definition of the covariance function $C_X(t,t') = \langle X(t)X^*(t')\rangle$ (assuming zero mean values), we find

$$\langle S(\omega)\rangle \propto \int\int C_X(t,t')e^{-i\omega(t-t')}dtdt'. \tag{4.5}$$

This can also be written in matrix notation (when discretizing the time) as

$$\langle S(\omega)\rangle \propto E^\dagger C_X E, \tag{4.6}$$

where E is the column vector $E = (e^{-i\omega t_1}, e^{-i\omega t_2}, ..., e^{-i\omega t_N})^{tr}$, $t_1, t_2, ..., t_N$ are the discretized time points and tr denotes transpose.

4.3.3 Measured spectra

We now present the measured spectra for the shot noise and the light noise measurements. The light noise measurement was repeated 40.000 times and the shot noise measurement was repeated 30.000 times. From the measured covariance

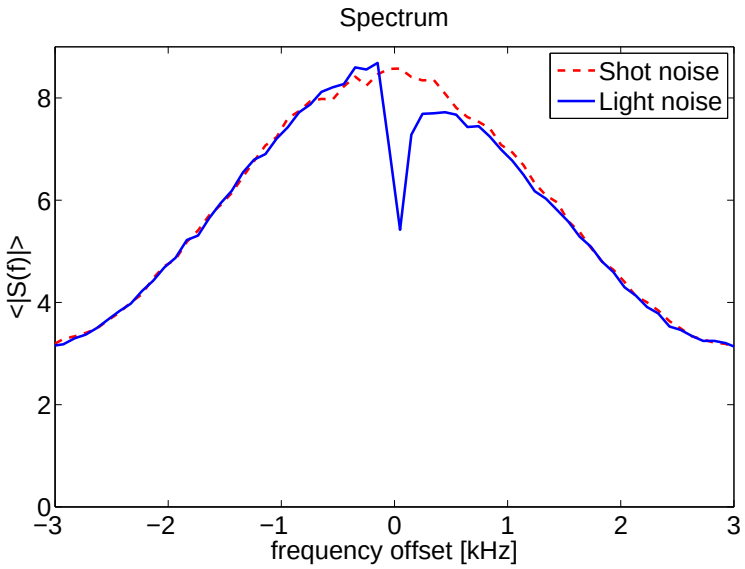

Figure 4.5: Power spectrum of the output light noise. Dashed line represent the shot noise of light. Solid line represent the noise when atoms are present. The dip in the spectrum at zero frequency offset shows that the light exiting the cells is squeezed.

matrices, we calculate the noise spectra using Eq. (4.6). The results are plotted in Fig. 4.5 which shows the noise power as a function of frequency offset in kHz. A frequency offset of zero corresponds to the 322 kHz lock-in detection frequency. The dashed line shows the shot noise spectrum of the probe light when the atoms are not present. The spectral shape of the spectrum of the shot noise is a feature of the detection system, in particular of the lock-in amplifier detection bandwidth. The light noise spectrum is shown in Fig. 4.5 with a solid line. When the atoms are present, a dip in the spectum occurs. The dip is a feature of the squeezing of the output light. As seen in Fig. 4.5, the width of the dip is a few hundreds of Hz. As expected from the theory, the width is comparable to the inverse of the decay time of the atomic coherences measured independently to be $\gamma = 1/T_2 = 1/\left(5.7 \text{ ms}\right) = 175$ Hz.

As a remark, note that the light noise spectrum is asymmetric. Using the definition of the covariance function given by Eq. (3.14) and the formula for the spectrum given by Eq. (4.5), we conclude that the spectrum is asymmetric only if the covariance function has an imaginary part. The covariance function is imaginary only if there are correlations between the cosine and sine components of the output light operator since

$$C_X(t,t') = \langle X(t)X^*(t')\rangle \propto \left\langle \left(q_c^{\text{out}}(t) + i\cdot q_s^{\text{out}}(t)\right)\left(q_c^{\text{out}}(t) - i\cdot q_s^{\text{out}}(t)\right)\right\rangle . \quad (4.7)$$

We believe that the observed (but small) correlations between the cosine and sine

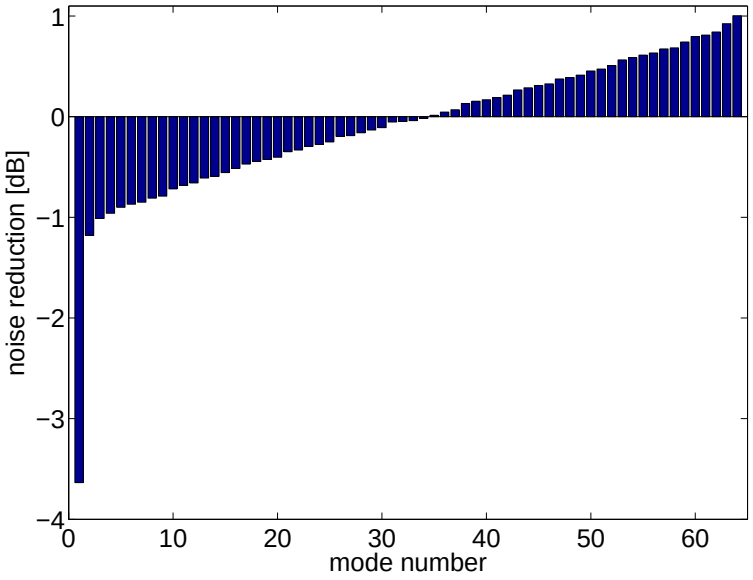

Figure 4.6: For each of the uncorrelated modes v_n, the variance Var (X_n) normalized to shot noise is plotted (see appendix A for how the variances are calculated). The first mode is squeezed by 3.6 dB.

components might be due a small difference between the Larmor frequency Ω_L and the detection frequency of 322 kHz.

4.3.4 Temporal mode analysis

We now turn to the temporal mode analysis of the data. According to the Karhunen-Loéve theorem [55, 56], we can find a set of *mutually uncorrelated modes* by performing a spectral decomposition of the C_X matrix. The interesting modes are the eigenfunctions and the variances of these modes are the eigenvalues. Details of how to perform the spectral decomposition can be found in appendix A.

From the measured covariance matrices C_X (the light noise) and C_Y (the shot noise) [4] we find a set of mutually uncorrelated modes. The variances of these modes normalized to the shot noise (see Eq. (A.12)) are sorted in ascending order and plotted in Fig. 4.6. The total number of eigenvalues (and modes) is equal to the size of the covariance matrix which is 64 for this specific measurement. In Fig. 4.6, we see that the first mode is squeezed by 3.6 dB. Besides this first mode, there is a whole background of modes which are either slightly squeezed or slightly anti-squeezed by up to 1 dB. The structure of the squeezed modes is

[4] Since the spectrum of the shot noise is not flat (as seen in Fig. 4.5), both C_X and C_Y are needed to find the interesting uncorrelated modes. For more details see appendix A.

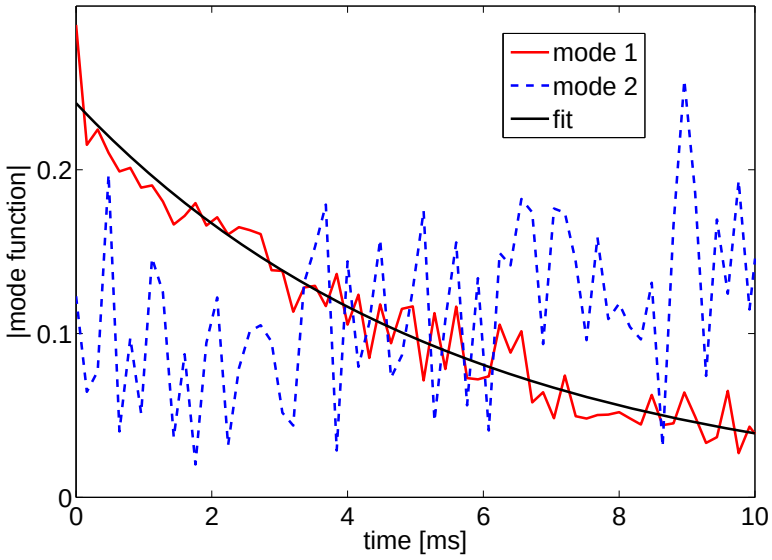

Figure 4.7: Absolute value of the first and second temporal mode functions. The first mode is fitted to an exponential falling function.

in qualitative agreement with the theory including decoherence which predicts a single dominant squeezed mode and several less squeezed modes.

We now estimate the statistical uncertainties on the eigenvalues plotted in Fig. 4.6. The eigenvalues are calculated from the measured covariance matrices, which in the experiment are calculated by averaging the results obtained with 40.000 measurement cycles. To see how the eigenvalues depends on the numbers of averages, we calculated the degree of squeezing/anti-squeezing (eigenvalues) for the first and last mode using 10.000, 20.000, 30.000 and 40.000 averages. For the four different number of averages, we obtained the degree of squeezing of -3.9 dB, -3.67 dB, -3.65 dB and -3.64 dB for the first mode and the degree of anti-squeezing by +1.56 dB, +1.22 dB, +1.04 dB and +1.00 dB for the last mode. We see that both the squeezing and anti-squeezing gets lower when averaging more data. However, the numbers are not that different, so we expect that more averages (> 40.000) would not change the degree of squeezing as plotted in Fig. 4.6 dramatically.

The absolute value of the first modefunction $|\phi_1(t)|$ is plotted in Fig. 4.7 together with a fit to an exponentially decaying function. The decay time for the exponential fit is 5.5 ms which is very close to the measured $T_2 = 5.7$ ms. The shape of the first temporal mode function is in agreement with the theory which predicts squeezing in an exponentially falling temporal mode with time constant T_2.

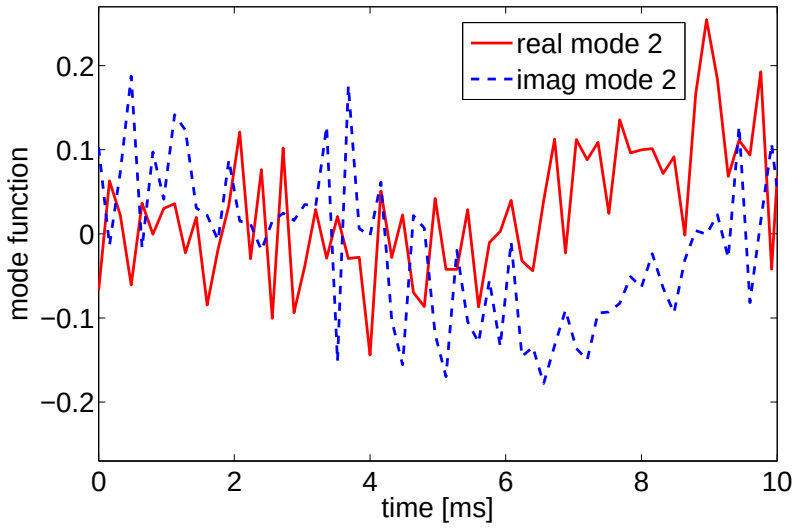

Figure 4.8: Real and imaginary part of the second temporal mode function.

The second mode function is also plotted in Fig. 4.7 which shows the absolute value of the modefunction and in Fig. 4.8 which shows the real and imaginary part of the modefunction. This second temporal mode function is very noisy. The absolute value of the modefunction is slightly rising in time.

As a comment, it should be noted that the temporal mode of the squeezed light can in principle be shaped by varying the intensity of the probe light. This way, it should be possible to for instance achieve a flat top (or an exponentially rising) squeezed temporal light mode. Such temporal modes would be interesting if one would like to couple the squeezed light to a different atomic ensemble.

4.4 Conclusions

We have demonstrated a squeezed light source based on the swap and squeezing interaction of light with two spin-polarized atomic ensembles. The experimentally obtained degree of squeezing was 3.6 dB. From the theory where atomic decoherence and light losses are neglected, we expected $10\log_{10}(Z^2)$ dB of squeezing. For our experimental probe detuning where $Z^2 \approx 6.4$, this corresponds to 8 dB of squeezing. The fact that the measured squeezing is lower than the expected is contributed to atomic decoherence and light losses (detection efficiency). Detuning the probe light further away from the atomic resonance will increase the expected degree of squeezing. However, this comes at the cost of a lower swap rate γ_{sw} and less coherent interaction compared to decoherence processes such as atomic collisions. In this experiment, the atoms were kept at room-temperature.

Increasing the number of atoms might have positive effects on the squeezed light generation since the coherent part of the interaction in this way can be increased compared to decoherence processes such as spontaneous emission.

The squeezed light is generated in a near single mode with a bandwidth of a few hundreds of Hertz. This kind of narrowband squeezing can be of relevance for some quantum cryptography protocols. The light is naturally compatible with atomic ensembles or atomic memories based on the same atom (cesium) since the wavelength of the squeezed light match the wavelength of the atomic transition (cesium $D2$ transition in our case). Furthermore, the squeezing is centered at the Larmor frequency of the atoms and has the bandwidth comparable to the inverse atomic decay time $1/T_2$. The squeezed light can for instance be used in combination with an atomic ensemble for improved QND measurements.

Chapter 5

Atomic magnetometry

5.1 Introduction

In this chapter I describe the "Quantum Noise Limited and Entanglement-Assisted Magnetometry" experiment. The results have been published in Physical Review Letters [2]. In the experiment, two ensembles of cesium atoms are used as a sensor for radio-frequency (RF) magnetic fields. Our sensor has a high sensitivity to the magnetic field, and the sensitivity is mainly limited by the projection noise (PN) of atoms. Furhermore, we demonstrate that entanglement between the two atomic ensembles can improve the atomic magnetometer.

In atomic magnetometry [57], one uses the Faraday interaction of a spin polarized atomic ensemble with light to measure the strength of a magnetic field. The sensitivity of an atomic magnetometer is limited by quantum mechanical principles. The measured signal will be noisy due to shot noise (SN) of the probing light, intrinsic atomic spin projection noise and backaction noise arising from the measurement.

Entanglement can reduce the atomic noise below the projection noise and thereby lead to better sensitivity as discussed in theoretically in [58, 59, 60, 61, 62, 63, 64, 65]. Entanglement of a few ions has been used for spectroscopy [66, 67]. There have also been measurements with atomic ensembles demonstrating sub projection noise sensitivity. These include interferometry with 10^3 atoms [68] and Ramsey spectroscopy with up to 10^5 atoms [15, 69].

Backaction evading measurements can be done using QND techniques. In a QND measurement, an atomic spin component J_z can be measured without being disturbed. Instead, the backaction noise piles up in the conjugate spin component J_y. In the field of atomic magnetometry, QND measurements are of great interest. In our group, QND measurements are implemented using a two cell setup [16]. It is also possible to achieve a backaction evading measurement using stroboscopic probe light as demonstrated recently in [70].

The Faraday rotation signal is noisy due to the shot noise of the probe light. The shot noise can be reduced by utilizing squeezed light. In [48] the noise on the Faraday rotation signal was reduced by utilizing squeezed probe light.

In this chapter, we demonstrate backaction evading measurements of the magnetic field. We also show that the magnetometer sensitivity is limited mainly by the projection noise of atoms. The combination of a large number of atoms $N_A \approx 1.5 \cdot 10^{12}$ and near projection noise limited sensitivity enables us to achive high sensitivity to the magnetic field in the sub-femtoTesla/$\sqrt{\text{Hz}}$ range.

Furthermore, we demonstrate that using entanglement between the two ensembles created by a near QND measurement, the atomic noise can be reduced below the projection noise limit. This way, entanglement is used to improve the uncertainty on the measurement and improve our magnetometer signal to noise ratio (SNR).

5.2 Interaction in terms of spin and Stokes vector

When discussing atomic magnetometry, the interaction between atoms and light is typically described in terms of the total spin vector $\vec{J} = (J_x, J_y, J_z)$ of an ensemble of atoms and the Stokes vector $\vec{S} = (S_1, S_2, S_3)$ describing the polarization of the light. Previously, we denoted the Stokes vector $\vec{S} = (S_x, S_y, S_z)$, but to match the notation in this chapter with the notation used in the article [2], we here use the $\vec{S} = (S_1, S_2, S_3)$ notation instead. In chapter 2, the equations describing the swap and squeezing interaction were written in terms of the canonical variables. We will start by translating those equations into the spin/Stokes vector language.

To keep the notation simple, the vector $\vec{J}$ is in this chapter understood as a rotating frame operator while the vector in the lab frame is denoted $\vec{J}^{\text{lab}}$ [1]. We can define dimensionless integrated Stokes operators such as

$$\begin{aligned} S_{2c}^{\text{in}} &\propto \int_0^T S_2^{\text{in}}(t) \cos(\Omega_L t)\, e^{+\gamma t} dt \\ S_{2c}^{\text{out}} &\propto \int_0^T S_2^{\text{out}}(t) \cos(\Omega_L t)\, e^{-\gamma t} dt, \end{aligned} \tag{5.1}$$

where the normalization is chosen such that a coherent light state has the variances $\text{Var}(S_{2c}) = \text{Var}(S_{3c}) = \Phi/2$ (and similar for the sine operators). Φ is here defined as the number of photons in a pulse. The variance of $\Phi/2$ is denoted the shot noise of light. For convinience I do not write the subscript $+$ or $-$ on the integrated Stokes operators. The input light operators are in this chapter always

[1] This is a bit different than in chapter 2 where a prime was used to denote rotating frame spin-operators.

integrated with an exponentially rising mode function and the output light operators with an exponentially falling mode function. The input-output equations (presented later in Eq. (5.2)) rely on that the time constant of the mode function is $1/\gamma = T_2$. However, one might improve SNR by using a time constant T_m shorter than T_2. This is discussed later in Sec. 5.6.2.

5.2.1 Swap and squeezing interaction

We can directly translate the swap and squeezing input-output equations given by Eq. (2.18) if we insert the definitions of the canonical operators (given by Eq. (2.2) for atomic variables and Eq. (2.5) for light variables) and the definition of the integrated Stokes operators given by Eq. (5.1) [2]. We find

$$
\begin{aligned}
S_{2c}^{\text{out}} &= t \cdot S_{2c}^{\text{in}} + \kappa \sqrt{\frac{\Phi}{2\left|J_x\right|}} \left(J_{z1}^{\text{in}} + J_{z2}^{\text{in}}\right) \\
S_{2s}^{\text{out}} &= t \cdot S_{2s}^{\text{in}} + \kappa \sqrt{\frac{\Phi}{2\left|J_x\right|}} \left(J_{y1}^{\text{in}} + J_{y2}^{\text{in}}\right) \\
S_{3c}^{\text{out}} &= t \cdot S_{3c}^{\text{in}} - \zeta^2 \kappa \sqrt{\frac{\Phi}{2\left|J_x\right|}} \left(J_{y1}^{\text{in}} - J_{y2}^{\text{in}}\right) \\
S_{3s}^{\text{out}} &= t \cdot S_{3s}^{\text{in}} + \zeta^2 \kappa \sqrt{\frac{\Phi}{2\left|J_x\right|}} \left(J_{z1}^{\text{in}} - J_{z2}^{\text{in}}\right) \\
J_{y1}^{\text{out}} - J_{y2}^{\text{out}} &= t \cdot \left(J_{y1}^{\text{in}} - J_{y2}^{\text{in}}\right) + \kappa \sqrt{\frac{2\left|J_x\right|}{\Phi}} S_{3c}^{\text{in}} \\
J_{z1}^{\text{out}} - J_{z2}^{\text{out}} &= t \cdot \left(J_{z1}^{\text{in}} - J_{z2}^{\text{in}}\right) - \kappa \sqrt{\frac{2\left|J_x\right|}{\Phi}} S_{3s}^{\text{in}} \\
J_{z1}^{\text{out}} + J_{z2}^{\text{out}} &= t \cdot \left(J_{z1}^{\text{in}} + J_{z2}^{\text{in}}\right) - \zeta^2 \kappa \sqrt{\frac{2\left|J_x\right|}{\Phi}} S_{2c}^{\text{in}} \\
J_{y1}^{\text{out}} + J_{y2}^{\text{out}} &= t \cdot \left(J_{y1}^{\text{in}} + J_{y2}^{\text{in}}\right) - \zeta^2 \kappa \sqrt{\frac{2\left|J_x\right|}{\Phi}} S_{2s}^{\text{in}},
\end{aligned}
\tag{5.2}
$$

where we used the definition $t \equiv \sqrt{1 - \zeta^2 \kappa^2}$. For our setting of the probe detuning $\Delta = -850$ MHz, $\zeta^{-2} \approx 6.4$. For a fully pumped ensemble, we have $|J_x| = F N_A$ where N_A is the number of atoms in a single cell and $F = 4$ is the ground state hyperfine quantum number.

[2] Notice the sign in the definition of $X_s = -\left(J_{z1} - J_{z2}\right)/\sqrt{2\left|J_x\right|}$ changes the signs in Eq. (5.2) as compared to Eq. (2.18) when a term $(J_{z1} - J_{z2})$ is present.

5.3 A pulsed radio frequency magnetometer and the projection noise limit

In this section, we describe how an atomic ensemble can be used as a sensor for magnetic fields. We consider the special case of measuring RF magnetic fields with a pulsed scheme. The atomic ensemble can be described in terms of the spin vector $\vec{J}$ depicted in Fig. 5.1. The atoms are first polarized in the x-direction by optical pumping (see pulse sequence in Fig. 5.4b). In this case the atomic spins can be represented as a long vector with an uncertainty disk on the top. The length of the vector is $J_x = 4N_A$ which is a macroscopic classical value. On the other hand, the transverse spin components J_y and J_z are small and can be treated as quantum variables which must satisfy the Heisenberg uncertainty relation $\Delta J_y \cdot \Delta J_z \geq |J_x|/2$. For atoms in a CSS, the transverse spin components have equal uncertainties $\Delta J_y = \Delta J_z = \sqrt{|J_x|/2}$. The atoms are as usual located in a bias magnetic field pointing in the x-direction such that a transverse spin component (J_y or J_z) will precess at the Larmor frequency Ω_L.

We then apply an RF pulse with amplitude B_{RF} for a certain duration τ. This creates a transverse spin component

$$\langle J_\perp \rangle = \Gamma B_{\mathrm{RF}} J_x T_2 \left[1 - \exp\left(-\tau/T_2\right)\right]/2. \tag{5.3}$$

$\Gamma = \Omega_L/B = 2.2 \cdot 10^{10}$ rad/ (sec $\cdot$ Tesla) for cesium. Often one uses the notation $\Gamma = g_F \mu_B/\hbar$ where g_F is the Landé factor (F is the hyperfine quantum number, $F = 4$ in our case) and μ_B is the Bohr magneton. T_2 is the transverse spin coherence time. In a pulsed scheme, the atoms decay slower during the RF pulse (when no light is on the atoms) than during the probing pulse (where the probe light is on the atoms). In Eq. (5.3), T_2 should be understood as the coherence time during the RF pulse. For a pulsed scheme, this coherence time equals the decay time in the dark T_2^{dark}.

The transverse spin component can be measured with a pulse of light. Assuming that the only noise source is the PN of atoms, we can find the minimal detectable field by equating Eq. (5.3) to the projection noise $\Delta J_\perp = \sqrt{|J_x|/2}$. The result is

$$B_{\min} = \left[\Gamma \sqrt{|J_x|/2} T_2 \left\{1 - \exp\left(-\tau/T_2\right)\right\}\right]^{-1}. \tag{5.4}$$

We call this the "minimal detectable field", but it should really be understood as the standard deviation ΔB of the measurement of the magnetic field using the measurement time $\approx \tau$. Notice that $B_{\min}$ depends on T_2 and τ. This dependence is discussed in detail in Sec. 5.4.

The PN-limited sensitivity is defined as $\mathcal{S}_{PN} \equiv B_{\min}\sqrt{\tau}$ and has the unit Tesla/$\sqrt{\mathrm{Hz}}$. It equals the standard deviation of the measured field if one uses repeated measurements for a total duration of 1 second [3].

[3] Repeating the same measurement M times for a total duration $M\tau$ improves the uncertainty

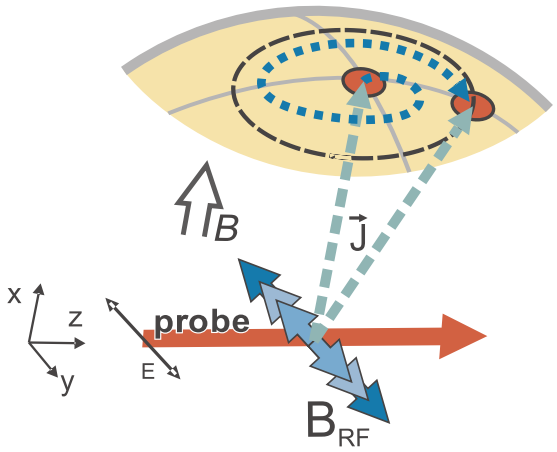

Figure 5.1: Radio-frequency magnetometer. The atomic spin $\vec{J}$ precesses in crossed dc and RF magnetic fields (the blue dashed spiral). The precessing $\vec{J}$ imposes an oscillating polarization rotation on the probe light.

5.3.1 Projection noise limited...

In the thesis and in particular in this chapter the term "projection noise limited ..." is used with different meanings. To make sure that there is no confusion, I here go through the different expressions.

PN-limited atomic noise

If the atomic noise in PN-units is $\Sigma_{\mathrm{EPR}} = 1$, we say that the atomic noise is PN-limited. The CSS is an example of an atomic state with PN-limited atomic noise. The two atomic ensembles are entangled if $\Sigma_{\mathrm{EPR}} < 1$. The noise of an entangled atomic state is therefore below the PN limit.

PN-limited measurement

The magnetometer signal is proportional to $S_{2c}^{\mathrm{out}} + i \cdot S_{2s}^{\mathrm{out}}$ (here written using complex notation). For simplicity, in the following we only consider the cosine component of the signal. In our two cell magnetometer, the signal S_{2c}^{out} carries information of the atomic spin component $J_{z1} + J_{z2}$. Assume the mean signal can be written as [4]

$$\left\langle S_{2c}^{\mathrm{out}} \right\rangle = \kappa \sqrt{\frac{\Phi}{2\,|J_x|}}\,\langle J_{z1} + J_{z2} \rangle\,. \tag{5.5}$$

ΔB on the magnetic field by the factor $\sqrt{M}$. The sensitivity is however the same independent of the number of averages M (and the averaging time $M\tau$).

[4] In Eq. (5.5) we *only* assume that the mean signal $\langle S_{2c}^{\mathrm{out}} \rangle$ is proportional to the mean atomic spin $\langle J_{z1} + J_{z2} \rangle$. The proportionality constant is here denoted $\kappa\sqrt{\frac{\Phi}{2|J_x|}}$.

If the variance of the signal satisfy [5]

$$\mathrm{Var}\left(S_{2c}^{\mathrm{out}}\right) \leq \kappa^2 \cdot \frac{\Phi}{2}, \tag{5.6}$$

we say that the measurement (of the spin component) is PN-limited. If we use the measurement of the spin to measure B_{RF}, we say that the measurement of B_{RF} is PN-limited.

In a standard atomic magnetometer, it is not possible to do a PN-limited measurement of the spin. This is because the SN of the probe light also contribute to the variance of the signal. In order to achieve a PN-limited measurement, one needs to either (A) suppress the shot noise or (B) reduce the atomic noise below the PN-level. Later in Sec. 5.3.5, we show that the light noise can be suppressed using the swap and squeezing interaction and that the atomic noise can be reduced below the PN-level by entangling the two atomic ensembles

PN-limited sensitivity

As already stated earlier, the PN-limited sensitivity is defined as $\mathcal{S}_{PN} \equiv B_{\mathrm{min}}\sqrt{\tau}$ where B_{min} is given by Eq. (5.4). In the experiment, the minimal detectable field equals B_{RF}/SNR where B_{RF} is the applied field and SNR is the signal to noise ratio. We use two different expressions for the measured sensitivity. We consider either $\mathcal{S}_{\tau} \equiv (B_{\mathrm{RF}}/SNR)\sqrt{\tau}$ or $\mathcal{S}_{\mathrm{tot}} \equiv (B_{\mathrm{RF}}/SNR)\sqrt{T_{\mathrm{tot}}}$. T_{tot} is the total cycle time which includes the time spent on pumping and probing. The last expression for the sensitivity gives a worse sensitivity since $T_{\mathrm{tot}} > \tau$. We say that the measured sensitivity is PN-limited if it is less than $B_{\mathrm{min}}\sqrt{\tau}$.

5.3.2 Single cell magnetometer

In Sec. 5.3 we considered a PN-limited measurement of the magnetic field. In an experiment there are other noise sources than the PN of atoms, this is true in particular if only one atomic ensemble is used as the magnetic field sensor. We now go through the details of how much extra noise one would expect for such a single cell magnetometer.

Consider a single cell atomic magnetometer based on the Faraday interaction which can be described by the Hamiltonian $\mathcal{H}_{\mathrm{int}} \propto S_z J_z$. We here neglect the tensor polarizability of atoms, which give rise to the a_2-terms in the full Hamiltonian given by Eq. (2.20). The atomic signal is encoded in the S_{2c} and S_{2s} integrated

[5] Equation (5.6) is derived assuming that the fluctuations on the output light are smaller than the fluctuations orignating from the projection noise of atoms: $\mathrm{Var}\left(S_{2c}^{\mathrm{out}}\right) = \kappa^2 \cdot \frac{\Phi}{2|J_x|} \cdot \mathrm{Var}\left(J_{z1} + J_{z2}\right) \leq \kappa^2 \cdot \frac{\Phi}{2|J_x|} \cdot |J_x| = \kappa^2 \cdot \Phi/2$.

Stokes operates. For a single atomic ensemble the output cosine light operator is

$$S_{2c}^{\text{out}} = S_{2c}^{\text{in}} + \frac{\tilde{\kappa}}{\sqrt{2}}\sqrt{\frac{\Phi}{|J_x|}}J_z^{\text{in}} - \left(\frac{\tilde{\kappa}}{2}\right)^2 S_{3s}^{\text{in}} - \frac{1}{\sqrt{3}}\left(\frac{\tilde{\kappa}}{2}\right)^2 S_{3,s1}^{\text{in}} \tag{5.7}$$

This equation can be found from the single cell input-output Eq. (2.14) and the definitions of the canonical operators. The sine operator is given by a similar expression. Assuming all input operators are in the vacuum states, we find

$$\text{Var}\left(S_{2c}^{\text{out}}\right) = \frac{\Phi}{2}\left[1 + \frac{\tilde{\kappa}^2}{2} + \frac{\tilde{\kappa}^4}{12}\right]. \tag{5.8}$$

From this equation it is obvious that we do not have a PN-limited measurement. Besides the term $\frac{\Phi}{2}\cdot\frac{\tilde{\kappa}^2}{2}$ arising from the PN, we have the shot noise term $\frac{\Phi}{2}\cdot 1$ and the backaction noise term $\frac{\Phi}{2}\cdot\frac{\tilde{\kappa}^4}{12}$. The signal grows linearly with $\tilde{\kappa}$ and the noise grows as $\sqrt{1+\tilde{\kappa}^2/2+\tilde{\kappa}^4/12}$. One can calculate the optimal interaction strength $\tilde{\kappa}^2 = 2\sqrt{3} \approx 3.5$ where the signal to noise ratio is maximal. For $\tilde{\kappa}^2 > 2\sqrt{3}$ the backaction noise prevails and the signal to noise ratio decreases.

5.3.3 Two cell QND magnetometer

The single cell magnetometer has the disadvantange that one is not performing a QND measurement of the spin. In other words, the backaction noise piles up in the atoms for large $\tilde{\kappa}$.

For two atomic ensembles, the interaction can be described by the Hamiltonian $\mathcal{H}_{\text{int}} \propto S_z\left(J_{z1} + J_{z2}\right)$, if the tensor terms proportional to a_2 are neglected, see Eq. (2.20). With two oppositely oriented ensembles one can achieve the QND interaction since the backaction noise on the two ensembles cancel each other. In this case, the input-output equations for the Stokes operators are given by

$$\begin{aligned} S_{2c}^{\text{out}} &= S_{2c}^{\text{in}} + \tilde{\kappa}\sqrt{\frac{\Phi}{2\,|J_x|}}\left(J_{z1}^{\text{in}} + J_{z2}^{\text{in}}\right) \quad \text{and} \quad S_{3c}^{\text{out}} = S_{3c}^{\text{in}} \\ S_{2s}^{\text{out}} &= S_{2s}^{\text{in}} + \tilde{\kappa}\sqrt{\frac{\Phi}{2\,|J_x|}}\left(J_{y1}^{\text{in}} + J_{y2}^{\text{in}}\right) \quad \text{and} \quad S_{3s}^{\text{out}} = S_{3s}^{\text{in}}, \end{aligned} \tag{5.9}$$

and the equations for the collective atomic operators are given by

$$\begin{aligned} J_{y1}^{\text{out}} - J_{y2}^{\text{out}} &= \left(J_{y1}^{\text{in}} - J_{y2}^{\text{in}}\right) + \tilde{\kappa}\sqrt{\frac{2\,|J_x|}{\Phi}}S_{3c}^{\text{in}} \quad \text{and} \quad J_{z1}^{\text{out}} + J_{z2}^{\text{out}} = J_{z1}^{\text{in}} + J_{z2}^{\text{in}} \\ J_{z1}^{\text{out}} - J_{z2}^{\text{out}} &= \left(J_{z1}^{\text{in}} - J_{z2}^{\text{in}}\right) - \tilde{\kappa}\sqrt{\frac{2\,|J_x|}{\Phi}}S_{3s}^{\text{in}} \quad \text{and} \quad J_{y1}^{\text{out}} + J_{y2}^{\text{out}} = J_{y1}^{\text{in}} + J_{y2}^{\text{in}}. \end{aligned} \tag{5.10}$$

We focus on the signal S_{2c}^{out} and its variance

$$\text{Var}\left(S_{2c}^{\text{out}}\right) = \text{Var}\left(S_{2c}^{\text{in}}\right) + \tilde{\kappa}^2 \frac{\Phi}{2\left|J_x\right|} \text{Var}\left(J_{z1}^{\text{in}} + J_{z2}^{\text{in}}\right). \tag{5.11}$$

Assuming that all input operators are in the vacuum state, we find

$$\text{Var}\left(S_{2c}^{\text{out}}\right) = \frac{\Phi}{2}\left[1 + \tilde{\kappa}^2\right]. \tag{5.12}$$

If we could reach the limit $\tilde{\kappa}^2 \to \infty$, the contribution from the shot noise would be negligible and the measurement would be PN-limited. In the experiment this limit can not be reached for several reasons. Classical noise typically become a problem for high $\tilde{\kappa}$. This is because classical noise in $\vec{J}$ or $\vec{S}$ scales as N_A^2 or N_{ph}^2 in the variance where N_{ph} is the number of photons. The quantum noise however scales as N_A or N_{ph} in the variance which means that classical noise will dominate for large N_A or N_{ph}. One could also try to increase $\tilde{\kappa}^2$ by increasing the interaction time T. This can only be done to some extend, since atomic decoherence will ruin the signal for interaction times comparable to or larger than T_2. Also, for large interaction strengths, the interaction between light and two oppositely oriented ensemblesis is not of the QND type (due to the tensor polarizability of atoms). Instead the interaction is better described using the swap and squeezing theory. This is discussed in detail in Sec. 5.3.5.

5.3.4 Comparison of single cell and two cell magnetometers

We now compare the performance of the single cell magnetometer and the two cell QND magnetometer. The two cell magnetometer uses $2N_A$ atoms. For a fair comparison we assume that the single cell magnetometer also uses $2N_A$ number of atoms. For the two cell case, we assume that the RF magnetic field B_{RF} is applied to both ensembles at the same time. With this in mind, the mean signals $\langle S_{2c}^{\text{out}} \rangle$ for the single cell and the two cell cases have equal magnitudes. The variance of the signals are however different. For the single cell case (with twice the number of atoms), the variance is

$$\text{Var}\left(S_{2c}^{\text{out}}\right) = \frac{\Phi}{2}\left[1 + \frac{\left(\sqrt{2}\tilde{\kappa}\right)^2}{2} + \frac{\left(\sqrt{2}\tilde{\kappa}\right)^4}{12}\right] = \frac{\Phi}{2}\left[1 + \tilde{\kappa}^2 + \frac{\tilde{\kappa}^4}{3}\right], \tag{5.13}$$

where $\tilde{\kappa}$ is the coupling constant for N_A number of atoms and $\sqrt{2}\tilde{\kappa}$ is the coupling constant for $2N_A$ number of atoms. For the two cell case, the variance is given by Eq. (5.12). The variances differes by the backaction noise term $\tilde{\kappa}^4/3$. We can also consider the signal to noise ratio's for the different magnetometers. Assuming the spins are displaced by one PN-unit ($\langle J_{z1} + J_{z2} \rangle = \sqrt{|J_x|}$), we find $SNR = \tilde{\kappa}/\sqrt{1+\tilde{\kappa}^2}$ for the two cell QND magnetometer and $SNR = \tilde{\kappa}/\sqrt{1+\tilde{\kappa}^2+\tilde{\kappa}^4/3}$

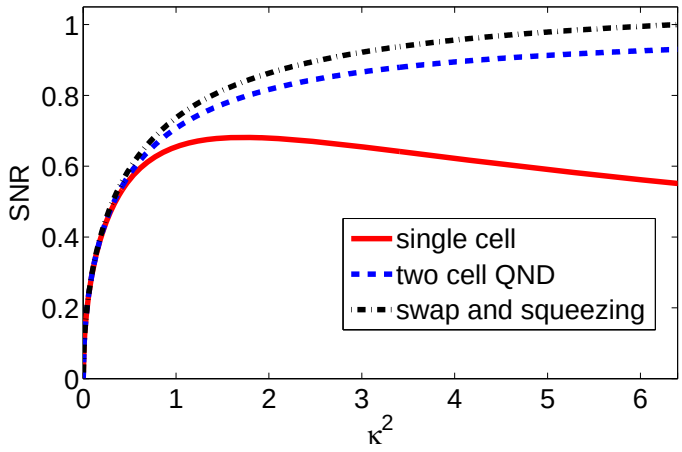

Figure 5.2: Signal to noise ratio's for the different magnetometers as a function of $\tilde{\kappa}^2$ (or κ^2). Single cell magnetometer: $SNR = \tilde{\kappa}/\sqrt{1+\tilde{\kappa}^2+\tilde{\kappa}^4/3}$, two cell QND magnetometer: $SNR = \tilde{\kappa}/\sqrt{1+\tilde{\kappa}^2}$ and swap and squeezing magnetometer: $SNR = \kappa/\sqrt{1-\zeta^2\kappa^2+\kappa^2}$. For the swap and squeezing magnetometer κ^2 can maximally reach the value $\kappa^2_{\max} = \zeta^{-2} \approx 6.4$.

for the single cell magnetometer. These expressions are plotted in Fig. 5.2. The maximum SNR equals 1 (for $\tilde{\kappa}^2 \to \infty$) for the two cell QND magnetometer and 0.68 for the single cell magnetometer.

We can achieve the backaction evading QND measurement using two oppositely oriented atomic ensembles. As described above, the single cell magnetometer is not backaction evading, and the two cell QND magnetometer is therefore preferable. I want to mention that there are some tricks which enables a QND measurement on a single atomic ensemble. If we are only interested in measuring the atomic spins of a single ensemble for a duration shorter than $1/\Omega_L$ then the measurement can be of the QND type. This was the approach in the first paper on spin-squeezing using QND measurements [42]. This approach obviously has the disadvantage that the time $1/\Omega_L$ is short. In our experiments $\Omega_L = 322$ kHz such that the time $1/\Omega_L \approx 3$ μs. A different approach is to stroboscopically turn the probe light on and off with twice the Larmor frequency [70]. This way the probe only interacts with the atoms when the rotating frame operator J_z equals the lab operator J_z^{lab}. This therefore enables a QND measurement of the J_z.

The measurement of the magnetic field using a single cell or a two cell QND magnetometer is not PN-limited since the variance of the signal consists of both SN of light and PN of atoms. One can improve both the single cell and the two cell QND magnetometer by using squeezed light. This reduces the variance $\text{Var}\left(S_{2c}^{\text{in}}\right) < \Phi/2$ and thereby increases the magnetometer signal to noise ratio.

Magnetometry with squeezed light was recently demonstrated in [48]. One can also squeeze the atomic spins such that the atomic noise is reduced below the PN limit. For a single ensemble, the spins can be squeezed by "Nuclear-Electronic spin entanglement" [5]. For two ensembles, the spins can be entangled using a QND measurement [16] as discussed earlier in Sec. 3.8. In Sec. 5.7 we will present results of such an entanglement-assisted magnetometer.

5.3.5 Two cell swap and squeezing magnetometer

The interaction between light and two oppositely oriented atomic ensembles is *not* of the QND type due to the tensor polarizability of the atoms. Instead, the interaction is better described by the swap and squeezing interaction theory which leads to the input-output equations (5.2). In the absence of atomic decay ($\epsilon^2 = 0$) and for long interaction times $2\gamma_{\rm sw}T \gg 1$, the light and atomic operators are completely swapped

$$S_{2c}^{\rm out} = \frac{1}{\zeta}\sqrt{\frac{\Phi}{2\left|J_x\right|}}\left(J_{z1}^{\rm in} + J_{z2}^{\rm in}\right) \tag{5.14}$$

With this input-output equation, the signal $S_{2c}^{\rm out}$ is proportional to the atomic operator $\left(J_{z1}^{\rm in} + J_{z2}^{\rm in}\right)$. The only noise source is in this case the atomic noise. If the atomic noise is PN-limited, the measurement will also be PN-limited.

The measurement described by Eq. (5.14) is a perfect PN-limited measurement of the spin. The measurement is backaction evading and the noise of the meter (the input shot noise) is completely squeezed and is therefore not present.

If we do not have a complete swap, the swap and squeezing interaction leads to the signal (see Eq. (5.2))

$$S_{2c}^{\rm out} = t \cdot S_{2c}^{\rm in} + \kappa\sqrt{\frac{\Phi}{2\left|J_x\right|}}\left(J_{z1}^{\rm in} + J_{z2}^{\rm in}\right). \tag{5.15}$$

The variance of $S_{2c}^{\rm out}$ is

$$\mathrm{Var}\left(S_{2c}^{\rm out}\right) = t^2 \cdot \mathrm{Var}\left(S_{2c}^{\rm in}\right) + \kappa^2\frac{\Phi}{2\left|J_x\right|}\mathrm{Var}\left(J_{z1}^{\rm in} + J_{z2}^{\rm in}\right). \tag{5.16}$$

If the atomic noise in PN-units is denoted $\Sigma_{\rm EPR}$ and we assume the input light is in a coherent state such that $\mathrm{Var}\left(S_{2c}^{\rm in}\right) = \Phi/2$ then

$$\mathrm{Var}\left(S_{2c}^{\rm out}\right) = \frac{\Phi}{2}\left[t^2 + \kappa^2 \cdot \Sigma_{\rm EPR}\right]. \tag{5.17}$$

The signal to noise ratio (assuming the spins are displaced by one PN-unit and that the atomic noise equals PN) for the swap and squeezing interaction is plotted

in Fig. 5.2. In the swap and squeezing interaction theory $\kappa^2 = \left(1 - e^{-2\gamma_{\rm sw}T}\right)/\zeta^2$ can maximally reach the value $\kappa^2_{\rm max} = \zeta^{-2} \approx 6.4$. For this value SNR equals 1. In Fig. 5.2 we also see that SNR is higher for the swap and squeezing interaction than for the QND interaction. This is because the input light noise is reduced below the shot noise level $\Phi/2$ by the factor $t^2 = (1 - \zeta^2\kappa^2)$. One should notice that $\tilde{\kappa}$ is different from κ for large interaction strengths, and that the QND interaction is an approximation to the swap and squeezing interaction for the case of two oppositely oriented atomic ensembles (see Eq. 2.5).

If we do not have a complete swap such that $t^2 = 1 - \zeta^2\kappa^2 > 0$, we see from Eqs. (5.6) and (5.17) that the measurement is not PN-limited even for PN-limited atomic noise ($\Sigma_{\rm EPR} = 1$) due to the residual light noise contribution to the variance. On the other hand, if we can reduce the atomic noise via entanglement, it is possible that the measurement can be PN-limited.

When including bad decoherence in the swap and squeezing interaction, the reduction of the light noise changes. For a non-zero ϵ^2 parameter we should use the factor t_m^2 defined in Eq. (2.83) instead of the factor t^2 when calculating the output noise using Eq. (5.17). Since $t_m^2 > t^2$ the reduction of the light noise gets smaller. The bad decay therefore limits how well the light noise can be suppressed. If ϵ^2 is large, the reduction of the light noise is small and we instead have to utilize the backaction evading measurement together with entanglement between the atomic ensembles to achieve the near PN-limited measurement.

5.4 Magnetometry and Bandwidths

The PN-limited sensitivity of an atomic magnetometer depends on the magnetometer bandwidth $\delta_A \equiv 1/T_2$ and the bandwidth of the RF pulse $\delta_{\rm RF} \equiv 1/\tau$. Below we examine how the sensitivity scales with these bandwidths.

We consider the constant $B_{\rm RF}$ which is applied for a certain duration τ. The PN-limited sensitivity equals $\mathcal{S}_{PN} \equiv B_{\rm min}\sqrt{\tau}$, where $B_{\rm min}$ is given by Eq. (5.4). Inserting the expression for $B_{\rm min}$, we find the full expression for the sensitivity:

$$\mathcal{S}_{PN} = \frac{1}{\Gamma}\sqrt{\frac{2}{|J_x|}}\frac{\sqrt{\tau}}{T_2\left(1 - \exp\left(-\tau/T_2\right)\right)} \tag{5.18}$$

We can consider the two limits of short/long RF pulses compared to the atomic

T_2-time. We find

$$\mathcal{S}_{PN} = \frac{1}{\Gamma}\sqrt{\frac{2}{|J_x|}}\frac{1}{\sqrt{\tau}} \quad \text{for} \quad \tau \ll T_2 \quad \text{or} \quad \delta_{\mathrm{RF}} \gg 1/T_2$$
$$\mathcal{S}_{PN} = \frac{1}{\Gamma}\sqrt{\frac{2}{|J_x|}}\frac{\sqrt{\tau}}{T_2} \quad \text{for} \quad \tau \gg T_2 \quad \text{or} \quad \delta_{\mathrm{RF}} \ll 1/T_2. \tag{5.19}$$

The sensitivity given by Eq. (5.18) together with the asymptotic expressions in Eq. (5.19) (all divided by $\frac{1}{\Gamma}\sqrt{\frac{2}{|J_x|}}$) are shown in Fig. 5.3. The upper left figure show the sensitivity as a function of T_2 for a fixed value of $\tau = 1$. The lower left shows the same but with the 1st axis equal to $\delta_A = 1/T_2$. The upper right figure shows the sensitivity as a function τ with a fixed value for $T_2 = 1$, and the lower right figure shows the same but with the 1st axis equal to δ_{RF}.

The upper right figure shows that for an atomic magnetometer with a fixed T_2 time there is an optimal RF pulse duration $\tau \approx T_2$ where the magnetometer has the best sensitivity. In this sense, the RF bandwidth and the atomic bandwidth should be matched. On the other hand, for a specific RF duration τ (see upper and lower left figures) the sensitivity improves with larger T_2. For $T_2 \gg \tau$ the sensitivity becomes independent of T_2 as also seen in Eq. (5.19). This is the setting where the magnetometer has the *best sensitivity*. If one would like to demonstrate a magnetometer with as good sensitivity as possible, one would need a magnetometer with as large T_2 as possible, and then measure the RF pulses with duration $\tau \approx T_2$.

In the experiment we will entangle the two atomic ensembles by a near QND measurement prior to the RF magnetic pulse. The entanglement has a certain lifetime T_{2E}. For RF durations $\tau \geq T_{2E}$ the entanglement has decayed and the entanglement will not improve the performance of the magnetometer. Under our experimental conditions, the entangled states decays faster than coherent states such that $T_{2E} < T_2$. Entanglement will therefore only improve the magnetometer in the situation described by the in-equalities

$$\tau \leq T_{2E} < T_2 \quad \text{or} \quad \delta_{\mathrm{RF}} \geq 1/T_{2E} > 1/T_2. \tag{5.20}$$

As argued above, this is *not* the limit where the magnetometer has the best sensitivity. The best sensitivity (reached in the limit $\tau \gg T_2$) will not be improved by entanglement. Instead, entanglement improves the magnetometer for short RF pulses. This will also be apparent in the experiment results presented later in Sec. 5.7

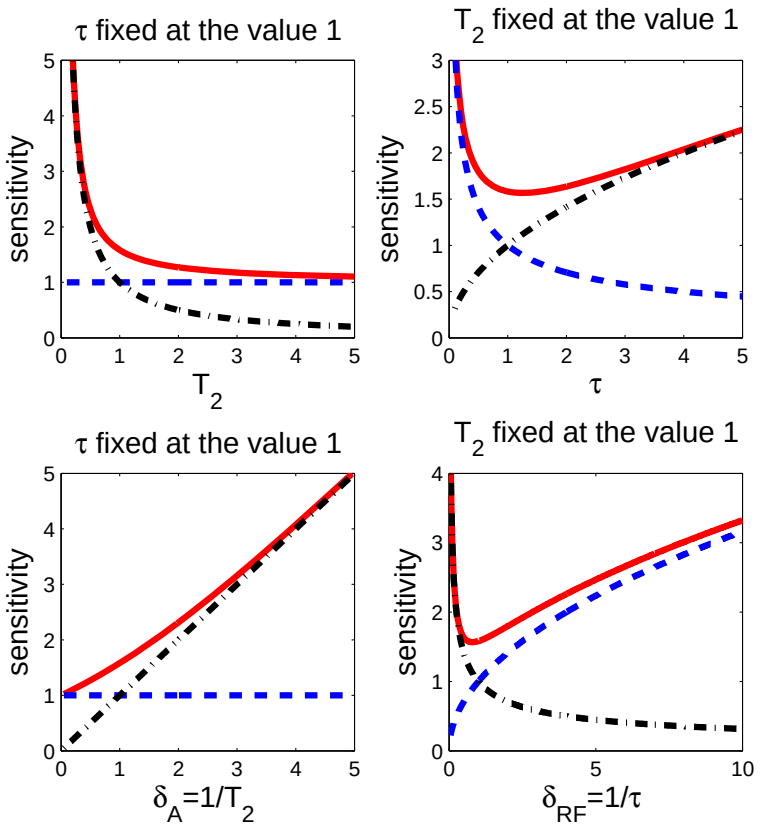

Figure 5.3: Red solid line: normalized sensitivity $\frac{\sqrt{\tau}}{T_2(1-\exp(-\tau/T_2))}$. Blue dashed line: Asymptotic expression $1/\sqrt{\tau}$ valid for $\tau \ll T_2$. Black dashed dotted line: Asymptotic expression $\sqrt{\tau}/T_2$ valid for $\tau \gg T_2$.

5.5 Setup, pulse sequence and procedure

A sketch of a two cell magnetometer is shown in Fig. 5.4a. The RF magnetic field B_{RF} is generated by sending a current through a coil. In the sketch, the coil is arranged such that both atomic ensembles are located in the same RF magnetic field. The ensembles, which are located in a bias magnetic field, are oppositely oriented using optical pumping methods, and probed by linearly polarized light. In the real setup (which differs from the setup shown in the sketch in Fig. 5.4), the two ensembles are located in separate magnetic shieldings, and two separate RF coils, one located around each ensemble, are used to make the RF magnetic fields. The two mirrors are also not present and the cells are put in a linear arrangement as shown in Fig. 3.2. The Stokes operator $S_2^{\mathrm{out}}(t)$ is measured by polarization homodyning. The output of the detectors are sent to a lock-in amplifier where the $\cos(\Omega_L t)$ and $\sin(\Omega_L t)$ components of the photocurrent are extracted. The outputs of the lock-in amplifier are measured using a FPGA data acquisition card. On the computer, the cosine and sine components are integrated over the pulse duration to obtain the signals S_{2c}^{out} and S_{2s}^{out}. For more details of the data aquisition and the data analysis procedure see Sec. 3.7.

Fig. 5.4b shows the pulse sequence for the experiment. First, optical pumping light polarizes the two atomic ensembles. Then, the RF magnetic field is applied for a certain duration τ. During the RF magnetic pulse, no light is on the atoms. The decay time in the dark (when no light is on the atoms) is $T_2^{\mathrm{dark}} > 30$ ms. This long coherence time is needed for high sensitivity RF magnetic field measurements as discussed in Sec. 5.4 [6]. Then a probe pulse is used to measure the atomic spins and thereby the RF field amplitude B_{RF}. In Fig. 5.4b, we see that the temporal mode function of the probe is chosen to be exponentially falling. The optimal time constant of the mode function is discussed in Sec. 5.6.2.

The pulse sequence for the entanglement-assisted measurements is shown in Fig. 5.4c. A first probe pulse prior to the RF pulse is used to entangle the two ensembles. Afterwards the RF pulse is applied and finally a second probe pulse is used for measuring the magnetic field amplitude B_{RF}. The method for creating the conditional entanglement has been discussed earlier in Sec. 3.8. Measurements of conditional entanglement has also been presented earlier in Sec. 3.11. As seen in Fig. 5.4c, we choose the temporal mode function of the 1st probe to be exponentially rising and the modefunction of the 2nd probe pulse to be exponentially falling. The temporal mode functions for the case of conditional entanglement have been discussed in Sec. 3.8.

[6] On the other hand, in a DC magnetometer, the RF field, the pump light and the probe light are all applied simultaneously. This has the disadvantage that the decay time T_2 is short due to spontaneous emission.

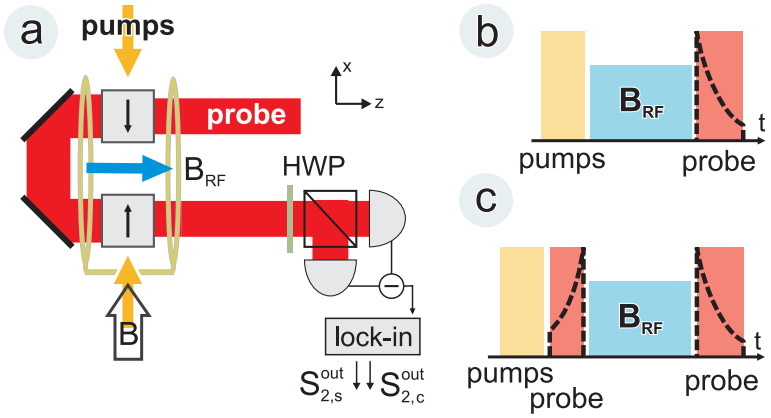

Figure 5.4: (a) Sketch of the experimental setup. Cubic 22mm paraffin coated cells filled with cesium are placed in the DC bias field B in two separate magnetic shields. The atoms are optically pumped so that the directions of the collective spins in the two cells (black arrows) are opposite. A pulse of B_{RF} at the frequency Ω is applied orthogonally to the B field. The polarization rotation of the top-hat shaped probe beam pulse (diameter 21mm) is detected by two detectors (HWP - half wave plate). The lock-in amplifier measures the $\cos(\Omega t)$ and $\sin(\Omega t)$ components of the photocurrent. (b) Pulse sequence for projection noise limited magnetometry. The temporal mode function for the probe is shown with a dashed black curve. (c) Pulse sequence and temporal modes for entanglement-assisted magnetometry.

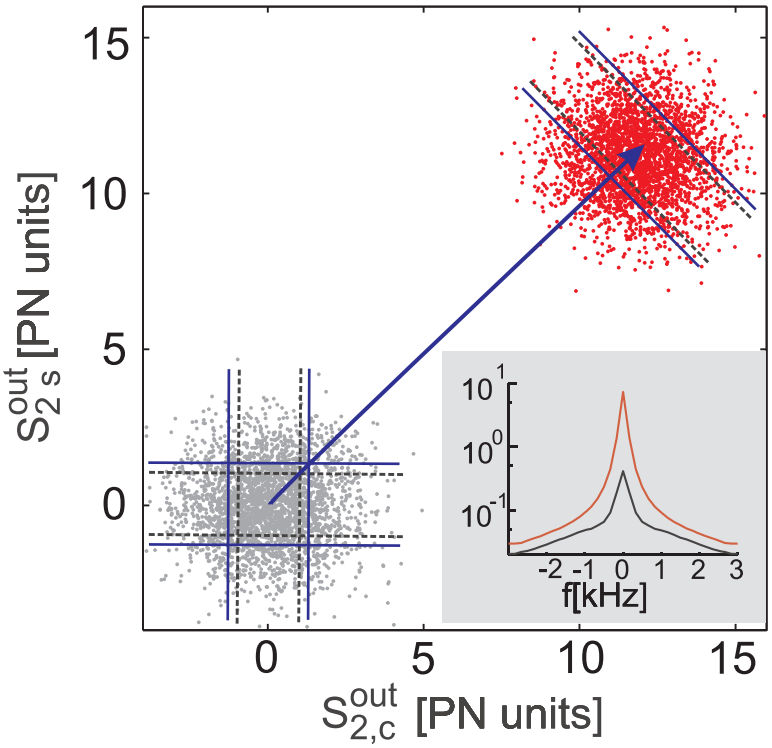

Figure 5.5: Results of a series of measurements of $\hat{S}_{2s,c}$ without B_{RF} (grey points) and after a 15 ms RF pulse with $B_{\mathrm{RF}} = 30(7)$ fT (red points). The solid and the dashed lines show the standard deviation of the experimental points, and of the the projection noise (PN) limited measurement, respectively. The spin displacement in the rotating frame is indicated by the blue arrow. (Inset) Power spectrum of the photocurrent (arb. units, centered at Ω) The narrow peak of the red/black spectrum is the atomic spin signal/projection noise. The broad part of the spectrum is the shot noise of light with the width set by the detection bandwidth.

5.6 Experimental results

5.6.1 The PN-limited magnetometer

We now present the results of the magnetic field measurements very close to the PN limit. Figure 5.5 shows two series (grey and red) of raw data points of the integrated signals S^{out}_{2c} and S^{out}_{2s} normalized to PN-units. This means that we have plotted $S^{\mathrm{out}}_{2c}/\sqrt{\frac{\Phi}{2}\cdot\kappa^2}$, such that the standard variation $\Delta\left[S^{\mathrm{out}}_{2c}/\sqrt{\frac{\Phi}{2}\cdot\kappa^2}\right] = 1$ for the PN-limited measurement. In order to normalize the raw data to PN-units, one needs to know the shot noise $\Phi/2$ and the coupling constant κ^2. SN is proportional to light power P and κ^2 is a function of light power and Faraday angle θ_F. Both P and θ_F are continuously monitored. The details of the shot

noise measurements have been discussed in Sec. 3.9 and the details of the κ^2 measurements (using the mean value transfer method) have been discussed in Sec. 3.6.

The grey points in Fig. 5.5 correspond to measurements of S_{2c}^{out} and S_{2s}^{out} where no B_{RF} is applied to the atoms. The mean values $\langle S_{2c}^{\text{out}} \rangle$ and $\langle S_{2s}^{\text{out}} \rangle$ are therefore zero. The standard deviations $\Delta \left[S_{2c}^{\text{out}} / \sqrt{\frac{\Phi}{2} \cdot \kappa^2} \right]$ and $\Delta \left[S_{2s}^{\text{out}} / \sqrt{\frac{\Phi}{2} \cdot \kappa^2} \right]$ of the measurements are plotted with blue solid lines such that the distance between the horizontal (or vertical) solid lines equal twice the standard deviation. The variances of S_{2c}^{out} and S_{2s}^{out} are equal in magnitude.

The black dashed lines represent the PN-limited measurement. The horizontal (or vertical) dashed lines are separated by two PN-units. The measured standard deviations represented by the blue solid lines are a bit larger than the black dashed lines which correspond to the PN of atoms. This is expected due to the contribution from the shot noise of light to the total magnetometer noise. By comparing the solid lines with the dashed lines, one can directly see that we are very close to having a PN-limited measurement.

For the measurements presented in Fig. 5.5, we measured the faraday angle $\theta_F = 17.1$ deg in the beginning of the probe pulse. From the measured Faraday angle, the numbers of atoms can be estimated to be [7] $N_A = 2 \cdot 7.8(7) \cdot 10^{11}$ using Eq. (3.2). The atomic decoherence time in the dark was measured to be $T_2^{\text{dark}} = 32$ ms.

We now perform a measurement where the RF magnetic field $B_{\text{RF}} = 30(7)$ fT is applied for the duration $\tau = 15$ ms (see appendix B for the calibration of the RF magnetic field [8]). This RF field tilts the spin vector and results in a non-zero mean value in the signal $S_{2c}^{\text{out}} + iS_{2s}^{\text{out}}$ as shown with red points in Fig. 5.5. An important figure of merit is the signal to noise ratio defined by

$$SNR = \frac{|\langle S_{2c}^{\text{out}} + iS_{2s}^{\text{out}} \rangle|}{\sqrt{\frac{1}{2} \cdot [\text{Var}\,(S_{2c}^{\text{out}}) + \text{Var}\,(S_{2s}^{\text{out}})]}}. \tag{5.21}$$

The signal to noise ratio can easily be found from the data in Fig. 5.5 since SNR equals the signal (the length of the arrow in Fig. 5.5) divided by standard deviation (1/2 of the distance between the blue lines). This way we find the value

[7] The factor of two on the number of atoms comes from the fact that we have two ensembles. The uncertainty on the number of atoms comes from the uncertainty on the length of the cells $L = 22(1)$ mm which has $\delta L/L = 4.5\%$ relative uncertainty. The symbol δL is used for the uncertainty on L. Since $N_A \propto L^2$ as seen in Eq. (3.2), we have $\delta N_A/N_A = 2 \cdot \delta L/L$, such that the relative uncertainty on N_A is $\delta N_A/N_A = 2 \cdot 4.5\% = 9\%$. The symbol δN_A is used for the uncertainty on N_A.

[8] In the paper [2] we used a slightly higher value for the applied RF magnetic field. However, in this thesis I will use the value $B_{\text{RF}} = 30(7)$ fT. This leads to slightly better results for the magnetometer sensitivity as compared to numbers stated in [2].

$SNR = 12.3$ for the data presented in Fig. 5.5. Note, that the signal to noise ratio depends on the applied B_{RF}.

The minimal detectable field can be calculated from the applied RF magnetic field and the signal to noise ratio: $B_{\min} = B_{\mathrm{RF}}/SNR = 30$ fT$/12.3 = 2.4(5)$ fT. The sensitivity is then calculated as $\mathcal{S}_\tau = B_{\min}\sqrt{\tau} = 2.9(6) \cdot 10^{-16}$ T$/\sqrt{\mathrm{Hz}}$ where we neglected the time used for optical pumping and probing. The uncertainties on the measured sensitivity and the measured $B_{\min}$ are estimated to be 22% due to the uncertainty on the applied B_{RF}.

We can compare the measured sensitivity with the PN-limited sensitivity of $\mathcal{S}_{PN} = 2.6(1) \cdot 10^{-16}$ T$/\sqrt{\mathrm{Hz}}$ [9] which can be calculated using the $B_{\min}$ from Eq. (5.4) and multiplying by $\sqrt{\tau}$. One need to use the numbers for $N_A = 2{\cdot}7.8(7){\cdot}10^{11}$, $T_2^{\mathrm{dark}} = 32$ ms and $\tau = 15$ ms. The experimentally measured sensitivity $\mathcal{S}_\tau = 2.9(6) \cdot 10^{-16}$ T$/\sqrt{\mathrm{Hz}}$ is 10% higher than the calculated PN-limited sensitivity. Since the measured sensitivity is very close to the PN-limited sensitivity (in fact the sensitivities are equal to within the uncertainties), we can claim that our magnetometer is PN-limited or at least very close to being PN-limited. The difference between the two sensitivities is due to the residual shot noise, atomic decay, and classical noise of the atomic spins. I emphasize that the measurements have been done utilizing the backaction evading swap and squeezing interaction and that the contribution from the shot noise to the total magnetometer noise is reduced.

5.6.2 The best experimental sensitivity

We now present the results for the best experimental sensitivity. The best means here that we have optimized the sensitivity with respect to different experimental parameters such as the pump duration T_{pump}, the probe power P, the probe duration T, the mode function, the RF duration τ and the number of atoms N_A. Since these are many experimental parameters which should be varied, I can not guarantee that we could not have done slightly better by choosing slightly different experimental settings. I will not go in depth with the optimization procedures except for the optimization of the mode function.

For a specific measurement set, we used the total cycle time $T_{\mathrm{tot}} = 30$ ms including the RF duration $\tau = 22.5$ ms, the probe duration $T = 1.5$ ms and the optical pumping duration $T_{\mathrm{pump}} = 6$ ms. The applied RF field was $B_{\mathrm{RF}} = 30(7)$ fT and the faraday angle was $\theta_F = 17.9$ deg. The probe power was $P = 9.5$ V leading to a quite short decay time $T_2 = 1.9$ ms when the probe light is on the atoms. This time corresponds to the decay rate $\gamma = 1/T_2 = 0.51\mathrm{ms}^{-1}$. The decay

[9] The uncertainty on the calculated PN-limited sensitivity originates in the uncertainty in the number of atoms (which is due to the uncertainty on the length on the cell). To be specific we have $\delta B_{\min}/B_{\min} = \frac{1}{2}\delta N_A/N_A = \delta L/L = 4.5\%$. The symbol $\delta B_{\min}$ is used for the uncertainty on $B_{\min}$.

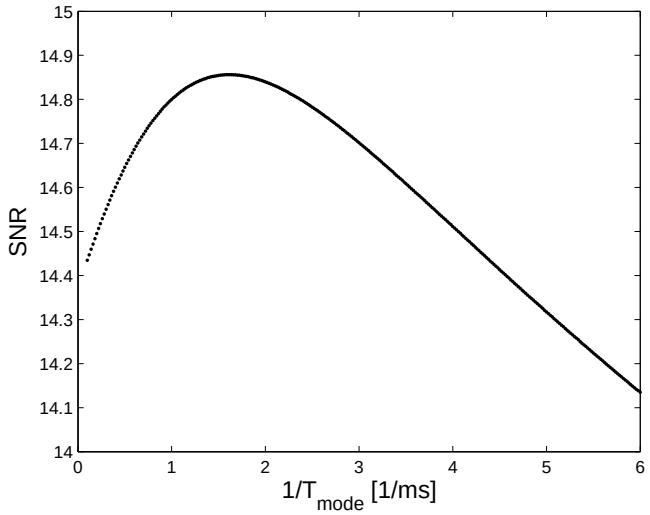

Figure 5.6: The signal to noise ratio SNR is plotted as a function of the mode constant $\gamma_m = 1/T_m$.

time with probe light on the atoms T_2 is significantly smaller than the decay time in the dark T_2^{dark}. In a pulsed atomic magnetometer, it is important to have a long T_2^{dark} in order to obtain high sensitivity. However, the probe duration T should be short in order not to "waste time" on the probing stage. The probe power is therefore chosen to be large, such that the decay time T_2 with the probe light on is short (remember, the T_2-time depends on P as shown for instance in Fig. 3.11). The readout of the atomic spins can then be fast since this happens on the fast time scale T_2.

For the above mentioned measurement set, we optimized the signal to noise ratio SNR with respect to the modefunction. We considered exponentially falling mode functions with time constant $\gamma_m = 1/T_m$. Using such a mode function means that the data are weighted by the exponentially falling temporal mode $\propto e^{-\gamma_m t} = e^{-t/T_m}$. The signal and the noise was calculated using the covariance matrix method described in Sec. 3.7.1.

Fig. 5.6 shows the calculated SNR as a function of the temporal mode constant $\gamma_m = 1/T_m$. We see that SNR has a maximum $SNR = 14.86$ at the value $\gamma_{\text{opt}} = 1.62$ ms^{-1} corresponding to $T_{\text{opt}} = 0.62$ ms. The maximum is quite broad. In the range γ_m from 0.1 ms^{-1} to 4 ms^{-1}, SNR only differs by up to around 3-4% from the maximum value. The optimal mode constant γ_{opt} differs significantly from the decay constant $\gamma = 1/T_2$, it is larger by a around a factor of three. Using SNR obtained with the optimal mode constant γ_{opt}, we calculate the best experimental senstivity $\mathcal{S}_{\text{tot}} = B_{\text{RF}}\sqrt{T_{\text{tot}}}/SNR = 3.5(8) \cdot 10^{-16}$ T$/\sqrt{\text{Hz}}$ [10].

[10]The uncertainty on the best experimental sensitivity is estimated to be 22% due the un-

Our best experimental sensitivity is close to the best to-date sensitivity optained by an atomic magnetometer [71]. The magnetometer [71] is a so-called Spin Exchange Relaxation Free (SERF) atomic magnetometer and operates with 10^4 times more atoms. Our magnetometer can achieve a similar sensitivity with less atoms since our measurement of the magnetic field is (almost) PN-limited.

5.7 Entanglement-assisted magnetometry

One can reduce the atomic noise below the PN limit by the use of entanglement between the two atomic ensembles. Entanglement is quantified in terms of the Einstein-Podolsky-Rosen variance Σ_{EPR} defined in Eq. (2.9), and the criterion for having entanglement between the ensembles is $\Sigma_{\mathrm{EPR}} < 1$.

In our case, the two atomic ensembles are entangled prior to the RF pulse (see Fig. 5.4c) using a 1st probe pulse. The magnetic field B_{RF} is afterwards measured with a 2nd probe pulse. Using the measurement result obtained with the 1st probe pulse, we can reduce the uncertainty on the 2nd probe measurement. This leads to a better SNR for the magnetic field B_{RF} measurement.

When utilizing the 1st pulse measurement to reduce the noise on the 2nd pulse measurement, we use the notion of conditional variance described earlier in Sec. 3.8. The conditional light operator was defined in Eq. (3.18) using the language of canonical operators. In terms of the Stokes vector language, the conditional Stokes operator is defined as

$$S_{2c}^{\mathrm{cond}} = S_{2c,-}^{\mathrm{out,2nd}} - \alpha S_{2c,+}^{\mathrm{out,1st}}. \tag{5.22}$$

The sine operator S_{2s}^{cond} is defined similarly. The parameter α is optimized in the experiment in order to minimize the conditional Stokes variance defined by $\left[\mathrm{Var}\left(S_{2c}^{\mathrm{cond}}\right) + \mathrm{Var}\left(S_{2c}^{\mathrm{cond}}\right)\right]/2$. From the conditional Stokes variance, we can calculate the conditional atomic variance $\Sigma_{\mathrm{EPR}}^{\mathrm{cond}}$. The condition for conditional entanglement is $\Sigma_{\mathrm{EPR}}^{\mathrm{cond}} < 1$. For the case of the entanglement-assisted magnetometry, we define the signal to noise ratio as

$$SNR = \frac{\left|S_{2c}^{\mathrm{out,2nd}} + iS_{2s}^{\mathrm{out,2nd}}\right|}{\sqrt{\frac{1}{2}\cdot\left[\mathrm{Var}\left(S_{2c}^{\mathrm{cond}}\right) + \mathrm{Var}\left(S_{2s}^{\mathrm{cond}}\right)\right]}}. \tag{5.23}$$

Since $\mathrm{Var}\left(S_{2c}^{\mathrm{cond}}\right) + \mathrm{Var}\left(S_{2c}^{\mathrm{cond}}\right) < \mathrm{Var}\left(S_{2c}^{\mathrm{out}}\right) + \mathrm{Var}\left(S_{2c}^{\mathrm{out}}\right)$, we see that entanglement improves the signal to noise ratio.

One way to verify that we have entanglement is to use the two ensembles as a magnetometer, calculate the minimal detectable field B_{RF}/SNR for some B_{RF}

certainty on the applied B_{RF}.

and compare with the PN-limited $B_{\min}$ given by Eq. (5.4). If the experimental B_{RF}/SNR is smaller than the PN-limited $B_{\min}$, the atoms are entangled. This procedure for verifying entanglement is however not very good. This is because the noise of the signal S_{2c}^{out} contains both a contribution from the shot noise of light and the projection noise of atoms. However, the contribution from the shot noise is not included in Eq. (5.4) for $B_{\min}$.

In order to verify entanglement, we instead calculate $\Sigma_{\mathrm{EPR}}^{\mathrm{cond}}$ from the measured output light variances. We use the full swap and squeezing interaction theory including the decoherence when calculating Σ_{EPR} and $\Sigma_{\mathrm{EPR}}^{\mathrm{cond}}$. This is done using the atomic noise reconstruction formula given by Eq. (2.85). To do this reconstruction, we need to know the κ^2 parameter. The calibration of κ^2 was in the magnetometry experiment done using the mean value transfer method described in Sec. 3.6.1 and by measuring the mean value of the output signal $\langle S_{2c}^{\mathrm{out}} + iS_{2s}^{\mathrm{out}} \rangle$ which is proportional to κ. More details can be found in appendix C.

5.7.1 Results of entanglement-assisted magnetometry

We now present the measurements which demonstrate that entanglement can improve our atomic magnetometer. The results presented here are obtained at room-temperature corresponding to the faraday angle of $\theta_F \approx 8$ deg. The RF magnetic field B_{RF} with a variable duration τ applied to one of the ensembles is measured using two approaches. In the first approach (see pulse sequence in Fig. 5.4b) the RF magnetic field is applied directly after the optical pumping stage and measured with a probe pulse. In the second approach (see pulse sequence in Fig. 5.4c) the two atomic ensembles are entangled using a 1st probe pulse located after the optical pumping. Then, the RF magnetic field is applied and measured with a 2nd probe pulse. The data sets for the first and second approaches are denoted "without" and "with" entanglement, respectively. The data without entanglement serves as a reference data set with which the data with entanglement can be compared.

The results of the measurements are shown in Fig. 5.7 (a,b,c). In the three figures, circles represent data with entanglement and squares represent data without entanglement.

We start by considering Fig. 5.7a. The square data points without entanglement show the variance of the signal $\left[\mathrm{Var}\left(S_{2c}^{\mathrm{out}}\right) + \mathrm{Var}\left(S_{2s}^{\mathrm{out}}\right)\right]/2$ normalized to the shot noise $\Phi/2$ as a function of RF pulse duration τ. In Fig. 5.7a, we also plot the results one would obtain with a PN-limited measurement of the spin. This is shown with a solid black line. If we include a detection efficiency η_{det} in the analysis, we have the following criterion for the PN-limited measurement

$$\frac{1}{2} \cdot \left[\mathrm{Var}\left(S_{2c}^{\mathrm{out}}\right) + \mathrm{Var}\left(S_{2s}^{\mathrm{out}}\right)\right] \leq \eta_{\mathrm{det}} \cdot \kappa^2 \cdot \frac{\Phi}{2}, \tag{5.24}$$

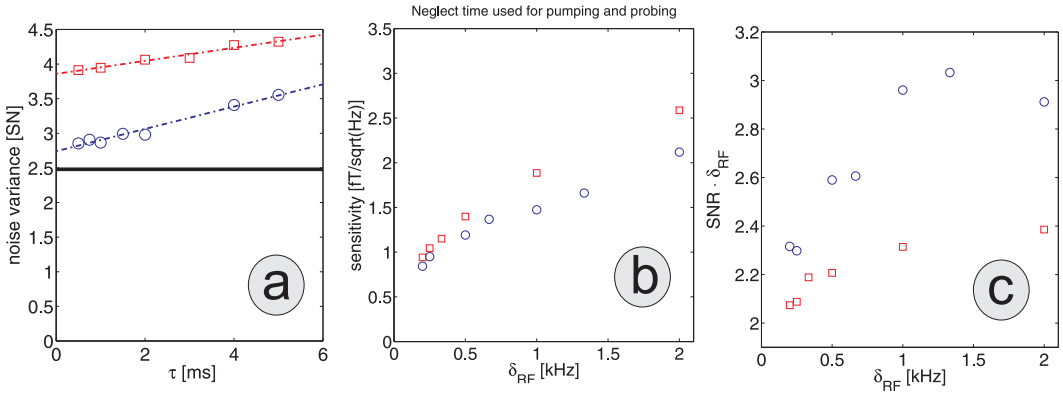

Figure 5.7: Entanglement-assisted magnetometry results. Circles and squares represent data with and without entanglement, respectively. (a) Magnetometer read out noise in units of shot noise of light. Dashed lines are linear fit. The solid line at 2.5 is the limit for the PN-limited measurement of the magnetic field given by Eq. (5.24). (b) Sensitivity $\mathcal{S}_\tau = B_{\mathrm{RF}}\sqrt{\tau}/SNR$ of the magnetic field measurement. (c) Signal to noise ratio SNR times the RF bandwidth δ_{RF} for the magnetometer. Since SNR depends linearly on the applied magnetic field amplitude B_{RF}, SNR has been normalized to the value $B_{\mathrm{RF}} = 138$ fT.

which is very similar to Eq. (5.6). Using the procedure described in appendix C, we measured the value of $\kappa^2 = 3.1$ for the specific experimental settings used for obtaining the results plotted in Fig. 5.7. Using this κ^2 and the estimated detection efficiency $\eta_{\mathrm{det}} \approx 0.8$, we find that the PN-limited measurement has $[\mathrm{Var}\,(S_{2c}^{\mathrm{out}}) + \mathrm{Var}\,(S_{2s}^{\mathrm{out}})]\,/2 \approx 0.8 \cdot 3.1 \cdot (\Phi/2) \approx 2.5 \cdot (\Phi/2)$. The data without entanglement has $[\mathrm{Var}\,(S_{2c}^{\mathrm{out}}) + \mathrm{Var}\,(S_{2s}^{\mathrm{out}})]\,/2 \approx 3.9 \cdot (\Phi/2)$ (for short RF durations). In terms of the standard deviation, the measurement has $\sqrt{3.9/2.5} \approx 1.25$ times higher standard deviation than the PN-limited measurement. This is slightly higher than the 10% above the PN-limited measurement stated in Sec. 5.6.1. The difference could be due to the lower optical depth [11] used in the entanglement-assisted magnetometry since for low optical depths the reduction of the light noise is smaller than for high optical depths [12].

It is also possible to calculate the atomic noise in projection noise units from the measured output variances and the κ^2 calibration using the full swap and squeezing interaction theory which includes bad decoherence. This is done using Eq. (2.85) for the reconstruction of the atomic noise. For short RF durations we find the atomic noise $\Sigma_{\mathrm{EPR}} = 1.10(8)$.

[11] The optical depth is proportional to the Faraday angle.
[12] This is because ϵ^2 decreases with increasing optical depth as seen in Fig. 3.9.

Measured conditional variances

We now turn to the data with entanglement plotted as blue circles in Fig. 5.7a. As discussed, the two atomic ensembles are entangled using a 1st probe pulse prior to the RF magnetic pulse. The magnetic field B_{RF} is afterwards measured with the 2nd probe pulse. The entanglement between the ensembles is visible in the conditional variances $\left[\mathrm{Var}\left(S_{2c}^{\mathrm{cond}}\right)+\mathrm{Var}\left(S_{2s}^{\mathrm{cond}}\right)\right]/2$ which are plotted with blue circles in Fig. 5.7a.

In Fig. 5.7a we see that the conditional variances are significantly lower than the variances obtained without entanglement. The difference is largest for short RF durations where the conditional variance is 25-30% lower than the variance obtained without entanglement. This is exactly the strength of the entanglement-assisted magnetometer. The noise on the measured output light is reduced by entangling the two atomic ensembles.

For RF magnetic pulse durations $\tau \leq 2$ ms, the measured conditional variances are $\left[\mathrm{Var}\left(S_{2c}^{\mathrm{cond}}\right)+\mathrm{Var}\left(S_{2s}^{\mathrm{cond}}\right)\right]/2 \approx 2.9 \cdot (\Phi/2)$. In terms of the standard deviation, the entanglement-assisted measurement has $\sqrt{2.9/2.5} \approx 1.08$ higher standard deviation than the PN-limited measurement. This is even closer to the PN-limited measurement than when no entanglement was utilized (which had the standard deviation 25% higher than the PN-limited measurement). We conclude that the entanglement-assisted measurement of B_{RF} is very close to being PN-limited. It should be possible to achieve the better than PN-limited measurement of B_{RF} by improving the detection efficiency and increasing the optical depth. Since the data was taken at room-temperature, the optical depth can easily be increased by a factor 2 or 3 by increasing the temperature of the cells.

We can also find the conditional atomic noise in PN-units $\Sigma_{\mathrm{EPR}}^{\mathrm{cond}}$. This quantity is found from the measured conditional variance and the κ^2 calibration. Again, we use the full swap and squeezing interaction theory including bad decoherence when estimating the (conditional) atomic noise in PN-units. For short RF pulses ($\tau \leq 1$ ms) we obtain the atomic noise reduction of approximately 30% below the PN-level. For longer RF pulses the entanglement degrades due to atomic decoherence.

With increasing RF pulse duration, the measured output light noise increases as seen in Fig. 5.7a. This is true both for the case with and without entanglement. To illustrate this, we make linear fits to the data (squares and circles). The fits are shown in Fig. 5.7a as dash-dotted lines. From the slopes of the linear fits, it is seen that the conditional variance decays faster than the variance obtained without entanglement.

From the measurements presented in Fig. 5.7a, it is clear that the atomic decay is not towards the vacuum state. The long term decay in the dark (during the

RF pulse) is expected to be towards the thermal state [13]. The output variance when measuring on the thermal state is $1 + \tilde{\kappa}^2 \cdot \frac{15}{8}$ in SN units (see the thesis [33]), which for our setting of the κ^2 parameter is around 7.

SNR

In Fig. 5.7a we plotted the variance and not the standard deviation on the measurement. The standard deviation equals the squareroot of the variance. In magnetometry an important figure of merit is the signal to noise ratio SNR where the noise is here meant as the standard deviation. With entanglement the noise is reduced compared to the case without entanglement. The signal is in the two cases the same, if one neglects the small decay of the mean spin during the 1st probe pulse. The reduction of the noise using entanglement is therefore directly transferred into an improved SNR.

Fiugre 5.7c shows the signal to noise ratio times the bandwidth $SNR \cdot \delta_{\mathrm{RF}}$ as a function of the bandwidth. For large bandwidths the product $SNR \cdot \delta_{\mathrm{RF}}$ approximately reaches a constant value. Using entanglement this product is improved due to the lower noise of the entangled atomic state.

Sensitivity

From the measured SNR, the applied B_{RF} and the duration of the RF field τ, we calculate the sensitivity $\mathcal{S}_\tau = B_{\mathrm{RF}}\sqrt{\tau}/SNR$ for the case with and without entanglement. Note that we here neglect the time it takes for the pumping T_{pump} and probing T_{probe}. When neglecting T_{pump} and T_{probe}, the improvement in SNR due to entanglement is directly translated into an improvement of the sensitivity.

This sensitivity as a function of RF bandwidth is plotted in Fig. 5.7b for the cases with and without entanglement. As expected, the best sensitivity is reached for long RF pulses or equivalent small bandwidths. We also see that entanglement improves the magnetometer sensitivity in particular for large bandwidths. This is expected since the conditional variance decays faster than the variance obtained without entanglement, as discussed earlier in Sec. 5.4.

We can also calculate the sensitivity $\mathcal{S}_{\mathrm{tot}} = B_{\mathrm{RF}}\sqrt{T_{\mathrm{tot}}}/SNR$ where both the pumping and probing time is included. For the case without entanglement, we have $T_{\mathrm{pump}} = 4$ ms and $T_{\mathrm{probe}} = 2$ ms leading to the $T_{\mathrm{tot}} = \tau + 6$ ms, and for the case with entanglement, we have $T_{\mathrm{pump}} = 4$ ms, $T_{\mathrm{probe,1st}} = 2$ ms and $T_{\mathrm{probe,2nd}} = 3$ ms leading to $T_{\mathrm{tot}} = \tau + 9$ ms. When including these times, the sensitivity is worse than compared to what is plotted in Fig. 5.7b due to non-zero pumping and probing times.

We use an extra probe pulse for generating entanglement as seen in the pulse sequences Fig. 5.4b/c. In our case, this means that the total cycle time is 3 ms

[13] The state of a completely unpolarized atomic ensemble is denoted the thermal state.

longer for the data with entanglement compared to the data without entanglement. When taking this extra time into account, we find that the sensitivity for the data with entanglement is approximately the same as for the data without entanglement. Again I point out, that this is due to non-zero pumping and probing times. In the experiments, we could have shortened both of these times. This could have been done by increasing the power of the pump and the probe to compensate for the shorter durations. Also note that for higher optical depths the swap rate γ_{sw} increases such that one needs shorter probe pulses to obtain a fixed interaction strength κ^2.

5.8 Conclusions

In conclusion, we have demonstrated an atomic RF magnetometer mainly limited by the projection noise of the atoms. This can be achieved due to the backaction evading measurement and the reduction of the shot noise from the probing light. Our magnetometer has a high sensitivity to the magnetic field with a best measured sensitivity $\mathcal{S}_{\mathrm{tot}} = 3.5(8) \cdot 10^{-16}\ \mathrm{T}/\sqrt{\mathrm{Hz}}$. This sensitivity is comparable with the sensitivity obtained with the state-of-the-art (SERF) atomic magnetometer. Since the PN-limited sensitivity increases with the number of atoms, it is possible to further increase the sensitivity by using larger cells or heating the cells further. It is also possible to obtain higher sensitivity to long RF pulses by improving the atomic coherence time (in the dark). This could be done by improving the bias magnetic field homogeneity and by improving the anti-relaxation coating of the cells [40]. In this way, it should be possible to reach the sensitivity of the best superconducting SQUID magnetometers [72].

To the best of our knowledge, we have demonstrated entanglement-assisted metrology with the highest to-date numbers of atoms. The degree of entanglement can in principle be $\Sigma_{\mathrm{EPR}} = \zeta^{-2} \approx 1/6.4$ for our detuning. This corresponds to 8 dB of spin-squeezing. This expected degree of entanglement can be even larger for a further detuned probe. Due to different decoherence effects including spontaneuos emssion, the entanglement generated in our experiment is lower than this value 1/6.4. With higher optical depth (i.e. more atoms), we expect that the experimental obtainable degree of entanglement can be improved.

We demonstrated that using entanglement it is possible to get very close to the PN-limited measurement of the magnetic field. It should be possible to surpass the limit with only slightly higher optical depth. We demonstrated that using entanglement we can improve the signal to noise ratio of the magnetometer. However, for short RF durations non-zero pumping and probing times limit the magnetometer sensitivity. This is true both for the measurement with and without entanglement. Our magnetometer can therefore be improved by shortening

these times.

The entanglement-assisted magnetometer is more affected by the non-zero probe time due to the additional probe pulse used for generating entanglement. Since entanglement improves the magnetometer mainly for short RF durations or equivalent large RF bandwidths, we need to reduce the probing time in order to fully take advantage of the entanglement-assisted magnetometry.

Chapter 6

Quantum memory for entangled continuous-variables states

6.1 Introduction

In this chapter we describe the "quantum memory for entangled continuous-variables states" experiment published in Nature Physics [1]. The main result is the demonstration of the storage of a new class of states: displaced two-mode squeezed states. We store an extensive alphabet of states which are squeezed by 6 dB and where the squeezing direction and displacement of the states are varied. The performance of the memory is quantified in terms of the fidelity. For a range of input states, we obtain the experimental memory fidelity of 0.52 ± 0.02. We show that this fidelity exceeds a calculated classical benchmark proving that our memory is true quantum memory. This means that our memory can outperform any classical memory, and that the memory is capable of preserving entanglement.

A quantum memory for light is an important ingredient in a future quantum information network [11]. There have been many experiments with storage of single photons (see the reviews [73, 11, 19]) and few experiments towards a quantum memory for non-classical continuous variables (CV) states. In the field of CV quantum information processing, a quantum memory for non-classical CV states has many applications in for instance quantum communications [74], CV quantum repeaters [75, 76], entanglement-enhanced quantum metrology [1, 15] and CV cluster state quantum computation [77].

A quantum memory should be able to store a wide range of inputs and should be able to preserve quantum information better than any classical memory. An earlier experiment using the same setup demonstrated storage of displaced coherent states [17]. Storage of non-classical CV squeezed vacuum states based on electromagnetically induced transparency (EIT) has been performed [22, 78] but with a fidelity below the classical benchmark [79].

We store two entangled sideband modes of light described by the creation operators $a_+^\dagger$ and $a_-^\dagger$ with the frequencies $\omega_\pm = \omega_0 \pm \Omega_L$ where ω_0 is an optical frequency (corresponding to the wavelength 852 nm for the cesium $D2$ transition) and $\Omega_L = 2\pi \cdot 322$ kHz. The two modes are stored in our atomic system consisting of two separate atomic ensembles. With our kind of memory protocol, the upper sideband mode is stored in the first cell and the lower sideband mode is stored in the second cell (see Sec. 6.2.3). It is convinient to also consider the cosine and sine modes which are defined as the sums and differences of the upper and lower sideband modes (see Eq. łeq:relationlightmodes). As discussed in Sec. 2.3.2, entanglement between the upper and lower sidebands is equivalent to two-mode squeezing of the cosine and sine modes. For the experimental value of 6dB of squeezing in the cosine and sine modes, the two-mode squeezed vacuum can be written in the photon number representation of the upper and lower sideband modes as (see for instance the textbook [80])

$$|\Psi\rangle = 0.8\,|0\rangle_+\,|0\rangle_- + 0.48\,|1\rangle_+\,|1\rangle_- + 0.29\,|2\rangle_+\,|2\rangle_- + 0.17\,|3\rangle_+\,|3\rangle_- + ... \quad (6.1)$$

6.2 Memory protocol

We now describe the memory protocol used in the experiment. The protocol is an improved version of the protocol used in the earlier experiment which demonstrated the storage of displaced coherent states [17]. In order to emphasize the transfer of quantum states from light to atoms, we use the notation X_L, P_L and X_A, P_A for the canonical operators of light and atoms, respectively. The interaction between atoms and light given by the input-output Eq. (2.18) is described in terms of the cosine and sine modes. The index c, s on the atomic and light operators is in most cases omitted, since the input-output equations are similar for the cosine and sine modes. However, it should be kept in mind that in the experiment the cosine and sine modes are stored simultaneously.

The light state to be stored has the canonical variables X_L^{pure} and P_L^{pure}. This state is assumed to be "pure" meaning that

$$\text{Var}\,(X_L^{\text{pure}}) \cdot \text{Var}\,(P_L^{\text{pure}}) = \frac{1}{2s} \cdot \frac{s}{2} = \frac{1}{4}, \quad (6.2)$$

where s is the squeezing factor. This state travels trough transmission and entrance losses given by η_{tr} and η_{ent} before reaching the atomic system (see Fig. 6.2 and Sec. 6.3.4). The state, which is input to the memory, is described by the operators X_L^{in} and P_L^{in}. It is important to note the difference between the states denoted "pure" and "input". The relation between the pure states and the input states is given by

$$\begin{pmatrix} X_L^{\text{in}} \\ P_L^{\text{in}} \end{pmatrix} = \sqrt{\eta_{\text{ent}}\eta_{\text{tr}}} \begin{pmatrix} X_L^{\text{pure}} \\ P_L^{\text{pure}} \end{pmatrix} + \sqrt{1-\eta_{\text{ent}}\eta_{\text{tr}}} \begin{pmatrix} X_L^{\text{vac}} \\ P_L^{\text{vac}} \end{pmatrix}. \quad (6.3)$$

6.2.1 Storage of the input light states

We start by discussing how the *input* light states are stored in the final atomic states. For simplicity we neglect atomic decoherence when discussing the memory protocol. The input-output equations for the light-atom interaction are in this case given by Eq. (2.18). The protocol consists of (1) an interaction between the light and the atoms, (2) a measurement of the X_L quadrature of the output light and (3) a feedback of the measurement to the atomic P_A operator with gain g. One should note that the measured light operator differs from the output light operator due to a less-than unity detection efficiency $\eta_{\rm det}$. We have

$$X_L^{\rm meas} = \sqrt{\eta_{\rm det}} X_L^{\rm out} + \sqrt{1-\eta_{\rm det}} X_L^{\rm vac}, \tag{6.4}$$

where $X_L^{\rm vac}$ is a vacuum operator with zero mean and variance 1/2. After the feedback the final atomic variables are

$$\begin{aligned} X_A^{\rm fin} &= tX_A^{\rm in} + \kappa P_L^{\rm in} \\ P_A^{\rm fin} &= tP_A^{\rm in} - \frac{\kappa}{Z^2} X_L^{\rm in} - gX_L^{\rm meas} \\ &= tP_A^{\rm in} - \frac{\kappa}{Z^2} X_L^{\rm in} - g\left[\sqrt{\eta_{\rm det}}\left(tX_L^{\rm in} + \kappa P_A^{\rm in}\right) + \sqrt{1-\eta_{\rm det}} X_L^{\rm vac}\right] \\ &= \left(t - g\sqrt{\eta_{\rm det}}\kappa\right) P_A^{\rm in} - \left(\frac{\kappa}{Z^2} + g\sqrt{\eta_{\rm det}} t\right) X_L^{\rm in} - g\sqrt{1-\eta_{\rm det}} X_L^{\rm vac}, \end{aligned} \tag{6.5}$$

where $t = \sqrt{1-\kappa^2/Z^2}$. In the experiment, we made the specific choice of $\kappa = 1$ and $g\sqrt{\eta_{\rm det}} = t$ (see Sec. 6.3.1). With this choice, we find

$$\boxed{\begin{aligned} X_A^{\rm fin} &= \sqrt{1-1/Z^2} X_A^{\rm in} + P_L^{\rm in} \\ P_A^{\rm fin} &= -X_L^{\rm in} - \sqrt{1-1/Z^2}\sqrt{\frac{1-\eta_{\rm det}}{\eta_{\rm det}}} X_L^{\rm vac}. \end{aligned}} \tag{6.6}$$

For Gaussian states, a perfect state transfer means that both the mean values and the variances of the final operators equal the mean values and the variances of the initial operators. Using Eq. (6.6), we find the relation for the transfer of mean values

$$\left\langle X_A^{\rm fin} \right\rangle = \left\langle P_L^{\rm in} \right\rangle \quad \text{and} \quad \left\langle P_A^{\rm fin} \right\rangle = -\left\langle X_L^{\rm in} \right\rangle, \tag{6.7}$$

since both $\left\langle X_A^{\rm in} \right\rangle = 0$ and $\left\langle X_L^{\rm vac} \right\rangle = 0$. We see that the mean values of an *input* state are transferred perfectly to the final state (up to a rotation in X-P phase space). For the transfer of variances, we find

$$\begin{aligned} {\rm Var}\left(X_A^{\rm fin}\right) &= \left(1-1/Z^2\right){\rm Var}\left(X_A^{\rm in}\right) + {\rm Var}\left(P_L^{\rm in}\right) \\ {\rm Var}\left(P_A^{\rm fin}\right) &= {\rm Var}\left(X_L^{\rm in}\right) + \left(1-1/Z^2\right)\left(\frac{1-\eta_{\rm det}}{\eta_{\rm det}}\right){\rm Var}\left(X_L^{\rm vac}\right). \end{aligned} \tag{6.8}$$

Due to a detection efficiency $\eta_{\rm det} < 1$, a part of the measured vacuum noise $\mathrm{Var}\left(X_L^{\rm vac}\right)$ is transferred to the final atomic operator $P_A^{\rm fin}$. Also note, that the initial atomic noise $\mathrm{Var}\left(X_A^{\rm in}\right)$ is reduced by the factor $1-1/Z^2$. For our usual detuning $\Delta = -850$ MHz, we have $Z^2 \approx 6.4$ and find the reduction $1-1/Z^2 = 0.84$. In the original protocol [17], there was no reduction of the input atomic noise. The protocol described here will therefore lead to a better storage compared to the original protocol.

In the original protocol, the atoms are initially prepared in a CSS such the the input noise is $\mathrm{Var}\left(X_A^{\rm in}\right) = 1/2$. In our improved protocol, we choose to spin-squeeze the $X_A^{\rm in}$ operator prior to the storage. This results in less initial atomic noise $\mathrm{Var}\left(X_A^{\rm in}\right) < 1/2$. The combination of spin-squeezing and the reduction of the initial atomic noise by the factor $1-1/Z^2$ are important improvements of the original protocol.

For perfect atomic squeezing and unity detection efficiency, the memory protocol described here in principle results in a perfect transfer of the initial operators to the final operators. This does not rely on the inputs being Gaussian states, and the memory would also work for non-Gaussian states such as single photon states (Fock states) or Schrödinger cat states.

We can evaluate the performance of the memory for our experimental parameters. In terms of the variances, we find

$$\begin{aligned} \mathrm{Var}\left(X_A^{\rm fin}\right) &= \mathrm{Var}\left(P_L^{\rm in}\right) + 0.36 \\ \mathrm{Var}\left(P_A^{\rm fin}\right) &= \mathrm{Var}\left(X_L^{\rm in}\right) + 0.11, \end{aligned} \tag{6.9}$$

where we inserted the experimental values $\eta_{\rm det} = 0.79$, $Z^2 \approx 6.4$ and $\mathrm{Var}\left(X_A^{\rm in}\right) = 0.43$ into Eq. (6.8). We see that our memory is expected to add only a small amount of noise (less than one vacuum unit in total for both atomic quadratures) if we consider the storage of the input states.

6.2.2 Storage of the pure light states

In the previous section we described how an input state is transferred to the final atomic state. We will now instead discuss the storage of the pure states. The pure states and the input states are related by Eq. (6.3). Since the mean values of the *input* states are transferred with unity gain, the mean values of the *pure* states will be transferred with a gain $G = \sqrt{\eta_{\rm tr}\eta_{\rm ent}} = 0.85$ lower than one due to transmission and entrance losses.

The storage of the pure states can be described by the following simple equation

$$\begin{aligned} X_A^{\rm fin} &= G P_L^{\rm pure} + O_X \\ P_A^{\rm fin} &= -G X_L^{\rm pure} + O_P. \end{aligned} \tag{6.10}$$

	Expected		Measured		Difference	
ϕ	$\mathrm{Var}\left(P_A^{\mathrm{fin}}\right)$	$\mathrm{Var}\left(X_A^{\mathrm{fin}}\right)$	$\mathrm{Var}\left(P_A^{\mathrm{fin}}\right)$	$\mathrm{Var}\left(X_A^{\mathrm{fin}}\right)$	$\mathrm{Var}\left(S_P\right)$	$\mathrm{Var}\left(S_X\right)$
0	0.34	1.94	0.52	1.99	0.18	0.05
90	1.69	0.59	1.95	0.73	0.26	0.14

Table 6.1: The Table shows the expected final atomic state variances $\mathrm{Var}\left(P_A^{\mathrm{fin}}\right)$ and $\mathrm{Var}\left(X_A^{\mathrm{fin}}\right)$, the measured atomic variances and the extra noise $\mathrm{Var}\left(S_P\right)$ and $\mathrm{Var}\left(S_X\right)$ which is not accounted for in the theoretical model. The measured atomic variances are also found in the Table 6.2.

The two noise operators O_x and O_P (with zero mean) describe the noise added during the storage process. Since the mean values and variances of both the pure and final state operators are measured, the gain G and the variances of the noise operators $\mathrm{Var}\left(O_X\right)$ and $\mathrm{Var}\left(O_P\right)$ can easily be found from the experimental data.

By inserting Eq. (6.3) into Eq. (6.6), we find the operators O_X and O_P

$$\begin{aligned} O_X &= \sqrt{1-\frac{1}{Z^2}}X_A + \sqrt{1-G^2}P_L^{\mathrm{vac}} + S_X \\ O_P &= -\sqrt{1-G^2}X_L^{\mathrm{vac}} - \sqrt{1-\frac{1}{Z^2}}\sqrt{\frac{1-\eta_{\mathrm{det}}}{\eta_{\mathrm{det}}}}\widetilde{X}_L^{\mathrm{vac}} + S_P. \end{aligned} \tag{6.11}$$

We here choose to introduce two new noise operators S_X and S_P. These noise operators describe noise processes which are not included in the theoretical model, but are present in the experiment.

The variance of the noise operators can be estimated, and we find $\mathrm{Var}\left(O_X\right) = 0.50$ and $\mathrm{Var}\left(O_P\right) = 0.25$ for the theoretical case $\mathrm{Var}\left(S_x\right) = \mathrm{Var}\left(S_P\right) = 0$. Using these values, we can find the expected final atomic state variances for the case where the pure states are squeezed by 6 dB in either the X_L (with squeezing phase $\phi = 0$ deg) or the P_L-direction ($\phi = 90$ deg). The results are shown in Table 6.1. These expected values will later be compared with the experimental results.

6.2.3 Storage of the upper and lower sidebands

So far we have discussed the memory protocol in terms of the cosine and sine canonical operators for atoms and light. We will now describe the protocol in terms of the upper and lower sideband modes and the local (cell 1 and cell 2) atomic operators.

The local atomic operators and the non-local atomic operators are related by

$$\begin{aligned} X_{A1} &= \frac{1}{\sqrt{2}}\left(X_{Ac} + P_{As}\right), & P_{A1} &= \frac{1}{\sqrt{2}}\left(P_{Ac} - X_{As}\right), \\ X_{A2} &= \frac{1}{\sqrt{2}}\left(X_{Ac} - P_{As}\right), & P_{A2} &= \frac{1}{\sqrt{2}}\left(P_{Ac} + X_{As}\right), \end{aligned} \tag{6.12}$$

where the subscripts 1 and 2 refers to the first and second atomic ensemble, respectively. We can also find the relations between the upper and lower sideband modes of light and the cosine and sine modes

$$\begin{aligned} X_{Lc} =& \frac{1}{\sqrt{2}} \left(X_+ + X_- \right), & P_{Lc} =& \frac{1}{\sqrt{2}} \left(P_+ + P_- \right), \\ X_{Ls} =& \frac{1}{\sqrt{2}} \left(P_- - P_+ \right), & P_{Ls} =& \frac{1}{\sqrt{2}} \left(X_+ - X_- \right). \end{aligned} \tag{6.13}$$

We write the input-output equations for the quantum memory as

$$\begin{aligned} X_{Ac}^{\text{fin}} =& G P_{Lc}^{\text{pure}} + O_X, & P_{Ac}^{\text{fin}} =& - G X_{Lc}^{\text{pure}} + O_P, \\ X_{As}^{\text{fin}} =& G P_{Ls}^{\text{pure}} + O_X, & P_{As}^{\text{fin}} =& - G X_{Ls}^{\text{pure}} + O_P, \end{aligned} \tag{6.14}$$

in the same way as was done in Eq. (6.10) but where we here write the cosine and sine components explicitly. Equation (6.14) can be rewritten by inserting Eqs. (6.12) and (6.13), and we find

$$\begin{aligned} X_{A1}^{\text{fin}} =& G P_{+}^{\text{pure}} + \frac{O_X + O_P}{\sqrt{2}}, & P_{A1}^{\text{fin}} =& - G X_{+}^{\text{pure}} + \frac{O_P - O_X}{\sqrt{2}}, \\ X_{A2}^{\text{fin}} =& G P_{-}^{\text{pure}} + \frac{O_X - O_P}{\sqrt{2}}, & P_{A2}^{\text{fin}} =& - G X_{-}^{\text{pure}} + \frac{O_P + O_X}{\sqrt{2}}. \end{aligned} \tag{6.15}$$

We see that the upper sideband is stored in the first atomic ensemble and the lower sideband is stored in the second ensemble. We also see that the amount of noise added to each local atomic canonical variable equals $\left\{ \text{Var}\left(O_X \right) + \text{Var}\left(O_P \right) \right\} / 2$. These calculations will be used later in Sec. 6.6.

6.3 Methods

6.3.1 Calibration of the gains

The method for calibrating the gains of the memory is now described. Using Eq. (6.5), an equation describing the mean value transfer can be found

$$\begin{aligned} \left\langle X_A^{\text{fin}} \right\rangle &= \kappa \left\langle P_L^{\text{in}} \right\rangle \\ \left\langle P_A^{\text{fin}} \right\rangle &= - \left(\frac{\kappa}{Z^2} + g \sqrt{\eta_{\text{det}}} t \right) \left\langle X_L^{\text{in}} \right\rangle. \end{aligned} \tag{6.16}$$

In the above it is assumed that the intial atomic operators and the vacuum operator have zero mean $\left\langle X_A^{\text{in}} \right\rangle = \left\langle P_A^{\text{in}} \right\rangle = \left\langle X_L^{\text{vac}} \right\rangle = 0$. The two prefactors κ and $- \left(\frac{\kappa}{Z^2} + g \sqrt{\eta_{\text{det}}} t \right)$ are denoted the gains of the memory. Prior to the storage, we calibrated the gains such that $\kappa = 1$ and $\frac{\kappa}{Z^2} + g \sqrt{\eta_{\text{det}}} t = 1$. This was done in the following way similar to the κ-calibration method described in Sec. 3.6.

Procedure

Calibration of the input modulation: Using electro-optical modulators, mean values $\langle X_L^{\text{in}} \rangle$ and $\langle P_L^{\text{in}} \rangle$ can be created in the input light. These input mean values can be calibrated beforehand.
Calibration of κ^2: A 1st probe pulse with a non-zero mean value $\left\langle P_L^{\text{in,1st}} \right\rangle \neq 0$ is sent through the atomic ensembles. This mean value is transferred to the atomic system through the light-atom interaction as seen in Eq. (6.16). Then, a magnetic π-pulse is utilized to rotate X_A^{fin} into P_A^{fin}. Finally, a 2nd probe pulse is used to measure P_A^{fin}. The mean value of the 2nd pulse measurement equal

$$\left\langle X_L^{\text{out,2nd}} \right\rangle = \kappa \left\langle X_A^{\text{fin}} \right\rangle = \kappa^2 \left\langle P_L^{\text{in,1st}} \right\rangle . \tag{6.17}$$

The κ^2 parameter can be found from the measured ratio $\left\langle X_L^{\text{out,2nd}} \right\rangle / \left\langle P_L^{\text{in,1st}} \right\rangle$. κ^2 is roughly proportional to the light power, and the light power is adjusted such that $\kappa^2 = 1$.
Calibration of the feedback gain g: A 1st probe pulse with a non-zero mean value $\left\langle X_L^{\text{in,1st}} \right\rangle \neq 0$ is sent through the atoms. Then, the measurement results are fed back to the atomic system using the RF coils. Finally, a 2nd probe pulse is used to measure P_A^{fin}. The mean of the 2nd pulse measurement result equal

$$\left\langle X_L^{\text{out,2nd}} \right\rangle = \kappa \left\langle P_A^{\text{fin}} \right\rangle = -\kappa \left(\frac{\kappa}{Z^2} + g\sqrt{\eta_{\text{det}}} t \right) \left\langle X_L^{\text{in,1st}} \right\rangle . \tag{6.18}$$

From the measured ratio $\left\langle X_L^{\text{out,2nd}} \right\rangle / \left\langle X_L^{\text{in,1st}} \right\rangle$, we find the factor $\kappa \left(\frac{\kappa}{Z^2} + g\sqrt{\eta_{\text{det}}} t \right)$. The electronic gain g is adjusted such that $\left(\frac{\kappa}{Z^2} + g\sqrt{\eta_{\text{det}}} t \right) = 1$. For $\kappa^2 = 1$, this condition is equivalent to $g\sqrt{\eta_{\text{det}}} = t$.

6.3.2 Experimental setup

The experimental setup together with the pulse sequence are shown in Fig. 6.1. The displaced two-mode squeezed light together with the local oscillator (LO) light are produced in the "Preparation" part of the setup. The light from the Ti:Sa laser is split into several parts. One part is used as the LO which is pulse-shaped using an elector-optical modulator (EOM) followed by a polarizing beamsplitter (PBS). In each experimental cycle, three local oscillator pulses are shaped: the "QND spin-squeezing pulse", the "input pulse $|\Psi\rangle$" and the "probe" (see pulse sequence).

A second part of the light is used as a "seed". This light is amplitude (AM) and phase modulated (ϕM) using EOM's and a PBS. Amplitude and phase modulation at the specific frequency of $\Omega_L = 2\pi \cdot 322$ kHz creates displaced coherent light states in the upper and lower sidebands with frequencies $\omega_\pm = \omega_0 \pm \Omega_L$. Equivalently, coherent states are created in the cosine and sine modes. The last

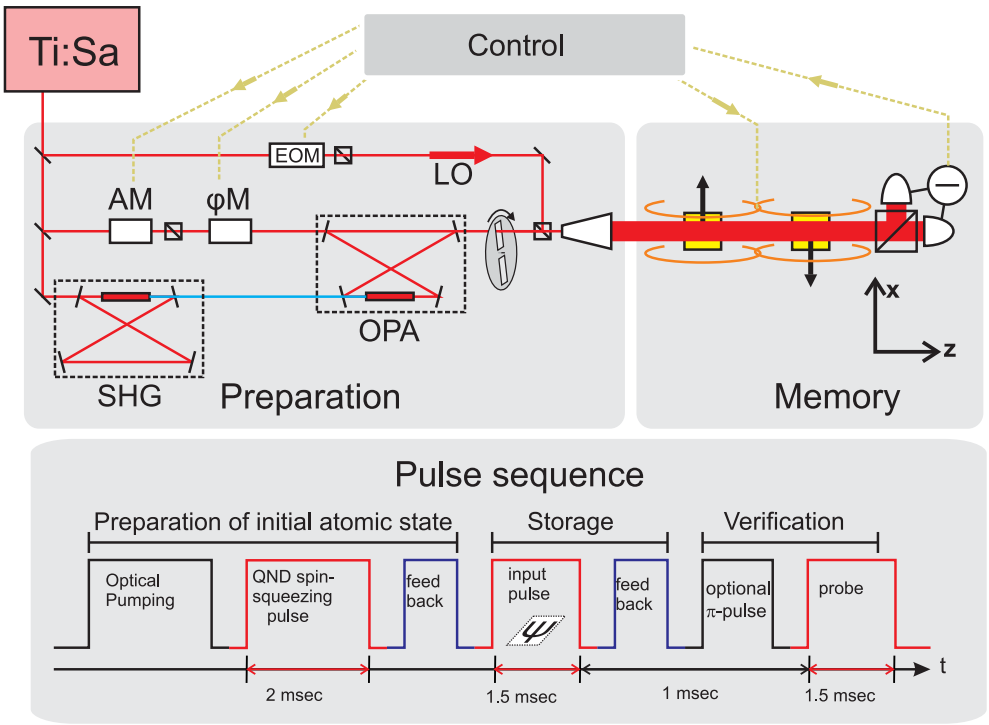

Figure 6.1: **Setup and pulse sequence.** At the sender station, two-mode squeezed light is generated by the Optical Parametric Amplifier (OPA). A variable displacement of the state is achieved by injecting a coherent input into OPA modulated by electro-optical modulators (EOM's). The output of the OPA is shaped by a chopper, and combined on a polarizing beamsplitter with the local oscillator (LO) beam, such that the squeezed light is only on during the "input pulse". A beamshaper and a telescope create an expanded flattop intensity profile. The light is then send to the receiver (memory) consisting of two oppositely oriented ensembles of spin-polarized cesium vapour in paraffin coated cells and a homodyne detector. The detector signal is processed electronically and used as feedback onto the spins obtained via RF magnetic field pulses. Pulse sequence for the initiation of the memory, storage and verification. Each RF "feedback" pulse is 0.15 msec long and centered between two consecutive light pulses.

part of the light is used as input to a nonlinear crystal located inside a cavity (the second harmonic generation SHG). Here, the infra-red light at frequency ω_0 is frequency converted into blue light with frequency $2\omega_0$. The blue light is then used to input the optical parametric amplifier (OPA) where the blue photons are downconverted back into pairs of infra-red photons with frequencies around ω_0. With a blocked seed beam, the output of the OPA will be two-mode squeezed vacuum as described in Eq. (6.1) . If we add the seed beam into the OPO, the output of the OPO will instead be a displaced two-mode squeezed state. The output of the OPO is then combined at a PBS with the LO. A chopper (rotating disk with a hole) makes sure that the squeezed light is on only during the "input pulse".

6.3.3 Pulse sequence and the initial atomic states

The initial atomic state

The pulse sequence for the experiment is shown in Fig. 6.1. In the "preparation of the initial atomic state" part, the atoms are first initialized in a state close to the coherent spin state (CSS) by the use of resonant pumping and repumping light for the duration of 5 ms. The experiments are done at room-temperature and the Faraday angle proportional to the number of atoms was measured to be $\theta_F \approx 7$ deg. The atoms are probed with a $T = 1.5$ ms probe pulse with power $P = 3$ V. The initial atomic state is characterized to have $\mathrm{Var}\,(X_A) = \mathrm{Var}\,(P_A) = 0.55(4)$ in terms of the canonical operators. This state is 10% more noisy than the CSS which has the variances of 1/2. This is not optimal, but since it is only 10% extra noise it will only slightly reduce the memory performance.

The state characterization is done using the swap and squeezing input-output Eq. (2.18). By sending light through the atoms and measuring the X_L^{out} canonical operator, we can reconstruct the atomic variance using the equation

$$\mathrm{Var}\left(X_L^{\mathrm{out}}\right) = t^2 \mathrm{Var}\left(X_L^{\mathrm{in}}\right) + \kappa^2 \mathrm{Var}\left(P_A^{\mathrm{in}}\right). \tag{6.19}$$

If one applies a magnetic π-pulse prior to the probe pulse, it is possible to measure X_A^{in} instead of P_A^{in}. The π-pulse rotates X_A into P_A by the use of a DC magnetic field applied for a certain duration. This way, $\mathrm{Var}\left(X_A^{\mathrm{in}}\right)$ can similarly be determined. The detection efficiency is also included in reconstruction of the atomic variances using Eq. (6.4).

The coupling parameters t^2 and κ^2 are measured using the mean value transfer method. Remember that κ^2 equals one in the experiment. The measured $t^2 = 0.80(4)$ agrees with the expected $1 - 1/Z^2 \approx 0.84$ (using $Z^2 \approx 6.4$) within the experimental uncertainties. Notice, that we here do not use the full swap and squeezing theory, which includes bad decoherence parametrized by the ϵ^2 param-

eter, since this was how the results for the atomic variances were calculated in the Nature Physics Letter.

Full swap and squeezing theory for data analysis

We now discuss how atomic decoherence can be included in the data analysis, and how this changes the calculated atomic variances $\mathrm{Var}(X_A)$ and $\mathrm{Var}(P_A)$. When using the full swap and squeezing theory, Eq. (2.82) is used for analyzing the noise instead of Eq. (6.19). The only difference between the two equations is that t^2 should be replaced with t_m^2 parameter and κ^2 should be replaced with κ_m^2.

Since we use the mean value method for measuring $\kappa^2 = 1$, the same value will also be our estimate for the $\kappa_m^2 = 1$. On the other hand, t_m^2 is calculated from Eq. (2.83) and is not a measured parameter (it is found from the probe duration T, the T_2-time, ϵ^2 and Z^2). We can calculate t_m^2 using the measured parameters, and we find $t_m^2 = 0.87(1)$. To calculate this value, we used the values $T = 1.5$ ms, $Z^2 \approx 6.4$ and $\epsilon^2 = 0.35(5)$. ϵ^2 is found from the equation $\epsilon^2 = 1 - \kappa_m^2 / \{Z^2 (1 - \exp(-2T/T_2))\}$ using the measured $T_2 = 11(1)$ ms.

When reconstructing the atomic variances, the difference between the results using the two models will be approximately $(t_m^2 - t^2) \cdot \frac{1}{2} \approx 0.07 \cdot \frac{1}{2}$ where the $\frac{1}{2}$ is the variance of the vacuum. This means that if we would use the full swap and squeezing interaction theory, our atomic variances would be less noisy by the amount $0.07 \cdot \frac{1}{2}$. In all of this chapter, we will keep the numbers for the variances as stated in the Nature Physics Letter, but it should be kept in mind, that using the more advanced reconstruction procedure with $\epsilon^2 = 0.35$, we would get lower estimates for the atomic noise and thereby a better storage.

The spin-squeezed state

After the optical pumping stage, the atoms interact with the off-resonant "QND spin-squeezing pulse", the output light is measured and the results are fed back to the atoms by the "feedback" pulse. The feedback is applied with RF magnetic fields to the two ensembles. This creates a spin-squeezed collective atomic state with $\mathrm{Var}(X_A) = 0.43(3)$ and $\mathrm{Var}(P_A) = 1.07(5)$. The spin-squeezed state has the variances reduced by 14% compared to the CSS and 22% compared to the state after the optical pumping. The more squeezing the better, and one would improve the memory if one could increase the squeezing. The product of the variances is $\mathrm{Var}(X_A) \cdot \mathrm{Var}(P_A) = 0.46 > 1/4$, and the atomic state is therefore not a minimal uncertainty state.

Storage and verification

During the "storage" part, a displaced squeezed state $|\Psi\rangle$ is sent to the memory. The output light operators X_{Lc}^{out} and X_{Ls}^{out} are measured and the signals are fed

back to the atomic system using the RF coils. According to Eq. (6.6), the light state is transferred to the final atomic state.

Finally, during the "verification" stage, the final atomic state is characterized by the "probe pulse". Using a measurement of the X_L^{out} operator, we can probe either the X_A^{fin} or the P_A^{fin} operator (depending on if we apply the optional π-pulse). If we store the same state $|\Psi\rangle$ in the memory many times, we can build up the statictics (mean and variances) of the final atomic operators X_A^{fin} and P_A^{fin}.

6.3.4 Measured Losses

The total losses η_{tot} are divided into three parts as shown in Fig. 6.2. The total loss includes the transmission losses η_{tr} (including the OPA output efficiency 0.97), the entrance losses η_{ent} and the detection losses η_{det} such that $\eta_{\text{tot}}=\eta_{\text{tr}} \cdot \eta_{\text{ent}} \cdot \eta_{\text{det}}$. Remember that the η-paramters are intensity transmission coefficients.

The physical memory consist of two glass cells, which introduce quite some losses due to reflections at glass-air or air-glass interfaces. Each interface introduce around 4% losses [1]. Since our light-atom interaction model does not include losses between the cells, we assign one half of the losses through the cells to the entrance losses and the other half to the detection losses.

From the measurement of the quadratures of the squeezed light (with variances 0.29(1) and 1.34(6), we find the total losses $\eta_{\text{tot}} = 0.567(35)$. We measure the transmission through the cells of 0.817(20), the transmission through the optics after the cells of 0.889(10) and estimate the efficiency of the photodiodes to be 0.98(1). Assigning one half of the losses through the cells to the entrance losses and another half to the detection losses we find $\eta_{\text{ent}} = \sqrt{0.817} = 0.90(1)$, $\eta_{\text{det}} = \sqrt{0.817} \cdot 0.889 \cdot 0.98 = 0.79(2)$ and $\eta_{\text{tr}} = \eta_{\text{tot}} / (\eta_{\text{ent}}\eta_{\text{det}}) = 0.80(4)$.

6.4 Experimental results

Input states

A quantum memory should be able to store a range of states. In the experiment, we choose to store 18 different pure states. The states are characterized by their mean values $\{\langle X_L^{\text{pure}}\rangle ; \langle P_L^{\text{pure}}\rangle = 0, 3.8, 7.6; 0, 3.8, 7.6\}$ and variances. The states are squeezing by 6 dB in either the X_L or P_L-direction. The squeezing phase is defined to be $\phi = 0$ deg for squeezing along X_L-direction and $\phi = 90$ deg for squeezing along P_L-direction. We choose to divide the states into three alphabets shown in the inset in Fig. 6.2. The alphabets are parametrized by the parameter $d_{\max} = \max\{\langle X_L^{\text{pure}}\rangle, \langle P_L^{\text{pure}}\rangle\}$ where the maximum is taken over states in the alphabet. The first alphabet with $d_{\max} = 0$ contains two vacuum states with

[1] The cells have anti-reflection coated windows attached at the outside. This way, only *inside* glass-air or air-glass interfaces contribute to the losses from the cells.

Initial pure states $\|\Psi\rangle$			Final atomic states				overlap
$\langle X_L^{\text{pure}} \rangle$	$\langle P_L^{\text{pure}} \rangle$	ϕ	$\langle P_A^{\text{fin}} \rangle$	$\langle X_A^{\text{fin}} \rangle$	Var (P_A^{fin})	Var (X_A^{fin})	Θ
0.0	0.0	0	-0.06	0.25	0.52(2)	1.99(3)	0.62
0.0	3.8		-0.06	3.19			0.60
3.8	0.0		-3.47	-0.42			0.57
3.8	3.8		-3.39	2.89			0.49
0.0	0.0	90	-0.07	0.06	1.95(6)	0.73(1)	0.55
0.0	3.8		-0.06	3.14			0.42
3.8	0.0		-3.22	0.48			0.46
3.8	3.8		-3.21	3.59			0.50
0.0	7.6	0	-0.03	6.30	0.55(2)	2.01(4)	0.49
7.6	0.0		-6.83	-0.46			0.37
3.8	7.6		-3.20	6.07			0.35
7.6	3.8		-6.54	2.80			0.22
7.6	7.6		-6.40	6.03			0.15
0.0	7.6	90	-0.08	6.24	2.12(8)	0.78(3)	0.18
7.6	0.0		-6.37	0.59			0.35
3.8	7.6		-3.13	6.75			0.32
7.6	3.8		-6.38	3.79			0.43
7.6	7.6		-6.36	6.72			0.27

Table 6.2: The three first columns display the mean displacements and the squeezing phase ($\phi = 0$ corresponds to X_L being squeezed) of the initial pure light states. The next four columns display the mean values and variances of the final atomic states after the storage. The last column displays the overlap between the initial pure light states and the final atomic states. Vacuum state variances are 1/2. The uncertainties on the variances are calculated as the standard deviation of the variances within each subgroup of the input states.

squeezing phase $\phi = 0$ deg or $\phi = 90$ deg. The next aplphabet with $d_{\max} = 3.8$ contains 8 states and the last alphabet with $d_{\max} = 7.6$ contains all 18 states.

Transfer of mean values

The mean and variances of the final states are shown in Table 6.2 for the 18 different pure states $|\Psi\rangle$. The first thing to notice is that the mean values of the final atomic states are lower than the pure states. By averaging over all states, we calculate the average gain of the memory (the ratios $-\langle P_A^{\text{fin}} \rangle / \langle X_L^{\text{pure}} \rangle$ and $\langle X_A^{\text{fin}} \rangle / \langle P_L^{\text{pure}} \rangle$) to be $G = 0.85$. This number agrees with the factor $\sqrt{\eta_{\text{tr}}\eta_{\text{ent}}} = 0.85$ by which the mean values of the pure states are attenuated with before they enter the memory. With the chosen settings $\kappa = 1$ and $\kappa/Z^2 + g\sqrt{\eta_{\text{det}}}t = 1$, this attenuation is expected. Even though the average gain is as expected, the gains for the single input states vary quite a bit. The reason for this variation is not exactly known. It is probably related to technical issues such as the phase stability of the interferometer, the stability of the Larmor precession frequency and the stability of the electronic feedback gain and of κ. These things could lead to wrong mean values in the final atomic operators, rotations in X_L-P_L space of the light operators and rotations in X_A-P_A space of the final atomic operators.

Transfer of variances

The variances of the final atomic states are also shown in Table 6.2. For the first four input states in Table 6.2 with mean values 0 or 3.8 and squeezing phase $\phi = 0$, the variances of the stored states do not vary significantly. We have therefore only showed the average values for these four states. Similarly, the variances has been grouped for other sets of states.

Earlier in Sec. 6.2.2, the expected final atomic variances were estimated and displayed in table 6.1. The table also shows the measured final atomic variances for input states in the alphabet with $d_{\max} = 3.8$. The differences between the measured final atomic state variances and the expected variances are denoted $\mathrm{Var}\,(S_X)$ and $\mathrm{Var}\,(S_P)$ depending on if we consider X or P operators. As shown in Table 6.1, the experimental measured variances differ from the expected ones by the amounts $\mathrm{Var}\,(S_X) \approx 0.10$ and $\mathrm{Var}\,(S_P) \approx 0.22$ (which are averaged over the squeezing phase ϕ). The calculated differences are small (only a fraction of the vacuum variance) which means that the measured data agrees well with the expected theoretical estimates.

The small discrepancy between measured and expected variances could be due to mixing of the anti-squeezing into the squeezed direction due to phase instabilities. This would lead to higher noise, mainly in the squeezed direction. We also see from Table 6.1 that the atomic noise is slightly higher when we are storing light states with large displacements. This is probably due to technical noise orignating from the EOM's which are modulating the input light.

6.5 Fidelity of the storage

6.5.1 Overlap formula

The overlap integral Θ between the initial pure state of light and the final atomic state equals

$$\Theta = \frac{\exp[-\frac{\langle X_A^{\mathrm{fin}}\rangle - \langle P_L^{\mathrm{pure}}\rangle}{2[\mathrm{Var}(X_A^{\mathrm{fin}}))+\mathrm{Var}(P_L^{\mathrm{pure}})]}]}{\sqrt{\mathrm{Var}\left(X_A^{\mathrm{fin}}\right) + \mathrm{Var}\left(P_L^{\mathrm{pure}}\right)}} \cdot \frac{\exp[-\frac{\langle P_A^{\mathrm{fin}}\rangle + \langle X_L^{\mathrm{in}}\rangle}{2[\mathrm{Var}(P_A^{\mathrm{fin}})+\mathrm{Var}(X_L^{\mathrm{pure}})]}]}{\sqrt{\mathrm{Var}\left(P_A^{\mathrm{fin}}\right) + \mathrm{Var}\left(X_L^{\mathrm{pure}}\right)}}, \tag{6.20}$$

and is used as the figure of merit for the transfer of a single quantum state. The overlap is a good measure of quantum state transfer only if either the initial or final state is pure. This means, that the overlap between the input light state and the final atomic state is *not* a good measure of the state transfer. We therefore focus on the overlap between the pure states and the final atomic states. For a pure state squeezed along for instance the P_L-direction, the overlap

reaches unity when $\langle X_A \rangle = \langle P_L \rangle, \langle P_A \rangle = -\langle X_L \rangle$ and $\mathrm{Var}(X_A) = \mathrm{Var}(P_L) = 1/(2s), \mathrm{Var}(P_A) = \mathrm{Var}(X_L) = s/2$.

6.5.2 Experimental overlaps and fidelities

The overlaps between the pure light states and the final atomic states can be calculated using Eq. (6.20) and are also shown in Table 6.1. We see that the overlap depends highly on the input state. The overlap is small when the input displacement is large due to the non-unity gain $G = 0.85$ of the state transfer. Furthermore, we see that the overlap is smaller for squeezing angles $\phi = 90$ deg due to the the more noisy final atomic states.

We now focus on the experimental fidelity which is defined as the average overlap between the input pure states and the final atomic states for a certain input alphabet. For each of the three alphabets shown in the inset to Fig. 6.2, we calculate the fidelity as the average overlap. The results are plotted in Fig. 6.2 as circles connected by lines. The experimental fidelity decreases with larger $d_{\max}$ mainly due to the mismatch in mean values of the pure light states and the final atomic states.

6.5.3 Classical benchmark

A classical benchmark is also plotted in Fig. 6.2 as squares connected by lines. The benchmark has been calculated by the theory team of the authors to Ref. [1]. The benchmark is an upper bound for the fidelity of state transfers for a classical memory. The inputs to the classical memory are states squeezed by 6dB and displaced in phase space. Before entering the classical memory, the states travel through the transmission losses which equals the experimental value η_{tr}. A comparison of our memory and the classical memory is depicted in Fig. 6.2. The benchmark values have been obtained by first truncating the Hilbert space to a finite photon number and then solving the finite-dimensional optimization employing semi-definite programming [81]. The result of the truncation of the Hilbert space is the constant upper bound of 0.45 of the benchmark for $d_{\max} > 3.5$, whereas the actual benchmark decreases further for a larger $d_{\max}$ (the benchmark for an infinite Gaussian distribution of displacements is 0.38). For more details, see the Supplementary Information to [1].

Since the experimental fidelity $F = 0.52 \pm 0.02$ for $d_{\max} = 3.8$ is higher than the classical benchmark 0.45, our memory outperforms any classical memory for this set of input states. This means that our memory is a true quantum memory.

Beating the classical benchmark means that our memory is able to preserve entanglement if only one part of an EPR pair (for instance the upper sideband mode a_+) is stored in the memory and the other part (the lower sideband mode

a_-) is left as a propagating mode. Based on the performance of our memory, we can calculate the expected EPR variance $\Sigma_{\rm EPR} = 0.77 < 1$ between the stored mode and the propagating mode (see Sec. 6.6). This variation of the experiment could be implemented if the two co-propagating modes a_+ and a_- could be separated prior to the storage. The separation could for instance be done by using a narrowband filter cavity where one mode is transmitted and the other mode is reflected.

6.6 Storage of one part of an EPR-entangled pair

In the experiment, the sender (Alice) prepares and sends a two-mode entangled state to the receiver (Bob) who then stores it in his quantum memory. Although the memory is a true quantum memory as proven by its ability to outperform the classical benchmark, the noise added in the storage process to both EPR modes leads to a separable state of the two memory cells. Note that for input states with the squeezing direction $\phi = 0$ displaced up to 3.8 (Table 6.1), we are very close to having two displaced entangled atomic ensembles after the storage since the parameter $\Sigma_{\rm EPR}$ describing EPR-entanglement for this case equals

$$\begin{aligned}\Sigma_{\rm EPR} &= \mathrm{Var}\left(\frac{X_{A1}^{\rm fin} - X_{A2}^{\rm fin}}{\sqrt{2}}\right) + \mathrm{Var}\left(\frac{P_{A1}^{\rm fin} + P_{A2}^{\rm fin}}{\sqrt{2}}\right) \\ &= \mathrm{Var}\left(P_{Ac}^{\rm fin}\right) + \mathrm{Var}\left(P_{As}^{\rm fin}\right) \\ &= 0.52 + 0.52 = 1.04, \end{aligned} \tag{6.21}$$

which is only slightly above 1.

Since outperforming the classical benchmark is sufficient to prove that the memory is capable of storing entanglement, we should be able to think of a modification of the experiment which can do exactly that. One example of such an experiment is the protocol where Alice sends only one mode of the EPR-entangled pair to Bob for storage, and the other mode is sent to a third person, Charlie. In this case only one of the two entangled modes gets distorted by the memory. After the storage, Bob and Charlie perform a joint measurement to test whether there is entanglement between Bob's stored atomic state and Charlie's light state. In practice, Alice would have to separate the upper and lower sidebands, which could for instance be done using a cavity which transmits one sideband and reflects the other. The initial entanglement of the upper and lower sidebands is characterized by

$$\Sigma_{\rm EPR} = \mathrm{Var}\left(\frac{X_+^{\rm pure} - X_-^{\rm pure}}{\sqrt{2}}\right) + \mathrm{Var}\left(\frac{P_+^{\rm pure} - P_-^{\rm pure}}{\sqrt{2}}\right) = 1/s. \tag{6.22}$$

Alice then sends the EPR-entangled upper sideband (together with a lower sideband in the vacuum state) to Bob who stores the upper sideband in the first

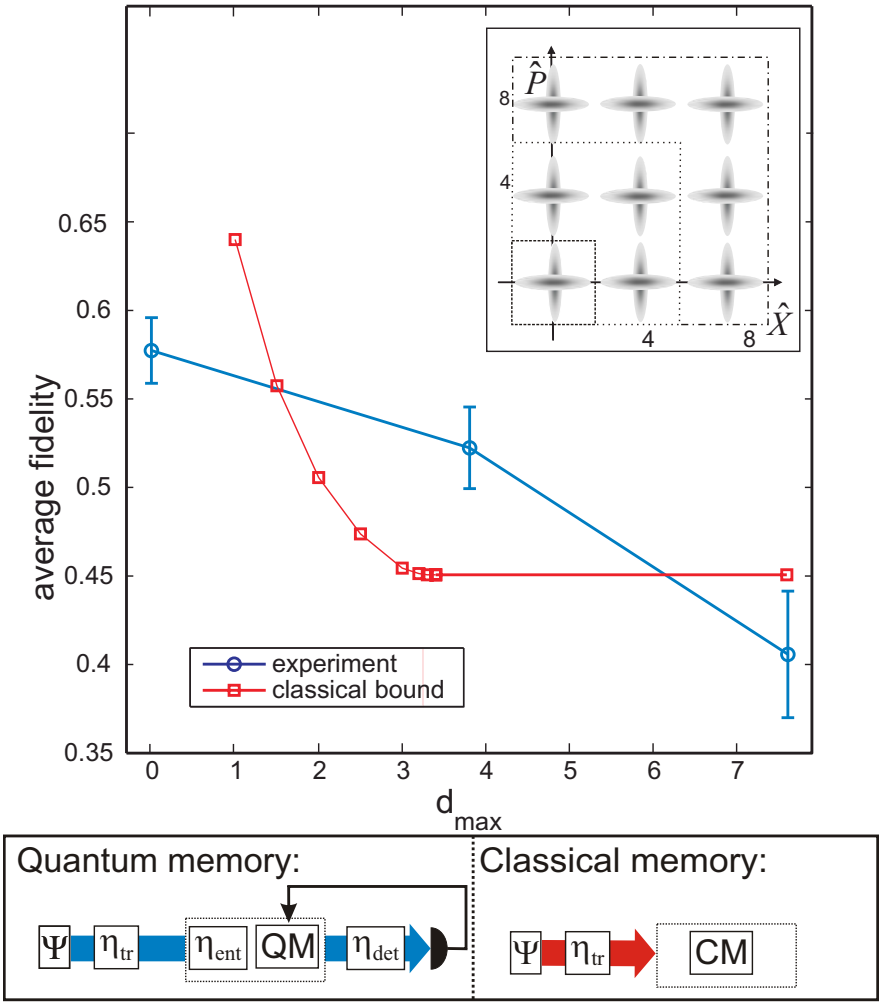

Figure 6.2: **Fidelities.** The figure shows the values of the experimental fidelity (circles) and the theoretical benchmark values (squares) as a function of the size of the set of states $d_{\max}$ with one vacuum unit of displacement corresponding to $d_{\max} = 1/\sqrt{2}$. The inset illustrates the alphabet of states used in the experiment. The three sets of states with $d_{\max} = 0; 3.8; 7.6$ used for the determination of the experimental values of the fidelity plotted in the graph are shown in the inset within dashed, dotted and dashed-dotted squares, respectively. The panel in the bottom shows schematically the propagation channels used in the calculations of the fidelity of the quantum memory (left part) and of the benchmark fidelity of the classical memory (right part). Errorbars on the experimental data represent the standard deviations of the results where all statistical and systematic errors have been included.

ensemble (and the vacuum in the lower sideband in the second ensemble). After the storage Bob and Charlie share entanglement since

$$\begin{aligned}\Sigma_{\mathrm{EPR}} &= \mathrm{Var}\left(\frac{X_{-}^{\mathrm{pure}} + P_{A1}^{\mathrm{fin}}}{\sqrt{2}}\right) + \mathrm{Var}\left(\frac{P_{-}^{\mathrm{pure}} - X_{A1}^{\mathrm{fin}}}{\sqrt{2}}\right) \\ &= \frac{1}{2}\left[\frac{1}{2s}(1+G)^2 + \frac{s}{2}(1-G)^2 + \mathrm{Var}(O_x) + \mathrm{Var}(O_p)\right] \\ &= 0.77 < 1, \end{aligned} \tag{6.23}$$

which has been calculated using the experimentally obtained parameters of our memory from Table 6.1, Eq. (6.15) and utilizing the fact that $\mathrm{Var}\,(X_{+}^{\mathrm{pure}} + X_{-}^{\mathrm{pure}}) = s$ and $\mathrm{Var}\,(P_{+}^{\mathrm{pure}} + P_{-}^{\mathrm{pure}}) = s$. We conclude, based on the experimental performance of our quantum memory for the storage of both modes of the two-mode entangled states, that if we instead stored only one part of the EPR-pair, one of the atomic memories would be entangled with the other part of the EPR-pair after the storage.

6.7 Conclusions and outlook

We have demonstrated the storage of a new class of light states: the displaced two-mode squeezed states. In the experiment, the two modes of light are stored in two atomic modes which are implemented in the experiment using two atomic ensembles.

For each of the 18 pure input states, we have characterized the final stored atomic states. When storing pure states with squeezing phase $\phi = 0$ deg and small displacements $d_{\max} \leq 3.8$, the final atomic states have EPR variance $\Sigma_{\mathrm{EPR}} = 1.04(4)$. If the memory had performed only slightly better (such that $\Sigma_{\mathrm{EPR}} < 1$), we would have succeded in transferring the entanglement between the two sidebands to entanglement between the two atomic ensembles.

Our memory is capable of preserving entanglement if only one part of an EPR pair is stored in the memory and the other part is left as a propagating mode. This has been demonstrated by calculating a classical benchmark fidelity and showing that the experimental fidelity is higher than the benchmark. Direct calculations using the measured variances of the final atomic states also show that entanglement can be preserved for the case where one part of the EPR pair is stored and the other part is left as a propagating mode. Our memory is therefore a true quantum memory.

There are several ways the experiment can be optimized. In the experiment the atoms were first initialized in a state close to the CSS and was then prepared in a spin-squeezed state with variance 14% below the PN limit. However, it should be possible to increase the degree of spin-queezing further. One should first be more careful to start from the CSS with an EPR variance of 1. Then

a realistic value of the attainable squeezing is 40% below the PN limit. This degree of squeezing should be possible to obtain by careful optimizing the aligment, the polarization, the power and the duration of the QND spin squeezing probe. One could also increase the density of atoms. This typically increases the amount of attainable spin-squeezing as showed in the Fig. 3.13 in Sec. 3.11. Since squeezed light is available in the experiment, it could also be possible to squeeze the QND spin-squeezing probe. This should also lead to a higher degree of atomic squeezing.

In the experiment, the mean values of the pure states are transferred with less than unity gain. This is the main reason for the decrease in fidelity for large displacements. In a future experiment this can easily be changed by simply increasing the light power and the electronic gain.

The losses play an important role when working with non-classical light states, and any loss will degrade the memory performance. The glass cells used in the experiment are anti-reflection (AR) coated on the outside of the windows. AR-coating on also the inside of the windows will reduce the losses on two cells from the measured 18% to only a few percent. Such cells are under the investigation in the group.

The memory storage time is in the experiment 1 ms which equals the time between the "input pulse $|\Psi\rangle$" and the "probe" (see Fig. 6.1). We did not attempt to vary the storage time in the experiment. The decay-time in the dark is typically $T_2^{\text{dark}} \geq 30$ ms so it should be possible to store quantum states for times longer than the 1 ms done in the experiment.

We use the fidelity as the figure of merit for the storage. When increasing the storage time, the fidelity will decrease. The maximal storage time is reached when the experimental fidelity equals the benchmark fidelity. The maximal storage time will depend on the size d_{max} of the input distribution, since the overlap between a final atomic state (after some storage time) and the initial pure light state depends on both the T_2^{dark}-time and the initial light displacement.

We have demonstrated the quantum storage of the two-mode squeezed states. However, we have not demonstrated that it is possible to retrieve the stored states. The retrieval of states should be feasible in our setup. Several retrieval protocols have been discussed in the thesis [33], but the protocols have not yet been implemented in our setup.

Chapter 7

Entanglement generated by dissipation & Steady state entanglement

7.1 Introduction

In this chapter we present experiments where entanglement between two atomic ensembles is generated using dissipation as the entangling mechanism. The generated entanglement is long lived, and we present experimental results which demonstrate that the ensembles can maintained in an entangled state for around 40 ms.

In previous experiments using our setup [16, 2, 1], entanglement was created using a measurement of the collective atomic spin operators. After the measurement, the entangled state decayed rapidly and the entanglement lasted only for a few milliseconds. With the method denoted "entanglement generated by dissipation", the ensembles are entangled without the use of a measurement.

We also combine the dissipative entangling mechanism with continuous measurements. Using this combined method, we demonstrate that the atomic ensembles can be maintained in an entangled steady state. In this case, the entanglement does not decay but instead "lives for ever". The results demonstrating entanglement generated by dissipation & steady state entanglement are submitted and available on the archive [3] [1].

The method "entanglement generated by dissipation" is based on the idea that if two atomic systems share a common enginered reservoir, dissipation can drive the two systems into an entangled steady state [82, 83, 84, 85]. Such a

[1] At the time of writing, the results demonstrating steady state entanglement are not in the current arXiv version (v1). An updated version or a new arxiv paper including those results should appear soon.

steady state will be robust, the entanglement will not depend on the initial state of the atomic systems, and the entanglement will be present at all times. This kind of entanglement can be used on-demand at any instance of time. In our case, the common reservoir shared between the two atomic ensembles consists of the modes of a drive light field passing though the ensembles.

In most of the experiments presented in this chapter, the atoms are first initialized in a fully polarized state. Then, a drive field is applied and the atoms will evolve into an entangled state. Due to spontaneous emission, the atoms will depolarize, prohibiting the entanglement to persist for long times. In order to achieve a true steady state, both pump and repump fields should therefore be applied to the atoms to keep them well polarized. We demonstrate that the addition of pump light increases the time the entanglement generated by dissipation can be maintained. A theoretical analysis presented in [3] shows that for high optical depths and in the presence of both pump and repump fields, entanglement should persist in a steady state. For the optical depths used in the presented experiments, unfortunately, the atoms did not reach an entangled steady state by means of dissipative processes only.

Measurements on the atomic systems can be used to create entanglement as discussed several times earlier in this thesis. Using a method combining dissipative processes (by the drive, the pump and the repump light) with continuous measurements, we demonstrate that entanglement can be generated in a steady state. With this combined method, we generate atomic entanglement 20% below the projection noise limit which "lives for ever".

7.2 Theory

In our experimental system, the generation of entanglement by dissipation can to a large extend be explained by the swap and squeezing interaction theory developed in chapter 2. However, the theory has some limitations which makes it hard to predict the time evolution of the atomic state over long periods of time. A related theory presented in [86, 3], here denoted the "master equation approach", has been developed. This theory can be used to describe the long term dynamics and the steady state of the atomic systems.

Below we discuss the entanglement generated by dissipation experiment using the swap and squeezing interaction. The master equation approach is also discussed and compared to the swap and squeezing interaction theory.

7.2.1 Swap and squeezing interaction theory

The simplest form of the swap and squeezing interaction theory is the input-output equations (2.19). From these input-output equations, one can see that it is possible to generate entanglement in a steady state. After a long interaction

time $2\gamma_{\rm sw}T \gg 1$, the collective atomic P-operator is squeezed by the amount $Z^2 = 1/\zeta^2$. Since this is true for both the P_c and P_s operators, the EPR variance criterion $\Sigma_{\rm EPR} = \zeta^2 < 1$ is satisfied and the two atomic ensembles are entangled in a steady state. For our experimental value of the detuning $\Delta = -850$ MHz, we have $\zeta^2 \approx 1/6.4$ and the theory predicts a substantial amount of entanglement.

As seen in the input-output Eq. (2.19), the interaction between light and atoms is symmetric. This means that entanglement is not only generated between the two atomic ensembles but also between the upper and lower sidebands of the output light. In the paper [2] where the swap and squeezing interaction was first introduced, the entanglement between the sidebands of light was demonstrated. This was the topic of chapter 4.

We now move on to the more complicated input-output equations for the full swap and squeezing interaction theory which also include "bad decoherence" processes. The bad decoherence originates from unwanted processes such as spontaneous emission, atomic collisions, dephasing due to magnetic field inhomogeneity and so on. First a comment on how the entanglement is influenced by the bad decoherence $\gamma_{\rm bad}$. In the input-output equations, the bad decay is parametrized in terms of the parameter $\epsilon^2 = \gamma_{\rm bad}/\gamma$ where $\gamma = 1/T_2$. In the limit of long interaction times, one finds from Eq. (2.71) that

$$\mathrm{Var}\left(P_c^{\rm out}\right) \to \left(1-\epsilon^2\right)\zeta^2 \mathrm{Var}\left(y_{c,+}^{\rm in}\right) + \epsilon^2 \mathrm{Var}\left(F_{pc,+}\right) \quad \text{for} \quad \gamma T \gg 1. \tag{7.1}$$

If we assume that the input light operators and the noise operators are in the vacuum state, the EPR variance equals $\Sigma_{\rm EPR} = \zeta^2 + (1-\zeta^2)\,\epsilon^2$. We see that a non-zero ϵ^2 will reduce the generated entanglement. However, entanglement will always be generated no matter how large $\gamma_{\rm bad}$ is. We just need an $\epsilon^2 < 1$. This will always be the case as long as $\gamma_{\rm sw} \neq 0$. The fact that entanglement should be generated for all $\epsilon^2 < 1$ relies heavily on the assumption that the input light and noise operators are in the vacuum state. In the experiment, this is unfortunately not necessarily true. This will be discussed later when presenting the experimental results.

We now discuss the T_1 and T_2 decay times and how they are related to the entanglement generated by dissipation. In the experiment, typical values are $T_2 \approx 6$ ms and $T_1 \approx 34$ ms when the drive light is on the atoms. The T_1-time is the characteristic decay time of the mean spin J_x. The decay of the mean spin is a problem since the collective coupling is proportional to J_x. If the mean spin decays, the swap rate $\gamma_{\rm sw} \propto J_x$ goes down and the coupling constant κ^2 decreases with time. This means that the collective effects responsible for the entanglement gets smaller and smaller with time. When $\gamma_{\rm sw}$ decreases, ϵ^2 goes up and we also expect less entanglement as seen from Eq. (7.1). Similarly, if T_2 is short due to bad decoherence processes, ϵ^2 goes up and the degree of entanglement is reduced.

In earlier experiments in our setup such as the generation of entanglement by a QND measurement [16], the time that entanglement could be sustained was limited by the T_2-time. On the other hand, in the swap and squeezing interaction theory, entanglement is expected only for times $\gamma T \gg 1 \Leftrightarrow T \gg T_2$. As explained earlier, the T_1-time limits the time entanglement can be maintained, since for times comparable with the T_1-time, the collective coupling (the swap rate) decreases. However, the T_1-time is significantly longer than the T_2-time, and we expect to see entanglement generated for a long duration on the order of the T_1-time.

When deriving the input-output equations, we assume that the mean spin J_x is constant in time and that the atoms are highly oriented. For interaction times comparable with T_1, both of the assumptions are typically not true.

The two assumptions are related to the use of pump and repump fields. In the beginning of each measurement cycle, all atoms are prepared in the highly polarized $F = 4, m = \pm 4$ state by applying resonant pump and repump fields for some duration. In the fully pumped state, the mean spin of the atoms in the $F = 4$ manifold is maximal $J_x = \pm 4N_A$. The orientation of the $F = 4$ atoms defined by $p_4 = \frac{1}{4}\sum_{m=-F}^{F} m\rho_{Fm,Fm}$ where $\rho_{Fm,Fm}$ is the density matrix for the $2F + 1 = 9$ states in the $F = 4$ manifold equals one for this fully pumped state.

After the pumping stage, entanglement will be generated by using a drive pulse. If the pump and repump fields are turned completely off during the drive pulse (see Fig. 7.2a), the mean spin J_x and the orientation p_4 will decay towards zero. The mean spin decays mainly due to the loss of atoms to states with $F = 3$ but also slightly due to depolarization of the atoms in the $F = 4$ manifold. If instead the pump light is kept on simultaneously with the drive light (see Fig. 7.2b), the orientation p_4 will still be high. And if also the repump light is kept on simultaneously with the drive (see Fig. 7.2c), the mean spin J_x will still be large. In the cases where pump and/or repump light is applied during the drive pulse, J_x and p_4 will reach non-zero steady state values. The exact values will depend on the power of the pump, the repump and the drive.

If we are interested in generating an entangled steady state, it is now clear that we need to apply both pump and repump fields simultaneously with the drive light. The pump light re-orients atoms in the $F = 4$ manifold, and the repump light makes sure that atoms lost to the $F = 3$ manifold are recycled and put back in the $F = 4$ manifold, such that they can take part in the collective interaction.

7.2.2 Comparison between theories

We are interested in a theory which can describe the light-atom interaction for long interaction times. The theory should include processes such as spontaneous emission due to the drive, pump and repump fields and also atomic collisions.

These processes influence the time evolution of the collective state of the two atomic ensembles. In particular, a steady state will be highly dependent on these processes. Such a theory has been developed by C. Muschik *et al* [86]. This theory is also used in [3] to describe the experiment and the experimental results.

I would like to point out some differences between the theory developed in [86] and the swap and squeezing interaction theory described in chapter 2. In the swap and squeezing interaction theory, the decay of the transverse spin was put in the model by including the bad decoherence rate γ_{bad} and the noise operators F_x and F_p. However, the theory does not include a way to calculate the magnitude of γ_{bad} or the variance of the noise operators. In the theory presented in [86], the effect of spontaneous emission is calculated using the relevant level structure of cesium and the appropriate dipole matrix elements. This way, both the decay rates and the noise properties can be calculated from the light intensities of the drive, pump and repump fields. Also, the decay of the mean spin J_x is included in the model presented in [86] which is important for predicting the steady state.

In the experiment, entanglement is generated by a long drive pulse of light. The atomic state is then measured using a short pulse of light. It is important to note that the swap and squeezing input-output equations for the light operators are still valid if we only consider interaction times which are short compared to the T_1-time and highly polarized atomic ensembles. We will therefore still be able to measure the atomic state as described by Eq. (2.82) under these conditions. In conclusion, we will be able to measure the atomic state using the swap and squeezing theory, but we will have to use the theory from [86] to be able to predict the atomic state.

7.2.3 Master equation approach

I will now go through some main points of the master equation approach described in [86, 3]. In the theory, the time evolution of the density operator is calculated using a master equation. In the derivation, the light fields are traced out such that one ends up with an effective Hamiltonian describing the spin dynamics only. The drive light is acting as a reservoir or environment which can be thought of as dissipation. This motivates the name "entanglement generated by dissipation".

As usual, we consider two oppositely polarized atomic ensembles with level structure as shown in Fig. 7.1. Atoms in ensemble 1 (2) initially occupy the level $F = 4, m_F = 4$, ($F = 4, m_F = -4$). The ensembles interact with strong linearly y-polarized light represented in the x-quantization axis as a superposition of right hand and left hand circularly polarized light. Situated in this light field, the atoms can be excited and spontaneously emit photons in all directions. The photons are

described by modes $\hat{a}_{\vec{k}}$ where $\vec{k}$ is the wavevector. Since spontaneous emission is a resonant process, and the atomic ground state levels are separated by the energy $\hbar\Omega_L$ where Ω_L is the Larmor frequency, the frequency of the spontaneously emitted photons will be ω_+ or ω_-. Here $\omega_\pm = \omega_0 \pm \Omega_L$ and ω_0 is the laser frequency. Atoms in ensemble 1 (2) couple to σ_--polarized light with coefficient χ_1 (χ_2) and to σ_+-polarized light with coefficient χ_2 (χ_1). For the cesium $D2$ line, several excited states ($F' = 3, 4, 5$) contribute to χ_1 and χ_2. Each contribution is proportional to the dipole matrix elements for the specific transition divided by the specific detuning. The χ_1 and χ_2 coefficients are closely related to the a_1 and a_2 cofficients used in the Hamiltonian given by Eq. (2.20). Upon absorption of a σ_--polarized photon, a collective spin excitation $b_1^\dagger$ can be created in the first ensemble together with the creation of a photon in the upper sideband (see Fig. 7.1). This leads to a term proportional to $\int_{\Delta\omega_{us}} d\vec{k}\chi_1 a_{\vec{k}} b_1 + h.c.$ in the Hamiltonian. The integration (over $\vec{k}$) runs over modes within a narrow frequency interval $\Delta\omega_{us}$ centred around ω_+ (*us* stands for upper sideband.) In total, we find four such terms which give rise to the total Hamiltonian

$$\mathcal{H} \propto \int_{\Delta\omega_{ls}} d\vec{k} \left(A a_{\vec{k}}^\dagger + A^\dagger a_{\vec{k}} \right) + \int_{\Delta\omega_{us}} d\vec{k} \left(B a_{\vec{k}}^\dagger + B^\dagger a_{\vec{k}} \right), \tag{7.2}$$

where Δ_{ls} is a narrow frequency interval centred around ω_- and where we have defined the variables

$$A = \chi_2 b_1 + \chi_1 b_2^\dagger \quad \text{and} \quad B = \chi_2 b_2 + \chi_1 b_1^\dagger. \tag{7.3}$$

This Hamiltonian leads to a master equation for the density matrix ρ of the ensembles [86]

$$\frac{\partial \rho}{\partial t} = \frac{d\Gamma}{2} \left(A\rho A^\dagger - A^\dagger A\rho + B\rho B^\dagger - B^\dagger B\rho + h.c. \right) + \mathcal{L}_{\text{noise}}\rho. \tag{7.4}$$

Γ is the single atom radiative decay rate and $\mathcal{L}_{\text{noise}}$ represents undesired noise arising from single atom spontaneous emission or atomic collisions. Emission in the forward propagating modes is enhanced by the optical depth d as compared to the modes into other directions and give rises to the first terms in Eq. (7.4) which are proportional to d. In the absence of the noise term, the term in the parentheses will drive the collective state of the atomic ensembles into an entangled steady state with $\Sigma_{\text{EPR}} = \zeta^2 < 1$ [86]. The emission of a forward propagating photon could arise from both the first and second ensemble, the two paths are indistingishable, and this leads to entanglement between the two atomic ensembles.

The master equation (7.4) has been solved for the special case where only three levels in each ensemble are included. I.e., the multilevel cesium atom is simplied as a three-level atom consisting of the two states $F = 4, m = 4$ and

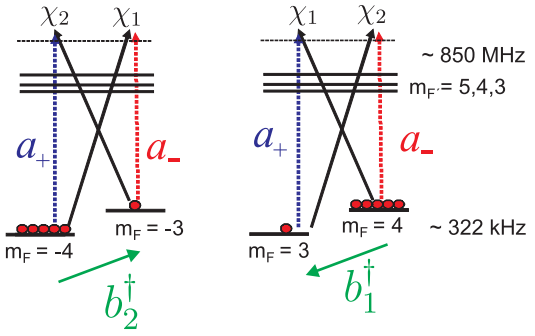

Figure 7.1: Level structure and light fields for the two atomic ensembles. $\hat{a}_+$ and $\hat{a}_-$ are annihilation operators for the upper and lower sidebands. $\hat{b}_1^\dagger$ and $\hat{b}_2^\dagger$ are creation operators for the collective atomic excitation for the first and second ensemble. χ_1 and χ_2 are coupling strengths.

$F = 4, m = 3$ in the $F = 4$ manifold and the auxillary state $F = 3, m = 3$ in the $F = 3$ manifold for the case of the first ensemble. For the second ensemble, we only consider the three levels $F = 4, m = -4$, $F = 4, m = -3$, and $F = 3, m = -3$. The auxillary level $F = 3, m = \pm 3$ is included to simiulate loss of atoms from the $F = 4$ manifold. This reduction of the density matrix is quite similar to what was done in Sec. 2.4.4 where the swap and squeezing interaction was derived. The big difference is that the $F = 3, m = \pm 3$ state is now included such that the decrease in J_x can be modelled.

Consider the situation where three levels per ensemble are included in the model. The Langevin noise term $\mathcal{L}_{\text{noise}}$ in Eq. (7.4) consists of several terms which will now be discussed briefly. We can can consider noise processes which take an atom from the initial state to a final state $|initial\rangle \rightarrow |final\rangle$. There will be terms representing processes such as $|F = 4, m = 4\rangle \rightarrow |F = 4, m = 4\rangle$, $|F = 4, m = 4\rangle \rightarrow |F = 4, m = 3\rangle$, and $|F = 4, m = 4\rangle \rightarrow |F = 3, m = 3\rangle$. These terms represent dephasing, de-polarization (of the $F = 4$ manifold) and loss of atoms (from the $F = 4$ manifold to the $F = 3$ manifold), respectively. The origin of these terms can for example be spontaneous emission from the drive, pump and repump fields. In this case, the strength of these processes can be calculated from the dipole matrix elements. One can also put in atomic collisions by hand. In [3], all these noise processes were included in the master equation for the three atomic levels (in each ensemble). This model was used for fitting the experimental data. Since the fitting was done by C. Muschik, I choose to not present the fits in this thesis. For more details of the the theory one should refer to [86, 3].

7.3 Quasi steady state entanglement generated by dissipation

In this section, we present the results of entanglement generated by dissipation. The entanglement can be sustained for a long time before it eventually decays.

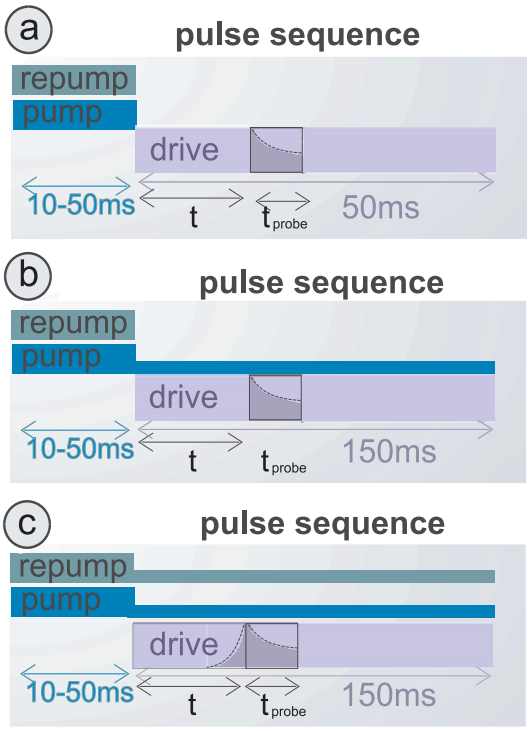

Figure 7.2: Pulse sequences used in the experiments. Pump and repump fields create the initial atomic state at $t = 0$ close to the CSS. The drive field creates the entanglement. In (a) and (b), the atomic state at time t is measured using the output light within the time interval from t to $t + t_{\text{probe}}$. In (c), the output light before time t is used to estimate the atomic state at time t.

We therefore call this quasi steady state entanglement. Some of the procedures for analyzing the data are presented in this section, while other more detailed methods are presented in appendix D.

The pulse sequence for this kind of measurement is shown in Fig. 7.2a. The atoms are first initialized in a state close to the CSS using pump and repump light. This initial atomic state is characterized beforehand using the methods described in Sec. 3.11. As discussed in appendix D.1, the value of the coupling constant κ^2 at time $t = 0$ can be found from the characterization of the initial atomic state.

At time $t = 0$, the pump and repump light is turned off. Then, the drive light responsible for the entangling mechanism is turned on. Starting from the CSS, the atomic state now evolves into some state, hopefully an entangled state.

The generation of entanglement by dissipation does *not* require a measurement. However, in order to *verify* that entanglement is generated, the output light is measured. From the measurement of the output light, the time-evolution of the atomic noise in PN-units $\Sigma_{\text{EPR}}(t)$ can be estimated, and it can be determined whether the atoms are entangled or not.

In the experiment, the cosine and sine components of the output light, $S_{2c}^{\text{out}}(t)$ and $S_{2s}^{\text{out}}(t)$, are measured and the covariance matrix (discussed earlier in Sec. 3.7.1) is recorded. Figure 7.3 shows the recorded covariance matrix. The elements along the diagonal decrease with time, demonstrating some time-evolution of the

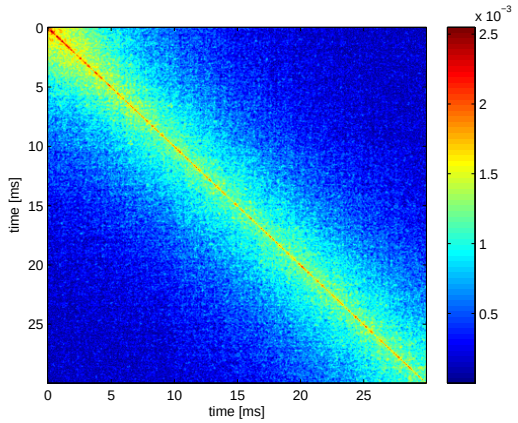

Figure 7.3: The covariance matrix for the entanglement generated by dissipation measurements. Atoms are on during the probing, room-temperature data. The light noise contribution to the correlation matrix has been subtracted.

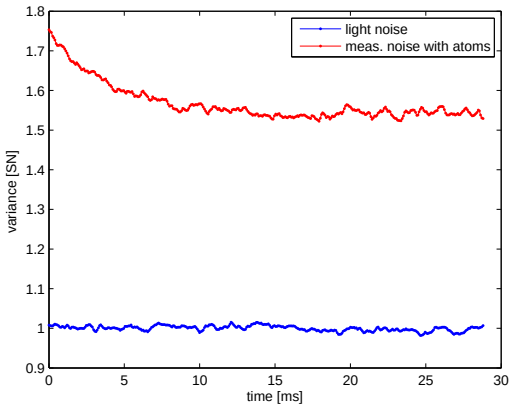

Figure 7.4: The output light noise in shot noise units without atoms (blue) and with atoms (red). For these specific measurements we chose $t_{\rm probe} = 1$ ms.

atomic state.

The atomic noise $\Sigma_{\rm EPR}(t)$ at time t can be estimated using the output light measured in the time interval from t to $t + t_{\rm probe}$ (see the pulse sequence in Fig. 7.2a). $t_{\rm probe}$ is a short time interval typical in the range 0.5-1 ms. Notice that (a) the evolution of the atomic state is slow compared to $t_{\rm probe}$ and (b) only the output light *after* time t is used to estimate the atomic state at time t.

The measured covariance matrix is used for the atomic noise reconstruction. Since the whole covariance matrix is recorded from time $t = 0$ to $t = T$, where T is a long time, typically 30-180 ms, we can extract the atomic noise evolution in the whole time interval $0 < t < T - t_{\rm probe}$.

To get an idea of how the "raw" data looks, we plotted the measured output light noise at time t in Fig. 7.4. To be specific, the figure shows the calculated variances $\left[\mathrm{Var}\left(S^{\rm out}_{2c,-}(t)\right) + \mathrm{Var}\left(S^{\rm out}_{2s,-}(t)\right)\right]/2$ normalized to shot noise units. The time dependent integrated cosine Stokes operator is defined as

$$S^{\rm out}_{2c,-}(t) \propto \int_{t'=t}^{t+t_{\rm probe}} S^{\rm out}_2(t') \cos(\Omega_L t') e^{-\gamma t'} dt'. \tag{7.5}$$

The sine operator is similarly defined. The variances of these operators can be calculated from the covariance matrix as described in Sec. 3.7.1.

From the measured variances $\left[\mathrm{Var}\left(S^{\rm out}_{2c,-}(t)\right) + \mathrm{Var}\left(S^{\rm out}_{2s,-}(t)\right)\right]$, the atomic noise $\Sigma_{\rm EPR}(t)$ at time t can be estimated using Eq. (2.85). In order to have

a good signal to noise ratio, we choose the coupling strength κ^2 around one. The coupling strength κ^2 depends on for instance the probe power P, the number of atoms N_A and the time interval t_{probe}. For our experimental settings of P and N_A, we obtain κ^2 around one for t_{probe} =0.5-1 ms.

Figure 7.4 shows two things. In blue, it shows the measured shot noise of light at time t. The shot noise is normalized such that it has the (average) value of 1. In red, we have the output light variance when the atoms are present. The variance starts at the value around 1.75 and then decreases to the value 1.65. This change happens due to a time evolution of the atomic state. The decrease in the output light noise can happen for two reasons. Either because the atomic noise in PN-units Σ_{EPR} decreases, or because the mean spin J_x decreases. Only with the combined measurement of J_x and the output light noise, we can calculate the atomic noise in PN-units $\Sigma_{\text{EPR}}(t)$ and determine whether the atomic ensembles are entangled.

We present results for two experimental settings: room-temperature (RT) and high-temperature (HT). The two settings correspond to two different values for the density of atoms. The density of atoms can be found from the initial Faraday angle which has the values $\theta_F \approx 8$ deg (RT) and $\theta_F \approx 14$ deg (HT). The main results are presented in Fig. 7.5 which shows the calculated atomic noise in PN-units and the Faraday angle as a function of time for the RT and the HT data.

The Faraday angle θ_F is recorded continuously with an auxillary weak "Faraday probe". The Faraday angle is an important parameter since we can find the mean spin J_x from the Faraday angle measurement. For reasons explained in appendix D.3, we calculate a compensated Faraday angle θ_4 from the measured θ_F. The mean spin of the atoms in the $F = 4$ hyperfine manifold is proportional to the *compensated* angle $J_x \propto \theta_4$. The compensated angle as a function of time is plotted in Fig. 7.5. We see that the angle decreases from the initial value with time [2].

The atomic noise in PN units as a function of time can be calculated from the noise of the output light operators $\left[\text{Var}\left(S^{\text{out}}_{2c,-}(t)\right) + \text{Var}\left(S^{\text{out}}_{2s,-}(t)\right)\right]$ and the compensated Faraday angle $\theta_4(t)$ by using the knowledge of the initial atomic noise at $t = 0$ measured beforehand. More details of the data analysis is presented in appendix D.

Starting with the RT-data: The atomic state starts from the CSS with noise $\Sigma_{\text{EPR}} = 1.00(6)$ at $t = 0$ [3]. When the drive is turned on, the atomic noise

[2]From calculations using the dipole matrix elements of cesium, we believe that the main reason for this decrease in the Faraday angle is due to atoms lost to the $F = 3$ manifold and only slightly due to the de-polarization of atoms in $F = 4$.

[3]The uncertainties on Σ_{EPR} and $\Sigma^{\text{cond}}_{\text{EPR}}$ are estimated to be 6%. Uncertainties on the detection efficiency, the shot noise, the measured output variances, the coupling constant κ^2_m and the reduction of the light noise t^2_m are included.

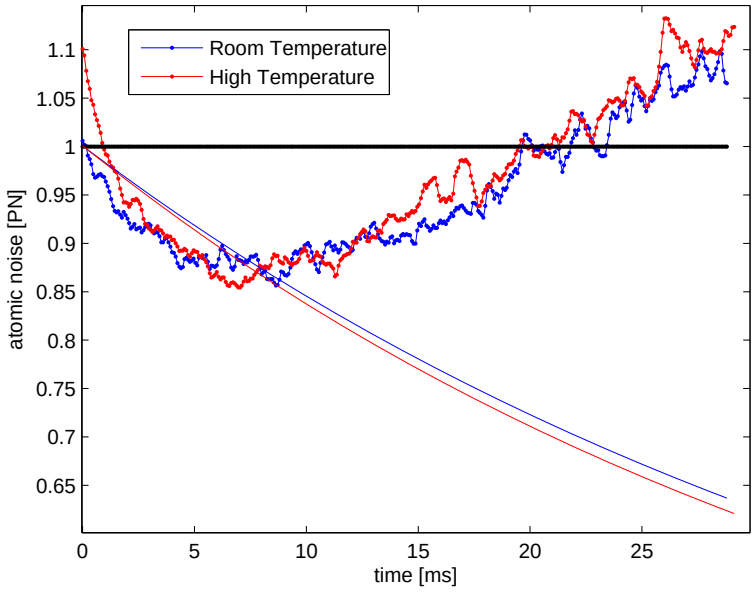

Figure 7.5: Dots connected with lines: Atomic noise in projection noise units as a function of time. Solid lines: Compensated Faraday angles $\theta_4/\theta_{\max}$, see Sec. D.3. Blue is room-temperature data, red is high-temperature data.

decreases below one ($\Sigma_{\rm EPR} < 1$), demonstrating that the atomic ensembles are entangled. In the period from $t \approx 5, ...10$ ms, the atoms are in a quasi steady entangled state with the variance reduced by almost 15%. Then the atomic noise starts to increase, and for $t \geq 20$ ms, the atomic noise $\Sigma_{\rm EPR} \geq 1$ and the atomic ensembles are no longer entangled.

The reason for the increase in noise after $t = 10$ ms is twofold. First, due to the reduction of the mean spin $J_x \propto \theta_4$, the collective interaction looses strength. Second, with time, the atoms in the $F = 4$ hyperfine manifold depolarize. The initial CSS has the least amount of noise possible without entanglement, and depolarization will inevitably add noise with time. The main reason for the depolarization is spontaneous emission due to the drive light. In the dark, the decay times have the values $T_1 \approx 130$ ms and $T_2 \approx 40$ ms. With drive light on, these values reduce to $T_1 \approx 34$ ms and $T_2 \approx 6$ ms.

We now continue with discussing the high-temperature data. The atomic state at $t = 0$ has $\Sigma_{\rm EPR} = 1.10(7)$. The state is a bit more noisy than the CSS [4]. When the drive is turned on, the atomic noise decreases. We see from Fig. 7.5 that initially the noise decreases faster than for the RT-data. This is expected due to the higher density of atoms in the HT-data. Similar to the RT-data, the HT-data shows that the atoms reach an entangled quasi steady state. The

[4] In our experiments, it is typical that the initial atomic noise increases with the density of atoms. This was discussed in Sec. 3.11.

variance is reduced to 15% below the PN limit after $t = 5$ ms, similar to the RT data. For $t \geq 20$ ms, the atomic ensembles are no longer entangled.

The maximal degree of entanglement depends on the initial atomic noise at $t = 0$. The fact that the initial atomic noise is above one (for the HT-data), therefore limits the maximal degree of entanglement. On the other hand, if entanglement could be generated in a steady state (as demonstrated later in Sec. 7.4), the generated entanglement would be independent of the initial atomic state.

For both the RT and HT settings, no steady state entanglement is reached. Instead, the atoms reach a quasi steady state. The entanglement last for approximately 20 ms for both the RT and the HT settings. In earlier experiments in our setup where entanglement was generated by a measurement, we obtained entanglement which lasted for a few ms only. With the method of generating entanglement by dissipation, entangled states can be maintained for an order of magnitude longer time.

7.3.1 Lifetime measurement

So far, we demonstrated that entanglement between the atomic ensembles can be maintained for a long time ≈ 20 ms if the drive is on during this whole period. But what happens if the drive is suddenly turned off? This situation has been tested. First, the atoms are entangled by applying a drive of 8 ms duration. Then, after a variable delay t_{dark}, a probe pulse of 1 ms duration is used to measure the atomic state. This way, the decay of the entanglement "in the dark" can be measured. The results for Σ_{EPR} as a function of t_{dark} are plotted in Fig. 7.6. For this measurement, the initial atomic noise at $t = 0$ was $\Sigma_{\mathrm{EPR}} = 1.06(6)$. This is a bit higher than for the RT data presented in the Sec. 7.3. After 8 ms with drive light on the atoms and 1 ms delay, the noise is $\Sigma_{\mathrm{EPR}} = 0.93(6)$ as seen in Fig. 7.6. Again, this is slightly higher that the 15% noise reduction obtained in Sec. 7.3. This is mainly due to the higher initial atomic noise.

Figure 7.6 shows that the atomic noise increases with t_{dark}. After 2.5-3 ms, the atoms are no longer entangled. For long times, the atomic noise increases significantly above the projection noise ($\Sigma_{\mathrm{EPR}} = 1$). It is clear from this measurement that the decay in the dark is not directed towards the vacuum but instead towards a more noisy state. I will not go into more details of which state the atoms decay to in the dark.

7.3.2 Addition of pump and repump fields

It is important that the atoms are well polarized in order to be able to reach an entangled steady state. Using pump light, it is possible to keep the atoms highly polarized. In this section, we demonstrate that is possible to maintain an

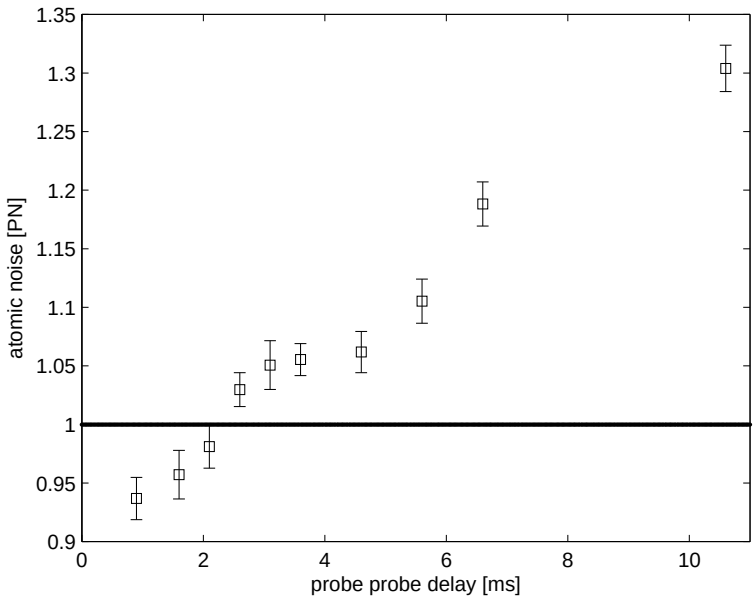

Figure 7.6: Decay in the dark. An entangled state is first generated by dissipation. After a variable delay t_{dark} the atomic noise Σ_{EPR} is measured. It is here plotted as a function of the delay. Errorbars represent statistical uncertainties on the measured output variances only.

entangled state for ≈ 40 ms by applying pump light simultaneous with the drive light.

The pulse sequence for this measurement is shown in Fig. 7.2b. During the drive pulse, the pump light is kept on. The repump light is off during the drive pulse. The results are plotted in Fig. 7.7. The compensated Faraday angle divided by the initial maximal Faraday angle $\theta_4/\theta_{\mathrm{max}}$ is shown as a black line. During the drive period of 180 ms, the angle drops significantly. The fact, that the angle does not decay to zero is mainly due to a small leak-through of the repump light.

The atomic noise Σ_{EPR} is plotted in Fig. 7.7 with red dots connected by lines. After 5 ms of drive light, the noise is reduced to 10% below the PN-limit. This is slightly worse than what was obtained with the pump light off during the drive pulse (see Sec. 7.3). This is because the bad decay rate is significantly higher when the pump light is on the atoms. The entanglement can be maintained for ≈ 40 ms as seen in the inset to Fig. 7.7. This is a factor of two longer than the 20 ms obtained in Sec. 7.3 without the pump light. This demonstrates that de-polarization of the $F = 4$ atoms was limiting the entanglement generation demonstrated in Sec. 7.3. It also demonstrates that depolarization can be partially circumvented using pump light.

For long interaction times $t \approx 180$ ms, the Faraday angle $\theta_F(t \to \infty)$ stabilizes at a low value and the noise reaches the value $\Sigma_{\mathrm{EPR}} = 1.30(8)$. The noise is above the projection noise because the decay of the atomic state is not directed

towards the vacuum, as explained below Eq. (7.1). The noise added due to the pump is towards the vacuum if the pump puts atoms in the state $F = 4, m = \pm 4$ (x-quantization axis). However, misaligment of the pump beam and classical intensity noise on the pump light might give rise to additional noise. In these cases, the decay will be towards a state with noise higher than vacuum.

When the Faraday angle decreases, the collective interaction parametrized by γ_{sw} also decreases. This makes the ratio $\epsilon^2 = \gamma_{\mathrm{bad}}/\gamma$ worse, and less entanglement will be generated. We have therefore also performed experiments where repump light was shone on the atoms during the drive. Adding the repump light makes the Faraday angle decay slower. Also, the steady state Faraday angle increases with repump power. The outcome of these measurements was that the repump light did not improve the maximum attainable entanglement generated by dissipation or the period of time where the entanglement could be maintained. It is not understood why adding the repump light did not improve the entanglement generation. It might be due to misalignment, a too small beam size, non-perfect polarization or classical intensity noise.

In the paper [3], the experimental data presented in Fig. 7.5 and Fig. 7.7 are fitted using the master equation theory described in Sec. 7.2.3. See [3] for the actual fits. The theory is also used to predict whether it is possible to obtain entanglement generated by dissipation for long times $\gamma T \gg 1$. For the RT atomic density used in our experiment, the theory predicts no entanglement in the steady state. This is also what is seen in the experiment presented in Fig. 7.7. For densities higher (by more than a factor of two) than the RT density, the theory predicts that entanglement could be generated in a steady state if both pump and repump light is applied. Efforts to obtain entangled steady states generated by dissipation using higher densities of atoms have been made, but unfortunately without succes.

7.4 Steady state entanglement and continuous measurements

In this section we present two important results. (A) Using the combined method of dissipative processes by the drive, pump and repump light and continuous measurements, we demonstrate steady state entanglement between the two ensembles maintained for more than one hour. (B) We demonstrate that the entanglement is independent of the initial atomic state, as should be the case for a steady state.

Consider the pulse sequence shown in Fig. 7.2c. The atoms are first initialized in the CSS, and then the drive light is turned on. The pump and the repump

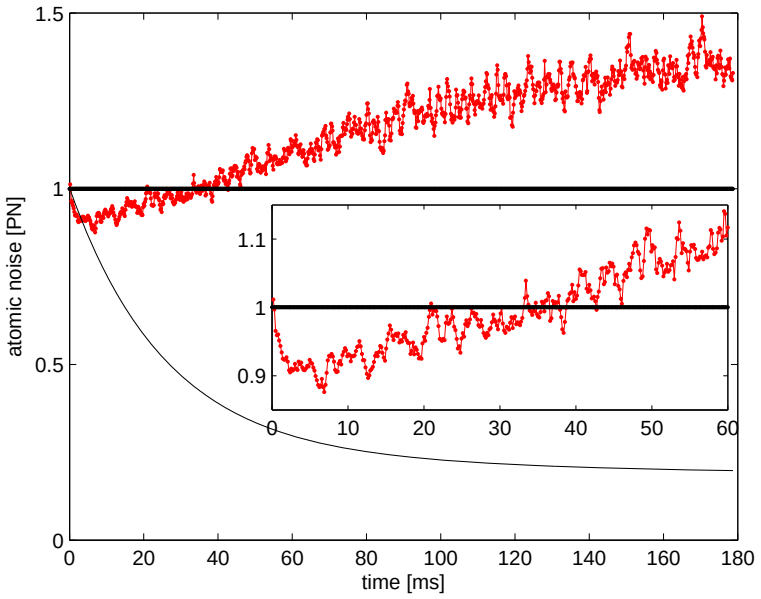

Figure 7.7: Room-temperature data. The pump field is on during the probing as shown in the pulse sequence in Fig. 7.2b. The solid black line shows the compensated Faraday angle $\theta_4/\theta_{\max}$ as a function of time. The red dots connected by lines show the atomic noise Σ_{EPR} in PN units. The inset is a zoom in of the first 60 ms.

light is kept on during the drive pulse. For this measurement, the atomic noise $\Sigma_{\mathrm{EPR}}(t)$ is plotted as a blue line in Fig. 7.8. At $t = 0$, the noise is slightly larger than one. After a few ms the noise decreases down to around one. Then, the noise increases slightly and reaches a steady value above one for the whole measurement duration of 150 ms. The Faraday angle (not plotted in Fig. 7.8) also reaches a steady state value $\theta_4(t \to \infty) \approx 0.97 \cdot \theta_{\max}$. Since both the Faraday angle and the atomic noise reach constant values, the atoms are indeed in a steady state. But since in the steady state $\Sigma_{\mathrm{EPR}} > 1$, no entanglement is generated by dissipation only.

The output light is measured continuously in time. Until now, we have measured the atomic state at time t using the output light measured *after* time t (see Eq. (7.5)). If we also utilize the measurements *prior* to time t, the estimate for the atomic state can be improved.

Entanglement can in this way be generated *conditioned* on the measurements prior to time t. The conditional atomic noise is denoted $\Sigma_{\mathrm{EPR}}^{\mathrm{cond}}$ and was discussed extensively in Sec. 3.8. The criterion for conditional entanglement is $\Sigma_{\mathrm{EPR}}^{\mathrm{cond}} < 1$.

The conditional atomic noise can be calculated from the measurement of the conditional output light operators $S_{2c}^{\mathrm{out,cond}}(t)$ and $S_{2s}^{\mathrm{out,cond}}(t)$. The cosine operator is defined as

$$S_{2c}^{\mathrm{out,cond}}(t) = S_{2c,-}^{\mathrm{out}}(t) - \alpha S_{2c,+}^{\mathrm{out,prior}}(t), \tag{7.6}$$

and the sine operator is defined similarly. $S_{2c}^{\mathrm{out}}(t)$ was defined earlier in Eq. (7.5). The integrated output light operator $S_{2c,+}^{\mathrm{out,prior}}(t)$ prior to time t is defined as

$$S_{2c,+}^{\mathrm{out,prior}}(t) \propto \int_{t'=0}^{t} S_2^{\mathrm{out}}(t') \cos(\Omega_L t') e^{+\gamma_m (t'-t)} dt'. \tag{7.7}$$

The sine operator is defined similarly. The conditional light noise equals the sum $\left[\mathrm{Var}\left(S_{2c}^{\mathrm{out,cond}}(t)\right) + \mathrm{Var}\left(S_{2s}^{\mathrm{out,cond}}(t)\right)\right]$. α should be optimized in order to minimize the conditional light noise variances. The conditional atomic noise $\Sigma_{\mathrm{EPR}}^{\mathrm{cond}}(t)$ can then be calculated from the conditional light noise using Eq. (3.19).

The atomic coherences decay on the T_2 time scale. This is the reason for weighting the integrated output light operator given by Eq. (7.5) with a falling exponential modefunction. If we want to estimate the atomic state at time t using the measured output light *prior* to time t, we instead use an exponentially rising modefunction $\propto e^{+\gamma_m t'}$. The time constant of this exponentially rising mode is denoted $1/\gamma_m$, and typically is $1/\gamma_m$ chosen to be one half or one third of the T_2-time. This optimizes the knowledge of the atomic state at time t. The exponential rising and falling modefunctions are depicted in the pulse sequence in Fig. 7.2c.

The conditional atomic noise is plotted in Fig. 7.8 in green. After a short evolution lasting around 20 ms, the conditional noise reaches a constant value $\Sigma_{\mathrm{EPR}}^{\mathrm{cond}} = 0.80(5)$. This value is below one, demonstrating the steady state entanglement between the two atomic ensembles. This steady state entanglement is one of the main results of this chapter.

In the above experiment, the atoms started in the CSS and then evolved into an entangled steady state. We also performed an experiment where all light fields where at DC, meaning that the light fields were not pulsed. Instead, the intensities were kept at constant values similar to the peak values in the pulsed experiment. The atomic state was then measured continuously in time. The results for the atomic noise and the conditional atomic noise are shown in Fig. 7.8 in black and cyan. The results are similar to the ones obtained in the pulsed experiment. The black and cyan measurement points were obtained during more than one hour of measurement time. This demonstrates that the entanglement is maintained for the extremely long duration of one hour. The one hour limit is not a fundamental limit to how long time the entanglement can be maintained. By keeping the drive light on the atoms, the entanglement can be maintained for as long as one wishes.

We also tested that the steady state is independent of the initial state. In the pulsed experiment before, the initial atomic state was the fully pumped CSS. Now, we instead prepare an initial "noisy state" which is only partially pumped. The Faraday angle at $t = 0$ for the noisy state is $\theta_F \approx 0.6 \cdot \theta_{\mathrm{max}}$. Then, the drive light is turned on. Pump and repump light is applied simultaneous with the drive light with intensities similar to the ones used in the experiments where we started from the CSS. The atomic noise and the conditional atomic noise are plotted in Fig. 7.8 in red and yellow, respectively. After an initial evolution lasting around 50 ms, the noise settle at constant values similar to the values obtained when the initial state was the CSS. Similarly, the Faraday angle settles at a value close to the value obtained when the initial state was the CSS. This demonstrates that the steady state is independent of the initial state.

7.5 Conclusions

In this chapter, we demonstrated (a) quasi steady state entanglement generated by dissipation and (b) steady state entanglement generated by a method combining the dissipation due to the drive, pump and repump light with continuous measurements. The steady state entanglement between the two ensembles was maintained for more than one hour.

In previous experiments in our setup [16, 2, 1] where entanglement was generated by (near) QND measurements, the entanglement had a limited lifetime of

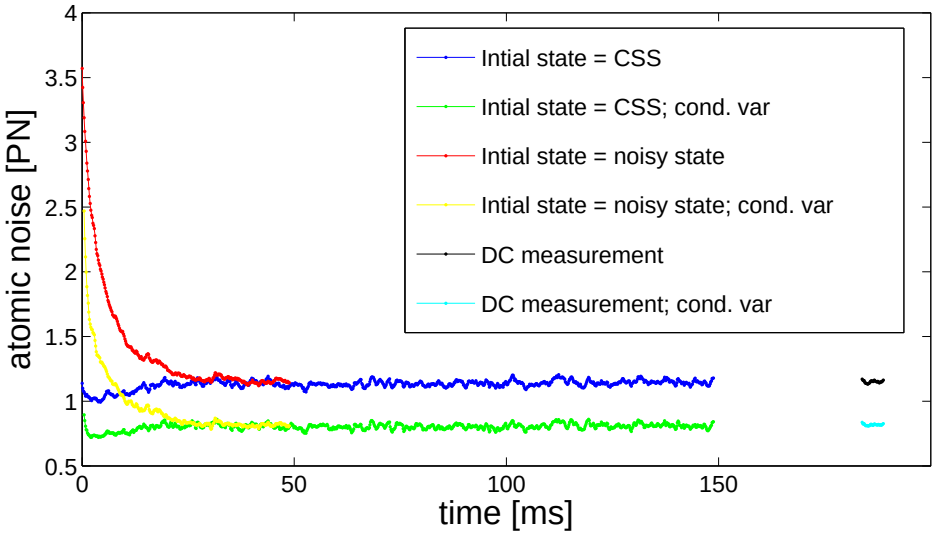

Figure 7.8: The blue and green lines show the atomic noise and the conditional atomic noise, when the initial atomic state is close to the CSS. The red and yellow lines show the atomic noise and the conditional atomic noise, when the initial atomic state equals the noisy (not fully polarized) state. The black and cyan lines show the atomic noise and the conditional atomic noise, when the drive, pump and repump fields are at DC.

a few ms. The results presented in this chapter is therefore a big step forward in terms of the time the entanglement can be maintained. Compared to the previous experiments, the obtained degree of entanglement is slightly lower. This is due to the extra decoherence introduced by the pump and repump light which was not present in the previous experiments. However, there is still room for improvements. First of all, one should increase the density of atoms. The demonstrated steady state entanglement was performed with room-temperature atoms. With a higher density of atoms, the degree of entanglement is should increase. However, with increasing number of atoms, classical noise might become a problem. This is not a fundamental limitation, and the problem should be possible to overcome. Also, the effect of the repump light is not fully understood. For instance, the repump light did not help getting better experimental results when considering the entanglement generated by dissipation only. Better understanding of the effect of the repump light might also lead to more entanglement.

The entanglement generated in the steady state was conditioned on the measurement. A variation of the experiment would be to actually do a feedback of the measured light to the atomic system using the RF magnetic coils. The entanglement will in this case be un-conditional (see the thesis [33]).

Entanglement is a useful resource in the fields of quantum information and quantum metrology. In this thesis, entanglement has been utilize to improve both a quantum memory and an atomic magnetometer. The entanglement can also be a used as resource for dissipative entanglement distillation and repeater schemes [87]. One of the strengths of entanglement generated in a steady state is that it does not depend on the initial conditions. In many of the previous experiment performed in our group, the generation of entanglement is only possible if one starts out in a state very close to the CSS. This condition is now relaxed, which might be useful in future experiments. The major strength of steady state entanglement is of course that it is in a *steady state*. This means that the entanglement can be maintained for a long period, and can be used on demand at any instance of time.

Chapter 8

Conclusions and outlook

8.1 Conclusions

In the thesis, we presented several experiments which have been implemented using an atomic system consisting of two spin-polarized atomic ensembles. The common theme of the experiments is entanglement or equivalently (for our system) two-mode squeezing. Even though entanglement between the two atomic ensembles was demonstrated 10 years ago in 2001 [16], it is still fascinating that it is possible to create entanglement between two macroscopic objects separated by half a meter and each consisting of approximately 10^{12} atoms which are contained in a volume of $(2\text{ cm})^3$. The atomic system is simple in the sense that the atoms are kept at room-temperature and contained in glass cells. There is therefore no need for cooling and trapping of the atoms using lasers or electric or magnetic fields.

During the years I have been a member of the QUANTOP group, we have succeeded in generating entanglement in several ways. These include generation of atomic entanglement by QND measurements, spin squeezing via nuclear-electronic spin entanglement [5] and generation of two-mode squeezed and entangled light [4]. The most recent experiment, which demonstrate that the atoms can be maintained in an entangled steady state for more than an hour, is truly fascinating.

Two applications of our atomic system were presented in the thesis. In the first application, the atoms are used as a magnetic sensor, and in the second application, the atoms are used as a memory for quantum information. In both of the experiments, the goal is to outperform any classical device. As a method for achieving that goal, we utilize entanglement to improve the performance of our quantum device.

The main results presented in the thesis are summarised below:

- The interaction between two spin-polarized atomic ensembles and polarized light is described with the swap and squeezing interaction theory. The

theory includes atomic decay in the model and agrees well with the experimental results for both small and large coupling strengths.

- The two spin-polarized atomic ensembles are used as a source for non-degenerate quadrature entangled two-mode squeezed light. In the experiment, 3.6 dB of squeezing is obtained. The squeezed light is generated in a single temporal mode and is naturally compatible with atomic systems based on the same (cesium) atom.

- We demonstrate an atomic magnetometer with a best sensitivity to the radio-frequency magnetic field in the sub-femtoTesla/$\sqrt{\text{Hz}}$ range comparable with the sensitivity of the state-of-the-art atomic magnetometer which uses 10^4 more atoms. Our magnetometer operates slightly above or at room-temperature. It consist of approximately 10^{12} atoms and is mainly limited by the quantum projection noise of the atoms. Using entanglement, the signal to noise ratio of the magnetometer was improved. To the best of our knowledge, our results present entanglement-assisted metrology with the highest to-date number of atoms. Our entanglement-assisted magnetometer is one of the first examples where entanglement-assisted and quantum limited sensing achives the absolute sensitivity which challenges state-of-the-art devices that do not use quantum information processing techniques.

- Entangled two-mode squeezed states of light are stored in a quantum memory consisting of two separate atomic ensembles. The input light states are squeezed by 6.0 dB and have variable squeezing phases and displacements in X-P phase space. The fidelity of the storage surpasses a calculated classical benchmark demonstrating that our memory is a true quantum memory which is capable of preserving entanglement.

- Entanglement is generated between the two atomic ensembles using dissipation as the entangling mechanism. This leads to entangled states which can be maintained for a duration up to 40 ms. Using a method combining the dissipative dynamics with a continuous measurement, we produce an entangled steady state which in the experiment is maintained for more than one hour.

8.2 Outlook

We now discuss how some of the obtained results can be improved and provide an outlook for the cell experiment.

8.2.1 Larger coupling strength

QND measurements can be utilized to entangle the two atomic ensembles. In this thesis, spin-squeezing of 25-30% (below the projection noise level) was demonstrated using near QND measurements. In the previous thesis [33], up to 36% of spin-squeezing was reported. Since a high degree of squeezing is important in many applications, it would be an important achievement to improve the degree of spin-squeezing.

In the experiment, we observe that the degree of entanglement increases with the number of atoms when the number of atoms is changed by heating the cells. However, at some point classical noise becomes a problem [1], and one no longer gains by heating. The classical noise is probably connected to imperfect optical pumping. If the classical noise could be reduced, it would be possible to obtain more squeezing by further heating the cells.

In order to obtain a high degree of squeezing, a large coupling strength κ^2 and long relaxation times (mainly T_2) are needed. This statement can also be expressed as $\gamma_{\mathrm{bad}} \ll \gamma_{\mathrm{sw}}$ where γ_{bad} is the decay rate from incoherent processes (such as for instance collisions and spontaneous emission) and γ_{sw} is the rate of the coherent swap and squeezing interaction. It is possible to achive $\gamma_{\mathrm{bad}} \ll \gamma_{\mathrm{sw}}$ only for large optical depths. Below, we present several options for increasing the optical depth using different cell geometries.

8.2.2 Cell geometry

The cells used in the current setup are cubic with inside length $L = 22$ mm. In the following, we consider other cell geometries where the area of the cell A_{cell} is different from the length L. The area and the length are defined with respect to the probe propagation direction which is chosen to be the z-direction. The dimension of the cell in the z-direction is L while the dimension of the cell perpendicular to the probe direction is $\sqrt{A_{\mathrm{cell}}}$ as depicted in Fig. 8.1.

Longer cells

Higher optical depths can be achieved with longer cells since the optical depth on resonance α is proportional to the product of the density of atoms $N_A/\left(A \cdot L\right)$ [2] and the length of the cell : $\alpha = \sigma_{\mathrm{CS}} \cdot \frac{N_A}{A \cdot L} \cdot L$ (see Eq. (2.88)). A high optical depth is good since $\tilde{\kappa}^2$ is proportional to the optical depth: $\tilde{\kappa}^2 = \alpha \cdot \eta_T$ (see Sec. 2.5).

[1] Quantum noise scales as N_A and classical noise scale as N_A^2 (in terms of variances). Classical noise therefore becomes a problem for large number of atoms.

[2] We assume that the probe beam fills the whole cell such that the cross-section area A of the probe beam equals the cell area A_{cell}.

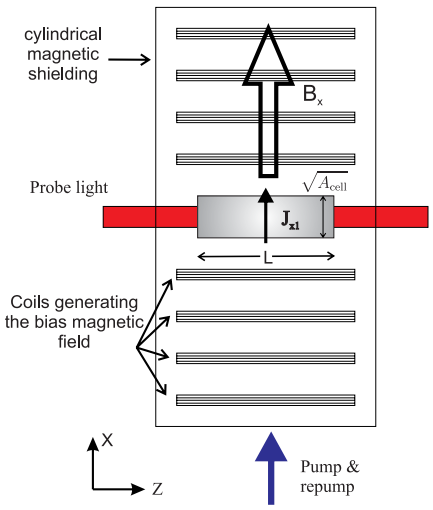

Figure 8.1: The figure shows a rectangular cell with length L and cross-section area A_{cell}. The cell is located in a cylindrical magnetic shielding with symmetry axis along the x-direction. A set of coils is used for creating the bias magnetic field B_x. The probe is propagating in the long direction of the cell.

The most important decoherence processes (spontaneous emission and two-body collisions) are independent of the length L. This means that the relaxation time T_2 should not change when increasing the length. Other decoherence processes depend on the size of the cell (for instance collisions with cell walls) and in particular can magnetic field inhomogeneity be a problem for larger cells. This is discussed below. It is realistic to increase the length of the cell by a factor of 2 or 4 (leading to a cell with length around 5 or 10 cm). The optical depth and $\tilde{\kappa}^2$ will go up with the same factor leading to a stronger interaction between the atoms and the light field.

With a longer cell, magnetic field inhomogeneity might become a problem. This is because, in our current setup, the long direction of the cell is in the z-direction, while the symmetry axis of the cylindrical magnetic shielding and the set of coils generating the static bias field is in the x-direction (see Fig. 8.1). The magnetic field is therefore most homogeneous in the x-direction and least homogeneous in the y and z-directions. With the current cell ($L = 22$ mm) and shielding (cylindrical with a length of 35 cm and a diameter of 19 cm), the decay rate due to magnetic field inhomogeneity (which should be less than the decay rate in the dark) is small compared to typical values for the swap rate (see Fig. 3.12). However, with a longer cell it will be neccesary to make new shieldings and bias coils with larger diameter to keep the magnetic field homogeneous over the entire cell length.

Using longer cells to increase the coupling between atoms and light has the clear advantage that the technology for making larger cells and larger shieldings is available.

μ-cells

In our group, there are plans for making μ-cells with dimensions around 100 μm $\times$ 100 μm $\times$ 5 mm. Such a cell has a small area $A \approx (100\ \mu\text{m})^2$ and a relatively large length $L \approx 5$ mm. Smaller cells have several advantages which are discussed below.

For a cell with a small area, less photons are needed to achieve a certain coupling strength. Remember that $\tilde{\kappa}^2 = \alpha \cdot \eta_T$ and that the depumping parameter (the probablity for spontaneous emission) $\eta_T = \frac{N_{\text{ph}}\sigma_{\text{CS}}}{A}\frac{(\gamma/2)^2}{\Delta^2}$ is proportional to the intensity of the probing light $I = N_{\text{ph}}/A$. Assume that we reduce the cell area while keeping the depumping parameter constant. When reducing the area by some factor, the number of photons should be reduced by the same factor (if we choose to not change the probe detuning). The number of photons can be reduced by either reducing the probe power or the probe duration. Reducing the probe duration has the obvious advantage that the interaction happens on a faster time-scale. In the current setup, the probe duration is around 1 ms, which means that the experiments can be run at a 1 kHz rate. Faster rates are of course important in applications where speed is important.

With shorter interaction times, the atomic system would be compatible with single photons which for instance could be stored in the atomic ensemble. Single photons with a bandwidth of less than 10 MHz are available in our group [88, 89].

An interesting experiment would be to generate a single collective excitation in an atomic ensemble by detecting a single photon as in the DLCZ scheme [12]. Such experiments have been done using cold [25] or stationary atoms in a cell filled with buffer gas [23] but not with room-temperature moving atoms.

In our experiments, a weak quantum field is co-propagating with a strong local oscillator (LO) field. The quantum field and the LO field have orthogonal polarizations. With our current setup, the LO field consists of approximately $N_{\text{ph}} = 10^{12}$ photons. If we want to detect a single photon in the quantum field, we should be able to filter out a single photon from the 10^{12} photons in the LO field. This is not possible with so many photons in the LO field. However, with smaller cells, less photons are needed in the LO field. This way, it might be possible to filter out a single photon in the quantum field.

The μ-cells can be located in a low-finess cavity [3] . Due to the several round-trips of the probe light, the probe sees an effective optical depth which is increased by the finesse. This might be a promising way for achiving a stronger coupling between light and a room-temperature atomic ensemble.

[3] There will be some optical losses since the light has to pass the glass walls of the cell several times. The finesse of the cavity will therefore be low.

8.2.3 Nano-mechanical membrane–atomic ensemble interface

In our group, there are plans to start a collaboration between the "membrane" sub-group and the "cell experiment" sub-group [4]. The membrane sub-group [90] is working on the physics of a nano-mechanical oscillator (the membrane). The membrane can be connected to an LC-circuit consisting of a capacitor and an RF coil. Oscillations of the membrane will give rise to an oscillating current flowing in the LC-circuit which generate a small RF magnetic field. An atomic ensemble can be used as a very sensitive sensor for this small RF field. In this way, the quantum state of the membrane can be measured. The approach with the RF coil can be used to make a nano-mechanical membrane–atomic ensemble interface. The membrane, the LC-circuit and the atomic ensemble are compatible since the Larmor frequency of the atoms and the LC resonance frequency can be tuned to match the mechanical resonance frequency of the membrane. A different approach would be to connect the membrane and an atomic ensemble optically with a laser beam [91]. A hybrid nano-mechanical membrane–atomic ensemble system would be very interesting, and possible experiments could be to transfer quantum states from one system to the other and entangle the membrane with the atomic ensemble.

8.2.4 Possible experiments using the current setup

There are several interesting experiments which can be done using our current setup. These include atom-atom teleportation and quantum memory.

Teleportation

Quantum teleportation between two atomic systems has been realized with ions (see the review [92]) in close proximity to one another, and also with ions separated by one meter [93]. However, atom-atom teleportation has not yet been demonstrated with atomic ensembles. Several schemes have been proposed for implementing atom-atom teleportation in our setup in the previous Ph.D. thesis [33]. Those protocols utilize either two or three atomic ensembles. We are currently considering a protocol with two atomic ensembles which are polarized in the same direction. In this protocol, either a high coupling strength or squeezed light is needed for a high fidelity of the teleportation. Implementing this protocol and achieving atom-atom teleportation is a future goal for the cell experiment which should be possible to achieve using our existing setup.

[4] See group webpage for a description of the current experiments. www.quantop.nbi.dk.

Quantum memory

Both coherent [17] and two-mode squeezed [1] light states have been stored in our atomic memory. The storage fidelities have been above the classical benchmark fidelities, but still far below unity. A future goal would be to improve the storage fidelity and also to increase the storage time which currently has been a few ms.

So far retrieval of the stored states has not been demonstrated in our setup. The retrieval could be done by (1) shining light through the ensembles with a first pulse (where one quadrature of the stored state is transferred to the first pulse), (2) perform a measurement on the atomic state with a second pulse (where the second quadrature of the stored state is measured), and (3) doing a feed-forward on the first pulse using the measurement result obtained with the second pulse. This way, the state of the atoms is transferred to the first pulse of light. With the current setup, the scheme is unfortunately unrealistic, since light travels at the speed of light, leaving not much time for the measurement and the feed-forward (in the previous experiments the pulses have been of millisecond duration). However, if the retrieved state should later be stored in a different quantum memory, it is not neccesary to do the feed-forward on the light. Instead the feed-forward can be done on the second memory. This is easier, since the coherence time of the memory would be at least several milliseconds. Then, there would be plenty of time to do the feed-forward.

8.2.5 Quantum network

A quantum network [11] consists of nodes (more than two) connected by quantum channels (light). At the nodes, which could be atomic ensembles, ions or other atomic systems, quantum information or entanglement is stored and processed.

In our setup, it would be interesting to increase the number of atomic ensembles from two to four. This can be done simply by duplicating the existing setup. This opens up for the possibility to have a network of multi-entangled atomic ensembles/memories. Multi-entangled states have been generated using ions [66, 94] and very recently with four cold atomic ensembles [95]. There has also been interest in studying the dynamics of multi-particle entangled states under the influence of decoherence and observing the evolution from a multi-particle entangled state to an unentangled state using trapped ions [96]. Similar experiments could be done with atomic ensembles.

8.3 Final remarks

In the thesis, it is demonstrated that a relatively simple system consisting of two room-temperature atomic ensembles can be utilized for many different experiments such as the generation of two-mode squeezed and entangled light, atomic

magnetometry, quantum memory and generation of atomic entanglement. With further developments as outlined in this chapter, stronger coupling between atoms and light is possible, leading to improved performance and the possibility to couple the atomic ensembles to single photons.

Appendix A

Details of the temporal mode analysis

In this appendix, we describe the details of the temporal mode analysis discussed in Sec. 4.3.4. The procedure described below is used for obtaining Figs. 4.6, 4.7 and 4.8 from the measured covariance matrices C_X (the light noise) and C_Y (the shot noise).

The recorded data is represented by the column vector $X = (X(t_1), ..., X(t_N))^{tr}$, where the total measurement time T is discretized into N time bins. Using the measured $N \times N$ covariance matrix C_X, we can find the variance of any temporal mode. For a given mode u_n, the variance of the signal X is $\mathrm{Var}(X_n) = u_n^\dagger C_X u_n$ using matrix notation. Note that u_n is a column vector and $u_n^\dagger$ is a row vector.

As discussed in Sec. 4.3.3, the measured spectrum of the shot noise (see Fig. 4.5) is not flat due to a peaked detection system. But let us for simplicity first analyze the situation with a flat shot noise spectrum. In time domain, this corresponds to a delta-correlation $\langle Y(t)Y(t')\rangle = \mathrm{Var}(Y)\,\delta(t-t')$ where $Y(t)$ is the data representing the shot noise. We use the notation Y for the shot noise data and X for the (squeezed) light noise data. For delta-correlated shot noise, the variance $\mathrm{Var}(Y_n) = \mathrm{Var}(Y)$ is independent of the modefunction (as long as the mode function u_n is normalized). We are interested in the ratio

$$\frac{LN_n}{SN_n} = \frac{\mathrm{Var}(X_n)}{\mathrm{Var}(Y_n)} = \frac{u_n^\dagger C_X u_n}{u_n^\dagger C_Y u_n}, \tag{A.1}$$

which is the output light noise normalized to the shot noise for the temporal mode u_n. If we can find a mode where this ratio is below one, the output light in this mode is squeezed. For delta-correlated shot noise, Eq. (A.1) is simplified to $LN_n/SN_n = \mathrm{Var}(X_n)/\mathrm{Var}(Y)$. Since $\mathrm{Var}(Y)$ is a constant, we just have to consider $\mathrm{Var}(X_n)$.

The question is now, which modes should we consider? The question is answered by the Karhunen-Loéve theorem [55, 56] which states that we can find a set of *mutually uncorrelated modes* by performing a spectral decomposition of the C_X matrix. The interesting modes are the eigenfunctions and the variances of these modes are the eigenvalues. To be specific, we need to solve the eigenvalue equation

$$C_X \phi_n = \lambda_n \phi_n \quad (n = 1, 2, ..., N), \tag{A.2}$$

where λ_n are the eigenvalues and ϕ_n are the eigenvectors (column vectors). Solving the eigenvalue equation means that given the matrix C_X, which is measured in the experiment, we should find the eigenvectors ϕ_n and the eigenvalues λ_n. In practice, this is done on a computer using some mathematical software (matlab). We can also write Eq. (A.2) in matrix notation

$$C_X \Phi = \Phi \Lambda. \tag{A.3}$$

Φ is the matrix where the n'th column consists of the n'th eigenvector ϕ_n, and Λ is a diagonal matrix with the eigenvalues λ_n in the diagonal. Since C_X is symmetric, or hermitian if the matrix is complex, the eigenvectors are othonormal. In matrix notation, this means that the matrix Φ is orthogonal (or unitary if the matrix is complex) $\Phi^\dagger \Phi = \Phi \Phi^\dagger = \mathbb{1}$. The matrix $\mathbb{1}$ is the unity matrix with ones in the diagonal and zeros elsewhere. The dagger symbol $\dagger$ means transposing the vector/matrix and complex conjugate the elements. The fact that the modes given by the eigenvectors ϕ_n are uncorrelated is in mathematical terms described by the equation

$$\phi_n^\dagger C_X \phi_m = 0 \quad \text{for all } n \neq m. \tag{A.4}$$

This equation is a direct consequence of the eigenvalue equation (A.3) which states that the matrix $\Phi^\dagger C_X \Phi = \Lambda$ is a diagonal matrix. Having found the eigenvectors and the eigenvalues, we can now calculate the light noise in shot noise units $LN_n/SN_n = \lambda_n/\mathrm{Var}\,(Y)$ for each mode ϕ_n.

Using the fact that Φ is unitary, one can show that the smallest eigenvalue equals the smallest variance which can be obtained with any mode. The best obtainable squeezing is therefore obtained with the mode ϕ_1 corresponding to the smallest eigenvalue λ_1 (where we labelled the eigenvalues in ascending order). Similarly, the largest eigenvalue λ_N equals the largest variance which can be obtained for any mode. I.e., the eigenvector ϕ_N corresponds to the most anti-squeezed mode.

In the above, it was assumed that the shot noise spectrum is flat, but in the experiment the shot noise spectrum is actually peaked. This makes the procedure described above a bit more complicated since both LN_n and SN_n depend on the mode u_n. In loose terms, we now have to first divide the light noise with the shot noise (see Eq. (A.1)) and then solve the eigenvalue equation. This way, we can

correct for the non-flatness of the shot noise spectrum. Below, we go through the different steps in this procedure.
(a) One should first solve the eigenvalue equation for the shot noise

$$\Phi_{SN}^{\dagger} C_Y \Phi_{SN} = \Lambda_{SN}, \tag{A.5}$$

where the subscript SN is used for the solution to this eigenvalue equation. The eigenfunctions are othonormal $\Phi_{SN}^{\dagger}\Phi_{SN} = \Phi_{SN}\Phi_{SN}^{\dagger} = \mathbb{1}$ since C_Y is hermitian.
(b) Now, do a transformation of the C_X covariance matrix. Let

$$C_X \rightarrow \Phi C_X \Phi, \tag{A.6}$$

where the transformation matrix Φ is defined by

$$\Phi = \Phi_{SN}\Lambda_{SN}^{-1/2}\Phi_{SN}^{\dagger}. \tag{A.7}$$

The matrix exponential $\Lambda_{SN}^{-1/2}$ makes sense since Λ_{SN} is a diagonal matrix. The matrix Φ is hermitian, i.e. $\Phi = \Phi^{\dagger}$. However, it is not unitary since $\Phi^{\dagger}\Phi = \Phi\Phi^{\dagger} = \Phi^2 = \Phi_{SN}\Lambda^{-1}\Phi_{SN}^{\dagger} \neq \mathbb{1}$. The transformation given by Eq. (A.6) does the job of dividing the light noise by the shot noise while taking into account that $\mathrm{Var}\,(Y_n)$ depends on the mode ϕ_n.
(c) Then, solve the eigenvalue equation

$$\Phi_{\widetilde{LN}}^{\dagger}\left(\Phi C_X \Phi\right)\Phi_{\widetilde{LN}} = \Lambda_{\widetilde{LN}} \tag{A.8}$$

The subscript $\widetilde{LN}$ is used for the solution to this eigenvalue equation. Solving the eigenvalue equation means finding the eigenvector matrix $\Phi_{\widetilde{LN}}$ and the eigenvalue matrix $\Lambda_{\widetilde{LN}}$.
(d) Construct a new matrix V which is defined by

$$V = \Phi\Phi_{\widetilde{LN}}. \tag{A.9}$$

In terms of the matrix V, the eigenvalue equation (A.8) reads

$$V^{\dagger} C_X V = \Lambda_{\widetilde{LN}}. \tag{A.10}$$

We can also calculate

$$V^{\dagger} C_Y V = \mathbb{1}, \tag{A.11}$$

where we used that Φ_{SN} is unitary and that it satisfy the eigenvalue equation (A.5).

The modes of interest v_n are the columns of the V matrix. For each of these modes, the shot noise variance is given by $v_n^{\dagger} C_Y v_n = 1$ and the light noise variance is given by $v_n^{\dagger} C_X v_n = \lambda_{\widetilde{LN}}(n)$ where $\lambda_{\widetilde{LN}}(n)$ is the (n,n) element of the diagonal matrix $\Lambda_{\widetilde{LN}}$. In matrix notation, the light noise divided by the shot noise is

$$\frac{LN}{SN} = \frac{V^{\dagger} C_X V}{V^{\dagger} C_Y V} = \frac{\Lambda_{\widetilde{LN}}}{\mathbb{1}} = \Lambda_{\widetilde{LN}}. \tag{A.12}$$

The modes v_n are uncorrelated since $V^{\dagger} C_X V$ is diagonal.

Appendix B

Calibration of the RF magnetic field

In the magnetometry experiment, we apply the RF magnetic field B_{RF} separately to the two atomic ensembles using the RF coils. The current through each coil is generated using an "RF card" which apply an oscillating voltage to the coil. The typical frequency of the voltage is $\omega = 2\pi \cdot 322$ kHz which is set to equal the atomic Larmor frequency. The RF card has the maximum *set* voltage $U_{set} = 1$ V. At this set voltage, the RF field amplitude B_{RF} was measured using a pick-up coil positioned close to the cell number two inside the shielding. This measurement is described in Sec. B.2, and we found the value $B_{\mathrm{RF}} = 1.1 \cdot 10^{-10}$ T. This field is "large", and we are interested in applying smaller magnetic fields. We typically use RF set voltages in the range from 312.5 μV to 1.25 mV which generate RF magnetic field amplitudes B_{RF} in the range of 30-140 fT (see table B.1). However, the pick-up coil is not sensitive enough for the detection of such small fields. We therefore extrapolate B_{RF} at low RF set voltages from the magnetic field amplitude B_{RF} measured at $U_{set} = 1$ V with the pick-up coil. At the low settings, the output voltage of the RF card is not proportional to the set voltage. This has to be taken into account, and the details can be found in Sec. B.3.

B.1 Impedance of the pick-up coil

The impedance of the pick-up coil is an important parameter we need to determine. The pick-up coil is modelled as a an inductor L in series with a resistor R_1. The inductor and the resistor are in parallel with a capacitance C. The schematic diagram of the pick-up coil is shown in Fig. B.1 top. We can calculate the impedance Z_{coil} of the pick-up coil to be

$$Z_{coil} = \frac{(R_1 + i\omega L) \cdot \frac{1}{i\omega C}}{R_1 + i\omega L + \frac{1}{i\omega C}}. \tag{B.1}$$

For large frequencies, where the resistance R_1 can be neglected ($R_1/L \ll \omega$), the above formula can be rewritten as

$$Z_{coil} \approx \frac{i\omega L}{1-(\omega/\omega_{res})^2} \quad \text{for} \quad R_1/L \ll \omega, \tag{B.2}$$

where $\omega_{res} \equiv 1/\sqrt{LC}$ is the resonance frequency of the coil. Below the resonance frequency the formula simplifies to

$$Z_{coil} \approx i\omega L \quad \text{for} \quad R_1/L \ll \omega \quad \text{and} \quad \omega^2 \ll \omega_{res}^2. \tag{B.3}$$

The approximation $Z \approx i\omega L$ is valid in the experiment for the frequency $\omega = 2\pi \cdot 322$ kHz.

The self-inductance L of the pick-up coil can be estimated in the following way. Suppose we apply an RF magnetic field at the position of the pick-up coil in the direction perpendicular to plane of the coil. The oscillating magnetic field induces an electro-motive force (EMF), and a current I will run through the coil. The pick-up coil makes its own magnetic field B to cancel the applied RF field (Lenz's law). The generated magnetic field can be calculated from the formula for a thin coil:

$$B = \frac{N_w \mu_0 I}{2r}, \tag{B.4}$$

where N_w equals the number of windings, μ_0 is the vacuum permeability, I is the current and r is the radius of the coil. B is the generated magnetic field in the center of the coil. The flux through the pick-up coil from the generated magnetic field can be estimated to be

$$\Phi \approx B \cdot A_{coil} = \frac{N_w \mu_0 I}{2r} \cdot N_w \pi r^2 = \frac{\pi}{2} N_w^2 \mu_0 I r, \tag{B.5}$$

where A_{coil} is the area of the coil. The self-inductance of the coil is defined by the equation $\Phi = L \cdot I$, and we therefore find

$$L \approx \frac{\pi}{2} N_w^2 \mu_0 r. \tag{B.6}$$

For the pick-up coil used in the experiment, we have the following numbers: $N_w = 60$, $2r = 0.021$ m, $\mu_0 = 4\pi \cdot 10^{-7}$ N/A^2. This leads to an inductance $L = 75$ μH. The impedance at the frequency $\omega = 2\pi \cdot 322 \cdot 10^3$ s^{-1} is $Z_{coil} = i\omega L = i \cdot 151$ Ω. The resistance $R_1 = 6.5$ Ω could also have been included in the calculation of the impedance, but since $R_1 \ll \omega L$ it can safely be neglected.

Measured inductance and resonance frequency of the pick-up coil

We now present measurements of the inductance and the resonance frequency of the pick-up coil. The schematic diagram of the measurement is shown in Fig.

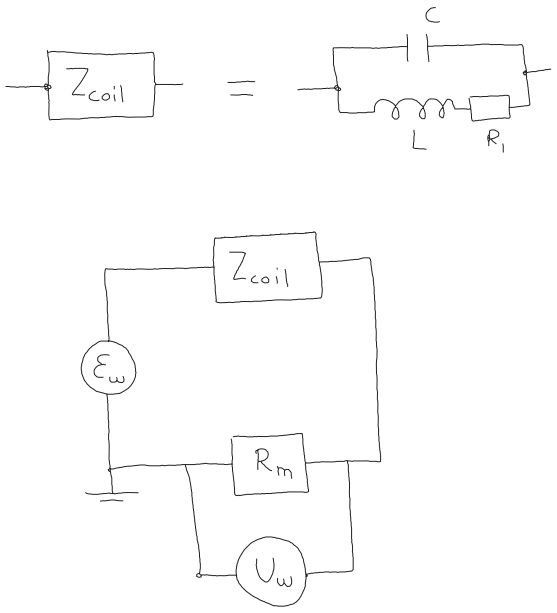

Figure B.1: Top: Impedance Z_{coil} of the pick-up coil. Bottom: Schematics of the setup for testing the coil/measuring the RF magnetic field.

B.1. The pick-up coil with impedance Z_{coil} was connected to a function generator which applied an oscillating voltage ϵ [1]. The amplitude of the applied voltage was fixed and the frequency was varied. The signal U was monitored on an oscilloscope with an input resistance $R_m = 50\ \Omega$. The amplitude $|U|$ and the phase of the signal (with respect to the applied voltage) was measured and the results are plotted in Fig. B.2. Circles represent the measured amplitude $|U|$, and the inset shows the measured phase as dots connected by lines. The frequency was varied from 200 Hz to 2 MHz. The measured signal is expected to be on the form

$$U = \frac{R_m \epsilon}{Z_{coil} + R_m}, \tag{B.7}$$

since $U = R_m I$ and $\epsilon = (Z + R_m)\, I$. The amplitude $|U|$ was fitted to a function of the form

$$|U| = R_m \, |\epsilon| \cdot \left\{ \frac{\omega^2 L^2}{\left[1 - (\omega/\omega_{res})^2\right]^2} + R_m^2 \right\}^{-1/2}, \tag{B.8}$$

where we used the expression given by Eq. (B.2) for the impedance of the coil. The fit is shown in Fig. B.2 as a solid line, and the obtained fit parameters are $L = 62.5(13) \cdot 10^{-5}\ \mu$H and $f_{res} \equiv 2\pi \cdot \omega_{res} = 2.8(3)$ MHz. Using the fitted parameters and Eq. (B.2), we calculate the impedance of the pick-up coil to be

[1] We use complex notation for the impedance and the voltages. The voltages have and amplitude (the absolute value of the complex signal) and a phase.

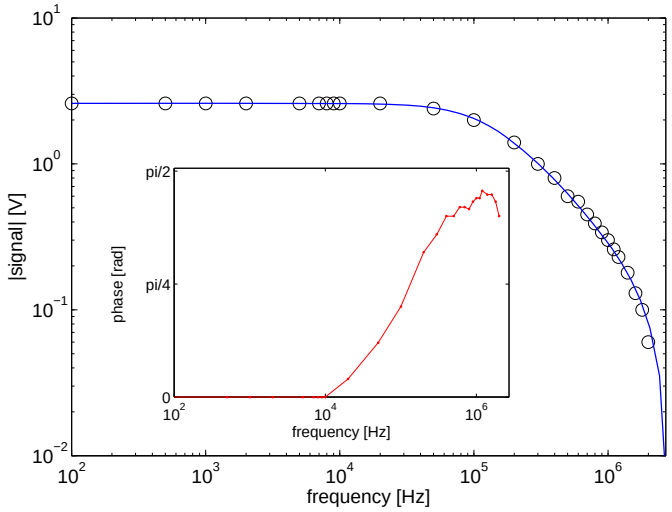

Figure B.2: The pick-up coil was connected to a function generator and the voltage U was measured on an oscilloscope with an input resistance of 50 Ω. The circles shows the amplitude of the measured signal. The solid line is a fit. The inset shows the phase difference between the input signal and the measured signal.

$Z = i \cdot 128(3)$ Ω at the frequency of 322 kHz (which is much below the resonance frequency).

B.2 Measurement of the RF field with the pick-up coil

The measurement of the RF magnetic field amplitude B_{RF} with the pick-up coil can be represented by the schematics shown in Fig. B.1 bottom. The pick-up coil is represented by the impedance Z_{coil}. The oscillating magnetic field creates a flux through the pick-up coil which generates an electromotive force ϵ_ω. The current through the pick-up coil can be found from measuring the voltage U_ω across the measurement resistor $R_m = 50\Omega$. The amplitude U_ω is defined from the time dependent voltage $U(t) = U_\omega e^{i\omega t}$ where we have used the complex notation for the voltage. The voltage U_ω and the electromotive force ϵ_ω are related by the formula

$$\epsilon_\omega = (R_m + Z_{coil})\, I_\omega = \left(1 + \frac{Z_{coil}}{R_m}\right) U_\omega, \tag{B.9}$$

since the measured voltage over the resistor R_m is given by $U_\omega = R_m I_\omega$. To convert voltage U_ω into ϵ_ω, we need to know the impedance of the pick-up coil Z_{coil} and the measurement resistance R_m.

The electromotive force can be related to the complex RF field $B_{\mathrm{RF}}(t) = B_{\mathrm{RF}} e^{i\omega t}$ by the formula

$$\epsilon_\omega = -\frac{d\Phi}{dt} = -N_w A_{coil} i\omega B_{\mathrm{RF}}. \tag{B.10}$$

Isolating B_{RF}, we find

$$B_{\mathrm{RF}} = \frac{-\epsilon_\omega}{N_w A_{coil} i\omega} = \frac{i\,(1 + Z_{coil}/R_m)\,U_\omega}{N_w A_{coil}\omega} \quad \text{and} \quad |B_{\mathrm{RF}}| = \frac{|1 + Z_{coil}/R_m|\,|U_\omega|}{N_w A_{coil}\omega}. \tag{B.11}$$

In the actual measurements, the pick-up coil was inserted in the magnetic shielding close to the cell number two. The RF magnetic field was then applied using the RF set value $U_{set} = 1$ V and the frequency 322 kHz. The pick up coil was connected to a spectrum analyzer, and we measured the signal $U_{SA} = 1.2\mu$V on the spectrum analyzer. Since the spectrum analyzer measures the power $P_{SA} = U_{SA}^2/R_m$ over the resistance $R_m = 50\Omega$, U_{SA} is an rms voltage. The amplitude of the voltage is $U_\omega = \sqrt{2}U_{SA} = 1.7\mu$V. If the voltage U_ω is inserted in Eq. (B.11) together with the measured impedance $Z_{coil} = i \cdot 128(3)\ \Omega$, we find the magnetic field $B_{\mathrm{RF}} = 1.11 \cdot 10^{-10}$ T for the RF set voltage $U_{set} = 1$ V.

We can estimate the uncertainty on B_{RF}. The uncertainty on U_ω is estimated to be 15%. The uncertainty on the coil diameter is estimated to be 5% giving a 10% uncertainty on A_{coil}. The uncertainties on Z_{coil}, R_m, N_w and ω are negligible. In total, we have the uncertainty on the $\delta B_{\mathrm{RF}}/B_{\mathrm{RF}} = \sqrt{0.15^2 + 0.1^2} = 18\%$. The result for the RF magnetic field including uncertainty is therefore $B_{\mathrm{RF}} = 1.1(2) \cdot 10^{-10}$ T.

B.3 RF card calibration

B.3.1 Extrapolation

As described in the previous section, the RF magnetic field amplitude $B_{\mathrm{RF}} = 1.1(2) \cdot 10^{-10}$ T was measured with the pick-up coil for the specific set voltage $U_{set} = 1$ V. Since the pick-up coil is not adapted to measuring smaller RF magnetic fields, we extrapolate B_{RF} at smaller set voltages using the measured value at $U_{set} = 1$ V. Assuming $B_{\mathrm{RF}} \propto U_{set}$, we find that $B_{\mathrm{RF}} = c \cdot U_{set}$ with $c = 1.1 \cdot 10^{-10}$ T/V. In the next sections it is shown that this formula is only valid for U_{set} in the range from 1.25 mV to 1 V. For smaller set voltages $U_{set} < 1.25$ mV, we estimate B_{RF} from either the measured output voltage of the RF card or the signal from the atomic magnetometer

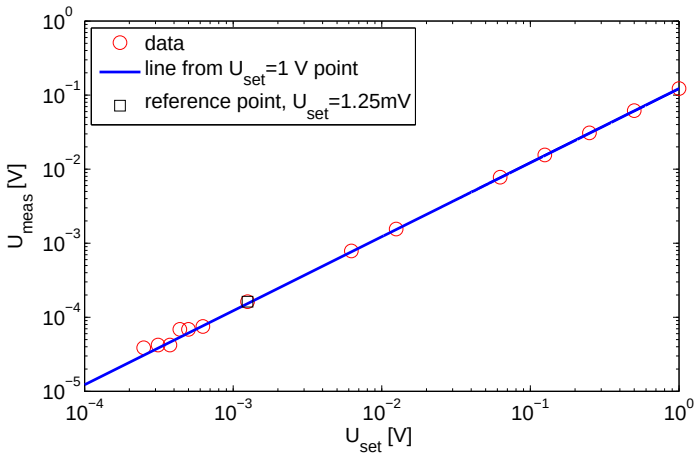

Figure B.3: The output of the RF card was connected to a spectrum analyzer. The figure shows the measured voltages for different set voltages. The line is found from the value at $U_{set} = 1$ V. The measured voltage is proportional to the set voltage except for the lowest set voltages.

B.3.2 Output RF voltage

It is first tested whether the output of the RF card is proportional to the set voltage. The output of the RF card was connected to a spectrum analyzer and the output voltage U_{meas} was measured for different set voltages U_{set}. The results are shown in a double logarithmic plot in Fig. B.3. The measured voltage for $U_{set} = 1$ V is used to plot a line $U_{meas} = \widetilde{c} \cdot U_{set}$ where $\widetilde{c}$ is the slope of the line. If the measured voltages would be proportional to the set voltage, all the data points would lie on the line. We see that the measured voltage is indeed proportional to the set voltage for voltages down to around $U_{set} = 1.25$ mV. Below this set voltage, the measured voltage is not proportional to the set voltage [2]. For set voltages $U_{set} < 1.25$ mV, we can use the actual measurements (red circles) and not the line to extrapolate B_{RF} if we assume that $B_{\mathrm{RF}} \propto U_{meas}$. The values for U_{meas} and the estimated B_{RF} are shown in table B.1 under the columns U_{meas} and $B_{\mathrm{RF}} \propto U_{meas}$.

B.3.3 Magnetometer signal

The most sensitive way of measuring the RF field amplitude B_{RF} is with the atomic magnetometer. We therefore measured B_{RF} for small set voltages using the atomic magnetometer. Figure B.4 shows the mean value of the measured signal $|\langle S_{2c}^{\mathrm{out}} + iS_{2s}^{\mathrm{out}} \rangle|$ as a function of the set voltage in a double logarithmic plot. The RF field was applied to cell number two only. A line $|\langle S_{2c}^{\mathrm{out}} + iS_{2s}^{\mathrm{out}} \rangle| = \overline{c} \cdot U_{set}$

[2] This is partly due to a digitization of the output voltage.

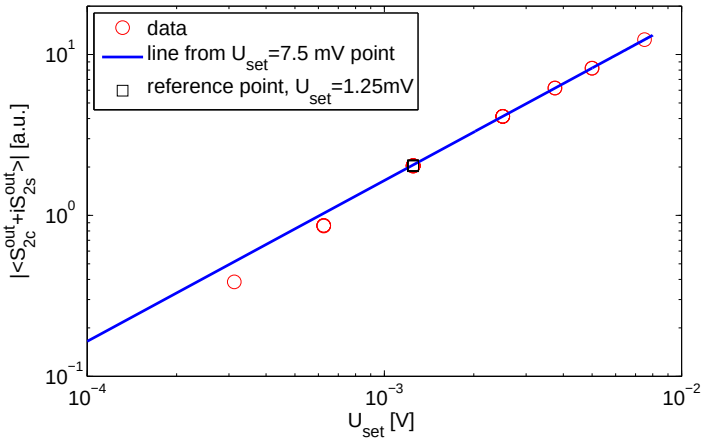

Figure B.4: Measured signal $|\langle S_{2c}^{\text{out}} + iS_{2s}^{\text{out}}\rangle|$ for different RF set voltages U_{set}. The line is found from the measured signal at the set voltages 7.5 mV. The measured signal is proportional to the set voltages except for the lowest set voltages.

is also plotted where the slope $\overline{c}$ is found from the measured signal at the set voltage $U_{set} = 7.5$ mV. For set voltages in the range 1.25 mV to 7.5 mV, we see from Fig. B.4 that the signal is proportional to the set voltage.

For set voltages smaller than 1.25 mV the signal is not proportional to the set voltage. If we assume that B_{RF} is proportional to the signal, we can find B_{RF} from the measured signals also for set voltages smaller than 1.25 mV. The measured signals and the estimated B_{RF} are shown in table B.1 under the columns $|\langle S_{2c}^{\text{out}} + iS_{2s}^{\text{out}}\rangle|$ and $B_{\text{RF}} \propto |\langle S_{2c}^{\text{out}} + iS_{2s}^{\text{out}}\rangle|$.

B.3.4 Comparison

As seen in table B.1, our estimate for B_{RF} (for $U_{set} < 1.25$ mV) depends on whether we assume $B_{\text{RF}} \propto U_{meas}$ or $B_{\text{RF}} \propto |\langle S_{2c}^{\text{out}} + iS_{2s}^{\text{out}}\rangle|$. This requires some explanation.

For the three set voltages $U_{set} = 1.25$ mV, 625 μV and 312.5 μV we measured both U_{meas} and $|\langle S_{2c}^{\text{out}} + iS_{2s}^{\text{out}}\rangle|$. The correlations between U_{meas} and $|\langle S_{2c}^{\text{out}} + iS_{2s}^{\text{out}}\rangle|$ are plotted in Fig. B.5. The figure also shows a linear fit $|\langle S_{2c}^{\text{out}} + iS_{2s}^{\text{out}}\rangle| = a \cdot U_{meas} + b$. The points lie almost perfect on the line which shows that the two measured parameters are strongly correlated [3].

The fitted offset b was expected to be zero, but from Fig. B.5 we see that it

[3] We are fitting two parameters (the slope and the offset of the line) using three data points. It would have been better with more data points, but unfortunately only three points were available. The statistical uncertainties on the measured points are small, so we still trust the fit even though only three points were used.

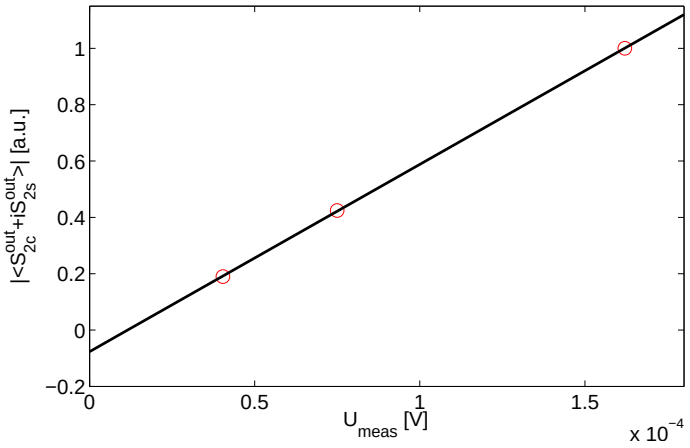

Figure B.5: The figure shows the correlation between the measured voltage and the measured signal for the three set voltages $U_{set} = 1.25$ mV, 625 μV and 321.5 μV. The black line is a linear fit to the data.

has a small non-zero value. It is not understood why there is this small offset. It could be due to a small leak-through of the RF card, such that when $U_{set} = 0$ V, then U_{meas} has a small value, and a small magnetic field B_{RF} is present. It could also be due to an electronic offset in the signal, such that even in the abscence of the magnetic field $B_{\mathrm{RF}} = 0$, the signal $|\langle S_{2c}^{\mathrm{out}} + iS_{2s}^{\mathrm{out}}\rangle|$ has a small value.

The fact that the offset b is non-zero implies that the estimate for B_{RF} depends on whether we assume that $B_{\mathrm{RF}} \propto |\langle S_{2c}^{\mathrm{out}} + iS_{2s}^{\mathrm{out}}\rangle|$ or $B_{\mathrm{RF}} \propto U_{meas}$. Since it is not clear what the reason for the offset is, I choose to average the estimates for the magnetic field. At the set voltage $U_{set} = 321.5$ μV, we obtain the average value $B_{\mathrm{RF}} \approx (26 + 34)$ fT ≈ 30 fT. The uncertainty on this value is estimated to be 22% (where most the uncertainty comes from the uncertainty on B_{RF} for the 1 V set voltage). Our estimate for the magnetic field is therefore 30(7) fT at the set voltage $U_{set} = 321.5$ μV [4].

[4] In the paper [2] we stated the number $B_{\mathrm{RF}} = 36$ fT for the RF magnetic field. This number is slightly different from the number $B_{\mathrm{RF}} = 30$ fT stated in this thesis. The numbers differ since in the paper we assumed $B_{\mathrm{RF}} \propto U_{meas}$ (see last column of Tab. B.1) and we used a slightly higher value for the impedance of the pick-up coil.

U_{set}	$\lvert\langle S_{2c}^{\text{out}} + iS_{2s}^{\text{out}}\rangle\rvert$ in a.u.	$B_{\text{RF}} \propto \lvert\langle S_{2c}^{\text{out}} + iS_{2s}^{\text{out}}\rangle\rvert$	U_{meas} in a.u.	$B_{\text{RF}} \propto U_{meas}$
1 V		$1.1 \cdot 10^{-10}$ T		$1.1 \cdot 10^{-10}$ T
1.25 mV	1	138 fT	1	138 fT
625 μV	0.424	59 fT	0.462	64 fT
312.5 μV	0.190	26 fT	0.249	34 fT

Table B.1: B_{RF} for different set voltages U_{set}. B_{RF} is assumed to be proportional to U_{set} for set voltages in the range from 1.25 mV to 1 V. For set voltages lower than 1.25 mV, B_{RF} is assumed to be proportional to the either the measured signal $\lvert\langle S_{2c}^{\text{out}} + iS_{2s}^{\text{out}}\rangle\rvert$ or the measured output voltage U_{meas} of the RF card.

Appendix C

κ-calibration by RF displacement

In the magnetometry experiment, κ^2 was measured for a specific value of the probe light power $P \approx 5$ V using the mean value transfer method described in Sec. 3.6.1. However, some magnetic field measurements were done with a higher probe power $P \approx 9$ V. We therefore want to extrapolate the value of κ^2 at this higher power. This was done in the following way.

We apply a particular RF magnetic field B_{RF} with a specific duration τ to the atomic ensembles. The magnetic field creates a mean value in the atomic spins $|\langle J_{z1} + J_{z2}\rangle + i\,\langle J_{y1} + J_{y2}\rangle|$ here written using complex notation. The mean value in the spins can be read out in the signal

$$\left|\left\langle S_{2c}^{\mathrm{out}} + iS_{2s}^{\mathrm{out}}\right\rangle\right| = \kappa\sqrt{\eta_{\mathrm{det}}}\sqrt{\frac{\Phi}{2\,|J_x|}}\,|\langle J_{z1} + J_{z2}\rangle + i\,\langle J_{y1} + J_{y2}\rangle|\,. \tag{C.1}$$

For the probe power $P = 5$ V where κ is known, we can find the atomic displacements normalized to $\sqrt{|J_x|}$:

$$|\langle J_{z1} + J_{z2}\rangle + i\,\langle J_{y1} + J_{y2}\rangle|\,/\sqrt{|J_x|}. \tag{C.2}$$

On the other hand, if we do not know κ (since we changed the probe power), but know the atomic displacement (since we apply the same magnetic field as before and uses the same number of atoms as before), we can find κ from the measured signal $|\langle S_{2c}^{\mathrm{out}} + iS_{2s}^{\mathrm{out}}\rangle|$ using Eq. (C.1).

Once we know κ, we can calculate the atomic noise in PN-units Σ_{EPR} from the measured output variances $[\mathrm{Var}\,(S_{2c}^{\mathrm{out}}) + \mathrm{Var}\,(S_{2s}^{\mathrm{out}})]$ using the atomic noise reconstruction formula given by Eq. (2.85).

Appendix D

Details of the data analysis

In this appendix, we describe some of the details regarding the data analysis procedures used in the experiments demonstrating entanglement generated by dissipation & steady state entanglement (chapter 7).

D.1 Initial atomic noise

The initial atomic noise is characterized using the methods detailed in Sec. 3.11. To be specific, this means that we calibrate κ^2 and T_2 beforehand. κ^2 is measured by the mean value transfer method (see Sec. 3.6), and both κ^2 and T_2 are measured for different atomic densities. We then measure the atomic noise of the fully pumped state with a one ms probe pulse. Using the calibration of κ^2 and T_2, we find the initial atomic noise in PN units at both the room-temperature and high-temperature settings.

The initial atomic noise is used as a fixed parameter when calculating the atomic noise for $t > 0$. This requires a small comment. When measuring κ^2 with the mean value transfer method, two probe pulses are used. The pulses have edges where the light intensity is ramped from zero to some peak value. In the experiments where entanglement is generated by dissipation, the atomic noise is *not* measured using a separate pulse of light. Instead, a long drive pulse is used and afterwards in the data-analysis (on the computer), the measured data are chopped into smaller time-bins (or pulses) which are analyzed separately. These time-bins have no edges.

κ^2 depends on the number of photons which differs in pulses with and without edges. The duration of an edge is approximately 100 μs. The duration of the time-bins is denoted t_{probe}. For the case $t_{\text{probe}} = 1$ ms, the edge duration is 10% of the whole duration. This would lead to a change in κ^2 of also 10% (this is a rough estimate). It is therefore problematic to use κ^2 found from the mean value transfer calibration in the data analysis of time bins of a long pulse.

On the other hand, the initial atomic noise should not depend on if the probe

pulse has edges or not. It should actually not depend on the probe duration either. We have therefore chosen to first calibrate κ^2 using the mean value transfer method using two 1 ms pulses. Then, the initial noise is measured using a similar 1 ms pulse. Afterwards, we measure the initial atomic noise using a time-bin (which has no edges) chopped out from the beginning of the long drive pulse. By equating the initial atomic noise measured by the 1 ms probe pulse and the atomic noise measured using the time-bin with duration t_{probe}, we can find a value for $\kappa^2(t=0)$ which is valid for the time-bin.

D.2 Time-evolution of the coupling constants

In the previous section, we detailed how the coupling constant κ^2 at the initial time $t = 0$ was calibrated. We now continue by describing how κ^2 is calculated for times $t > 0$. The main thing which needs to be incorperated in the data analysis is that the mean spin is time-dependent $J_x = J_x(t)$. This leads to a time-dependent coupling constant and decay time: $\kappa^2 = \kappa^2(t)$ and $T_2 = T_2(t)$.

The mean spin is proportional to the compensated Faraday angle: $J_x(t) \propto \theta_4(t)$ which can be calculated from the measured Faraday angle $\theta_F(t)$. To find out how κ^2 and T_2 depend on J_x, let us instead consider the rates γ_{sw} and γ_{bad}. The relation between these parameters is given by Eq. (2.64) and the fact that $\gamma = \gamma_{\text{sw}} + \gamma_{\text{bad}} = 1/T_2$.

$\gamma_{\text{sw}}(0)$ and $\gamma_{\text{bad}}(0)$ can be found using $\kappa^2(0)$ and $T_2(0)$. At later times, the following model is used for the time-evolution of the rates:

$$\gamma_{\text{sw}}(t) = \gamma_{\text{sw}}(0) \cdot \frac{\theta_4(t)}{\theta_{\text{max}}} \quad \text{and} \quad \gamma_{\text{bad}}(t) = \gamma_{\text{bad}}(0). \tag{D.1}$$

Here it is assumed that the atoms are fully pumped at time $t = 0$ such that $\theta_4(0) = \theta_{\text{max}}$. The above model is reasonable since the swap and squeezing interaction theory predicts that γ_{sw} is proportional to J_x (see Eqs. (2.51) and (2.57)).

Using the above model, it is possible to calculate the time evolution of the rates $\gamma_{\text{sw}}(t)$ and $\gamma_{\text{bad}}(t)$ for $t > 0$. The rates vary on the slow time-scale set by the T_1-time. Since the length of the time-bins $t_{\text{probe}} \approx 0.5$-1 ms is short compared to the T_1-time, the rates can be considered constant from time t to $t + t_{\text{probe}}$ Once the time-dependences of $\gamma_{\text{sw}}(t)$ and $\gamma_{\text{bad}}(t)$ are known, the atomic noise $\Sigma_{\text{EPR}}(t)$ at time t can be calculated from the measured light noise in the time interval t to $t + t_{\text{probe}}$ for any time $t > 0$ using the methods of Sec. 3.11.

D.3 Faraday angle compensation

The coupling strength κ^2 depends on the mean spin J_x of atoms in the $F = 4$ manifold. J_x is continuously monitored by measuring the Faraday rotation of

a weak probe beam denoted the Faraday probe. Usually, the mean spin J_x is considered proportional to the rotation angle θ_F. However, if many atoms are present in the $F = 3$ manifold, this is no longer true. This is because atoms in the $F = 3$ manifold also contribute slightly to the Faraday angle. Usually, we assume that the contribution from $F = 3$ atoms is small, since the Faraday probe is far detuned from transitions starting from the $F = 3$ states and since in many cases most atoms are in the $F = 4$ manifold.

In the experiments presented in this chapter, it happens that many atoms are located in the $F = 3$ manifold. Then, the measured Faraday angle should be corrected for the $F = 3$ atoms. There are two contributions to the Faraday angle. One contribution θ_4 from the atoms in the $F = 4$ manifold and one contribution θ_3 from the atoms in the $F = 3$ manifold. The total angle of rotation is given by

$$\theta_F = \theta_4 + \theta_3 = K \cdot \left[4p_4 N_4 \frac{a_1(\Delta_{45'})}{\Delta_{45'}} + 3p_3 N_3 \frac{a_1(\Delta_{32'})}{\Delta_{32'}} \right], \tag{D.2}$$

where K is a proportionality constant which can be found by comparing with Eq. (3.1). p_4 and p_3 are the orientations of the $F = 4$ and $F = 3$ manifolds, respectively. N_4 and N_3 are the number of atoms in the $F = 4$ and $F = 3$ manifolds. The total number of atoms is $N = N_4 + N_3$. $\Delta_{45'}$ and $\Delta_{32'}$ are the Faraday probe detunings from the transitions $F = 4 \rightarrow F' = 5$ and $F = 3 \rightarrow F' = 2$. $a_1(\Delta_{45'})$ and $a_1(\Delta_{32'})$ are the vector polarizablities of the cesium atom for the $F = 4$ and the $F = 3$ ground states [1]. For the detuning $\Delta_{45'} = -850$ MHz, we have $|\Delta_{23'}| = |\Delta_{\mathrm{hfs}}| - |\Delta_{2'5'}| + \Delta_{45'}$ (see cesium level scheme in Fig. 2.1). Using the hyperfine splitting $|\Delta_{\mathrm{hfs}}| = 9193$ MHz and the energy difference between the $F' = 2$ and the $F' = 5$ excited states $|\Delta_{2'5'}| = 603$ MHz, we find $\Delta_{23'} = 9193 - 603 + (-850)$ MHz $= 7740$ MHz. Remember the convention that a detuning is positive if the laser frequency is less than the atomic transition. For the above mentioned detunings, we have $a_1(\Delta_{45'}) = 1.14 > 0$ and $a_1(\Delta_{23'}) = -1.03 < 0$ such that $a_1(\Delta_{45'})/\Delta_{45'} < 0$ and $a_1(\Delta_{23'})/\Delta_{23'} < 0$. Since both of these numbers have the same sign (negative), θ_4 and θ_3 also have the same sign. Since $\theta_4 = \theta_F - \theta_3$, we see that the measured angle θ_F overestimates the contribution to the angle from the $F = 4$ atoms.

In the typical experiment all atoms are initally pumped into the state $F = 4, m = 4$. In this situation, the Faraday angle is maximal at $t = 0$ (for a given number of atoms N) and has the value (compare with Eq. (D.2))

$$\theta_{\max} = K \cdot 4 \cdot 1 \cdot N \cdot \frac{a_1(\Delta_{45'})}{\Delta_{45'}}. \tag{D.3}$$

[1] The vector polarizability for the $F = 4$ ground state should be evaluated with the detuning $\Delta_{45'}$. This is how a_1 for the $F = 4$ states was defined in the thesis [32]. Similarly, the vector polarizability for the $F = 3$ states should be evaluated with respect to the detuning $\Delta_{23'}$. Notice that in [32], the sign of $a_1(\Delta_{32'})$ is wrong.

We can now solve Eq. (D.2) for N_4/N or θ_4/θ_F using Eq. (D.3) and the fact $N_3 = N - N_4$. After defining the parameter

$$D \equiv \frac{3}{4}\frac{a_1(\Delta_{32'})}{a_1(\Delta_{45'})}\frac{\Delta_{45'}}{\Delta_{32'}}, \tag{D.4}$$

we find

$$\frac{N_4}{N} = \frac{\theta_F/\theta_{\max} - Dp_3}{p_4 - Dp_3} \quad \text{and} \quad \frac{\theta_4}{\theta_{\max}} = \frac{\theta_{\mathrm{F}}/\theta_{\max} - \mathrm{Dp_3}}{1 - \mathrm{D}\frac{\mathrm{p_3}}{\mathrm{p_4}}}. \tag{D.5}$$

For the above stated detunings we have $D = 0.074$.

In the analysis of the data presented in chapter 7, it is assumed that $p_4 = 1$ and $p_3 = 1$.

In the paper [3], experimental results of p_4 are presented. After the optical pumping stage, the orientation of the atoms equal $p_4 = 0.998(3)$. After 15 ms of drive light on the atoms, the orientation is reduced to $p_4 = 0.980(3)$. The assumption $p_4 = 1$ is therefore a good assumption.

$p_3 = 1$ is a worst case scenario which compensates maximally for the $F = 3$ atoms. If we instead had chosen a lower value for p_3, this would lead to an estimate of the atomic noise which is lower (than the estimate for the atomic noise using $p_3 = 1$). To be on the safe side, we stick to the value $p_3 = 1$. Also, experimental measurements of Magneto-Optical Resonance Signals (MORS) [41] of the $F = 3$ atoms shows that p_3 has a value close to 1 for our experimental settings.

Bibliography

[1] K. Jensen, W. Wasilewski, H. Krauter, T. Fernholz, B. M. Nielsen, M. Owari, M. B. Plenio, A. Serafini, M. M. Wolf, and E. S. Polzik. Quantum memory for entangled continuous-variable states. *Nature Physics*, 7:13–16, 2011.

[2] W. Wasilewski, K. Jensen, H. Krauter, J. J. Renema, M. V. Balabas, and E. S. Polzik. Quantum noise limited and entanglement-assisted magnetometry. *Phys. Rev. Lett.*, 104(13):133601, Mar 2010.

[3] H Krauter, C. A. Muschik, K. Jensen, W Wasilewski, J. M. Petersen, J. I. Cirac, and E. S. Polzik. Entanglement generated by dissipation. arXiv:1006.4344v1, 2010.

[4] W. Wasilewski, T. Fernholz, K. Jensen, L. S. Madsen, H. Krauter, C. Muschik, and E. S. Polzik. Generation of two-mode squeezed and entangled light in a single temporal and spatial mode. *Opt. Express*, 17:14444–14457, 2009.

[5] T. Fernholz, H. Krauter, K. Jensen, J. F. Sherson, A. S. Sørensen, and E. S. Polzik. Spin squeezing of atomic ensembles via nuclear-electronic spin entanglement. *Physical Review Letters*, 101(7):073601, 2008.

[6] K. Jensen, V. M. Acosta, J. M. Higbie, M. P. Ledbetter, S. M. Rochester, and D. Budker. Cancellation of nonlinear Zeeman shifts with light shifts. *Phys. Rev. A*, 79(2):023406, Feb 2009.

[7] M. V. Balabas, K. Jensen, W. Wasilewski, H. Krauter, L. S. Madsen, J. H. Müller, T. Fernholz, and E. S. Polzik. High quality anti-relaxation coating material for alkali atom vapor cells. *Opt. Express*, 18(6):5825–5830, 2010.

[8] A. Einstein, B. Podolsky, and N. Rosen. Can Quantum-Mechanical Description of Physical Reality Be Considered Complete? *Phys. Rev.*, 47(10):777–780, May 1935.

[9] J. S. Bell. On the Einstein Podolsky Rosen paradox. *Physics*, 1:195–200, 1964.

[10] Charles H. Bennett and Gilles Brassard. Quantum cryptography: Public key distribution and coin tossing. *Proceedings of IEEE International Conference on Computers Systems and Signal Processing, Bangalore, India*, pages 175–179, 1984.

[11] H. J. Kimble. The quantum internet. *Nature*, 453:1023–1030, 2008.

[12] L.-M. Duan, M. D. Lukin, J. I. Cirac, and P. Zoller. Long-distance quantum communication with atomic ensembles and linear optics. *Nature*, 414:413–418, 2001.

[13] Charles H. Bennett, Gilles Brassard, Claude Crépeau, Richard Jozsa, Asher Peres, and William K. Wootters. Teleporting an unknown quantum state via dual classical and Einstein-Podolsky-Rosen channels. *Phys. Rev. Lett.*, 70(13):1895–1899, Mar 1993.

[14] Pieter Kok, Hwang Lee, and Jonathan P. Dowling. Creation of large-photon-number path entanglement conditioned on photodetection. *Phys. Rev. A*, 65(5):052104, Apr 2002.

[15] J. Appel, P. J. Windpassinger, D. Oblak, U. B. Hoff, N. Kjærgaard, and E. S. Polzik. Mesoscopic atomic entanglement for precision measurements beyond the standard quantum limit. *Proceedings of the National Academy of Sciences*, 106(27):10960–10965, 2009.

[16] B Julsgaard, A Kozhekin, and E S Polzik. Experimental long-lived entanglement of two macroscopic objects. *Nature*, 413:400–403, 2001.

[17] B Julsgaard, J Sherson, J I Cirac, J Fiurášek, and E S Polzik. Experimental demonstration of quantum memory for light. *Nature*, 432:482–486, 2004.

[18] J Sherson, H Krauter, R K Olsson, B Julsgaard, K Hammerer, I Cirac, and E S Polzik. Quantum teleportation between light and matter. *Nature*, 443:557–560, 2006.

[19] Klemens Hammerer, Anders S. Sørensen, and Eugene S. Polzik. Quantum interface between light and atomic ensembles. *Rev. Mod. Phys.*, 82(2):1041–1093, Apr 2010.

[20] N. J. Cerf, G. Leuchs, and E. S. Polzik, editors. *Quantum Information with Continuous Variables of Atoms and Light*. Imperial College Press, 2007.

[21] D. F. Phillips, A. Fleischhauer, A. Mair, R. L. Walsworth, and M. D. Lukin. Storage of light in atomic vapor. *Phys. Rev. Lett.*, 86(5):783–786, Jan 2001.

[22] Jürgen Appel, Eden Figueroa, Dmitry Korystov, M. Lobino, and A. I. Lvovsky. Quantum memory for squeezed light. *Phys. Rev. Lett.*, 100(9):093602, Mar 2008.

[23] M. D. Eisaman, A. Andre, F. Massou, M. Fleischhauer, A. S. Zibrov, and M. D. Lukin. Electromagnetically induced transparency with tunable single-photon pulses. *Nature*, 438:837–841, 2005.

[24] Eugeniy E. Mikhailov and Irina Novikova. Low-frequency vacuum squeezing via polarization self-rotation in Rb vapor. *Opt. Lett.*, 33(11):1213–1215, Jun 2008.

[25] C. W. Chou, H. de Riedmatten, D. Felinto, S. V. Polyakov, S. J. van Enk, and H. J. Kimble. Measurement-induced entanglement for excitation stored in remote atomic ensembles. *Nature*, 438:828–832, 2005.

[26] T Chaneliere, D. N. Matsukevich, S. D. Jenkins, S.-Y. Lan, T. A. B. Kennedy, and A. Kuzmich. Storage and retrieval of single photons transmitted between remote quantum memories. *Nature*, 438:833–836, 2005.

[27] R. Zhao, Y. O. Dudin, S. D. Jenkins, C. J. Campbell, D. N. Matsukevich, T. A. B. Kennedy, and A. Kuzmich. Long-lived quantum memory. *Nat. Phys.*, 5(2):100–104, Feb 2009.

[28] Bo Zhao, Yu-Ao Chen, Xiao-Hui Bao, Thorsten Strassel, Chih-Sung Chuu, Xian-Min Jin, Jorg Schmiedmayer, Zhen-Sheng Yuan, Shuai Chen, and Jian-Wei Pan. A millisecond quantum memory for scalable quantum networks. *Nat. Phys.*, 5:95–99, 2009.

[29] M. Koschorreck, M. Napolitano, B. Dubost, and M. W. Mitchell. Sub-projection-noise sensitivity in broadband atomic magnetometry. *Phys. Rev. Lett.*, 104(9):093602, Mar 2010.

[30] S. Wildermuth, S. Hofferberth, I. Lesanovsky, S. Groth, P. Krueger, J. Schmiedmayer, and I. Bar-Joseph. Sensing electric and magnetic fields with Bose-Einstein condensates. *Applied Physics Letters*, 88(26), Jun 2006.

[31] M. Vengalattore, J. M. Higbie, S. R. Leslie, J. Guzman, L. E. Sadler, and D. M. Stamper-Kurn. High-resolution magnetometry with a spinor bose-einstein condensate. *Phys. Rev. Lett.*, 98(20):200801, May 2007.

[32] B Julsgaard. *Entanglement and Quantum Interactions with Macroscopic Gas Samples.* PhD thesis, University of Aarhus (2003). http://www.quantop.nbi.dk/pdfs/theses/brian_thesis.pdf.

[33] J Sherson. *Quantum Memory and Teleportation Using Macroscopic Gas Samples*. PhD thesis, University of Aarhus (2006). http://www.quantop.nbi.dk/pdfs/theses/jacob_thesis.pdf.

[34] H. Krauter. *Generation and application of entanglement of room temperature ensembles of atoms*. PhD thesis, University of Copenhagen (2011).

[35] T. Holstein and H. Primakoff. Field dependence of the intrinsic domain magnetization of a ferromagnet. *Phys. Rev.*, 58:1098, 1940.

[36] L. M. Duan, G. Giedke, J. I. Cirac, and P. Zoller. Inseparability criterion for continuous variable systems. *Phys. Rev. Lett.*, 84:2722, 2000.

[37] J. M. Geremia, John K. Stockton, and Hideo Mabuchi. Tensor polarizability and dispersive quantum measurement of multilevel atoms. *Phys. Rev. A*, 73(4):042112, Apr 2006.

[38] S. M. Rochester and D. Budker. Atomic polarization visualized. *American Journal of Physics*, 69(4):450, 2001.

[39] M. Koschorreck, M. Napolitano, B. Dubost, and M. W. Mitchell. Quantum nondemolition measurement of large-spin ensembles by dynamical decoupling. *Phys. Rev. Lett.*, 105(9):093602, Aug 2010.

[40] M. V. Balabas, T. Karaulanov, M. P. Ledbetter, and D. Budker. Polarized alkali-metal vapor with minute-long transverse spin-relaxation time. *Phys. Rev. Lett.*, 105(7):070801, Aug 2010.

[41] B Julsgaard, J Sherson, J L Sørensen, and E S Polzik. Characterizing the spin state of an atomic ensemble using the magneto-optical resonance method. *Journal of Optics B: Quantum and Semiclassical Optics*, 6(1):5, 2004.

[42] A. Kuzmich, L. Mandel, and N. P. Bigelow. Generation of spin squeezing via continuous quantum nondemolition measurement. *Phys. Rev. Lett.*, 85(8):1594–1597, Aug 2000.

[43] V. Shah, G. Vasilakis, and M. V. Romalis. High bandwidth atomic magnetometery with continuous quantum nondemolition measurements. *Phys. Rev. Lett.*, 104(1):013601, Jan 2010.

[44] T. C. Ralph. Continuous variable quantum cryptography. *Phys. Rev. A*, 61(1):010303, Dec 1999.

[45] A. Furusawa, J. L. Sørensen, S. L. Braunstein, C. A. Fuchs, H. J. Kimble, and E. S. Polzik. Unconditional Quantum Teleportation. *Science*, 282(5389):706–709, 1998.

[46] Seth Lloyd and Samuel L. Braunstein. Quantum computation over continuous variables. *Phys. Rev. Lett.*, 82(8):1784–1787, Feb 1999.

[47] Carlton M. Caves. Quantum-mechanical noise in an interferometer. *Phys. Rev. D*, 23(8):1693–1708, Apr 1981.

[48] Florian Wolfgramm, Alessandro Cerè, Federica A. Beduini, Ana Predojević, Marco Koschorreck, and Morgan W. Mitchell. Squeezed-light optical magnetometry. *Phys. Rev. Lett.*, 105(5):053601, Jul 2010.

[49] Z. Y. Ou, S. F. Pereira, H. J. Kimble, and K. C. Peng. Realization of the Einstein-Podolsky-Rosen paradox for continuous variables. *Phys. Rev. Lett.*, 68(25):3663–3666, Jun 1992.

[50] Henning Vahlbruch, Moritz Mehmet, Simon Chelkowski, Boris Hage, Alexander Franzen, Nico Lastzka, Stefan Goßler, Karsten Danzmann, and Roman Schnabel. Observation of squeezed light with 10-db quantum-noise reduction. *Phys. Rev. Lett.*, 100(3):033602, Jan 2008.

[51] R. E. Slusher, L. W. Hollberg, B. Yurke, J. C. Mertz, and J. F. Valley. Observation of squeezed states generated by four-wave mixing in an optical cavity. *Phys. Rev. Lett.*, 55(22):2409–2412, Nov 1985.

[52] A. Lambrecht, T. Coudreau, A. M. Steinberg, and E. Giacobino. Squeezing with cold atoms. *EPL (Europhysics Letters)*, 36(2):93, 1996.

[53] V. Josse, A. Dantan, A. Bramati, M. Pinard, and E. Giacobino. Continuous variable entanglement using cold atoms. *Phys. Rev. Lett.*, 92(12):123601, Mar 2004.

[54] J. Ries, B. Brezger, and A. I. Lvovsky. Experimental vacuum squeezing in rubidium vapor via self-rotation. *Phys. Rev. A*, 68(2):025801, Aug 2003.

[55] http://en.wikipedia.org/wiki/Karhunen-Loève_theorem.

[56] lecture notes on "Principal component analysis and Karhunen-Loeve transform". http://fourier.eng.hmc.edu/e161/lectures/klt/index.html.

[57] Dmitry Budker and Michael Romalis. Optical magnetometry. *Nature Physics*, 3:227–234, 2007.

[58] D. J. Wineland, J. J. Bollinger, W. M. Itano, F. L. Moore, and D. J. Heinzen. Spin squeezing and reduced quantum noise in spectroscopy. *Phys. Rev. A*, 46(11):R6797–R6800, Dec 1992.

[59] S. F. Huelga, C. Macchiavello, T. Pellizzari, A. K. Ekert, M. B. Plenio, and J. I. Cirac. Improvement of frequency standards with quantum entanglement. *Phys. Rev. Lett.*, 79(20):3865–3868, Nov 1997.

[60] M. Auzinsh, D. Budker, D. F. Kimball, S. M. Rochester, J. E. Stalnaker, A. O. Sushkov, and V. V. Yashchuk. Can a Quantum Nondemolition Measurement Improve the Sensitivity of an Atomic Magnetometer? *Phys. Rev. Lett.*, 93(17):173002, Oct 2004.

[61] A. André, A. S. Sørensen, and M. D. Lukin. Stability of atomic clocks based on entangled atoms. *Phys. Rev. Lett.*, 92(23):230801, Jun 2004.

[62] Vivi Petersen, Lars Bojer Madsen, and Klaus Mølmer. Magnetometry with entangled atomic samples. *Phys. Rev. A*, 71(1):012312, Jan 2005.

[63] John K. Stockton, J. M. Geremia, Andrew C. Doherty, and Hideo Mabuchi. Robust quantum parameter estimation: Coherent magnetometry with feedback. *Phys. Rev. A*, 69(3):032109, Mar 2004.

[64] I. K. Kominis. Sub-shot-noise magnetometry with a correlated spin-relaxation dominated alkali-metal vapor. *Phys. Rev. Lett.*, 100(7):073002, 2008.

[65] P. Cappellaro and M. D. Lukin. Quantum correlation in disordered spin systems: Applications to magnetic sensing. *Phys. Rev. A*, 80(3):032311, 2009.

[66] D. Leibfried, M. D. Barrett, T. Schaetz, J. Britton, J. Chiaverini, W. M. Itano, J. D. Jost, C. Langer, and D. J. Wineland. Toward Heisenberg-Limited Spectroscopy with Multiparticle Entangled States. *Science*, 304(5676):1476–1478, 2004.

[67] C. F. Roos, M. Chwalla, K. Kim, Riebe, and R. M., Blatt. 'Designer atoms' for quantum metrology. *Nature*, 443:316, 2006.

[68] J. Esteve, C. Gross, A. Weller, S. Giovanazzi, and M. K. Oberthaler. Squeezing and entanglement in a Bose-Einstein condensate. *Nature*, 455(7217):1216–1219, October 2008.

[69] Monika H. Schleier-Smith, Ian D. Leroux, and Vladan Vuletić. States of an ensemble of two-level atoms with reduced quantum uncertainty. *Phys. Rev. Lett.*, 104(7):073604, Feb 2010.

[70] G. Vasilakis, V. Shah, and M.V. Romalis. Stroboscopic back-action evasion in a dense alkali-metal vapor. arXiv:1011.2682v1, 2010.

[71] S.-K. Lee, K. L. Sauer, S. J. Seltzer, O. Alem, and M. V. Romalis. Subfemtotesla radio-frequency atomic magnetometer for detection of nuclear quadrupole resonance. *Applied Physics Letters*, 89(21):214106, 2006.

[72] H.C. Seton, J.M.S. Hutchison, and D.M. Bussell. Liquid helium cryostat for squid-based mri receivers. *Cryogenics*, 45(5):348 – 355, 2005.

[73] Alexander I. Lvovsky, Barry C. Sanders, and Wolfgang Tittel. Optical quantum memory. *Nature Photonics*, 3:706–714, 2009.

[74] Timothy C. Ralph and Ping K. Lam. A bright future for quantum communications. *Nature Photonics*, 3:671–673, 2009.

[75] J. B. Brask, I. Rigas, E. S. Polzik, U. L. Andersen, and A. S. Sørensen. Hybrid long-distance entanglement distribution protocol. *Phys. Rev. Lett.*, 105(16):160501, Oct 2010.

[76] Nicolas Sangouard, Christoph Simon, Nicolas Gisin, Julien Laurat, Rosa Tualle-Brouri, and Philippe Grangier. Quantum repeaters with entangled coherent states. *J. Opt. Soc. Am. B*, 27(6):A137–A145, Jun 2010.

[77] Mile Gu, Christian Weedbrook, Nicolas C. Menicucci, Timothy C. Ralph, and Peter van Loock. Quantum computing with continuous-variable clusters. *Phys. Rev. A*, 79(6):062318, Jun 2009.

[78] Kazuhito Honda, Daisuke Akamatsu, Manabu Arikawa, Yoshihiko Yokoi, Keiichirou Akiba, Satoshi Nagatsuka, Takahito Tanimura, Akira Furusawa, and Mikio Kozuma. Storage and retrieval of a squeezed vacuum. *Phys. Rev. Lett.*, 100(9):093601, Mar 2008.

[79] Gerardo Adesso and Giulio Chiribella. Quantum benchmark for teleportation and storage of squeezed states. *Physical Review Letters*, 100(17):170503, 2008.

[80] Christopher C. Gerry and Peter L. Knight. *Introductory Quantum Optics*. Cambridge University Press, 2005.

[81] M Owari, M B Plenio, E S Polzik, A Serafini, and M M Wolf. Squeezing the limit: quantum benchmarks for the teleportation and storage of squeezed states. *New Journal of Physics*, 10(11):113014, 2008.

[82] M. B. Plenio and S. F. Huelga. Entangled light from white noise. *Phys. Rev. Lett.*, 88(19):197901, Apr 2002.

[83] B. Kraus and J. I. Cirac. Discrete entanglement distribution with squeezed light. *Phys. Rev. Lett.*, 92(1):013602, Jan 2004.

[84] S. Diehl, A. Micheli, A. Kantian, B. Kraus, H. P. Buechler, and P. Zoller. Quantum states and phases in driven open quantum systems with cold atoms. *Nature Physics*, 4(11):878–883, Nov 2008.

[85] Frank Verstraete, Michael M. Wolf, and J. Ignacio Cirac. Quantum computation and quantum-state engineering driven by dissipation. *Nature Physics*, 5(9):633–636, Sep 2009.

[86] C. A. Muschik, E. S. Polzik, and J. I. Cirac. Dissipatively driven entanglement of two macroscopic atomic ensembles. arXiv:1007.2209v1, 2010.

[87] Karl Gerd H. Vollbrecht, Christine A. Muschik, and J. Ignacio Cirac. Entanglement distillation by dissipation and continuous quantum repeaters. arXiv:1011.4115v1, 2010.

[88] J. S. Neergaard-Nielsen, B. M. Nielsen, H. Takahashi, A. I. Vistnes, and E. S. Polzik. High purity bright single photon source. *Opt. Express*, 15(13):7940–7949, Jun 2007.

[89] B. Melholt Nielsen, J. S. Neergaard-Nielsen, and E. S. Polzik. Time gating of heralded single photons for atomic memories. *Opt. Lett.*, 34(24):3872–3874, Dec 2009.

[90] K. Usami, A. Naesby, T. Bagci, B. Melholt Nielsen, J. Liu, S. Stobbe, P. Lodahl, and E. S. Polzik. Optoelectronic cooling of mechanical modes in a semiconductor nanomembrane. arXiv:1011.3974v2, 2010.

[91] K. Hammerer, M. Aspelmeyer, E. S. Polzik, and P. Zoller. Establishing Einstein-Poldosky-Rosen Channels between Nanomechanics and Atomic Ensembles. *Phys. Rev. Lett.*, 102(2):020501, Jan 2009.

[92] Rainer Blatt and David Wineland. Entangled states of trapped atomic ions. *Nature*, 453:1008–1015, 2008.

[93] S. Olmschenk, D. N. Matsukevich, P. Maunz, D. Hayes, L.-M. Duan, and C. Monroe. Quantum Teleportation Between Distant Matter Qubits. *Science*, 323(5913):486–489, 2009.

[94] Christian F. Roos, Mark Riebe, Hartmut Häffner, Wolfgang Hänsel, Jan Benhelm, Gavin P. T. Lancaster, Christoph Becher, Ferdinand Schmidt-Kaler, and Rainer Blatt. Control and Measurement of Three-Qubit Entangled States. *Science*, 304(5676):1478–1480, 2004.

[95] K. S. Choi, A. Goban, S. B. Papp, S. J. van Enk, and H. J. Kimble. Entanglement of spin waves among four quantum memories. *Nature*, 468:412–416, 2010.

[96] Julio T. Barreiro, Philipp Schindler, Otfried Guhne, Thomas Monz, Michael Chwalla, Christian F. Roos, Markus Hennrich, and Rainer Blatt. Experimental multiparticle entanglement dynamics induced by decoherence. *Nature Physics*, 6:943–946, 2010.